

# Chemical Redox of Lithium Ion Battery Materials

A Dissertation

Presented to

The Faculty of the School of Engineering and Applied Science

University of Virginia

in partial fulfilment

of the requirements of the degree

Doctor of Philosophy in Chemical Engineering

by

Devanshi Gupta

August 2021

## Executive Summary

To achieve carbon neutrality by mid-21<sup>st</sup> century, rapid deployment of large-scale electrical energy storage options is required to integrate intermittent renewable energy resources such as solar and wind, and catalyze smart-grid infrastructure. Electrochemical energy storage technologies such as Li-ion batteries (LIBs) and redox flow batteries (RFBs) offer the modularity and scalability required for large-scale energy storage. RFBs operate by spatial separation of electrode and electrolyte, providing energy and power decoupling. This gives them an advantage over conventional LIBs, in terms of long life cycles (>10,000 cycle, 10-20 years) and inherent safety. However, the volumetric energy density of RFBs (<100 Wh l<sup>-1</sup>) is far lower than standard LIBs (600-650 Wh l<sup>-1</sup>). A hybrid electrochemical system called redox-targeting flow batteries (RTFBs) was suggested in 2013 that uses chemical redox of charge dense Li-ion battery materials through redox-targeting reactions, and has a theoretical capacity of > 500 Wh l<sup>-1</sup>. RTFBs however are in embryonic stages of development. The design principles of electroactive materials and the chemical redox reaction mechanism would need to be established to realize full-scale deployment of RTFBs.

To address these challenges, chemical redox kinetics and RTFB design were investigated in this dissertation. In Chapter II, chemical redox kinetics were compared to the well-studied electrochemical kinetics of LFP. Chemical redox of LFP by ferrocene-based redox shuttles was evaluated using *in-operando* UV-Vis spectroscopy, whereas LFP half-cells were potentiostatically charged/discharged. The kinetics and phase transformations of the two redox routes were estimated using Johnson-Mehl-Avrami-Erofeyev-Kolomogorov model (JMAEK). It was revealed that the reaction pathway and phase transformations are different for chemical and electrochemical redox.

The first-order rate constants were consistently lower for chemical redox than electrochemical redox. Additionally, apparent activation energy calculations suggested that the low redox shuttle concentrations ( $<1 \times 10^{-3} \text{ mol l}^{-1}$ ) could be the cause behind poor kinetics. This issue was mitigated in Chapter III by increasing the redox shuttle concentration by a hundredfold. Furthermore, six derivatives of ferrocene-based redox shuttles were characterized using cyclic voltammetry for the redox targeting kinetics with LFP. The reactions were analyzed using two first-order kinetic models – JMAEK and 1-D diffusion model. Chemical redox kinetics of LFP with the shuttles showed no significant dependence on the redox potential and diffusion coefficient of the shuttles. This suggests specific redox shuttle-particle interactions influence the reaction rates. Moreover, robust experimental system was designed to compare redox shuttles for redox-targeting applications.

In Chapter IV, the design of LFP packed bed reactor (PBR) as the chemical reservoir is explored by changing four design variables: packed-bed height, concentration of redox shuttle, flow rate of electrolyte, and operating temperature. It was found that concentration of redox shuttle is the leading factor affecting the rate of chemical oxidation of LFP PBR. Additionally, under the reaction conditions tested, the rate-limiting step was observed to be dependent upon operating conditions. To further explore the reaction mechanism in LFP PBR, spatiotemporal progression of chemical oxidation was mapped using X-ray and neutron tomography in Chapter V. Reaction heterogeneities observed using neutron tomography were found to be correlated to the LFP particle size and random distribution of LFP aggregates in the PBR.

# Bibliography

The publications that resulted/will result from this dissertation are listed below:

## Chapter II

- D. Gupta, C. Cai, G.M. Koenig, Comparative Analysis of Chemical Redox between Redox Shuttles and a Lithium-Ion Cathode Material via Electrochemical Analysis of Redox Shuttle Conversion, *J. Electrochem. Soc.* 168 (2021) 050546.  
<https://doi.org/10.1149/1945-7111/ac0068>.

## Chapter III

- D. Gupta, C. Cai, G.M. Koenig, Comparative Analysis of Chemical Redox between Redox Shuttles and a Lithium-Ion Cathode Material via Electrochemical Analysis of Redox Shuttle Conversion, *J. Electrochem. Soc.* 168 (2021) 050546.  
<https://doi.org/10.1149/1945-7111/ac0068>.

## Chapter IV

- D. Gupta, Y. Zhang, Z. Nie, J. Wang, G.M. Koenig, Chemical Redox of Lithium Ion Solid Electroactive Material in a Packed Bed Flow Reactor. *Submitted. Chemical Engineering Science*.

## Chapter V

- D. Gupta, Y. Zhang, H. Bilheaux, J.C. Bilheaux, Z. Nie, G.M. Koenig, Neutron Tomography of Chemical Redox Progression of Lithium-Ion Solid Electroactive Material. *In preparation*.

# Table of Contents

<b>Executive Summary.....</b>	<b>1</b>
<b>Bibliography.....</b>	<b>3</b>
<b>Chapter I. Research Background: Redox-targeting Flow Batteries.....</b>	<b>8</b>
1.1 Overview.....	8
1.2 Broader Scope.....	9
1.3 Redox Flow Battery Design.....	11
1.4 Redox-targeting Flow Batteries.....	16
1.4.1 Material Selection and Design.....	18
1.4.2 Kinetics of Redox-targeting Reactions.....	23
1.4.3 RTFB Extensions.....	25
1.5 Scope of Dissertation.....	28
1.6 References.....	31
<b>Chapter II. Analysis of Chemical and Electrochemical Lithiation/Delithiation of a Lithium-Ion Cathode Material.....</b>	<b>39</b>
2.1 Overview.....	39
2.2 Abstract.....	40
2.3 Introduction.....	41

2.4 Experimental.....	43
2.5 Results.....	46
2.6 Discussion.....	60
2.7 Conclusions.....	68
2.8 References.....	69

**Chapter III. Comparative Analysis of Chemical Redox between Redox Shuttles and a Lithium-Ion Cathode Material via Electrochemical Analysis of Redox Shuttle Conversion...xx**

3.1 Overview.....	74
3.2 Abstract.....	75
3.3 Introduction.....	76
3.4 Experimental.....	79
3.5 Results.....	83
3.6 Discussion.....	91
3.7 Conclusions.....	103
3.8 References.....	105

**Chapter IV. Chemical Redox of Lithium-Ion Solid Electroactive Material in a Packed Bed Flow Reactor.....111**

4.1 Overview.....	111
-------------------	-----

4.2 Abstract.....	112
4.3 Introduction.....	113
4.4 Materials and Methods.....	117
4.5 Results and Discussion.....	124
4.6 Conclusions.....	144
4.7 References.....	146
<b>Chapter V. Neutron Tomography of Chemical Redox Progression of Lithium-Ion Solid Electroactive Material.....</b>	<b>153</b>
5.1 Overview.....	153
5.2 Introduction.....	154
5.3 Experimental.....	155
5.4 Preliminary Results.....	158
5.5 Conclusions.....	163
5.6 References.....	164
<b>Chapter VI. Future Work.....</b>	<b>166</b>
Acknowledgements.....	170
Appendix A.....	173
Appendix B.....	184

Appendix C.....198

# Chapter I. Research Background: Redox-Targeting Flow Batteries

## *1.1 Overview*

This chapter demonstrates the scientific basis for the research presented in this dissertation. The progression of the strategies to improve the energy density of redox flow batteries (RFBs) is examined. The focus of this chapter and this dissertation will be the use of solid electroactive material as the primary charge storage material in RFBs to overcome the redox-active material solubility limit in conventional RFBs. The RFB design explored in the thesis employs redox-targeting reactions between solid electroactive material and redox shuttles. A comprehensive review of the material chemistries, characterization methods, and battery hybrids that have been implemented using redox-targeting reactions are listed, which provides the foundation for subsequent chapters in this dissertation. Based on the current challenges in the field, the scope of the dissertation is then discussed.

### *Definitions:*

Voltage efficiency = Discharge voltage/Charge voltage

Coulombic efficiency = Discharge capacity/Charge capacity

Energy efficiency = Voltage efficiency  $\times$  Coulombic efficiency

## ***1.2 Broader Scope***

As of June 2021, 34 countries with 3900 jurisdictions have declared climate change as a *climate emergency*[1]. The linguistic change is to acknowledge unprecedented extreme temperatures, wildfires, droughts that have become a common occurrence in the last decade. These events have forced policymakers, corporations, and public to take short-term and long-term measures to mitigate the effects of the climate emergency. Extreme weather conditions caused by the climate emergency are also the leading cause of power failures in the United States[2]. Power grids across the world are engineered to balance the change in demands over the course of days and seasons. However, extreme weather caused by climate emergency put the power supply at risk since there are no historical data to plan and engineer the grids accordingly. For instance, in February 2021, the Texas power grid failed after the temperature in the state plummeted to -19 °C, which is the lowest temperature in the region in seven decades. Since the Texas grids were not engineered for the power demands that follow cold temperatures, a power outage ensued putting 10 million people out of electricity[3]. Power blackouts from extreme events call for grid security and reliability. One of the recent studies found that the Southeast US would need to expand electric capacity by 35% by 2050 just to mitigate the hazards of climate change, which does not include the increase in energy demands by growing population and lifestyle needs[4]. According to World Energy Outlook (IEA 2020), the global energy demands emanating from growth in population and economy would increase by 19% from 2020 to 2040 [5]. Coupled with the goal of achieving carbon neutrality by 2050, sustainable energy resources such as wind, power, geothermal, biomass etc. are expected to be adopted for power generation. However, intermittency of renewable sources such as solar and wind slow down the decarbonization of the utilities landscape. Without technological intervention, the aging grid capabilities in the United States are expected to fail

beyond 20% integration of non-dispatchable renewable energy resources [6]. Hence, energy storage options need to be developed for both our short and long-term goals. In short term, small-scale energy-storage installations can support the rapidly advancing clean energy technologies[5]. For long-term, we would need to develop smart-grid storage options that enable the widespread adoption of renewables.

Among the options available, pumped hydro and compressed air convert potential energy to electrical energy, account for 99% of the current energy storage infrastructure[7]. Pumped hydro and compressed air have low life cycle cost, however they are limited by geographic constraints, environmental impacts, and have slow response to high power demands. On the other hand, flywheels that convert kinetic energy to electric energy have fast power response, but poor round-trip efficiency for slow discharge (several hours)[8]. Electrochemical energy storage (ECES) options, such as batteries and fuel cells, have both short- and long-term energy storage capabilities due to their modularity and site-versatility. ECES are expected to grow more than 10,000 times the current installed capacity, to 150 GW of power generation that includes technologies like Li-ion batteries (and related chemistries such as sodium-ion, Li-sulfur etc.), fuel cells, and redox flow batteries[9,10].

Robust operation lifetimes of ~10 years, cost of installment and operation, depth of discharge (DOD), high energy density, high power density, safety are among the many requirements for grid-level energy storage options. Fulfilling all the criteria is challenging for any technology. Hence, a portfolio of various different technologies that are versatile and modular would be needed. Among them, redox flow batteries are a promising technology that would underpin the scientific endeavors of this dissertation.

### ***1.3 Redox Flow Battery Design***

A redox flow battery (RFB) is a rechargeable battery that stores electrical energy in soluble redox species. RFBs comprise three main components 1) power stack, 2) chemical reservoirs, 3) accessories such as pumps, power conditioning systems, controllers, etc. A schematic of a RFB is shown in Figure 1. The power stack as a unit consists of porous electrodes separated by an ion-exchange membrane, and current collectors attached to the external circuit. The anodic and cathodic redox couple are dissolved in the electrolyte, and are referred to as anolyte and catholyte, respectively. The total energy storage depends upon the volume of the chemical reservoirs. Therefore, the volumetric energy density of RFBs can be improved by selecting high solubility anodic and cathodic redox couples. The anolyte/catholyte solutions are continuously pumped from the anode/cathode tanks to the power stack, where redox reactions occur on the surface of porous electrodes. The charge-balancing ions penetrate through the ion-exchange membrane, and the oxidized/reduced electrolytes are accumulated in the tank. Since the reactions occurring on redox-active sites of the porous electrodes are not accompanied by any structural changes of the electrode, the electrode degradation in RFBs is less severe relative to Li-ion intercalation batteries. For this reason, RFBs have been shown to last up to 10,000-20,000 cycles[11,12]. The power density of RFBs is dependent upon the power stack design and operation. In this way, the power density and energy density of RFBs are decoupled – the size of power stack and chemical reservoirs can be altered to meet specific demands, making them scalable and flexible. The other advantages of RFBs for use in stationary energy storage are – high coulombic efficiency, high DOD, long cycle-life, and fast response time [11].

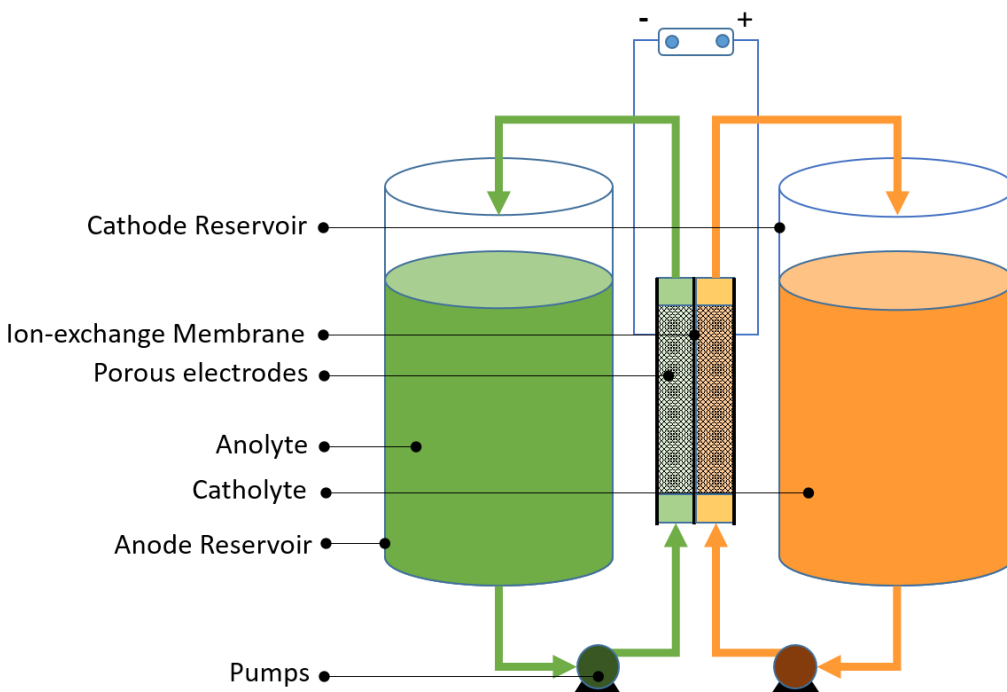


**Figure 1. Schematic of a redox flow battery (RFB)**

Currently, the most widely studied and commercially successful RFBs are all-vanadium redox flow batteries (VRFBs). VRFBs have vanadium in four oxidation states –  $V^{2+}/V^{3+}$  for anolyte and  $VO^{2+}/VO_2^+$ . Since the same chemistry is used for cathode and anode in VRFBs, the cross-contamination across ion-exchange membrane can be treated via a ‘rebalancing’ process thereby mitigating capacity decay, and results in a long operational lifetime. The use of aqueous electrolytes in VRFBs however limits the operational voltage (1.15-1.55 V vs SHE, limited by water electrolysis) resulting in low energy density[13]. Despite the efforts to increase the solubility of vanadium ions using organic and inorganic additives, electrolyte pH, VRFBs offer energy density ( $\sim 25 \text{ Wh l}^{-1}$ ) which is low compared to Li-ion batteries ( $100\text{-}450 \text{ Wh l}^{-1}$ ), or even lead-acid batteries ( $60\text{-}100 \text{ Wh l}^{-1}$ ). In addition, the vanadium resources used in VRFBs amount to a capital cost of  $\$450 \text{ (kW h)}^{-1}$ , which is much higher than the target cost of  $\$150 \text{ kW h}^{-1}$  set by US Department of Energy (DOE)[14]. Other chemistries that use cheaper transition metals such as all-

iron RFBs ( $\text{Fe}^{3+}/\text{Fe}^{2+}$  and  $\text{Fe}^{2+}/\text{Fe}$  as redox active species in the catholyte and anolyte, respectively) share the advantages of VRFBs, however they suffer from low voltage, energy density, and coulombic efficiency[15].

The energy density of RFBs can be increased in three ways- a) by using multi-electron redox couples, b) increase the solubility of redox active species, c) increase the operating cell voltage. Synthesis and application of multi-electron redox couples in RFBs has seen limited success due to poor coulombic efficiency and stability issues[16]. Several approaches have been used to overcome the limitations of VRFBs and similar systems using transition metals, such as the use of non-aqueous electrolytes, organic redox couples, and flowing suspensions of solid electroactive materials[17]. Non-aqueous electrolytes on the other hand provide a wide operational voltage window that enables selection of a range of redox active species such as metallocenes, organic redox molecules, and flexibility of design.

An alternative approach to circumvent solubility and stability issues that arise from soluble redox-active shuttles is to use solid electroactive species as the primary energy storage material. This scheme of using solid active material RFBs was introduced by Duduta et al., and are referred as semi-solid flow batteries (SSFBS)[18]. A schematic for SSFB is shown in Figure 2. Various active materials used primarily in conventional Li-ion batteries such as  $\text{LiCoO}_2$  (LCO),  $\text{LiNi}_{0.5}\text{Mn}_{1.5}\text{O}_4$  (LMNO),  $\text{LiNi}_{1/3}\text{Mn}_{1/3}\text{Co}_{1/3}\text{O}_2$  (NMC),  $\text{LiFePO}_4$  (LFP), silicon, and graphite have been demonstrated in this system[19–21]. The flowable suspension is made up of active materials (high volume fraction up to 20%), conductive agents, and lithium salts in organic electrolyte. Compared to the highest reported solubility of 5 M for conventional RFBs, a 20% volume fraction of LCO translates to 10 M of active material, thereby putting the theoretical volumetric energy density of SSFBs at  $\sim 200 \text{ Wh l}^{-1}$ . However, high concentration of active materials and conductive

carbon results in a highly viscous suspension that imposes parasitic loss from pumping during operation. For instance, at 12.6 vol % LFP in the catholyte, only  $57.4 \text{ Wh l}^{-1}$  capacity was realized[21].

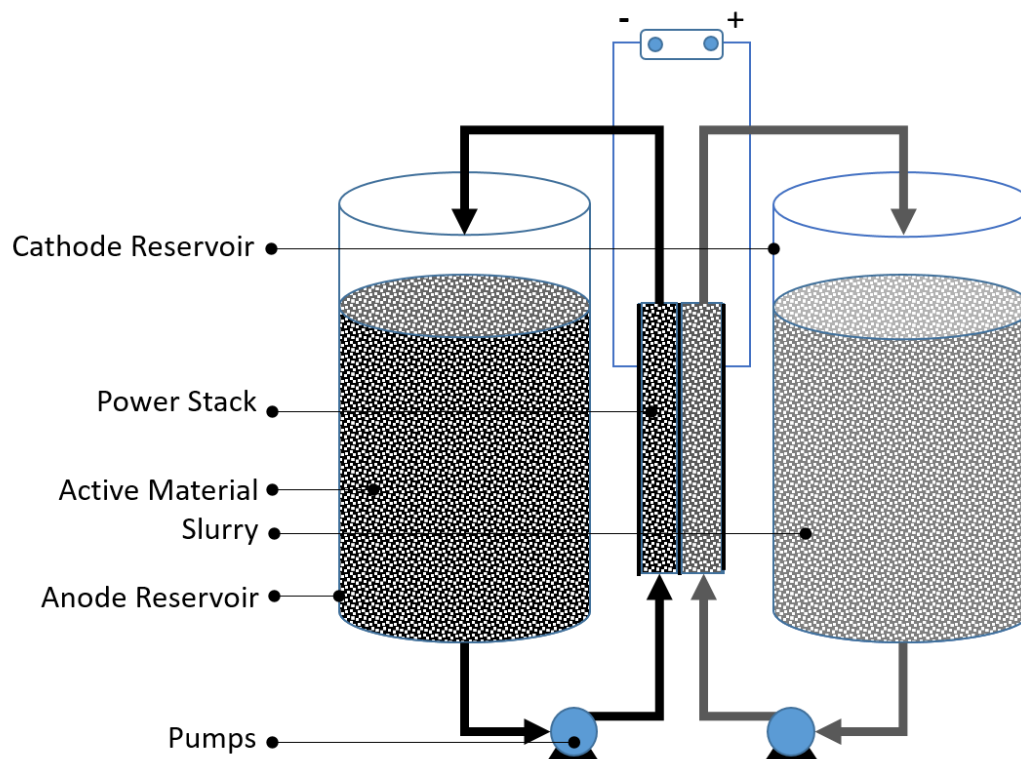


**Figure 2. Schematic of semi-solid flow batteries (SSFb).**

To improve upon the rheological challenges, conductive carbon can be eliminated from the suspension as it has been shown that addition of just 0.6% carbon black to 22.4 M LCO suspension increases the viscosity by more than tenfold. However, without the percolating network, the electrochemical reaction is facilitated by the collision between solid electroactive material and current collector. Our group used this approach to design cells based on LCO and  $\text{Li}_4\text{Ti}_5\text{O}_{12}$  (LTO) chemistries, however a low coulombic efficiency of  $\sim 38\%$  was realized[22]. Another strategy to

overcome the rheological limitations of SSFCs was proposed by Wei et al., where biphasic mixtures of repulsive LFP particles and attractive carbon black were stabilized in a colloidal mixture leading to well-dispersed suspensions[23]. This resulted in a remarkable improvement in cell performance, yielding a high energy density of  $93 \text{ Wh l}^{-1}$  and coulombic efficiency of 99% over 90 cycles. Changing the flow from continuous to intermittent flow has also been shown to improve cell performance. Despite the progress made in SSFBs in the past decade, the manageability and long-term cycling stability of suspended solid electroactive material in electrolytes has not been reported yet.

### 1.4 Redox-targeting Flow Batteries

To mitigate the use of solid suspensions and conductive carbon, while retaining the potential for high volumetric energy density from using solid electroactive material in RFBs, redox-targeting reactions were proposed by Prof. Wang and coworkers in 2013 [24]. Unlike SSFBs, the solid electroactive material remains static in the chemical reservoirs; the ion exchange is enabled by redox shuttles flown through the solid electroactive material and then to the power stack. We will refer this design as redox-targeting flow batteries (RTFBs) in this dissertation. A schematic for RTFB is shown in Figure 1.

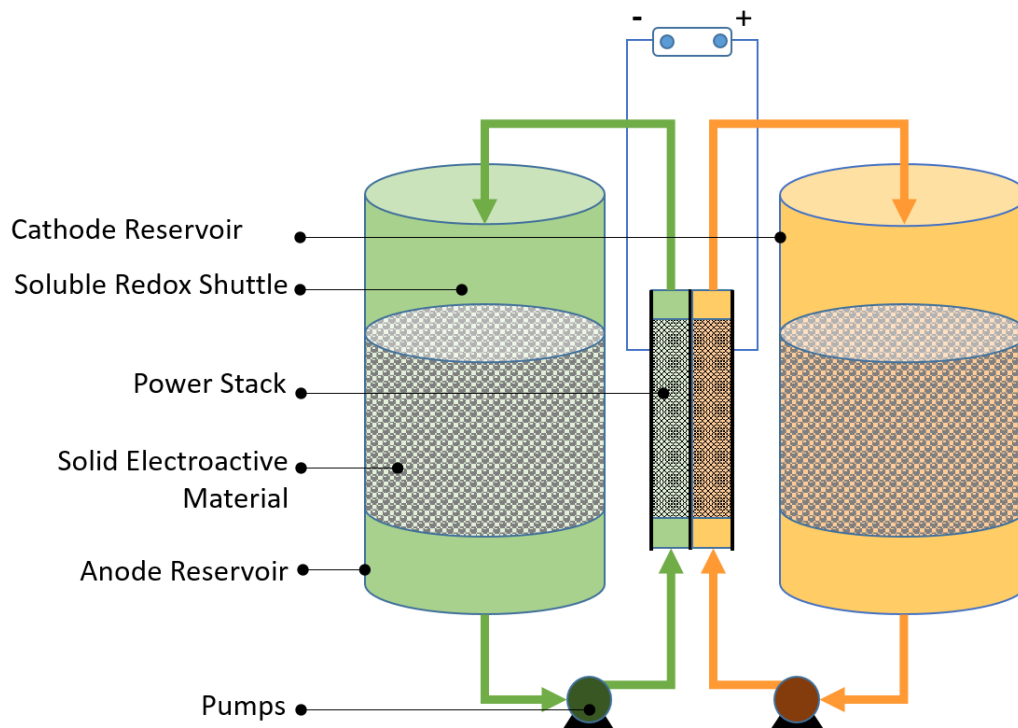
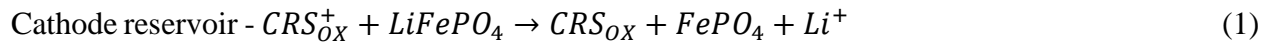


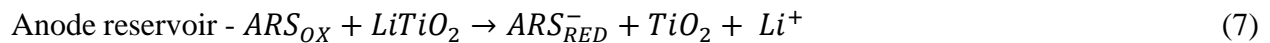
**Figure 3. Schematic of redox-targeting flow battery (RTFB).**

Two redox processes occur in the RTFBs. In the first process, redox shuttles perform chemical redox of solid electroactive material. RTFBs circulate a pair of redox shuttles for oxidation/reduction of cathode and anode each. The redox potential of redox shuttles should straddle the redox potential of solid electroactive material in the same electrolyte. In the second process, redox shuttles are regenerated in the power stack via electrochemical redox. Similar to RFBs, the power stack in RTFBs is composed of porous materials with high electronic conductivity (such as carbon or nickel foam, to facilitate charge transfer between redox shuttle and current collector). For example, for an RTFB made of LFP and  $TiO_2$  as solid electroactive material, and  $CRS_{OX}$ ,  $CRS_{RED}$ ,  $ARS_{OX}$ , and  $ARS_{RED}$  being the redox shuttles (where CRS and ARS stand for cathode redox shuttle and anode redox shuttle, the subscript OX and RED indicate oxidation or reduction), the following reactions would occur during charge and discharge of the battery-

### Charge-



### Discharge-





As expected, the six chemistries in the chemical reservoirs, and the ion-exchange membrane and porous electrodes in the power stack render RTFBs a complicated system. Since being first proposed in 2013, several studies on redox-targeting systems have been reported[25]. The research focus of these studies can be loosely divided into three categories: a) material selection and design, b) kinetics, and c) RTFB extension to other battery chemistries. These categories are discussed in detail in sections below.

#### *1.4.1 Material Selection and Design*

The design of RTFB based systems is still in early development stages. As a result, a standard methodology of designing and testing these batteries has not been established yet. Unlike conventional Li-ion batteries, where a standard protocol for slurry coated or sintered electrodes is used to measure cell performance, the solid electroactive material in RTFBs has been characterized as in a number of ways - pellets, dispersed particles, screen printed electrodes, etc. **Table 1** lists the solid electroactive materials, redox shuttles, and the characterization ‘design’ for solid electroactive material that have been reported in the last eight years. Some of the innovations towards solid electroactive material and redox shuttle are discussed in the sections below.

##### *1.4.1.1 Solid Electroactive Material*

The majority of the reports so far have used conventional Li-ion battery electrodes as the solid electroactive material, due to the high concentration of both ions ( $\text{Li}^+$ ) and electrons in these materials. For instance,  $\text{Li}^+$  concentration in LFP is 22.8 M, LCO is 26.6 M, and 22.5 M in LTO. The first demonstration of RTFBs was made in 2013 by Huang et al. using LFP (3.45 V vs  $\text{Li}/\text{Li}^+$ ) with 1,1'-dibromoferrocenium ( $\text{FcBr}_2^+$ , 3.55 V vs  $\text{Li}/\text{Li}^+$ ) and ferrocene (Fc, 3.25 V vs  $\text{Li}/\text{Li}^+$ ) as

cathode and lithium metal as anode [24]. Using the same cathodic chemistry, a full cell was later demonstrated with anatase  $\text{TiO}_2$  (1.8 V vs  $\text{Li/Li}^+$ ) an anode, paired with cobaltocene ( $\text{CoCp}_2$ , 1.90 V vs  $\text{Li/Li}^+$ ) and bis(pentamethylcyclopentadienyl) cobalt ( $\text{CoCp}^*_2$ , 1.36 V vs  $\text{Li/Li}^+$ ) as the redox shuttles[26].

In a study by Zanzola et al., polyaniline (PANI) was demonstrated as the solid electroactive material for both anode and cathode reservoirs of RTFBs[27]. PANI exists in three oxidation states; hence, by using redox shuttles of suitable voltage, redox-targeting of the cathodic and anodic pair was achieved. Although the all-PANI RTFB had a low cell voltage (0.4-0.6 V) and poor kinetics, using a single solid electroactive material significantly simplified the RTFB chemistry.

Recently, Wong et al. demonstrated a strategy to use polymer derivatives of redox-active organic molecules as solid electroactive material[28]. In this study, polystyrene derivatives of viologen were designed as spherical particles ( $\sim 200\text{-}\mu\text{m}$  diameter) and were oxidized and reduced by dimethyl and diphenyl viologens, respectively. If successful, this technique may allow tailoring of redox-targeting chemistries by pairing redox shuttles and polymers as solid electroactive material, providing greater flexibility and voltaic efficiency.

#### 1.4.1.2 Bifunctional and Nernstian Redox Shuttles

By using a pair of redox shuttles for cathode and anode each, along with solid cathode and anode material, electrolyte with conducting salt, the complexity of an RTFB system is increased. Depending upon the specific redox chemistry, the maximum concentration of redox shuttles in the electrolyte is also limited by using a pair of redox shuttles in catholyte and anolyte solution. To

address this, bifunctional redox shuttles have been proposed. For example,  $I^-/I_3^-$  and  $I_3^-/I_2$  have a half-wave potential of 3.15 and 3.7 V vs Li/Li<sup>+</sup>, respectively that has been shown to delithiate LFP[29]. Another bifunctional redox shuttle reported for LFP based RTFBs 2, 3, 5, 6- tetramethyl-p-phenylenediamine (TMPD) [30]. Both iodide and TMPD shuttles simplified the RTFB electrolyte chemistry, which is expected to be more stable for long term cycling.

The other issue that arises from having multiple redox shuttles is the intrinsic voltage loss, which decreases the voltage efficiency of the cell. The voltage efficiency of the cell is determined by the potential of the redox mediator(s). For instance, in case of an RTFB made of LFP as cathode being reversibly delithiated/lithiated by FcBr<sub>2</sub>/Fc, and anatase TiO<sub>2</sub> as anode redox-targeted by CoCp<sub>2</sub>/CoCp\*<sub>2</sub> shuttles results in a overpotential loss of 0.30 V on cathode end and 0.56 V on the anode side. The voltage efficiency, defined as the ratio of discharge and charge voltages, for this RTFB would be just 38.2%.

A proposed way to mitigate this issue is to use redox shuttles with half-wave potentials very close to the redox-targeted material, while still driving the chemical redox reactions forward at reasonable rates. In this case, the voltage loss arising from the voltage differences between shuttle and solid electroactive material would be eliminated. The driving force for chemical redox of solid electroactive material would arise from the Nernstian potential difference caused by the activity changes of the redox shuttles during charge and discharge. Using this strategy, ferrocene grafted ionic liquid, FcIL (3.43 V vs Li/Li<sup>+</sup>) for LFP [31] and [Fe(CN)<sub>6</sub>]<sup>3-</sup> for PANI [27] have been reported for RTFB with a voltage efficiency of 95% and 88%, respectively.

**Table 1: Summary of RTFB chemistries and solid electroactive material ‘designs’-**

<b>Solid Electroactive Material(s)</b>	<b>Redox Shuttles (Potential vs Li/Li<sup>+</sup>)</b>	<b>Design</b>	<b>Reference</b>
Li-LFP	Fc(3.25)/FcBr <sub>2</sub> (3.55)	Dispersed LFP particles	[24]
Li-LFP	I <sup>-</sup> (3.15/3.7)	100 μm screen printed LFP electrode	[29]
Li-TiO <sub>2</sub>	CoCp <sub>2</sub> (1.36)/CoCp* <sub>2</sub> (1.90)	Screen printed anatase TiO <sub>2</sub> electrode, dispersed TiO <sub>2</sub>	[32]
LFP- TiO <sub>2</sub>	Fc(3.25)/FcBr <sub>2</sub> (3.55)- CoCp <sub>2</sub> /CoCp* <sub>2</sub>	Porous LFP and TiO <sub>2</sub> granules static in tanks	[26]
Li-TiO <sub>2</sub>	CrCp* <sub>2</sub> (1.77)/CoCp <sub>2</sub> (1.92)	Dispersed TiO <sub>2</sub> powder	[33]
Li-S	CrCp* <sub>2</sub> (1.96)/NiCp* <sub>2</sub> (2.49)	Dispersed sulfur-based copolymer	[34]
Li-O <sub>2</sub>	Ethyl viologen (2.65)/I <sup>-</sup> (3.10/3.7)	Li <sub>2</sub> O <sub>2</sub> dispersed on porous material	[35]
Li-O <sub>2</sub>	DTBBQ (2.63)/TMPPA (3.63)	Li <sub>2</sub> O <sub>2</sub> dispersed on Ni foam	[36]

Li Fe <sub>4</sub> [Fe(CN) <sub>6</sub> ] <sub>3</sub> (Prussian blue)	- Ethyl viologen diiodide (2.45)/I <sup>-</sup> (3.15)	Prussian blue granules static in the chemical reservoir	[37]
Li-LFP	FeIL (3.43)	LFP granules static in the chemical reservoir	[38]
Li-LFP	TMPD (3.20/3.60)	LFP granules static in the chemical reservoir	[30]
PANI	Fe <sup>3+/2+</sup> (3.84)/V <sup>4+/3+</sup> (3.38)	PANI disk, fluidized packed bed	[27]
LFP	K <sub>4</sub> [Fe(CN) <sub>6</sub> ] (3.55)	LFP porous pellets	[39]
Zn- Fe <sub>4</sub> [Fe(CN) <sub>6</sub> ] <sub>3</sub>	K <sub>4</sub> [Fe(CN) <sub>6</sub> ] (3.55)	Prussian blue granules static in the chemical reservoir	[40]
LFP-O <sub>2</sub>	Li <sub>3</sub> [Fe(CN) <sub>6</sub> ]	LFP flakes dispersed in the chemical reservoir	[41]
Polystyrene derivative of viologen	Viologen derivatives	Dispersed polystyrene derivatives of viologen	[28]

Abbreviations: CrCp\*<sub>2</sub>, bis(pentamethylcyclopentadienyl)chromium; NiCp\*<sub>2</sub>, bis(pentamethylcyclopentadienyl)nickel; TMPPA, tris {4-[2-(2-methoxyethoxy) ethoxy]-phenyl}-amine; DTBBQ, 2, 5-di-tert-butyl-1, 4-benzoquinone.

### 1.4.2 Kinetics of Redox-targeting Reactions

The operation of RTFB is limited primarily by two kinetic processes- the electrochemical redox of redox shuttles in the power stack, and the chemical redox of solid electroactive material by redox shuttles. These two processes, along with material transport between chemical reservoirs and power stack will determine the charge/discharge rate. The electrochemical redox involves mass transfer in the electrolyte, electron exchange at current collector, and ion exchange via the ion-exchange membrane. The ion-exchange membranes pose a unique challenge of selective permeability and long cycle-life, and are in early development phase for RTFB applications[42]. The mass transfer of soluble redox species, and electron exchange between redox species and current collector is a feature shared by conventional RFBs and fuel cells. Optimization of the electrochemical kinetics in these systems have been extensively reported in these reviews [43,44].

On the other hand, the kinetics of redox-targeting reactions between solid electroactive materials and redox shuttles have been reported very few times. The charge-transfer kinetics between solid electroactive materials and redox shuttles indirectly affect the power and energy storage capacity of RTFBs. Yu et. al estimated the  $\text{Li}^+$  diffusion coefficient in LFP to be  $10^{-13} \text{ cm}^2 \text{ s}^{-1}$  during chemical oxidation with  $\text{NO}_2\text{BF}_4$  using X-ray absorption spectroscopy, consistent with electrochemical oxidation[45]. Chemical redox kinetics of LFP have been reported by Schougaard and coworkers by using bulk oxidants ( $\text{H}_2\text{O}_2$ ,  $\text{NO}_2$ ) [46,47] and reductants (LiI)[48] through techniques such as *in-situ* x-ray diffraction and UV/vis spectroscopy to track the progress of the reaction. The reaction parameters were extracted using 1-D diffusion model[46], Johnson-Mehl-Avrami-Kolmogorov model (JMAK)[45,48], and a statistical model[49]. In these reports, pseudo first-order reaction conditions were maintained by using redox shuttles in excess.

One of the techniques for probing chemical redox kinetics is to use scanning electrochemical microscopy (SECM)[50], where the ferrocene-based shuttles are oxidized/reduced at the electrode tip and at a controlled distance away the oxidized/reduced species reacts with the a dense LFP pellet as the solid electroactive material. The shuttle undergoes chemical redox at the substrate and is regenerated using electrochemical redox at the electrode. Assuming two-way pseudo-first order reaction model, effective rate constants for delithiation/lithiation for LFP/FP pellets by  $\text{FcBr}^{2+}/\text{Fc}$  solution were determined to be  $6.57 \times 10^{-3}$  and  $3.70 \times 10^{-3} \text{ cm s}^{-1}$ [51]. Jennings et al. reported a “double-layer electrode” of thin porous  $\text{Al}_2\text{O}_3$  layer with coated active material layer of LFP/FP to quantify the redox-targeting reaction kinetics by redox shuttles[52]. The double layer electrode film was reacted with very low concentration of redox shuttle and for short durations to create pseudo-first order reaction conditions. Following the classical catalytic-electrochemical mechanism [53], heterogeneous rate constants were obtained in the range of  $2.2 \times 10^{-6} - 4.4 \times 10^{-6} \text{ cm s}^{-1}$ . The 3 orders of magnitude difference between the two studies arises from the fact that LFP on double layer electrodes limits the electronic conductivity. Therefore, the reaction kinetics were limited by instead of electron transfer instead of interfacial kinetics between LFP and redox shuttles. These results suggest that the redox-targeting kinetics of solid electroactive materials with poor conductivity such as LFP can be improved by increasing surface area to volume ratio, would shorten the charge-transfer distance.

### 1.4.3 RTFB Extensions

This section explores the broader applications of redox-targeting approach to other electrochemical applications. While the focus of this dissertation would be chemical redox of Li-ion battery materials, the schemes explored in the systems discussed below establish redox-targeting as an intriguing technique to a wide variety of battery chemistries.

#### 1.4.3.1 Redox-targeting Li-S Batteries

Li-S batteries use sulfur as cathode that is a low-cost material with high capacity. Li-S batteries have a theoretical energy density of  $\sim 2600 \text{ Wh kg}^{-1}$ , however they suffer from poor ionic and electronic conductivities of sulfur, and polysulfide dissolution ( $\text{S}^{2-}$ ,  $\text{S}_2^{2-}$ , and  $\text{S}_4^{2-}$ ) in the electrolyte which causes severe capacity decay over more than hundred cycles[54]. Li-S based RTFBs were demonstrated by Li et al.[34], where S/Li<sub>2</sub>S cathode (2.15 V vs Li/Li<sup>+</sup>) paired with NiCp\*<sub>2</sub> (2.49 V vs Li/Li<sup>+</sup>) and CrCp\*<sub>2</sub> (1.96 V vs Li/Li<sup>+</sup>). The battery experienced more than 70% decay in charge/discharge capacity after 100 cycles due to polysulfide dissolution, and polysulfide and redox shuttle crossover to Li-anode through ion-exchange membrane. The results suggest that polysulfide dissolution and crossover issues must be addressed first before the full potential of redox-targeting Li-S batteries can be achieved.

#### 1.4.3.2 Redox-targeting Li-O<sub>2</sub> Batteries

Li-O<sub>2</sub> batteries (LOBs) have the highest theoretical energy density of all possible secondary batteries[55]. LOBs use Li metal anode and O<sub>2</sub>-air cathode, and Li-ion containing electrolyte. The cathode in LOBs is generally a porous substance enabling contact between O<sub>2</sub> and Li ions in the electrolyte phase. The discharge reaction is referred as oxygen reduction reaction (ORR). The electrochemical reaction pathway proposed for ORR is as follows-



The primary discharge product, lithium peroxide ( $Li_2O_2$ ) is insoluble in non-aqueous electrolytes and deposits on the surface of porous cathodes as thin films or precipitates. During charge or oxygen evolution reaction (OER),  $Li_2O_2$  undergoes oxidation to release molecular oxygen.

The  $Li_2O_2$  formed on porous electrodes is insulating and pore clogging, resulting in voltage hysteresis and poor discharge capacity. By using redox-targeting concepts, the reactants at the cathode during charge ( $Li_2O_2$ ) and discharge ( $O_2$ ) were chemically oxidized and reduced using redox shuttles in a gas-diffusion tank, separately. Therefore, the OER and ORR reactions are performed via chemical redox instead of electrochemical redox, mitigating the issue of  $Li_2O_2$  precipitation on porous electrodes. Li- $O_2$  based RTFBs employing iodine (3.1/3.7 V vs Li/Li<sup>+</sup> for I/I<sup>3-</sup>/I<sup>2</sup>) and ethyl viologen (2.65 V vs Li/Li<sup>+</sup>) as OER and ORR redox shuttles, were first reported by Zhu et. al [35]. This Li- $O_2$  battery exhibited large voltage hysteresis (voltaic efficiency 72%) and corrosion from iodine. Another pair of redox shuttles TMPPA (3.63 V vs Li/Li<sup>+</sup>) and DTBBQ (2.63 V vs Li/Li<sup>+</sup>) were later reported for Li- $O_2$  RTFBs[36]. Although, TMPPA and DTBBQ straddle the redox potential of  $Li_2O_2$  (2.96 V vs Li/Li<sup>+</sup>), the large overpotential between two redox shuttles resulted in poor voltaic efficiency. Additionally, DTBBQ were found to be chemically unstable upon three cycles (in 180 h duration). Despite the shortcomings, Li- $O_2$  RTFBs show promise towards solving the issue of surface passivation from  $Li_2O_2$  formation and subsequent pore clogging during discharge.

#### 1.4.3.3 Solar Rechargeable RTFBs

Fan et al. reported integrating redox-targeting approach in a photo electrochemical cell[37]. The solar-rechargeable used Prussian blue as the solid electroactive material along with the TiO<sub>2</sub> photoelectrode. The redox-targeting reaction between the photoelectrode and Prussian blue was achieved by using bifunctional redox shuttles, iodide ( $I^-/I^{3^-}/I_2$ ) and ethyl viologen ( $EV^0/EV^+/EV^{2+}$ ). This design achieved energy density of 117 Wh l<sup>-1</sup> with 66.8% of solid electroactive material utilization, thus demonstrating synergistic improvements in electrochemical performance by using Prussian blue as a capacity booster.

#### 1.4.3.4 Recycling

A recycling approach to spent Li-ion electrodes from conventional Li-ion batteries was demonstrated in a study by Yu et. al [41], where LFP-O<sub>2</sub> RTFB with ferricyanide as the redox shuttle regenerated high purity FePO<sub>4</sub> (99.97%) and LiOH (99.90%). This strategy minimized the use of corrosive chemicals and energy intensive processes commonly involved in Li-ion battery recycling.

## ***1.4 Scope of Dissertation***

The goal of this work is to develop techniques and analytical methods to probe chemical redox reactions between soluble redox shuttles and solid electroactive materials. The knowledge gained from development of these techniques is necessary for the rational design of RTFBs. Operation and design of RTFBs requires understanding of two reactor systems - chemical redox of solid electroactive material by redox shuttles, and electrochemical redox between redox shuttles and current collectors. The latter is equivalent to the charge transfer in the power stack in RFBs and fuel cells. Methods to optimize the electrochemical redox by material selection and cell design has been reviewed extensively in literature [17,43], and will not be explored in this study. On the other hand, chemical redox between solid electroactive material and redox shuttles is central to the functioning of RTFBs and compared to electrochemical redox, has not been well studied. Chemical redox processes relevant to RTFBs will be the focus of this dissertation.

In this dissertation, LFP has been used as the solid electroactive material. LFP was chosen due to its flat charge/discharge potential at 3.45 V vs Li/Li<sup>+</sup> (as shown in Fig. 4) that allows constant potential difference between LFP and redox shuttles during all states of oxidation/reduction. Additionally, since most non-aqueous electrolytes are unstable above 4.2 V vs Li/Li<sup>+</sup>, there is a voltage window of 0.8 V for the selection or design of oxidation shuttle of LFP. As a cathode material in Li-ion batteries, LFP has been shown to have high power density, voltaic efficiency, cost-effectiveness, and long-cycle life. We believe that these qualities would translate well into RTFBs as well.

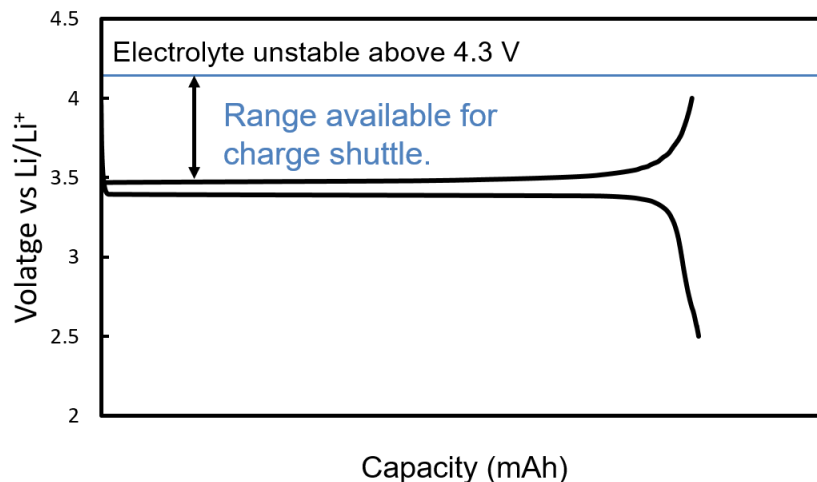


**Figure 4. Charge-discharge profile of LFP electrodes in a Li-ion battery.**

In this dissertation, the key research ideas can be understood in two parts. Part I explores redox shuttle design and characterization methods, detailed in Chapter II and III. In this part, ferrocene based redox shuttles were used in organic electrolytes with dispersed LFP in a batch reactor system. In chapter II, chemical redox of LFP was compared to the well-studied electrochemical redox. *in-operando* ultraviolet-visible (UV-Vis) spectroscopy probed the reaction progress and pseudo first order rate constants and phase transformations were extracted using JMAK equation. In Chapter III, the concentration limitations of redox shuttles imposed by UV-Vis spectroscopy were obviated by designing an electrochemical batch reactor. With this setup, the molar ratio of solid electroactive material to the redox shuttles were studied for maximum extent of redox-targeted conversion. Six ferrocene-based redox shuttles, with varying redox-potentials and steric factors (correlated to diffusion coefficient), were then tested for rate of redox-targeting reactions. The kinetic parameters were derived using JMAK model and an additional 1-D diffusion model was developed with greater sensitivity to Li-ion diffusion in LFP particles.

In Part II of this dissertation, the emphasis was shifted towards designing the chemical reservoir for RTFBs. In Chapter IV, a systematic investigation of design principles for a packed bed reactor (PBR) configuration as the cathode reservoir is described. The impact of variables such as the height of the PBR, redox shuttle concentration, electrolyte flow-rate, and operating temperature on the chemical oxidation of LFP PBR by  $[\text{Fe}(\text{CN})_6]^{3-}$  was measured using electroanalytical techniques. A reaction mechanism based on the observations was suggested. To verify the insights developed in Chapter IV, neutron imaging of the LFP PBR at different stages of chemical oxidation by  $[\text{Fe}(\text{CN})_6]^{3-}$  was done to visualize the spatiotemporal variations. 3D reconstructed neutron tomographs were then complemented with x-ray computed tomography to study the particle size and packing distribution of reaction heterogeneities in the LFP PBR.

## 1.6 References

- [1] W.J. Ripple, C. Wolf, T.M. Newsome, P. Barnard, W.R. Moomaw, World Scientists' Warning of a Climate Emergency, *Bioscience*. 70 (2020) 8–12. <https://doi.org/10.1093/biosci/biz088>.
- [2] E. National Academies of Sciences and Medicine, Enhancing the resilience of the nation's electricity system, National Academies Press, 2017.
- [3] J.W. Busby, K. Baker, M.D. Bazilian, A.Q. Gilbert, E. Grubert, V. Rai, J.D. Rhodes, S. Shidore, C.A. Smith, M.E. Webber, Cascading risks: Understanding the 2021 winter blackout in Texas, *Energy Res. Soc. Sci.* 77 (2021) 102106. <https://doi.org/10.1016/j.erss.2021.102106>.
- [4] F.R. Fonseca, M. Craig, P. Jaramillo, M. Berge, E. Severnini, A. Loew, H. Zhai, Y. Cheng, B. Nijssen, N. Voisin, J. Yearsley, Effects of climate change on capacity expansion decisions of an electricity generation fleet in the southeast U.S., *Environ. Sci. Technol.* 55 (2021) 2522–2531. <https://doi.org/10.1021/acs.est.0c06547>.
- [5] IEA (2020), World Energy Outlook 2020, IEA, Paris <https://www.iea.org/reports/world-energy-outlook-2020>, 2020.
- [6] W. Wang, Q. Luo, B. Li, X. Wei, L. Li, Z. Yang, Recent progress in redox flow battery research and development, *Adv. Funct. Mater.* 23 (2013) 970–986. <https://doi.org/10.1002/adfm.201200694>.
- [7] B. Dunn, H. Kamath, J.M. Tarascon, Electrical energy storage for the grid: A battery of choices, *Science* (80-. ). 334 (2011) 928–935. <https://doi.org/10.1126/science.1212741>.

- [8] H. Ibrahim, A. Ilinca, J. Perron, Energy storage systems-Characteristics and comparisons, *Renew. Sustain. Energy Rev.* 12 (2008) 1221–1250. <https://doi.org/10.1016/j.rser.2007.01.023>.
- [9] David Frankel, *Battery Storage: The Next Disruptive Technology in the Power Sector*, McKinsey Co. (2017).
- [10] T.M. Gür, Review of electrical energy storage technologies, materials and systems: Challenges and prospects for large-scale grid storage, *Energy Environ. Sci.* 11 (2018) 2696–2767. <https://doi.org/10.1039/c8ee01419a>.
- [11] A.Z. Weber, M.M. Mench, J.P. Meyers, P.N. Ross, J.T. Gostick, Q. Liu, Redox flow batteries : a review, (2011) 1137–1164. <https://doi.org/10.1007/s10800-011-0348-2>.
- [12] J. Liu, J.G. Zhang, Z. Yang, J.P. Lemmon, C. Imhoff, G.L. Graff, L. Li, J. Hu, C. Wang, J. Xiao, G. Xia, V. V. Viswanathan, S. Baskaran, V. Sprenkle, X. Li, Y. Shao, B. Schwenzer, Materials science and materials chemistry for large scale electrochemical energy storage: From transportation to electrical grid, *Adv. Funct. Mater.* 23 (2013) 929–946. <https://doi.org/10.1002/adfm.201200690>.
- [13] K.J. Kim, M.S. Park, Y.J. Kim, J.H. Kim, S.X. Dou, M. Skyllas-Kazacos, A technology review of electrodes and reaction mechanisms in vanadium redox flow batteries, *J. Mater. Chem. A.* 3 (2015) 16913–16933. <https://doi.org/10.1039/c5ta02613j>.
- [14] J. Hernández, C. Christensen, DOE Global Energy Storage Database – A Platform for Large Scale Data Analytics and System Performance Metrics, (2016) 0–5.
- [15] M. Park, J. Ryu, W. Wang, J. Cho, Material design and engineering of next-generation flow-

- battery technologies, *Nat. Rev. Mater.* (2016). <https://doi.org/10.1038/natrevmats.2016.80>.
- [16] Y. Ding, C. Zhang, L. Zhang, Y. Zhou, G. Yu, Molecular engineering of organic electroactive materials for redox flow batteries, *Chem. Soc. Rev.* 47 (2018) 69–103. <https://doi.org/10.1039/c7cs00569e>.
- [17] Y. Zhao, Y. Ding, Y. Li, L. Peng, H.R. Byon, J.B. Goodenough, G. Yu, A chemistry and material perspective on lithium redox flow batteries towards high-density electrical energy storage, *Chem. Soc. Rev.* 44 (2015) 7968–7996. <https://doi.org/10.1039/C5CS00289C>.
- [18] M. Duduta, B. Ho, V.C. Wood, P. Limthongkul, V.E. Brunini, W.C. Carter, Y.M. Chiang, Semi-solid lithium rechargeable flow battery, *Adv. Energy Mater.* 1 (2011) 511–516. <https://doi.org/10.1002/aenm.201100152>.
- [19] Z. Li, K.C. Smith, Y. Dong, N. Baram, F.Y. Fan, J. Xie, P. Limthongkul, W.C. Carter, Y.-M. Chiang, Aqueous semi-solid flow cell: demonstration and analysis., *Phys. Chem. Chem. Phys.* 15 (2013) 15833–9. <https://doi.org/10.1039/c3cp53428f>.
- [20] S. Hamelet, T. Tzedakis, J.-B. Leriche, S. Sailler, D. Larcher, P.-L. Taberna, P. Simon, J.-M. Tarascon, Non-Aqueous Li-Based Redox Flow Batteries, *J. Electrochem. Soc.* 159 (2012) A1360–A1367. <https://doi.org/10.1149/2.071208jes>.
- [21] J.J. Biendicho, C. Flox, L. Sanz, J.R. Morante, Static and dynamic studies on  $\text{LiNi}_{1/3}\text{Co}_{1/3}\text{Mn}_{1/3}\text{O}_2$ -based suspensions for semi-solid flow batteries, *ChemSusChem.* 9 (2016) 1938–1944. <https://doi.org/10.1002/cssc.201600285>.
- [22] Z. Qi, G.M. Koenig, A carbon-free lithium-ion solid dispersion redox couple with low viscosity for redox flow batteries, *J. Power Sources.* 323 (2016) 97–106.

<https://doi.org/10.1016/j.jpowsour.2016.05.033>.

- [23] T.S. Wei, F.Y. Fan, A. Helal, K.C. Smith, G.H. McKinley, Y.M. Chiang, J.A. Lewis, Biphasic Electrode Suspensions for Li-Ion Semi-solid Flow Cells with High Energy Density, Fast Charge Transport, and Low-Dissipation Flow, *Adv. Energy Mater.* 5 (2015) 1–7. <https://doi.org/10.1002/aenm.201500535>.
- [24] Q. Huang, H. Li, M. Grätzel, Q. Wang, Reversible chemical delithiation/lithiation of LiFePO<sub>4</sub>: towards a redox flow lithium-ion battery., *Phys. Chem. Chem. Phys.* 15 (2013) 1793–7. <https://doi.org/10.1039/c2cp44466f>.
- [25] R. Yan, Q. Wang, Redox-Targeting-Based Flow Batteries for Large-Scale Energy Storage, *Adv. Mater.* 1802406 (2018) 1802406. <https://doi.org/10.1002/adma.201802406>.
- [26] C. Jia, F. Pan, Y.G. Zhu, Q. Huang, L. Lu, Q. Wang, High – energy density nonaqueous all redox flow lithium battery enabled with a polymeric membrane, *Sci. Adv.* 1 (2015) 1–7. <https://doi.org/10.1126/sciadv.1500886>.
- [27] E. Zanzola, C.R. Dennison, A. Battistel, P. Peljo, H. Vrubel, V. Amstutz, H.H. Girault, Redox Solid Energy Boosters for Flow Batteries: Polyaniline as a Case Study, *Electrochim. Acta.* 235 (2017) 664–671. <https://doi.org/10.1016/j.electacta.2017.03.084>.
- [28] C.M. Wong, C.S. Sevov, All-Organic Storage Solids and Redox Shuttles for Redox-Targeting Flow Batteries, *ACS Energy Lett.* (2021) 1271–1279. <https://doi.org/10.1021/acseenergylett.1c00143>.
- [29] Q. Huang, J. Yang, C.B. Ng, C. Jia, Q. Wang, A redox flow lithium battery based on the redox targeting reactions between LiFePO<sub>4</sub> and iodide, *Energy Environ. Sci.* 9 (2016) 917–

921. <https://doi.org/10.1039/C5EE03764F>.
- [30] Y.G. Zhu, Y. Du, C. Jia, M. Zhou, L. Fan, X. Wang, Q. Wang, Unleashing the Power and Energy of LiFePO<sub>4</sub>-Based Redox Flow Lithium Battery with a Bifunctional Redox Mediator, *J. Am. Chem. Soc.* (2017) jacs.7b01146. <https://doi.org/10.1021/jacs.7b01146>.
- [31] A.K. Sharma, E. Birgersson, F. Pan, Q. Wang, Mathematical modeling and experiments of a half-cell redox flow lithium ion battery system, *Electrochim. Acta.* 204 (2016) 1–8. <https://doi.org/10.1016/j.electacta.2016.03.072>.
- [32] F. Pan, J. Yang, Q. Huang, X. Wang, H. Huang, Q. Wang, Redox Targeting of Anatase TiO<sub>2</sub> for Redox Flow Lithium-Ion Batteries, *Adv. Energy Mater.* (2014) n/a-n/a. <https://doi.org/10.1002/aenm.201400567>.
- [33] F. Pan, Q. Huang, H. Huang, Q. Wang, High-Energy Density Redox Flow Lithium Battery with Unprecedented Voltage Efficiency, *Chem. Mater.* 28 (2016) 2052–2057. <https://doi.org/10.1021/acs.chemmater.5b04558>.
- [34] J. Li, L. Yang, S. Yang, J.Y. Lee, The Application of Redox Targeting Principles to the Design of Rechargeable Li-S Flow Batteries, *Adv. Energy Mater.* 5 (2015) 1–6. <https://doi.org/10.1002/aenm.201501808>.
- [35] Y.G. Zhu, C. Jia, J. Yang, F. Pan, Q. Huang, Q. Wang, Dual redox catalysts for oxygen reduction and evolution reactions: Towards a redox flow Li-O<sub>2</sub> battery, *Chem. Commun.* 51 (2015) 9451–9454. <https://doi.org/10.1039/c5cc01616a>.
- [36] Y.G. Zhu, X. Wang, C. Jia, J. Yang, Q. Wang, Redox-Mediated ORR and OER Reactions: Redox Flow Lithium Oxygen Batteries Enabled with a Pair of Soluble Redox Catalysts,

- ACS Catal. 6 (2016) 6191–6197. <https://doi.org/10.1021/acscatal.6b01478>.
- [37] L. Fan, C. Jia, Y.G. Zhu, Q. Wang, Redox targeting of prussian blue: Toward low-cost and high energy density redox flow battery and solar rechargeable battery, ACS Energy Lett. 2 (2017) 615–621. <https://doi.org/10.1021/acsenergylett.6b00667>.
- [38] M. Zhou, Q. Huang, L. Fan, Q. Wang, M. Zhou, Q. Huang, T. Nguyen, P. Truong, J. Ghilane, Y.G. Zhu, Nernstian-Potential-Driven Redox-Targeting Reactions of Battery Materials Nernstian-Potential-Driven Redox-Targeting Reactions of Battery Materials, CHEMPR. 3 (n.d.) 1036–1049. <https://doi.org/10.1016/j.chempr.2017.10.003>.
- [39] J.F. Vivo-Vilches, A. Nadeina, N. Rahbani, V. Seznec, D. Larcher, E. Baudrin, LiFePO<sub>4</sub>-ferri/ferrocyanide redox targeting aqueous posolyte: Set-up, efficiency and kinetics, J. Power Sources. 488 (2021) 229387. <https://doi.org/10.1016/j.jpowsour.2020.229387>.
- [40] Y. Chen, M. Zhou, Y. Xia, X. Wang, Y. Liu, Y. Yao, H. Zhang, Y. Li, S. Lu, W. Qin, X. Wu, Q. Wang, A Stable and High-Capacity Redox Targeting-Based Electrolyte for Aqueous Flow Batteries, Joule. 3 (2019) 2255–2267. <https://doi.org/10.1016/j.joule.2019.06.007>.
- [41] J. Yu, X. Wang, M. Zhou, Q. Wang, A redox targeting-based material recycling strategy for spent lithium ion batteries, Energy Environ. Sci. 12 (2019) 2672–2677. <https://doi.org/10.1039/c9ee01478k>.
- [42] H. Chen, G. Cong, Y. Lu, Recent progress in organic redox flow batteries : Active materials , electrolytes and membranes, J. Energy Chem. 27 (2018) 1304–1325. <https://doi.org/10.1016/j.jechem.2018.02.009>.
- [43] B.R. Chalamala, T. Soundappan, G.R. Fisher, M.R. Anstey, V. V. Viswanathan, M.L. Perry,

- Redox flow batteries: An engineering perspective, *Proc. IEEE*. 102 (2014) 976–999.  
<https://doi.org/10.1109/JPROC.2014.2320317>.
- [44] H. Prifti, A. Parasuraman, S. Winardi, T.M. Lim, M. Skyllas-Kazacos, Membranes for redox flow battery applications., *Membranes (Basel)*. 2 (2012) 275–306.  
<https://doi.org/10.3390/membranes2020275>.
- [45] X. Yu, Q. Wang, Y. Zhou, H. Li, X.Q. Yang, K.W. Nam, S.N. Ehrlich, S. Khalid, Y.S. Meng, High rate delithiation behaviour of LiFePO<sub>4</sub> studied by quick X-ray absorption spectroscopy, *Chem. Commun.* 48 (2012) 11537–11539.  
<https://doi.org/10.1039/c2cc36382h>.
- [46] D. Lepage, F. Sobh, C. Kuss, G. Liang, S.B. Schougaard, Delithiation kinetics study of carbon coated and carbon free LiFePO<sub>4</sub>, *J. Power Sources*. 256 (2014) 61–65.  
<https://doi.org/10.1016/j.jpowsour.2013.12.054>.
- [47] C. Kuss, D. Lepage, G. Liang, S.B. Schougaard, Ultrafast charging of LiFePO<sub>4</sub> with gaseous oxidants under ambient conditions, *Chem. Sci.* 4 (2013) 4223–4227.  
<https://doi.org/10.1039/c3sc51195b>.
- [48] C. Kuss, M. Carmant-Dérival, N.D. Trinh, G. Liang, S.B. Schougaard, Kinetics of heterosite iron phosphate lithiation by chemical reduction, *J. Phys. Chem. C*. 118 (2014) 19524–19528. <https://doi.org/10.1021/jp502346f>.
- [49] P. Bai, G. Tian, Statistical kinetics of phase-transforming nanoparticles in LiFePO<sub>4</sub> porous electrodes, *Electrochim. Acta*. 89 (2013) 644–651.  
<https://doi.org/10.1016/j.electacta.2012.11.070>.

- [50] D. Polcari, P. Dauphin-Ducharme, J. Mauzeroll, Scanning Electrochemical Microscopy: A Comprehensive Review of Experimental Parameters from 1989 to 2015, *Chem. Rev.* 116 (2016) 13234–13278. <https://doi.org/10.1021/acs.chemrev.6b00067>.
- [51] R. Yan, J. Ghilane, K.C. Phuah, T.N. Pham Truong, S. Adams, H. Randriamahazaka, Q. Wang, Determining  $\text{Li}^+$ -Coupled Redox Targeting Reaction Kinetics of Battery Materials with Scanning Electrochemical Microscopy, *J. Phys. Chem. Lett.* (2018) 491–496. <https://doi.org/10.1021/acs.jpcclett.7b03136>.
- [52] J.R. Jennings, Q. Huang, Q. Wang, Kinetics of  $\text{Li}_x\text{FePO}_4$  Lithiation/Delithiation by Ferrocene-Based Redox Mediators: An Electrochemical Approach, *J. Phys. Chem. C.* 119 (2015) 17522–17528. <https://doi.org/10.1021/acs.jpcc.5b03561>.
- [53] C.P. Andrieux, J.M. Dumas-Bouchiat, J.M. Saveant, Homogeneous redox catalysis of electrochemical reactions. Part I. Introduction, *J. Electroanal. Chem.* 87 (1978) 39–53. [https://doi.org/10.1016/S0022-0728\(78\)80378-7](https://doi.org/10.1016/S0022-0728(78)80378-7).
- [54] A. Manthiram, Y. Fu, S. Chung, C. Zu, Y. Su, Rechargeable Lithium – Sulfur Batteries, (2014).
- [55] W.J. Kwak, Rosy, D. Sharon, C. Xia, H. Kim, L.R. Johnson, P.G. Bruce, L.F. Nazar, Y.K. Sun, A.A. Frimer, M. Noked, S.A. Freunberger, D. Aurbach, Lithium-Oxygen Batteries and Related Systems: Potential, Status, and Future, *ACS Appl. Mater. Interfaces.* (2020). <https://doi.org/10.1021/acs.chemrev.9b00609>.

## Chapter II. Analysis of Chemical and Electrochemical Lithiation/Delithiation of a Lithium-Ion Cathode Material

### 2.1 Overview

In this chapter, we compared the chemical lithiation/delithiation kinetics with the well-studied electrochemical lithiation/delithiation of lithium iron phosphate ( $\text{LiFePO}_4$ ). Chemical redox on  $\text{LiFePO}_4$  by ferrocene derivatives as redox shuttles was analyzed using *in-operando* ultraviolet-visible spectroscopy. The kinetics and phase transformations of chemical and electrochemical redox were calculated using Johnson-Mehl-Avrami-Erofeyev-Kolmogorov (JMAEK) model. Phase transformation of Li- rich and Li- poor  $\text{LiFePO}_4$  was found to be asymmetric for chemical lithiation/delithiation; which was not found to be the case for electrochemical lithiation/delithiation. Furthermore, under the experimental conditions chemical redox was found to have slower kinetics and higher activation energy than electrochemical redox.

Elements of this chapter have been published in Journal of The Electrochemical Society:

Gupta, D., & Koenig Jr, G. M. (2020). Analysis of Chemical and Electrochemical Lithiation/Delithiation of a Lithium-Ion Cathode Material. *Journal of The Electrochemical Society*, 167(2), 020537.

## ***2.2 Abstract***

Redox targeting reactions between lithium-ion battery materials and redox shuttles has been proposed to design high energy density redox flow batteries. Designing these batteries would require a deeper understanding of the kinetics of redox targeting reactions and the phase transformation of the materials involved. In this study, the oxidation and reduction of lithium iron phosphate,  $\text{LiFePO}_4$ , via chemical and electrochemical routes will be compared. Ultraviolet-visible spectroscopy was used as a technique to characterize the extent of chemical lithiation/delithiation during chemical redox of  $\text{LiFePO}_4$ , while the electrochemical redox was characterized using battery coin cells. The kinetic parameters extracted using Johnson-Mehl-Avrami-Erofeyev-Kolomogorov (JMAEK) model suggested that chemical redox was slower than electrochemical redox within the experimental regimes. Calculated apparent activation energies suggested the limitations in the chemical redox rate were due to different processes than the electrochemical redox. In addition, asymmetry observed for oxidation and reduction of  $\text{LiFePO}_4$  materials will be discussed. As pairs of solid battery electroactive particles and soluble redox shuttles are designed, tools and analysis such as those in this study will be needed for interrogating and comparing electrochemical and chemical oxidation and reduction of the solid particles to understand and design these systems.

## ***2.3 Introduction***

Soluble redox-active compounds (e.g., redox shuttles), and their use to promote chemical reduction and oxidation of solid electroactive lithium-ion (Li-ion) materials, have been under investigation for a number of years<sup>1-5</sup>. The most common target application for these materials has been providing overcharge protection via “redox shuttling”, where for example the soluble redox shuttle will oxidize at a potential above the cathode material but below an undesirable value for the electrode and electrolyte to be exposed<sup>5</sup>. Redox shuttles have also been reported for photo-assisted rechargeable Li-ion batteries where the redox shuttles facilitate lowering the potential required to delithiate the cathode and charge the battery when exposed to light<sup>6,7</sup>. Due to the relatively high potentials needed to protect Li-ion cathode materials and low potentials to protect Li-ion anode materials, redox shuttles themselves have been suggested and explored for organic flow battery applications<sup>8</sup>. Pairing a Li-ion anode and cathode redox shuttle has resulted in cell voltages which exceed that for conventional flow batteries<sup>9,10</sup>. However, the energy density of an organic flow battery (e.g., <40 Wh l<sup>-1</sup>)<sup>11</sup> will still be limited by the concentration of the redox shuttles, which can be limited by solubility and/or stability to values that result in volumetric energy densities much lower than conventional Li-ion batteries (600-650 Wh l<sup>-1</sup>)<sup>12</sup>. Recently, Huang et al. reported the use of redox shuttles as mediators to chemically charge/discharge Li-ion solid electroactive materials in a flow battery design, where the redox shuttles were still used in an electrochemical cell to provide power, but the energy was stored in solid electrochemically active particles<sup>13</sup>. This configuration took advantage of the high volumetric energy density of solid Li-ion active materials and the high power density provided by electrochemical oxidation/reduction of soluble species in a high surface area flow battery electrochemical cell<sup>14</sup>. One tradeoff for this type of flow battery was that for both the anode and cathode there must be a combination of redox shuttles (or a

multielectron shuttle) that has a potential high enough to drive chemical oxidation of the solid active material and low enough to drive chemical reduction of the active material <sup>15</sup>. These requirements thus result in a voltage efficiency penalty for charge and discharge in the cell due to the need to accommodate the chemical redox driving forces. However, very few studies have investigated the kinetics of the chemical redox between redox shuttles and Li-ion active materials, which will be needed to understand and potentially optimize these materials <sup>16,17</sup>.

Compared to electrochemical redox, there have been fewer reports quantifying the chemical redox of Li-ion battery materials. Among them, reports by Schougaard group <sup>18-20</sup> focused on the delithiation/lithiation of LiFePO<sub>4</sub> (LFP) by strong oxidizing/reducing agents in excess accompanied by experimental conditions (e.g., vigorous stirring) which remove the transport limitations arising from the oxidizing/reducing agents in the bulk reaching the surface of the active material particles. The kinetic data thus collected using in-situ XRD <sup>18</sup>, atomic emission spectroscopy <sup>19</sup>, or ultraviolet-visible (UV-Vis) photometry <sup>20</sup> were primarily attributed to the intrinsic transport limitations of Li<sup>+</sup>/e<sup>-</sup> through LFP particles. In another study done by Jennings et al. <sup>21</sup>, films made of nanoparticulate LFP particles were reacted with ferrocene-based shuttles and modeled with a 1-D diffusion reaction model under excess LFP concentration conditions. Another work by Yan et al. <sup>22</sup> used feedback mode of scanning electrochemical microscopy to determine the rate constant for blended pellets comprised of both LFP and FePO<sub>4</sub> (FP). None of these studies, however, included a detailed characterization of both chemical and electrochemical redox of the electrode material under investigation.

In this study, we have investigated the chemical lithiation/delithiation reaction of LFP (and FP formed from delithiation of LFP) using a pair of ferrocene derivatives and juxtaposed these results against electrochemical potentiostatic lithiation/delithiation of the same electroactive

particles. LFP has been targeted as a commercial cathode material for its high specific energy density (theoretical  $\sim 170 \text{ mAh g}^{-1}$ ), excellent rate capability, safety, and stability as an electrode material for mediated flow battery applications<sup>23</sup>. The success of LFP as a commercial electrode material has been accompanied by extensive research about its phase transformation and redox kinetics characterized electrochemically, providing a literature for results comparison. A particular additional desirable attribute of LFP for this study was the two-phase behavior of LFP-rich to LFP-poor transformation, which provided charge/discharge plateaus at relatively constant potentials<sup>23</sup>. This attribute allowed for an approximately constant potential for the LFP when reacting with the redox shuttles during chemical redox. This present study is the first to quantify both oxidation and reduction of the electroactive material by redox shuttles and to compare to electrochemical processes for the same materials. UV-Vis spectroscopy will be shown to be a simple and robust tool to estimate chemical redox kinetics for systems with appropriate redox shuttles. However, experimental limitations of concentration regimes due to the use of UV-Vis spectroscopy limited the ability of this study to explore higher concentrations of the redox shuttles.

## ***2.4 Experimental***

### *2.4.1 Materials Preparation and Redox Shuttle Characterization*

LFP (Xiamen TOB New Energy Technology, China) was purchased from a commercial supplier and used as received. The LFP used did not undergo a carbon-coating process in its production. In chemical redox experiments with a redox shuttle and  $\text{FePO}_4$  (FP), the LFP was first oxidized to FP by stirring vigorously in a solution of 2.4 mol% hydrogen peroxide and 0.1 mol% acetic acid in distilled water for 30 minutes following a previously reported procedure<sup>19</sup>. The delithiated product was characterized using inductively coupled plasma- optical emission spectrometry (ICP-OES,

Perkin Elmer Optima 8000) and was found to be 96.5% delithiated (see Appendix A, Table S1). Conversion from LFP to delithiated FP was also confirmed using powder X-ray diffraction (XRD, Panalytical X' pert diffractometer) and the patterns can be found in Appendix A, Figure A1. The XRD patterns for LFP and FP were consistent with previous literature reports for these two materials <sup>20</sup>.

Ferrocene (Fc, Sigma Aldrich) and 1, 1'-dibromoferrocene (FcBr<sub>2</sub>, Fischer Scientific) redox shuttles were dissolved into an electrolyte solution of 1.2 M LiPF<sub>6</sub> in 3:7 vol % ethylene carbonate: ethyl methyl carbonate (Gotion Inc.). All experiments with the redox shuttles were conducted in an argon-filled glove box (H<sub>2</sub>O < 1 ppm, O<sub>2</sub> < 1 ppm). The half-wave potentials of the redox shuttles were measured to be 3.6 V vs Li/Li<sup>+</sup> and 3.25 V vs Li/Li<sup>+</sup> for FcBr<sub>2</sub> and Fc, respectively, using cyclic voltammetry at a scan rate of 10 mV s<sup>-1</sup> in a custom-built glass electrochemical cell (for description of the custom cell and cyclic voltammograms see Appendix A, Figure A2).

#### 2.4.2 Chemical Redox of LFP/FP with Redox Shuttles

Chemical reduction of FP with Fc was conducted by preparing an 8 mM solution of Fc dissolved in the carbonate solvent electrolyte solution. Separately, FP powder, which had been thoroughly dried and stored in the glove box, was carefully weighed outside the glove box after addition to a cuvette (Spectrocell) which had also been dried in a vacuum oven at 80 °C. The range in the mass of FP used in experiments was 1.2-1.5 mg. A small stir bar was added, and then the cuvette was sealed with a cap containing a septum. The cuvette was placed into an UV-Vis spectrometer (Perkin-Elmer) within a cuvette holder that included a Peltier heater and the holder was set to the desired reaction temperature and allowed to equilibrate. The Fc-containing electrolyte solution was heated to the desired reaction temperature and then injected all at once into the cuvette through the septum. The cuvette holder also had stirring capability and a stir rate

of 60 rpm was initiated with the addition of the Fc-containing solution. UV-Vis scans were performed from 400-700 nm at a scan rate of  $10 \text{ nm s}^{-1}$  at a time resolution of 5 minutes throughout the Fc/FP chemical redox process.

Oxidation of LFP with  $\text{FcBr}_2^+$  was conducted in the same manner as the Fc/FP experiment described above except that 1) the initial concentration of  $\text{FcBr}_2^+$  was 2 mM, and 2)  $\text{FcBr}_2$  had to first be oxidized to  $\text{FcBr}_2^+$ . Oxidation of  $\text{FcBr}_2$  was conducted electrochemically using a custom electrolysis cell (see Appendix A, Figure A2) by applying a constant potential of 4 V (vs.  $\text{Li/Li}^+$  via a Li foil counter/reference electrode) to a Pt wire working electrode in a stirred solution until the coulombs of charge that were recorded were equal to the theoretical value based on 1 mol of  $e^-$  per mol of  $\text{FcBr}_2$  in the solution. The ion exchange membrane in the electrochemical cell was a blend of polyvinylidene difluoride and Nafion and was prepared using a procedure from the literature<sup>24</sup>. UV-Vis scans during  $\text{FcBr}_2^+/\text{LFP}$  chemical redox were performed from 500-800 nm at a scan rate of  $10 \text{ nm s}^{-1}$  at a time resolution of 2 minutes. Three replicates were performed for chemical redox experiments at each temperature.

#### *2.4.3 Electrochemical Redox of LFP/FP*

Electrochemical oxidation of LFP and reduction of FP was conducted in 2032-type coin cells. Cathodes were fabricated by casting a slurry of 80:10:10 wt% of LFP:carbon black: polyvinylidene difluoride in N-methyl-2-pyrrolidone onto an aluminum current collector using a doctor blade with a 125- $\mu\text{m}$  gap. The cathodes were dried overnight at  $80^\circ\text{C}$  in an ambient oven, and further dried for additional two hours at  $80^\circ\text{C}$  in a vacuum oven. The electrodes were measured with a digital micrometer to be  $\sim 70 \mu\text{m}$  thick and had a loading of 10-14 mg LFP within the  $1.6 \text{ cm}^2$  punched electrode. LFP cathodes were paired with a metallic Li foil anode separated by a Celgard 2325 separator, and the electrolyte was 1.2 M  $\text{LiPF}_6$  in 3:7 vol % ethylene carbonate:ethyl methyl

carbonate. The cells were cycled at room temperature for 13 charge/discharge cycles with cutoff voltages of 4.0 V and 2.5 V at rates ranging from C/20 to 1 C (where 1C was defined as 160 mA g<sup>-1</sup> LFP) on a MACCOR cyler. The cells were charged/discharged at C/20 (three times), C/10 (two times), C/5 (two times), C/2 (two times), 1 C (two times), and C/20 (two times). A minimum of 150 mAh g<sup>-1</sup> LFP at C/20, 80 mAh g<sup>-1</sup> LFP at 1 C, and more than 98% capacity retention in the last 2 cycles relative to the 2<sup>nd</sup> cycle was considered an acceptance criteria for a cell to be used for lithiation/delithiation kinetics characterization testing. Representative rate capability data can be found in Appendix A, Figure A3. For evaluation of kinetic parameters of the LFP/FP, electrochemical testing was conducted in a temperature-controlled incubator (VWR). The temperature-controlled experiments were conducted with a Biologic SP-150 potentiostat. Cells were equilibrated for 4 h at a given set temperature before conducting electrochemical evaluation. For electrochemical oxidation of LFP, a constant potential of 3.6 V was applied until the current dropped to below C/20 (8 mA g<sup>-1</sup> LFP). The cell was then allowed to rest for 1 h, after which it was charged at C/10 until reaching a cutoff voltage of 4.0 V. After reaching this completely charged stage (>99% FP based on mAh of charge measured), a cell was allowed to rest for 1 h. The potential was then set at 3.25 V to discharge the cell until the current dropped below C/20 (8 mA g<sup>-1</sup> LFP/FP), the cell was allowed to rest for 1 h, and then the cell was discharged at C/10 to a cutoff discharge voltage of 2.5 V to convert the active material back to the LFP form. Cells were charged and discharged three times at each temperature. Three independent cells were evaluated using this procedure.

## **2.5 Results**

### *2.5.1 Chemical oxidation/reduction using redox shuttles*

Among the molecular moieties available for chemical oxidation and reduction of Li-ion cathode material, metallocenes (e.g. ferrocene (Fc), nickelocene) are readily commercially available in a variety of redox potentials. These compounds consist of transition metals sandwiched between aromatic cyclopentadienyl rings ( $C_5H_5^-$ ), and the rings may be functionalized to shift the redox potential of the transition metal <sup>25</sup>. Many of these compounds have highly reversible electrochemical redox, stability in commonly used Li-ion battery electrolytes, and molecular tunability, thus there are shuttles available both to oxidize and reduce Li-ion cathode materials <sup>26</sup>. For the LFP material used in this study the redox potential was 3.45 V vs Li/Li<sup>+</sup>, thus the metallocene redox shuttles chosen were 1,1'-dibromoferrocenium (FcBr<sub>2</sub><sup>+</sup>) for LFP oxidation (half-wave redox potential of 3.6 V vs Li/Li<sup>+</sup>). Similarly, Fc was used for reduction of FP (half-wave redox potential of 3.25 V vs Li/Li<sup>+</sup>). The relevant chemical oxidation/reduction reactions for LFP/FP are:



To quantify the progression of chemical redox reactions between the redox shuttles and solid particles, the extinction peaks from UV-Vis spectrum were used. The intensity of UV-Vis peaks have been widely used for determination of the concentration of dissolved species in general <sup>27</sup>. For example, in this study when tracking the reaction progression of FcBr<sub>2</sub><sup>+</sup> with LFP, the UV-Vis spectra for FcBr<sub>2</sub><sup>+</sup> was used. FcBr<sub>2</sub><sup>+</sup> has a uniquely distinguishable peak at 705 nm (Figure 1a), and for a known initial concentration of FcBr<sub>2</sub><sup>+</sup> this peak can be used to quantitatively track the extent of reduction of FcBr<sub>2</sub><sup>+</sup> in solution back to FcBr<sub>2</sub>. Reduction of FcBr<sub>2</sub><sup>+</sup> was assumed to only be due to the oxidation of LFP via the reaction in Eq. 1. Thus, through tracking the UV-Vis

peak for  $\text{FcBr}_2^+$  the extent of chemical oxidation and delithiation of LFP by  $\text{FcBr}_2^+$  was monitored. An example of the progression of the  $\text{FcBr}_2^+$  oxidation peak at 705 nm after contacting LFP can be found in Figure 1a. Each extinction spectrum required nearly 30 seconds to collect within the wavelength range investigated, and spectra were continuously collected for 90 minutes at an interval of 2 minutes. For these experiments, LFP was used as received; however, as mentioned in the Experimental section the  $\text{FcBr}_2$  was electrochemically oxidized before use (to  $> 98\%$   $\text{FcBr}_2^+$  as determined by coulometry). Before conducting chemical redox experiments such as those found in Figure 1, first the range of redox shuttle concentrations that were accessible with the technique was determined. For UV-Vis peaks, at too low of a concentration a species will not be detectable and at too high of a concentration the linear assumption between the peak magnitude and concentration no longer holds. A dilution series was conducted with  $\text{FcBr}_2^+$  (see Appendix A, Figure A4), and it was determined that to stay within the linear regime for the UV-Vis measurements that the  $\text{FcBr}_2^+$  should not exceed  $\sim 2.5$  mM. It was also noted that the particles contribute to measured extinction through scattering of the UV-Vis incident light without selectivity for particular wavelengths. To avoid the scattering from the particles saturating the extinction that could be measured, the LFP particle concentration was limited to  $\sim 0.5$  mg mL<sup>-1</sup>. The particle concentration was typically at the upper limit of  $\sim 0.5$  mg mL<sup>-1</sup> because very low particle concentrations were difficult to accurately weigh.

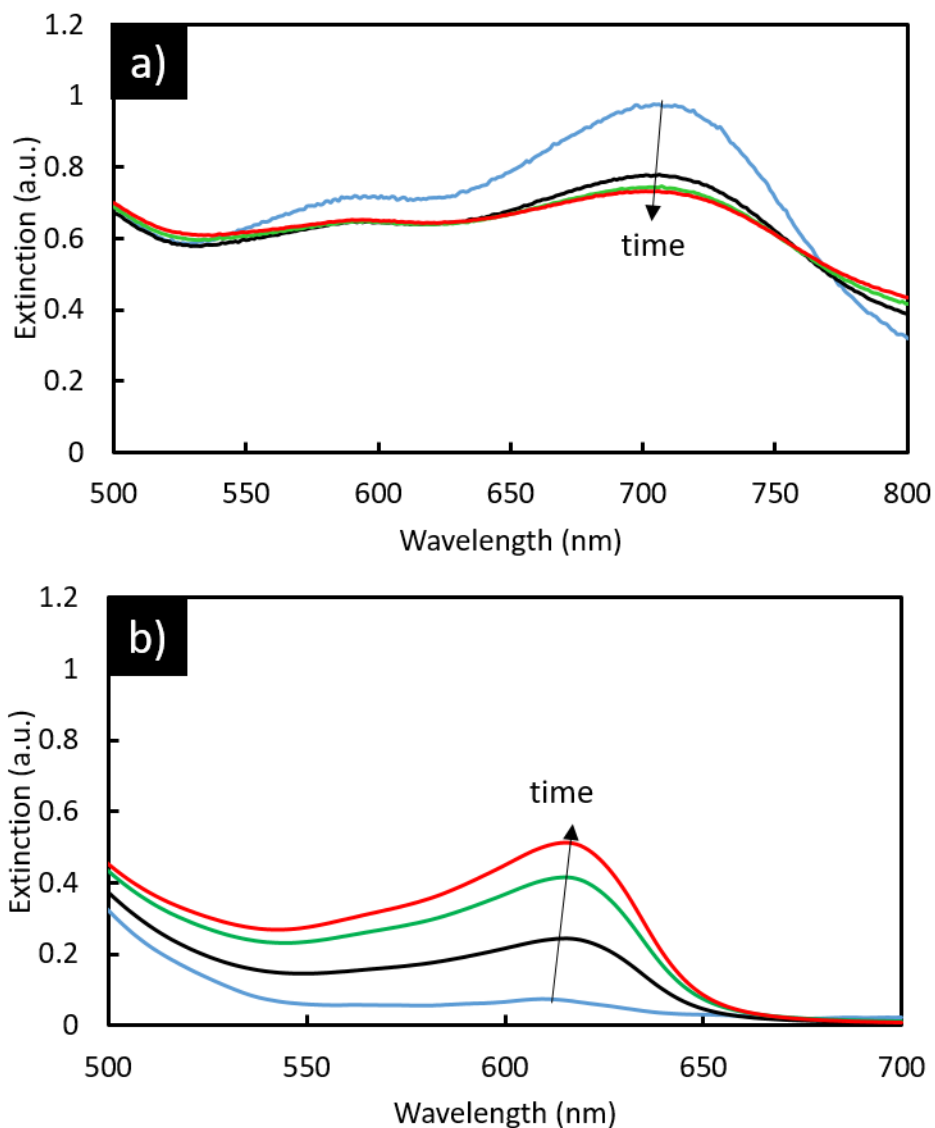


**Figure 1. UV-Vis spectra taken at different times during a) the oxidation of LFP with  $\text{FcBr}_2^+$  and b) the reduction of FP with Fc. Curves in a) and b) correspond to 0 min (blue), 30 min (black), 60 min (green) and, 90 min (red). The temperature for both experiments was  $35^\circ\text{C}$ .**

The other chemical redox conducted in this study was the reduction of FP with Fc, depicted in the reaction in Eq. 2. Chemical reduction of FP was described in the Experimental section, and the FP powder had  $\sim 96.5\%$  removal of lithium relative to the initial LFP powder.  $\text{Fc}^+$  has a unique peak at 615 nm (Figure 1b), and thus similar to the analysis described above for the chemical redox

of  $\text{FcBr}_2^+$  and LFP, it was assumed that the oxidation of Fc was only due to reduction of FP. This meant the reduction and lithiation of FP could be monitored by tracking the magnitude of the  $\text{Fc}^+$  peak. A dilution series was conducted for  $\text{Fc}^+$ , and the results can be found in the Appendix A, Figure A5. For  $\text{Fc}^+$ , the maximum concentration that could be used with the UV-Vis technique was determined to be  $\sim 8$  mM. Similar to the LFP particles, due to the scattering from the FP particles the targeted particle concentration was  $\sim 0.5$  mg  $\text{ml}^{-1}$ .

### 2.5.2 Chemical Redox at Varying Temperatures-

The sections above described how the concentration of  $\text{FcBr}_2^+$  and  $\text{Fc}^+$  were monitored using UV-Vis in order to track the relative extent of delithiation and lithiation of LFP and FP, respectively. For quantitative analysis and comparison between both these redox processes and the electrochemical oxidation of LFP and reduction of FP, the chemical redox reactions were monitored at different temperatures. Three representative experiments of the oxidation LFP with  $\text{FcBr}_2^+$  at temperatures of  $25^\circ\text{C}$ ,  $35^\circ\text{C}$ , and  $45^\circ\text{C}$  are shown in Figure 2. Both the  $\text{FcBr}_2^+$  concentration which was determined from the magnitude of the 705 nm UV-Vis peak (Figure 2a) and the corresponding extent of delithiation (and oxidation) of LFP (Figure 2b) are shown. The control experiment without LFP added to the solution at the most aggressive reaction condition of  $45^\circ\text{C}$  resulted in reduction of 2% of the  $\text{FcBr}_2^+$  after 90 minutes, indicating the redox shuttle was stable in the solution during the time course of the experiments and that nearly all of the reduction of the redox shuttle was due to the presence of LFP added to the solution (see Appendix A, Figure A6). The chemical redox between  $\text{FcBr}_2^+$  and LFP proceeds at an increased rate for increasing temperature, with the  $\text{FcBr}_2^+$  being nearly completely reduced at  $45^\circ\text{C}$ . This suggested that the reaction has an activation barrier that has sensitivity to an increase in temperature, which led to additional analysis of the apparent activation energy of this process as will be described in the

Discussion section. For the highest temperature, the extent of delithiation of LFP at 90 minutes was 70%.

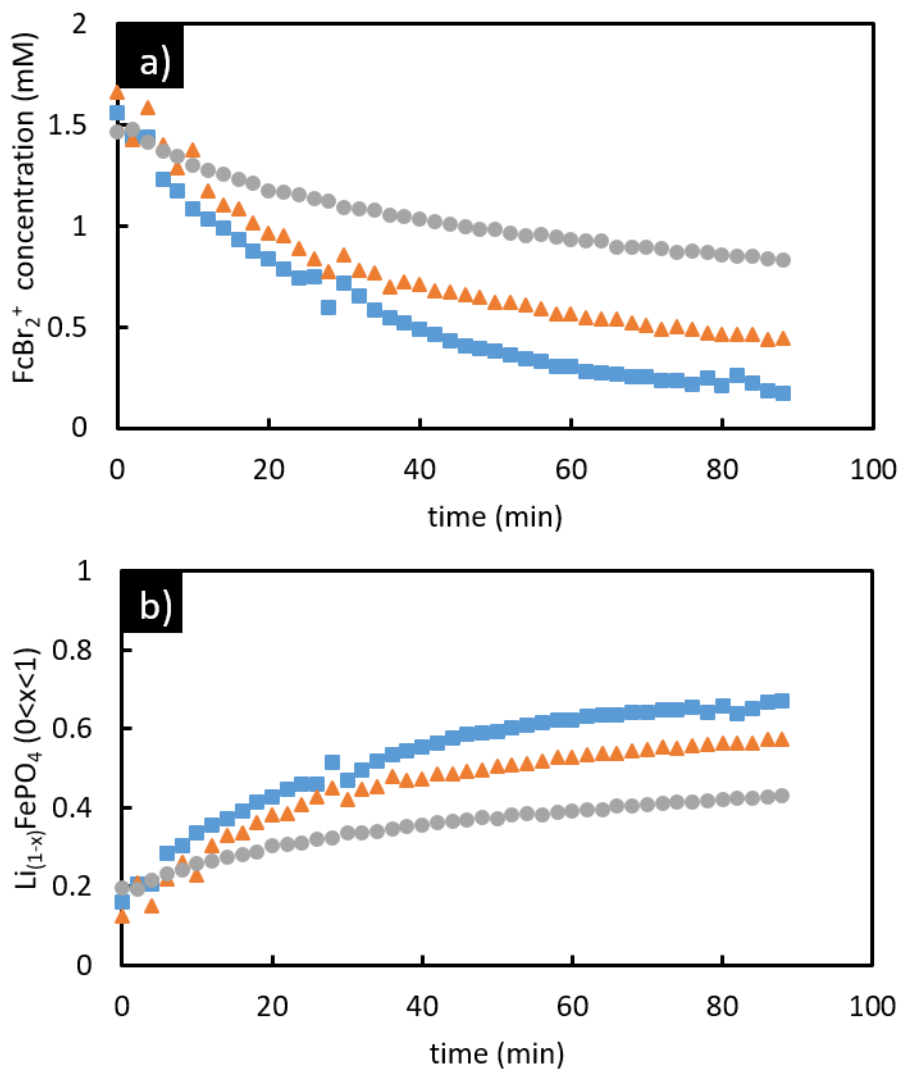


**Figure 2. a)  $\text{FcBr}_2^+$  concentration and b) extent of delithiation of LFP as a function of time during the first 90 minutes of the chemical redox reaction between the two species at 25 °C (gray circles), 35 °C (orange triangles), and 45 °C (blue squares).**

Complementary experiments were also conducted for the reduction of FP with Fc, at 25°C, 35°C, and 45°C. Representative results can be found in Figure 3. The Fc<sup>+</sup> concentration was determined from the UV-Vis peak magnitude at 615 nm (Figure 1b), and the lithiation and reduction of FP was determined by assuming every electron lost to form Fc<sup>+</sup> went to an FP particle (Figure 3b). It is noted control experiments of Fc without FP added indicated the Fc was very stable to oxidation in the electrolyte in general (See Appendix A, Figure A7). Inspection of Figure 3 revealed that as the temperature was increased that both the rate of the chemical redox reaction and the extent of the lithiation of the solid particles after 90 minutes were greater. However, the chemical redox reaction was slower for the Fc/FP system relative to the FcBr<sub>2</sub><sup>+</sup>/LFP system. For example, after 40 minutes at the highest temperature (45 °C), the LFP particles had reached 55% oxidation while the FP particles had reached 45% reduction. The total volume of the reaction solution and the target mass loading for the solid particles was the same as for the FcBr<sub>2</sub><sup>+</sup>/LFP redox reaction (and the FP and LFP were from the same source particles, thus the surface area of the solid electroactive material was the same in both experiments), however, the reduction of FcBr<sub>2</sub><sup>+</sup> proceeded much faster than the oxidation of Fc at all conditions. Due to the greater absorption coefficient for FcBr<sub>2</sub> relative to Fc, a smaller initial concentration of FcBr<sub>2</sub><sup>+</sup> had to be used (2 mM as opposed to 8 mM). This resulted in FcBr<sub>2</sub><sup>+</sup> being the limiting reagent in the chemical redox process, with a molar ratio of 0.75:1 FcBr<sub>2</sub><sup>+</sup>:LFP as opposed to 3:1 Fc:FP. All experiments were conducted using the same cells and mixing conditions. Both redox shuttles would be expected to have similar diffusion coefficients, although FcBr<sub>2</sub> would be expected to be slightly lower due to the higher molecular weight<sup>25</sup>. Given that FcBr<sub>2</sub><sup>+</sup> had lower concentration and lower expected diffusion coefficient than Fc, the observed higher reaction rate would suggest the kinetics of the FcBr<sub>2</sub><sup>+</sup>/LFP reaction were intrinsically faster than those of the Fc/FP reaction. The root cause of

the intrinsic kinetic difference is still under investigation; however, as will be discussed in more detail later it was suspected that both of the chemical redox processes were impacted by mass transport limitations.

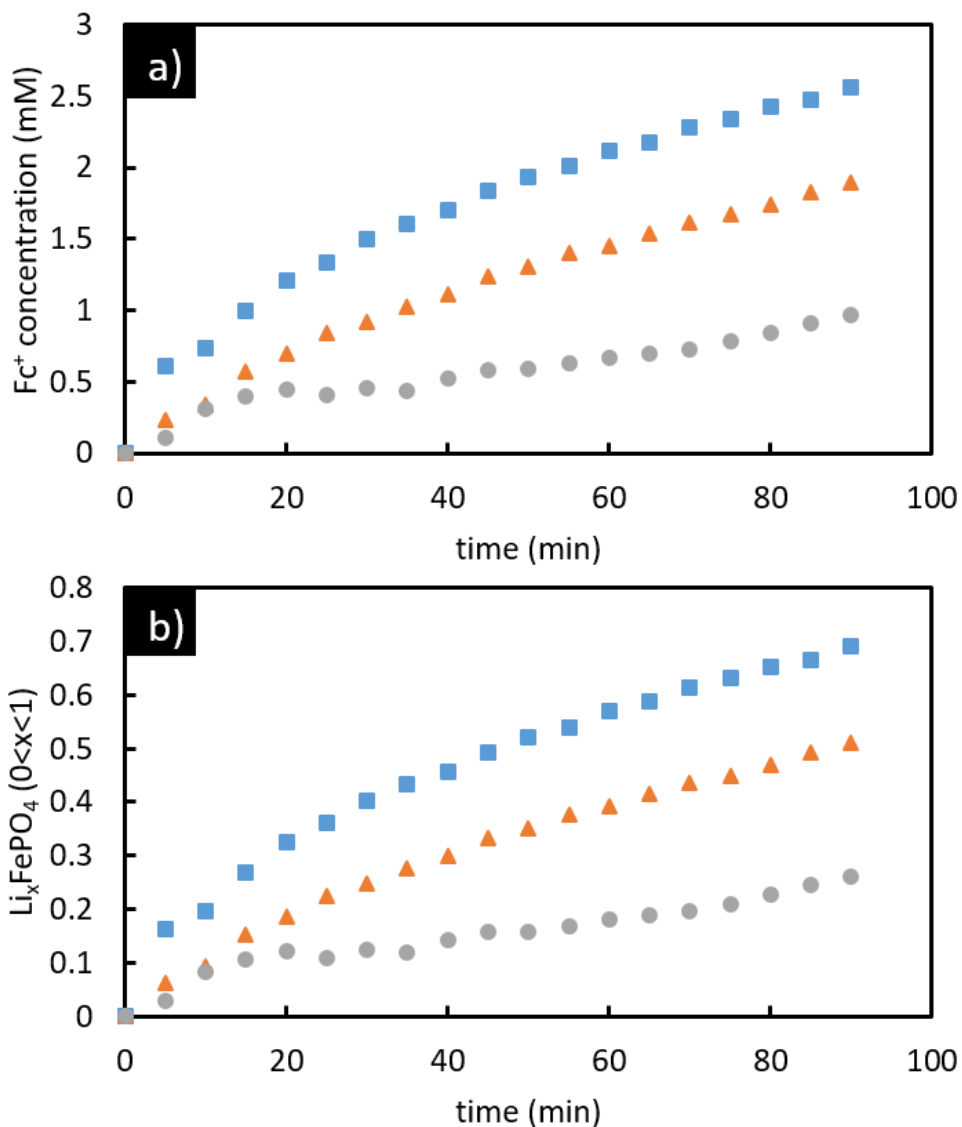


**Figure 3. a)  $\text{Fc}^+$  concentration from UV-Vis measurements and b) corresponding extent of lithiation of FP as a function of time during the first 90 minutes of the chemical redox**

**reaction between the two species at 25 °C (gray circles), 35 °C (orange triangles), and 45 °C (blue squares).**

### 2.5.3 *Electrochemical delithiation/lithiation of LFP/FP-*

To compare chemical lithiation/delithiation with electrochemical lithiation/delithiation, 2032-type coin cells with LFP as cathode and Li foil as anode were constructed. When the electrode active material was in the lithiated state (LFP), the delithiation and oxidation of LFP was conducted by applying a constant potential of 3.6V (vs. Li/Li<sup>+</sup>). When the electrode active material was in the delithiated state (FP), reduction and lithiation was conducted by applying a constant potential of 3.25 V (vs. Li/Li<sup>+</sup>). The constant potential electrochemical oxidation and reduction experiments were conducted at three temperatures: 25 °C, 35 °C, and 45 °C. Assuming that the measured current was only due to the oxidation of LFP during charge and reduction of FP during discharge, the extent of lithiation as a function of time was calculated for each electrochemical reaction (oxidation of LFP and reduction of FP in Figures 4a and 4b, respectively). Electrochemical oxidation and reduction of the electrode materials at all temperatures reached more than 90%, and as the temperature was increased the cell achieved conversion faster. This temperature dependence also suggested an activation barrier that could be overcome with elevation of temperature for the electrochemical redox processes. The lithiation of FP (Figure 4a) proceeded slower than delithiation of LFP (Figure 4b) at all temperatures. Note that the same electrodes were used for all electrochemical cycling experiments, thus differences in the rate of electrochemical redox reflect asymmetry in the reversible redox of the LFP active material loaded into the electrode and do not reflect variation in cell or electrode fabrication or impacts from processing the LFP to FP<sup>28</sup> (because there was not a chemical oxidation step applied to the LFP for the coin cell electrodes – FP was electrochemically produced).

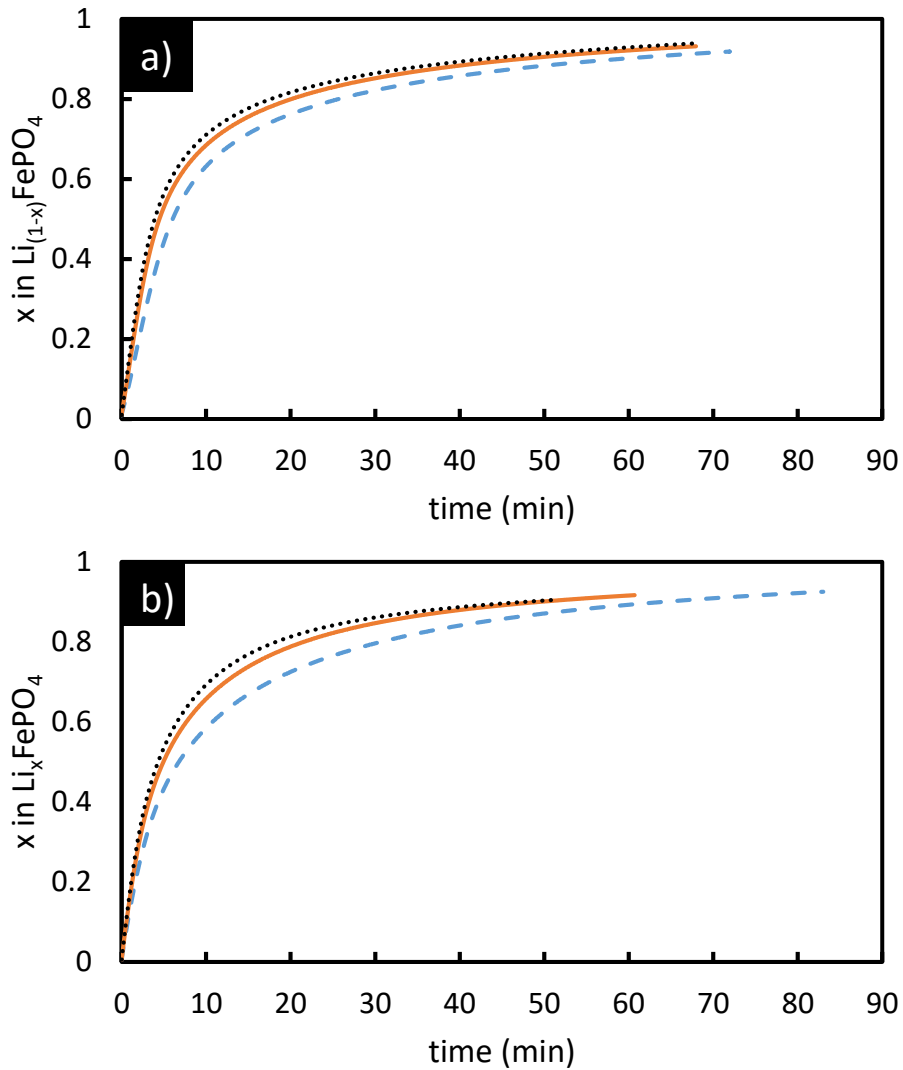


**Figure 4. a) Extent of electrochemical delithiation and oxidation of LFP within a composite electrode, starting from the fully lithiated state, during a chronoamperometry experiment held at 3.6 V (vs. Li/Li<sup>+</sup>). b) Extent of electrochemical lithiation and reduction of FP within a composite electrode, starting from the fully delithiated state, during a chronoamperometry experiment held at a potential of 3.25 V (vs. Li/Li<sup>+</sup>). The composite LFP cathode was paired with a lithium metal foil anode. Both a) and b) were completed**

using the same coin cell. The chronoamperometry was conducted at different temperatures of 25 °C (blue dashed), 35 °C (solid orange), and 45 °C (black dots).

#### 2.5.4 Johnson-Mehl-Avrami-Erofeyev-Kolmogorov (JMAEK) Analysis

Both chemical and electrochemical redox of LFP and FP were analyzed using the Johnson-Mehl-Avrami-Erofeyev-Kolmogorov (JMAEK) equation<sup>29-31</sup>. JMAEK is a solid-state model developed for phase transformations that assumes single step nucleation, infinite system volume, and homogeneous distribution of nucleation sites within the system volume. This model has previously been applied to lithiation and delithiation of FP/LFP materials, with the assumption of the limiting step being nucleation and propagation of the conversion of FP to/from LFP (or correspondingly lithiation or delithiation of the active material phase which includes the transport of Li<sup>+</sup> and e<sup>-</sup>)<sup>20,28,32-34</sup>. The first step was to use the experimentally obtained fractional conversion of FP/LFP (e.g., Figures 2b, 3b, and 4) and to apply these outcomes using Equation 3:

$$f = 1 - \exp(-kt)^n \quad (3)$$

where  $f$  is the volume fraction of the material that has been delithiated/lithiated during the reaction,  $k$  is a first order rate constant,  $t$  is time, and  $n$  indicates Avrami exponent, which is related to the dimensionality of growth.  $n$  can be written as

$$n = a + bc \quad (4)$$

where  $a$  is the nucleation index defined as  $N \approx t^a$ .  $N$  is the number of nuclei per unit volume and  $t$  is time.  $b$  is the dimensionality of the growth and  $b = 1, 2, 3$  for 1-D, 2-D, and 3-D growth, respectively.  $c$  is the growth index of the transformation and can take the value 1 for phase boundary control or 0.5 for diffusion-controlled growth. Figure 5 shows the dependence of rate constant on temperature during chemical oxidation of LFP (Figure 5a), chemical reduction of FP

(Figure 5b), electrochemical oxidation of LFP (Figure 5c), and electrochemical reduction of FP (Figure 5d).

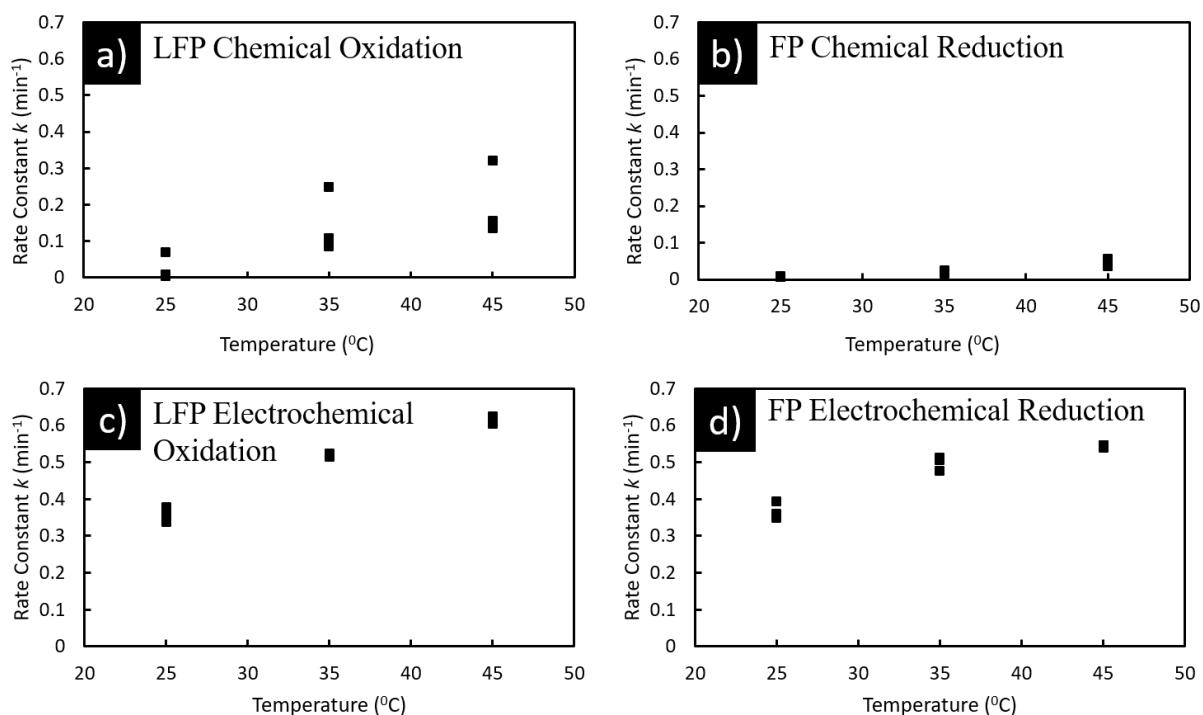


**Figure 5. Rate constant as a function of temperature determined for each experiment using either chemical (a, b) or electrochemical (c, d) redox. a) and c) are for delithiation and oxidation of LFP and b) and d) are for lithiation and reduction of FP. Note that there are three independent measurements and the corresponding data points at each temperature.**

Plots of  $\log(-\log(1-f))$  against  $\log t$  (see Appendix A, Figure A8 for representative plots for chemical redox at three temperatures) give  $n$  and  $k$  for reactions (1) and (2) (Table 1). For chemical redox,  $n$  was determined to range from 0.23-0.77. For LFP chemical oxidation,  $n$  varied from 0.2-0.4 and FP chemical reduction,  $n$  varied from 0.7-0.8.  $n$  did not follow any clear trend for increasing temperature. For electrochemical redox  $n$  was in the range of 0.57-0.65, with the coefficient of determination  $>95\%$ , and decreased with temperature. The rate constant  $k$  as

expected increased with temperature for both chemical and electrochemical redox.  $k$  lied between 0.01-0.32  $\text{min}^{-1}$  for chemical redox and 0.34-0.63  $\text{min}^{-1}$  for electrochemical redox. In the Avrami analysis done by Schougaard group,  $n$  for chemical oxidation was reported to be 0.6 and  $k$  in the range of 0.1-6.5  $\text{min}^{-1}$  (in temperature range 7-58  $^{\circ}\text{C}$ )<sup>20</sup> and the model was not found to capture chemical reduction of LFP<sup>19</sup>. For electrochemical reduction, Allen et al.<sup>32,33</sup> estimated  $n \sim 1$  and  $k$  between 0.014-0.036  $\text{min}^{-1}$  for the temperature range of 0-22  $^{\circ}\text{C}$ . Other studies conducted on electrochemical redox of LFP that include Avrami analysis demonstrated that  $n$  decreases with applied overpotential<sup>28,34</sup>.

**Table 1. Avrami exponent ( $n$ ), nucleation index ( $a$ ), and first order rate constant ( $k$ ) for LFP oxidation and FP reduction, each done using chemical and electrochemical methods.**

LFP Oxidation	Chemical			Electrochemical		
Temperature	$n$	$a$	$k$	$n$	$a$	$k$
25	0.23	-0.27	0.01	0.64	0.14	0.36
35	0.36	-0.14	0.10	0.60	0.10	0.52
45	0.38	-0.12	0.15	0.57	0.07	0.61
FP Reduction	Chemical			Electrochemical		
Temperature	$n$	$a$	$k$	$n$	$a$	$k$
25	0.84	0.34	0.01	0.61	0.11	0.37
35	0.72	0.22	0.02	0.60	0.10	0.50
45	0.77	0.27	0.04	0.60	0.10	0.54

### 2.5.5 Chemical Redox-

Using the experimental conditions and the Nernst equation <sup>35</sup>, it was found that just from changes in bulk concentration during the chemical redox reaction that the potential difference between the redox shuttles and electroactive LFP/FP powder decreased up to 8 mV and 30 mV for oxidation of LFP with  $\text{FcBr}_2^+$  and reduction of FP with Fc, respectively. This calculation of potential difference assumed the potential of the LFP or FP was constant and that changes were due to changes in the concentration of the oxidized or reduced state of the redox shuttle in bulk solution. The decrease in the thermodynamic driving force was in part responsible for the more gradual chemical conversion of FP/LFP by redox shuttles as shown in Figures 2a and 3a, and the decrease in the local concentration of the redox shuttle in the reactant form near the particle interface would further reduce this driving force. Changes in the concentration of redox shuttles will affect the rate of the chemical redox reaction through impacts in thermodynamic, transport, and kinetic driving forces. The limited concentration of redox shuttles was in contrast with previous studies of chemical redox of LFP, where excess concentration of oxidant/reductant ensured negligible change in thermodynamic driving force around LFP particles <sup>19,20</sup>. As a result, the calculated  $k_{chem}$  values in these reports were about two orders of magnitude higher than values estimated in this study. Jennings et al. reported  $k_{chem}$  in the range of  $\sim 0.02\text{-}0.1 \text{ min}^{-1}$ , which was comparable to the values in this study<sup>21</sup>. However, that study employed static LFP films at varying states of charge; the LFP film (excess reactant) was treated with low concentration redox shuttles diffusing from a constant distance. Another study that used low concentration redox shuttle was the chemical redox kinetics determined using scanning electrochemical microscopy by Yan et al. <sup>22</sup> where the lithiation/delithiation of dense LFP/FP pellets by redox shuttles was diffusion controlled, and the rate constant was interpreted in the context of interfacial charge transfer

(reported in the range of  $3.70\text{-}6.57 \times 10^{-3} \text{ cm s}^{-1}$ ) between redox shuttle and LFP/FP pellets. The calculated rate constant had a quasi-linear dependence on the LFP:FP ratio in the pellet and depended strongly upon pretreatment. Our work differs from these studies as the continuous lithiation/delithiation of LFP particles was monitored while introducing mild mixing. Another reason for chemical reduction of FP being slower than chemical oxidation of LFP in addition to the potential difference between the particles and redox shuttles may have been the intrinsic material performance. Coin cells made using FP obtained from oxidation of LFP using  $\text{H}_2\text{O}_2$  showed a sloping discharge potential on the first discharge rather than a flat plateau (Appendix A. Figure S9). Interestingly, the material recovered the flat charge/discharge behavior for all subsequent cycles; however, for the chemical redox experiment the first cycle would reflect the potential difference with the redox shuttle. The sloping profile suggested that the driving force for reduction of FP with Fc was even lower than expected. It is noted that similar degradation of electrochemical performance of LFP in vigorously stirred aqueous suspensions has been reported previously<sup>36</sup>.

## **2.6 Discussion**

When the averages of chemical rate constants were compared against electrochemical rate constants (Table 1),  $k_{chem} > k_{chem}$ . This was because electrochemical redox offered constant potentiostatic conditions, whereas in chemical redox both the mass transfer limitations increased and the thermodynamic driving force for reaction decreased with time as the redox shuttles participated in the reaction, where both effects would result in a lower rate of redox reaction near the FP/LFP particle interface. In comparing electrochemical and chemical oxidation and reduction, it is important to take into context the differing reaction processes for these two types of redox. As

an example, chemical reduction of FP with Fc (Eq. 2) was proposed to progress through the main following subset of steps (for cartoon schematic of the steps refer to Figure 6a):

1. Fc molecules diffuse from the bulk electrolyte solution to the surface of FP particles.
2. Fc molecule adsorbs on the surface of FP particles.
3. Fc reacts with FP ( $\text{Fc} \rightarrow \text{Fc}^+$  and  $\text{Fe}^{(3)+}\text{PO}_4 \rightarrow \text{Fe}^{(2)+}\text{PO}_4$ ) creating a local negative potential on  $\text{FePO}_4$  particles.
4.  $\text{Li}^+$  in the surrounding liquid diffuses in  $\text{FePO}_4$  lattice, resulting in  $\text{Li}_x\text{FePO}_4$  and  $\text{Li}^+$  progressing through the solid to appropriate positions within the structure.
5.  $\text{Fc}^+$  desorbs from the surface of  $\text{Li}_x\text{FePO}_4$  to the bulk electrolyte solution.

In contrast, electrochemical reduction of FP in a Li anode half-cell was proposed to involve the following main steps (for a cartoon schematic refer to Figure 6b):

1. At approximately constant potential ( $\sim 0$  V vs  $\text{Li}/\text{Li}^+$ ), Li anode undergoes electrochemical oxidation and  $\text{Li}^+$  ions were stripped off ( $\text{Li} \rightarrow \text{Li}^+ + \text{e}^-$ ).
2. There was a net flux of  $\text{Li}^+$  which transported from the Li metal foil surface to bulk electrolyte solution. Simultaneously, electrons transport through the Li foil to the current collector and external circuit.
3.  $\text{Li}^+$  undergoes a net flux towards the cathode.

4.  $\text{Li}^+$  undergoes a net flux through the tortuous paths within the electrolyte phase of the porous  $\text{Li}_x\text{FePO}_4$  electrode.

5.  $\text{Li}^+$  intercalates in the lattice of  $\text{Fe}^{(3)+}\text{PO}_4$  particle along with electrons which arrive from the external circuit ( $\text{Li}^+ + \text{Fe}^{(3)+}\text{PO}_4 + \text{e}^- \rightarrow \text{Li}_x\text{Fe}^{(2)+}\text{PO}_4$ ) The electron would also need to conduct through the current collector and the matrix of the electrode to the particles undergoing reaction.

6.  $\text{Li}^+$  and  $\text{e}^-$  undergo ambipolar co-diffusion through  $\text{Li}_x\text{FePO}_4$  lattice to appropriate sites.

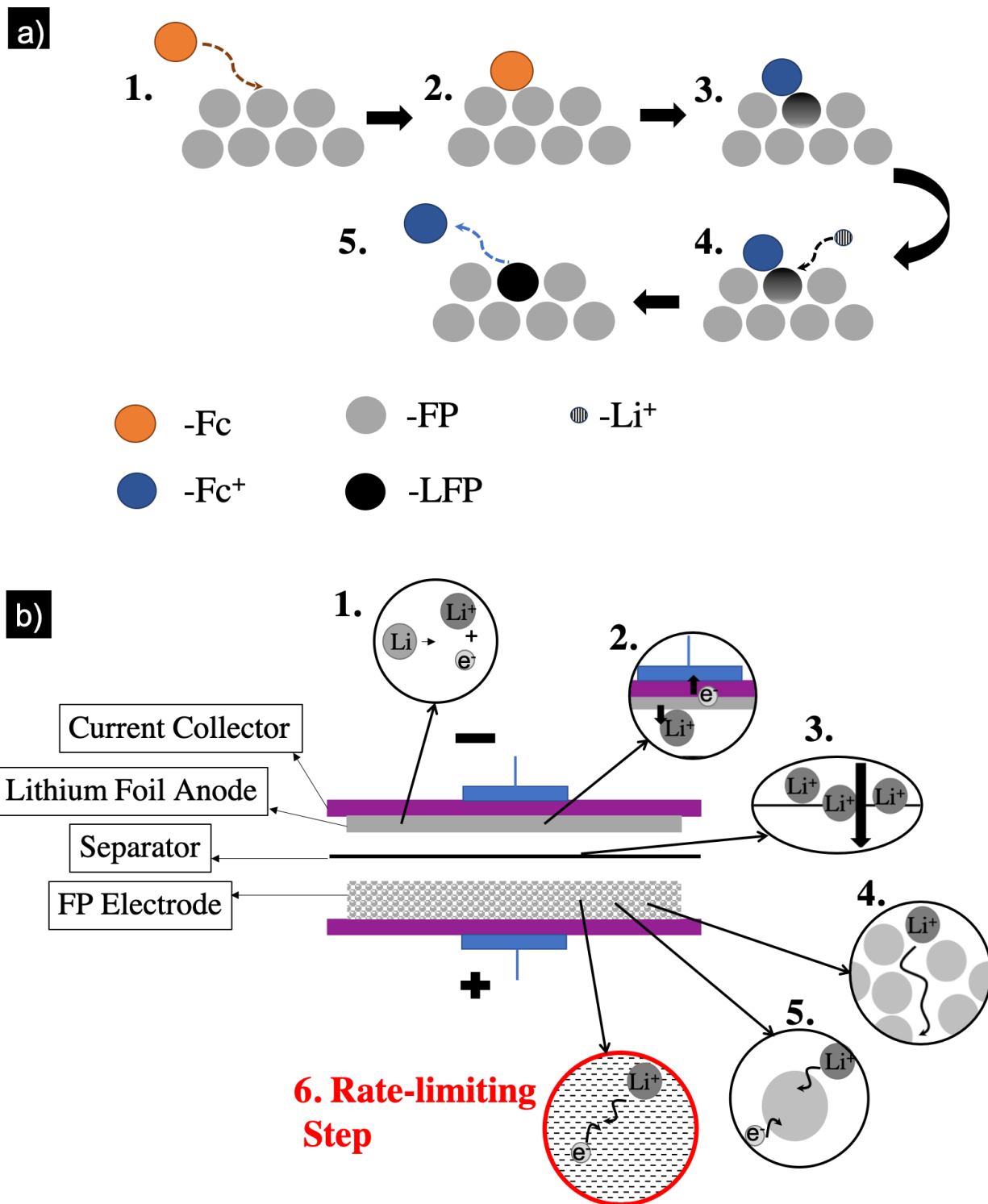


**Figure 6.** Schematic of the steps for a) chemical reduction of FP using Fc as redox shuttle and b) electrochemical reduction of FP in a half cell containing a lithium metal anode. Note that cartoons are not drawn to scale.

The limiting step for electrochemical intercalation/deintercalation is generally dependent on the materials used and cell configuration, however, for LFP/FP in thin porous electrodes often Step 6 has been assumed as the rate-limiting step for electrochemical redox<sup>37,38</sup>. With the electrode thickness of ~70-80  $\mu\text{m}$  used in this study,  $\text{Li}^+$  diffusion through Li-rich or Li-poor LFP lattice was assumed to be the limiting step in electrochemical redox. However, the reaction pathway of chemical redox has not been extensively studied and can be strongly dependent on experimental conditions. For example, in the study done by Weichert et al<sup>39</sup>, on single large crystals of LFP phase transformation during chemical delithiation suggested transport controlled phase growth. They also found an induction period ranging several hours before the first layer of FP started forming on the surface. The results shown in Figures 2a and 2b suggest no such induction period for LFP to FP transition in this study, which likely reflected that for the much smaller particles used in this study (~150 nm as opposed to ~2 mm used in<sup>39</sup>) that the limitations in chemical lithiation/delithiation of LFP were not purely solid-state transport limited – though this step would still be expected to impact the overall magnitude of the rate and apparent activation barrier. It is also noted that for materials like LFP which have one dimensional diffusion channels, diffusion of  $\text{Li}^+$  is dependent on particle size as has been noted in the literature<sup>40</sup>.  $\text{Li}^+$  diffusion through mesoscale agglomerates that dynamically form and dissociate in the chemical redox solution was expected to be different and have greater variation relative to a fabricated electrode in a coin cell. It is suspected that the variation and dynamic process of agglomerate formation was in part responsible for the greater variance in the parameters determined for chemical redox relative to electrochemical redox.

### *2.6.1 Avrami analysis*

Analysis with the JMAEK equation assumed conditions such as single step nucleation, infinite availability for phase growth, and homogeneous distribution of nucleation sites. The validity of JMAEK analysis may not be necessarily true in the case of chemical redox as it was not known whether it followed a single step nucleation, and the experimental conditions in the UV-Vis experiment offer a finite volume for the system undergoing transformation. Stirring may help in the distribution of nucleation sites i.e. solid Li-rich or Li-poor LFP particles, however, for the relatively mild stirring used in these experiments the particles were not expected to be perfectly homogeneously distributed. However, as noted in previous studies<sup>29,30,41</sup>, JMAEK analysis might fit the physical conditions of electrochemical redox if the LFP electrode can be approximated as an infinite system with nucleation sites considered homogeneous at a secondary particle level. At a potential difference of greater than or equal to 150 mV, electrochemical chronoamperometry of LFP (Appendix A, Figure A10) was consistent with previous reports of a two-phase reaction<sup>28,42</sup>, which is the case when reaction proceeds by nucleation and growth hence being a suitable scenario for JMAEK model. Additional mechanistic studies of chemical redox of battery active materials will be needed to understand the nucleation mechanism and validate the model for phase growth.

For the same  $n$  values,  $a$ ,  $b$  and,  $c$  have been interpreted with regards to providing insights into phase transformations.  $n$  for electrochemical redox has been consistently found to be close to 1 for LFP under various experimental conditions<sup>32-34</sup>. Allen et al. interpreted  $n$  values obtained during electrochemical delithiation as two-dimensional growth ( $b = 2$ ) with a diffusion controlled mechanism ( $c=1/2$ ), concluding instantaneous nucleation ( $a = 0$ ). However, in-situ synchrotron X-ray diffraction of LFP cathode has suggested phase transformations in nanoscale LFP have lithiation/delithiation which proceeded at a steady rate accompanied by two-phase coexistence of Li-rich and Li-poor domains<sup>41</sup>. Therefore, in this study the results for electrochemical redox were

interpreted similar to Xiang et al.<sup>34</sup>, with a one-dimensional ( $b = 1$ ), diffusion limited growth ( $c = 0.5$ ), and thus the variation  $0.07 < a < 0.14$  was a result of various parameters (temperature, secondary particle size) impacting the nucleation kinetics. In chemical discharge where values were calculated of  $a < 0.3$ , our speculation was that dispersed particles would undergo faster lithiation than porous electrodes and would approach instantaneous nucleation. The observed values of  $a < 0$  during chemical oxidation of LFP indicated that the number of nuclei decreased with time, and it was hypothesized that this outcome may have been a result of reaction conditions causing near instantaneous nucleation of the dispersed LFP particles.

### 2.6.2 Apparent Activation Energy

Using the Arrhenius equation, the apparent activation energy,  $E_a$ , for the redox processes were determined using plots of  $\ln k$  versus  $1/T$  (see Appendix A, Figure A11 for Arrhenius plots of oxidation of LFP and reduction of FP via chemical and electrochemical redox using the  $k$  values from Table 1). Linear regression was used to get the apparent activation energy from the slope of the regression line ( $-E_a/R$ , with  $R$  the ideal gas constant). The results obtained from this analysis can be found in Table 2.

**Table 2: Apparent activation energy for chemical and electrochemical redox of LFP.**

	LFP Oxidation (kJ mol <sup>-1</sup> )	FP Reduction (kJ mol <sup>-1</sup> )
Chemical	125 ± 21	72 ± 15
Electrochemical	21 ± 2	16 ± 3

The apparent activation energy determined for chemical oxidation and reduction was significantly higher than electrochemical oxidation and reduction for LFP/FP materials. This indicated that the reaction pathway for chemical redox has a stronger dependence upon temperature which may be due to a host of factors including mass transport limitations in redox shuttle lean chemical oxidation versus particle lean chemical reduction, molecular structure of redox shuttles used which may affect the shuttle-particle interaction, and/or the intrinsic material performance of LFP/FP

The apparent activation energy for chemical oxidation and reduction of LFP/FP were higher than the values reported by Lepage et al of  $18.4 \text{ kJ mol}^{-1}$ <sup>19</sup> and Kuss et al. of  $50 \text{ kJ mol}^{-1}$ <sup>20</sup>. However, these works employed more than tenfold excess of oxidizing agent accompanied by vigorous stirring, thereby minimizing mass transport limitations in their reaction system and providing a more constant thermodynamic driving force. Hence, values of apparent activation energies are specific to the conditions/environment of oxidation/reduction of LFP/FP. The factors affecting the apparent activation energy include concentration of solid electroactive species relative to redox shuttles, total concentration of redox shuttles (affecting the heterogeneity of the system and the thermodynamic driving force for redox), stirring rate (note in this study stirring was sufficient to prevent localization of the reaction, but higher stirring which would have improved mass transfer resulted in excessive agglomeration of LFP/FP), effective particle size, and the temperature range.

In comparison, electrochemical redox had a much lower apparent activation energy than chemical redox and the values observed in this report were in a similar range to the values reported by Allen et al.<sup>33</sup>, Maxisch et al.<sup>43</sup>, and Takahashi et al.<sup>44</sup>. Electrochemical oxidation and reduction also had similar activation energy. This was in agreement with the values reported by Oyama et al

<sup>28</sup>, confirming that in bulk electrode phase boundary movement was symmetric for oxidation and reduction of LFP.

## ***2.7 Conclusions***

In this work, ultraviolet-visible spectroscopy was used to monitor the chemical oxidation and reduction of a Li-ion battery electrode material facilitated by redox shuttles. Due to limitations in the ranges of detection using the technique, relatively low concentrations of both the active material particles and redox shuttles were used in the suspensions. To better understand the processes involved, the chemical redox experiments were compared in the context of electrochemical oxidation and reduction of the same electrode material. Relative to the electrochemical redox, the chemical redox was a much slower process. Analysis of the conversion of the redox processes as a function of time revealed that the first order rate constants were consistently higher for electrochemical redox, and that the apparent activation energy for the chemical redox was much larger. JMAEK analysis indicated that the phase transformations and reaction pathways were also different for electrochemical and chemical redox for the same materials. This study reported a robust method for tracking the progress of chemical redox reactions between Li-ion battery active materials and redox shuttles, requiring only a unique signature in the extinction spectra for the redox shuttle. In addition, this report demonstrates both the importance and challenges in evaluating both oxidation and reduction via both chemical and electrochemical means for Li-ion active materials. Understanding the chemical redox between redox shuttles and Li-ion active materials is important for a number of applications, including redox shuttle overcharge protection in Li-ion batteries and shuttle-mediated flow batteries <sup>1,3,45</sup>.

## 2.8 References

1. Chen, J., Buhrmester, C. & Dahn, J. R. Chemical Overcharge and Overdischarge Protection for Lithium-Ion Batteries. *Electrochem. Solid-State Lett.* **8**, A59 (2005).
2. Moshurchak, L. M. *et al.* Spectroelectrochemical Studies of Redox Shuttle Overcharge Additive for LiFePO<sub>4</sub>-Based Li-Ion Batteries. *J. Electrochem. Soc.* **112**, 2729–2735 (2005).
3. Zhang, L., Zhang, Z. & Amine, K. Redox Shuttle Additives for Lithium-Ion Battery. in *Lithium Ion Batteries - New Developments* (2012). doi:10.5772/26572
4. Behl, W. K. Electrochemical Overcharge Protection of Rechargeable Lithium Batteries. *J. Electrochem. Soc.* **135**, 21 (1988).
5. Chen, Z., Qin, Y. & Amine, K. Redox shuttles for safer lithium-ion batteries. *Electrochim. Acta* **54**, 5605–5613 (2009).
6. Li, Q. *et al.* ion batteries. 20903–20907 (2017). doi:10.1038/ncomms14643
7. Li, Q., Li, N. & Zhou, H. Saving electric energy by integrating a photoelectrode into a Li-ion battery †. 20903–20907 (2015). doi:10.1039/c5ta06908d
8. Brushett, F. R., Vaughey, J. T. & Jansen, A. N. An all-organic non-aqueous lithium-ion redox flow battery. *Adv. Energy Mater.* **2**, 1390–1396 (2012).
9. Hamelet, S. *et al.* Non-Aqueous Li-Based Redox Flow Batteries. *J. Electrochem. Soc.* **159**, A1360–A1367 (2012).
10. Leung, P. *et al.* Recent developments in organic redox flow batteries: A critical review. *J. Power Sources* **360**, 243–283 (2017).
11. Park, M., Ryu, J., Wang, W. & Cho, J. Material design and engineering of next-generation flow-battery technologies. *Nature Reviews Materials* (2016).

doi:10.1038/natrevmats.2016.80

12. Choi, J. W. & Aurbach, D. Promise and reality of post-lithium-ion batteries with high energy densities. *Nat. Rev. Mater.* **1**, 16013 (2016).
13. Huang, Q., Li, H., Grätzel, M. & Wang, Q. Reversible chemical delithiation/lithiation of LiFePO<sub>4</sub>: towards a redox flow lithium-ion battery. *Phys. Chem. Chem. Phys.* **15**, 1793–7 (2013).
14. Qi, Z. & Koenig, G. M. Review Article: Flow battery systems with solid electroactive materials. *J. Vac. Sci. Technol. B, Nanotechnol. Microelectron. Mater. Process. Meas. Phenom.* **35**, 040801 (2017).
15. Huang, Q., Yang, J., Ng, C. B., Jia, C. & Wang, Q. A redox flow lithium battery based on the redox targeting reactions between LiFePO<sub>4</sub> and iodide. *Energy Environ. Sci.* **9**, 917–921 (2016).
16. Sharma, A. K., Birgersson, E., Pan, F. & Wang, Q. Mathematical modeling and experiments of a half-cell redox flow lithium ion battery system. *Electrochim. Acta* **204**, 1–8 (2016).
17. Sharma, A. K., Birgersson, E., Pan, F. & Wang, Q. Analysis of a Validated Mathematical Model for a Redox-Flow Lithium Ion Battery System. *Electrochim. Acta* **247**, 183–192 (2017).
18. Kuss, C., Lepage, D., Liang, G. & Schougaard, S. B. Ultrafast charging of LiFePO<sub>4</sub> with gaseous oxidants under ambient conditions. *Chem. Sci.* **4**, 4223–4227 (2013).
19. Lepage, D., Sobh, F., Kuss, C., Liang, G. & Schougaard, S. B. Delithiation kinetics study of carbon coated and carbon free LiFePO<sub>4</sub>. *J. Power Sources* **256**, 61–65 (2014).
20. Kuss, C., Carmant-Dérival, M., Trinh, N. D., Liang, G. & Schougaard, S. B. Kinetics of heterosite iron phosphate lithiation by chemical reduction. *J. Phys. Chem. C* **118**, 19524–

- 19528 (2014).
21. Jennings, J. R., Huang, Q. & Wang, Q. Kinetics of  $\text{Li}_x\text{FePO}_4$  Lithiation/Delithiation by Ferrocene-Based Redox Mediators: An Electrochemical Approach. *J. Phys. Chem. C* **119**, 17522–17528 (2015).
  22. Yan, R. *et al.* Determining  $\text{Li}^+$ -Coupled Redox Targeting Reaction Kinetics of Battery Materials with Scanning Electrochemical Microscopy. *J. Phys. Chem. Lett.* 491–496 (2018). doi:10.1021/acs.jpcclett.7b03136
  23. Padhi, A. K., Nanjundaswamy, K. S. & Goodenough, J. B. Phospho-olivines as positive-electrode materials for rechargeable lithium batteries. *J. Electrochem. Soc.* (1997). doi:10.1149/1.1837571
  24. Jia, C. *et al.* High – energy density nonaqueous all redox flow lithium battery enabled with a polymeric membrane. *Sci. Adv.* **1**, 1–7 (2015).
  25. Hwang, B., Park, M. S. & Kim, K. Ferrocene and cobaltocene derivatives for non-aqueous redox flow batteries. *ChemSusChem* **8**, 310–314 (2015).
  26. Ding, Y., Zhao, Y., Li, Y., Goodenough, J. B. & Yu, G. A high-performance all-metallocene-based, non-aqueous redox flow battery. *Energy Environ. Sci.* (2017). doi:10.1039/c6ee02057g
  27. Kaim, W. & Fiedler, J. Spectroelectrochemistry: The best of two worlds. *Chem. Soc. Rev.* **38**, 3373–3382 (2009).
  28. Oyama, G., Yamada, Y., Natsui, R. I., Nishimura, S. I. & Yamada, A. Kinetics of nucleation and growth in two-phase electrochemical reaction of  $\text{Li}_x\text{FePO}_4$ . *J. Phys. Chem. C* **116**, 7306–7311 (2012).
  29. Avrami, M. Kinetics of phase change. I: General theory. *J. Chem. Phys.* **7**, 1103–1112

- (1939).
30. Avrami, M. Granulation, phase change, and microstructure kinetics of phase change. III. *J. Chem. Phys.* (1941). doi:10.1063/1.1750872
  31. Avrami, M. Kinetics of phase change. II Transformation-time relations for random distribution of nuclei. *J. Chem. Phys.* (1940). doi:10.1063/1.1750631
  32. Allen, J. L., Richard Jow, T. & Wolfenstine, J. Kinetic study of the electrochemical FePO<sub>4</sub> to LiFePO<sub>4</sub> phase transition. *Chem. Mater.* **19**, 2108–2111 (2007).
  33. Allen, J. L., Jow, T. R. & Wolfenstine, J. Analysis of the FePO<sub>4</sub> to LiFePO<sub>4</sub> phase transition. *J. Solid State Electrochem.* **12**, 1031–1033 (2008).
  34. Xiang, K., Yang, K., Carter, W. C., Tang, M. & Chiang, Y. M. Mesoscopic Phase Transition Kinetics in Secondary Particles of Electrode-Active Materials in Lithium-Ion Batteries. *Chem. Mater.* (2018). doi:10.1021/acs.chemmater.7b05407
  35. Gomadam, P. M., Weidner, J. W., Dougal, R. A. & White, R. E. Mathematical modeling of lithium-ion and nickel battery systems. *J. Power Sources* **110**, 267–284 (2002).
  36. Geng, L., Foley, S. B., Dong, H. & Koenig, G. M. LiFePO<sub>4</sub> -Accelerated Change in Surface and Electrochemical Properties in Aqueous Systems Induced by Mechanical Agitation. *Energy Technol.* **7**, 1–10 (2019).
  37. Gaberscek, M., Dominko, R. & Jamnik, J. Is small particle size more important than carbon coating? An example study on LiFePO<sub>4</sub> cathodes. *Electrochem. commun.* **9**, 2778–2783 (2007).
  38. Gaberscek, M. & Jamnik, J. Impact of electrochemical wiring topology on the kinetics of insertion electrodes. *Solid State Ionics* **177**, 2647–2651 (2006).
  39. Weichert, K. *et al.* Phase boundary propagation in large LiFePO<sub>4</sub> single crystals on

- delithiation. *J. Am. Chem. Soc.* **134**, 2988–2992 (2012).
40. Malik, R., Burch, D., Bazant, M. & Ceder, G. Particle size dependence of the ionic diffusivity. *Nano Lett.* **10**, 4123–4127 (2010).
  41. Tang, M., Belak, J. F. & Dorr, M. R. Anisotropic phase boundary morphology in nanoscale olivine electrode particles. *J. Phys. Chem. C* **115**, 4922–4926 (2011).
  42. Levi, M. D. & Aurbach, D. Electrochemical oxidation and nucleophilic addition reactions of metallocenes in electrospray mass spectrometry. *J. Solid State Electrochem.* **11**, 1031–1042 (2007).
  43. Maxisch, T., Zhou, F. & Ceder, G. Ab initio study of the migration of small polarons in olivine  $\text{Li}_x\text{FePO}_4$  and their association with lithium ions and vacancies. *Phys. Rev. B - Condens. Matter Mater. Phys.* **73**, 1–6 (2006).
  44. Takahashi, M., Tobishima, S.-I., Takei, K. & Sakurai, Y. *Reaction behavior of  $\text{LiFePO}_4$  as a cathode material for rechargeable lithium batteries.*
  45. Yan, R. & Wang, Q. Redox-Targeting-Based Flow Batteries for Large-Scale Energy Storage. *Adv. Mater.* **1802406**, 1802406 (2018).

## **Chapter III. Comparative Analysis of Chemical Redox between Redox Shuttles and a Lithium-Ion Cathode Material via Electrochemical Analysis of Redox Shuttle Conversion**

### ***3.1 Overview***

In this chapter, six ferrocene-based redox shuttles are investigated for the overpotential and steric effects dependence upon delithiation/lithiation kinetics of  $\text{LiFePO}_4$ . The reaction kinetics and phase transformation redox shuttles and  $\text{LiFePO}_4$  were estimated using two kinetic models, Johnson-Mehl-Avrami-Erofeyev-Kolomogorov model and 1-D diffusion model. To optimize the relative molar ratio of LFP/FP and redox shuttle, three particle loadings were studied- particle-rich, equimolar and, particle lean. It was found that the overpotential and steric effects did not play a significant role in the reaction kinetics of our system. In this chapter, a robust method for testing shuttles at high concentration for use in chemical redox is presented, along with guidelines to designing them.

Elements of this chapter have been published in Journal of The Electrochemical Society:

- D. Gupta, C. Cai, G.M. Koenig, Comparative Analysis of Chemical Redox between Redox Shuttles and a Lithium-Ion Cathode Material via Electrochemical Analysis of Redox Shuttle Conversion, *J. Electrochem. Soc.* 168 (2021) 050546.  
<https://doi.org/10.1149/1945-7111/ac0068>.

Author contribution:

C.Cai: Implementation of 1 D diffusion model

### ***3.2 Abstract***

Chemical redox reactions between redox shuttles and lithium-ion battery particles have applications in electrochemical systems including redox-mediated flow batteries, photo-assisted lithium-ion batteries, and lithium-ion battery overcharge protection. These previous studies, combined with interest in chemical redox of battery materials in general, has resulted in previous reports of the chemical oxidation and/or reduction of solid lithium-ion materials. However, in many of these reports, a single redox shuttle is the focus and/or the experimental conditions are relatively limited. Herein, a study of chemical redox for a series of redox shuttles reacted with a lithium-ion battery cathode material will be reported. Both oxidation and reduction of the solid material with redox shuttles as a function of time will be probed using ferrocene derivatives with different half-wave potentials. The progression of the chemical redox was tracked by using electrochemical analysis of the redox shuttles in a custom electrochemical cell, and rate constants for chemical redox were extracted from the using two different models. This study provides evidence that redox shuttle-particle interactions play a role in the overall reaction rate, and more broadly support that this experimental method dependent on electrochemical analysis can be applied for comparison of redox shuttles reacting with solid electroactive materials.

### ***3.3 Introduction***

Chemical redox between solid lithium (Li)-ion battery active materials and dissolved redox-active species (i.e., redox shuttles) has relevance in several electrochemical systems and applications including battery overcharge protection<sup>1-4</sup>, redox-mediated flow batteries<sup>5-9</sup>, and photo-assisted rechargeable Li-ion batteries<sup>10,11</sup>. The chemical redox process involves charge transfer between solid electroactive particles and soluble redox shuttles within an electrolyte. While the choice of solid active material to be used in a Li-ion battery is a thoroughly researched and constantly evolving field, the selection principles and properties for redox shuttles for the multiple applications mentioned above have not been as comprehensively investigated and reported. This study aims to achieve progress towards methods to rationally compare the properties of several redox shuttles desired for pairing for redox reactions with a target solid electroactive material.

In addition to measuring relative properties of the redox shuttles, in particular reaction rates under equivalent conditions, systematic study of several redox shuttles is expected to give insights into the interactions between the redox shuttles and the solid electroactive materials<sup>12-15</sup>. It was previously proposed that the process for redox reactions between redox shuttles and solid active materials proceeds through a multistep process where the shuttle diffuses to the surface of the solid particles, adsorbs, undergoes electron transfer, and desorbs<sup>12</sup>. The structure and composition of the redox shuttle, and interactions between the redox shuttle and solid electroactive material, would be expected to influence the overall redox reaction rate. The specific limiting process in the overall reaction will influence the extent to which different interactions impact the overall redox reaction rate. To the authors' knowledge, detailed understanding of how redox shuttle properties and composition, including chemical functional moieties and the electrochemical potentials of the

redox shuttles, impact rates of chemical redox with battery active materials has not been reported. A detailed model and understanding of the chemical redox reaction is outside of the scope of this manuscript, however, this initial study will report an experimental system for assessing the reaction rate of different redox shuttles with solid electroactive materials. This work will also provide insights into challenges in making these measurements and how different chemical modifications to the redox shuttles influenced the redox reaction rate.

The solid electroactive material chosen for this study was the cathode material  $\text{LiFePO}_4$  (LFP), as well as its oxidized and delithiated form  $\text{FePO}_4$  (FP)<sup>16</sup>. Chemical oxidation/delithiation of LFP, and reduction/lithiation of FP, is represented by equations (1) and (2), respectively.



where  $\text{RS}_{ox}$  is a redox shuttle used for the oxidation of LFP and  $\text{RS}_{red}$  is a redox shuttle used for the reduction of FP. The redox shuttles used in this manuscript have a net charge of either neutral or +1, however, other charge states for redox shuttles are possible<sup>15,17</sup>. To be thermodynamically favorable, the redox potential of  $\text{RS}_{ox}$  must be higher than LFP whereas, the redox potential of  $\text{RS}_{red}$  must be lower than that of FP. LFP has been previously studied for both chemical and electrochemical redox, and electrochemical oxidation/reduction of this material occurs at a relatively flat potential as a function of extent of lithiation near 3.45 V vs.  $\text{Li/Li}^+$ <sup>18,19</sup>. LFP thus has two attributes that make it well suited to chemical redox investigations: i) a relatively constant potential for oxidation or reduction, meaning that any potential difference and effective thermodynamic driving force will be dictated by the redox shuttle chemistry and conditions for a wide range of extents of lithiation of the solid electroactive material and, ii) there is a wide range

of oxidizing potentials available for appropriate redox shuttles that will still be within the thermodynamic stability window of common Li-ion battery electrolytes<sup>20</sup>.

Systematic studies of redox shuttles for overcharge protection in Li-ion batteries has been done using metallocenes<sup>21</sup>, aromatics<sup>22,23</sup> and, halogenated Li salts<sup>24,25</sup>. The focus in these studies was generally the overall stability and lifetime of the redox shuttle when electrochemically oxidized and reduced repeatedly in Li-ion cells. While intended for overcharge protection of cathodes, these shuttles can also be used for chemical oxidation in redox-targeting systems<sup>11,26</sup>. Kinetics of chemical redox have previously been reported with ferrocene-based molecules<sup>5,13,27</sup>, hydrogen peroxide<sup>28</sup>, lithium iodide<sup>29</sup> and, electrolyte-free compounds such as NO<sub>2</sub><sup>30</sup>. There has been a lack of understanding in the role of redox shuttle properties on the chemical redox rate and mechanism. For instance, Yu et. al recently reported that ferricyanide, despite having similar redox potential to dibromoferrocenium, has 1000 times faster delithiation kinetics when used to chemically oxidize LFP<sup>5</sup>. It is noted that the electrolytes used for the two redox shuttles were different, hence redox shuttle-electrolyte interactions might also play a role in the observed differences in reaction rate. In the study herein, the reaction rate for the oxidation/reduction of LFP/FP by six redox shuttles (three for oxidation of LFP and three for reduction of FP) are compared using electrochemical analysis to track the progression of the chemical redox reactions. The reaction rate is discussed in the context of the redox potential of the redox shuttles and their measured effective diffusion coefficients. The reactions were performed in a batch reactor system and the progression of the reaction was monitored *in situ* using electrochemical analytical techniques. Two first-order reaction models were used to quantify rate constants and LFP/FP phase transformation.

### ***3.4 Experimental***

#### *3.4.1 Materials*

Ferrocene (Fc), 1,1' dimethylferrocene (DMFc), ethylferrocene (EFc), 1,1' dibromoferrocene (DBFc), ferrocene carboxaldehyde (FcCX), and 1,1' diacetylferrocene (DAFc) were used as received from Sigma Aldrich without any further purification. The chemical structure of these species, which were used as the redox shuttles in this study, can be found in Table 1. 1.2 M LiPF<sub>6</sub> in 3:7 ethylene carbonate:ethyl methyl carbonate (wt.:%:wt.%) was used as electrolyte in all experiments (Gotion Inc.). Commercial LFP (Xiamen TOB New Energy Technology, China) was used as received. The surface area of the LFP used was 7.5 m<sup>2</sup> g<sup>-1</sup>, measured using the Brunauer-Emmett-Teller method (Quantachrome Instruments). Note that the LFP did not undergo a carbon coating step during production according to the manufacturer specification. Material and electrochemical properties for the LFP material have been detailed in previous publications<sup>31,32</sup>.

#### *3.4.2 FePO<sub>4</sub> preparation*

For experiments where FePO<sub>4</sub> (FP, which was oxidized and delithiated LFP) was used, the FP was produced from a chemical oxidation process. 5 g LFP was added to a 750 ml solution containing 25 ml hydrogen peroxide (30% in water), 25 ml glacial acetic acid, and deionized (DI) water<sup>29</sup>. The solution was kept unstirred for 1 hour, and then filtered to extract the solid product. The solid product was then dried at 80 °C for 8 hours in a convection oven and then for 4 hours under vacuum. Conversion of LFP into FP was confirmed using powder X-ray diffraction (XRD, Panalytical X'pert diffractometer). After the chemical oxidation procedure the XRD patterns were consistent with previous reports for FP (see Appendix B, Figure B1)<sup>29</sup>. The solution was intentionally unstirred during LFP oxidation to FP in order to prevent the degradation of LFP

surface induced by mechanical agitation <sup>31</sup>. Electrochemical evaluation of electrodes containing the FP confirmed the chemical oxidation process was reversible, although there was a small reduction in electrochemical capacity and rate capability (see Appendix B, Figure B2 and S3).

### 3.4.3 Electrochemical characterization

The prepared FP and original LFP were electrochemically evaluated as cathode active materials using 2032-type coin cells on a MACCOR battery cycler. The cathodes were fabricated using a slurry of 80:10:10 (by wt. %) active material : carbon black : polyvinylidene difluoride (PVDF, Sigma Aldrich), where the active material was LFP or FP. The components were blended into a slurry using N-methyl-2-pyrrolidone as added solvent, and the slurry was cast on an aluminum current collector using a doctor blade with a 125- $\mu\text{m}$  gap. The electrodes were dried overnight in an ambient oven at 80 °C, followed by a vacuum oven for another 2 hours at 80 °C. The thickness of the electrodes used in this study was measured using a digital micrometer to be  $70 \pm 5 \mu\text{m}$  and LFP/FP loading was  $6.2 \pm 0.3 \text{ mg cm}^{-2}$ , where the error is the standard deviation of 3 independent measurements. The LFP/FP electrodes were used as cathodes and were paired with Li foil as the anode. Celgard 2325 was used as the separator and the electrolyte was 1.2 M  $\text{LiPF}_6$  in 3:7 vol % ethylene carbonate : ethyl methyl carbonate. The cells were cycled at room temperature with the same rate used for both charge and discharge for each cycle with the following cycling profile: C/20 (three cycles), C/10 (two cycles), C/5 (two cycles), C/2 (two cycles), 1 C (two cycles), and C/20 (two cycles). The C rate was determined based on the mass of LFP/FP in the cell, where 1C was assumed to correspond to  $160 \text{ mA g}^{-1}$  LFP/FP. Representative rate capability results can be found in Appendix B, Figure B2 and Figure B3 for LFP and FP, respectively. Note that the Li/LFP cells were started with a charge cycle and Li/FP cells were started with a discharge cycle. The voltage window for all electrochemical measurements was 2.5 to 4 V (vs.  $\text{Li/Li}^+$ ).

#### *3.4.4 Bulk electrolysis of redox shuttles*

All experiments with redox shuttles were conducted within an argon-filled glove box ( $\text{H}_2\text{O} < 1$  ppm,  $\text{O}_2 < 1$  ppm). For the FcCX, DBFc, and DAFc redox shuttles, it was desired to have them in the oxidized form such that they could be used to chemically oxidize LFP, thus the redox shuttles were converted to the oxidized form using bulk electrolysis. 100 mM solutions of FcCX, DBFc, and DAFc were oxidized at a constant voltage of 4.2 V (vs Li/Li<sup>+</sup>) using platinum wire (Sigma Aldrich) as working electrode and Li foil as counter and reference electrode in an H-cell (Ace Glass). The solutions were oxidized at 4.2 V (vs Li/Li<sup>+</sup>) until a current cutoff of  $10^{-6}$  Amps. An image of the cell setup can be found in Appendix B, Figure B4. The ion selective polymer separator that was between the two compartments of the H-cell was a blend of Nafion and polyvinylidene difluoride, and the preparation of the separator has been described previously<sup>33,34</sup>. All electrochemical measurements using the H-cell were conducted using Biologic-50 or Biologic-150 potentiostats.

#### *3.4.5 Half-wave potential determination*

To determine half-wave potentials for the redox shuttles, cyclic voltammetry (CV) on 100 mM solutions containing redox shuttles (DMFc, Fc, EFc, DBFc, FcCX, and DAFc) were conducted after electrolysis of the solutions to a capacity consistent with 50% oxidation (e.g. a 50/50 mix of the redox shuttle in the oxidized and reduced form). The CV experiments were conducted using a 1.6 mm Pt disc (BASi) working electrode and Li metal combined reference and counter electrode with a sweep rate of  $100 \text{ mV s}^{-1}$  in the H-cell. The H-cell setup was similar to the bulk electrolysis experiment explained above (Figure B4).

### *3.4.6 Characterization of chemical redox reaction rate dependence on relative redox shuttle to solid active material ratio*

Monitoring of the progress of chemical oxidation of LFP with DBFc<sup>+</sup>, and chemical reduction of FP by Fc, was measured in a three-neck round bottom flask (Grainger) using Pt disc as working electrode, 100 mM Ag/AgNO<sub>3</sub> in 1.2 M LiPF<sub>6</sub> in 3:7 vol % ethylene carbonate:ethyl methyl carbonate electrolyte as reference electrode, and Pt wire as counter electrode (for a picture of the experimental setup, see Appendix B, Figure B5). For oxidation of LFP with DBFc<sup>+</sup>, 100 mM solution of oxidized DBFc (e.g. >97% DBFc<sup>+</sup> as determined by mAh of capacity passed during electrolysis) dissolved in the 1.2 M LiPF<sub>6</sub> in 3:7 vol % ethylene carbonate:ethyl methyl carbonate electrolyte was added to a round bottom glass. Mild stirring at 130 rpm was added to the solution to prevent sedimentation of the solid electroactive material particles. Reference cyclic voltammograms at 20, 40, 50, 60, 80 and, 100 mV/s were performed. Three case studies were evaluated by varying the molar ratio of LFP to DBFc<sup>+</sup>: particle-lean (1:2), equimolar (1:1), and particle-rich (2:1). Similar experiments were performed for the redox reaction of the reduction of FP using Fc by varying the amounts of FP added to 100 mM Fc electrolyte solution. Three independent experiments were performed for each reaction condition (LFP with DBFc<sup>+</sup> and FP with Fc) at the three different molar ratios of solid electroactive species to redox shuttle.

### *3.4.7 Comparing redox shuttles*

Chemical oxidation of LFP using FcCX<sup>+</sup> and DAFc<sup>+</sup> and reduction of FP using DMFc and EFc were performed in the particle-rich scenario (2:1 LFP or FP : redox shuttle concentration). The concentration used for each redox shuttle was 100 mM. The experimental setup was similar to the experiments mentioned above (Figure B5). Three independent measurements with each redox shuttle were performed with 200 mM of LFP/FP powder.

### 3.5 Results

The class of metallocene redox shuttles have been used for chemical redox of Li-ion battery solid active materials in previous reports <sup>6,33</sup>. Besides chemical redox of solid electroactive materials, metallocene-based redox flow batteries have also been reported <sup>35,36</sup>. Criteria for their selection has included ease of availability, solubility, electrolyte stability, and molecular tunability <sup>36</sup>. Metallocenes have two cyclopentadienyl anions ( $C_5H_5^-$ ) bound to a transition metal ion, thus forming a  $(C_5H_5)_2M$  compound (where M is a metal, e.g., Fe). The cyclopentadienyl rings may be substituted with different chemical functional groups, thus making the properties of a given metallocene highly tunable. Ferrocenes are one such group of metallocenes and have been used as redox shuttles, including towards energy storage applications <sup>6,33,36</sup>.

This study focuses on how properties of redox shuttles affect the rate of chemical redox of a solid Li-ion electroactive material. Commercially available derivatives of ferrocene have been evaluated herein, all having solubility of at least 100 mM in the electrolyte and without observed reactions with the electrolyte, at least in the neutral form of the redox shuttle. Based on equations (1) and (2), redox shuttles with a redox potential above 3.45 V vs. Li/Li<sup>+</sup> were studied for oxidation of LFP, whereas shuttles with half-wave potential lower than 3.45 V vs Li/Li<sup>+</sup> were used for reduction of FP. Cyclic voltammograms of the shuttles with respect to Li/Li<sup>+</sup> can be found in Appendix B, Figure B6 Three oxidizing shuttles (FcCX<sup>+</sup>, DBFc<sup>+</sup>, and DAFc<sup>+</sup>) and three reducing shuttles (Fc, EFc, and DMFc) were selected. It is noted here that an additional redox shuttle, Decamethylferrocene, was evaluated but could not be included in the study due to solubility limitations in the electrolyte, and what appeared to be the facilitation of formation of a passivation layer on the Pt disc working electrode <sup>37</sup>.

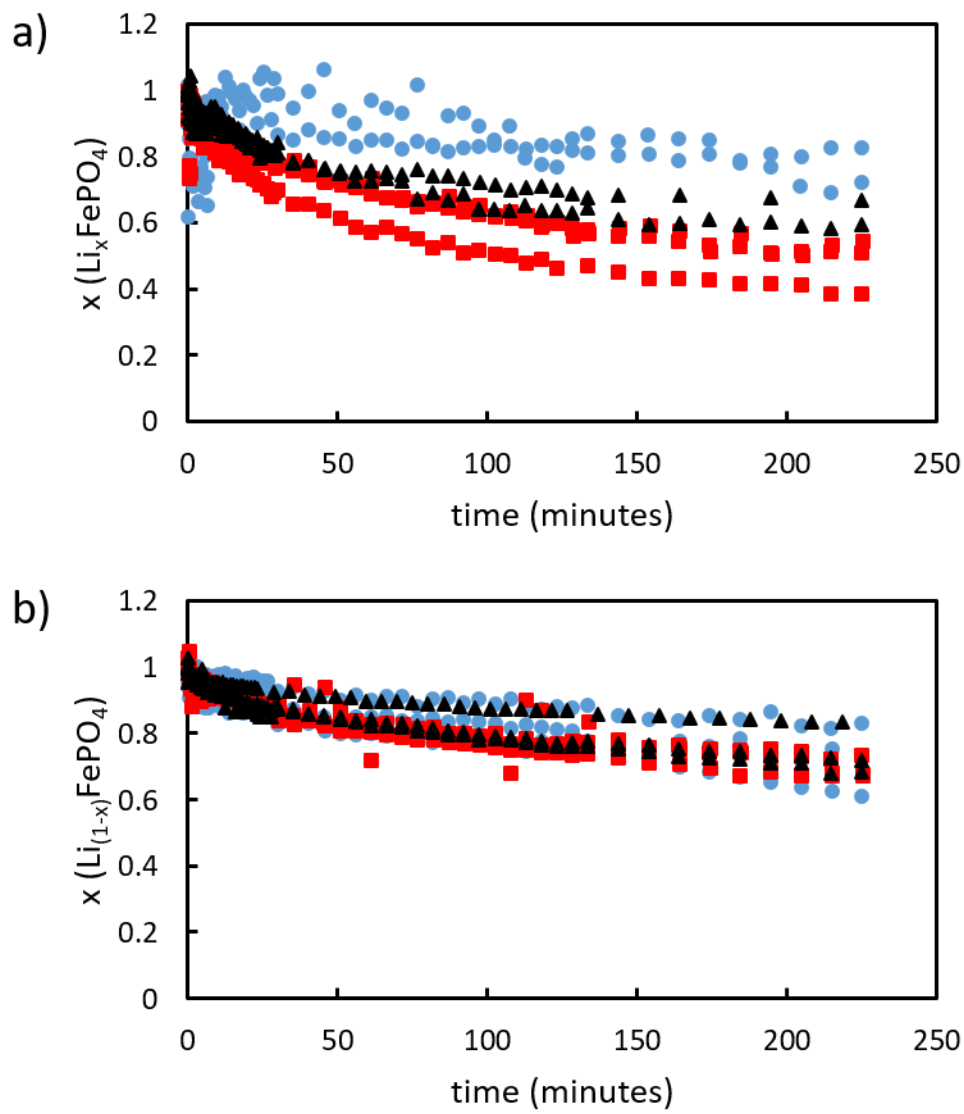


**Figure 2. Degree of delithiation/lithiation at different solid powder : redox shuttle molar ratios of particle-rich (2 : 1, black triangles), equimolar (1 : 1, red squares) and, particle-lean concentrations (1 : 2, blue circles) for a) LFP oxidation using 100 mM  $\text{FcBr}_2^+$  solution and b) FP reduction using 100 mM Fc solution.**

To design the experimental system for comparison between redox shuttles, first the impact of relative molar concentration of redox shuttles to solid electroactive particles was investigated. Three scenarios were considered: particle-rich, equimolar, and particle lean. The redox shuttle concentration was kept constant at 100 mM, and the solid electroactive material concentration was varied at 200 mM (particle-rich), 100 mM (equimolar), and 50 mM (particle-lean). Fc and DBFc<sup>+</sup> were used as reducing and oxidizing redox shuttles, respectively, because this pair of shuttles has been previously reported for reversible chemical redox of LFP/FP<sup>6</sup>. The progress of the reaction was evaluated using a three-electrode configuration within a batch reactor system. After the addition of powder to the batch reactor, cyclic voltammograms were collected continuously at a sweep rate of 100 mV s<sup>-1</sup> using a Pt disc electrode. The reaction between LFP and DBFc<sup>+</sup> and FP and Fc proceeded according to equations (1) and (2), respectively. The Randles-Sevcik equation was applied to convert measured peak currents to concentrations of the oxidized and/or reduced form of the redox shuttles during the chemical redox reaction progression<sup>38</sup>. Further description of this analysis can be found in the Appendix B. Under the assumption that changes in the concentration of the different oxidation states of the redox shuttles were only due to the chemical redox between the redox shuttles and the solid electroactive material, conversion of solid electroactive material was calculated from the electrochemical redox shuttle concentration analysis. The extent of oxidation and thus delithiation of LFP by DBFc<sup>+</sup> at three different redox shuttle : particle molar ratios can be found in Figure 1a, and the corresponding conditions for reduction/lithiation of FP by Fc can be found in Figure 1b. Effective diffusion coefficient of the redox shuttles in the electrolyte used was also determined by varying sweep rate of CV scans at constant concentration and applying the Randles-Sevcik equation. These results can be found in Table 1.

**Table 1. The redox shuttles for reduction of FP (DMFc, EFc and, Fc) and oxidation of LFP (FcCX<sup>+</sup>, DBFc<sup>+</sup> and, DAFc<sup>+</sup>). The half-wave potential and effective diffusion coefficient was calculated in 100 mM solution of redox shuttle in 1.2 M LiPF<sub>6</sub> in 3:7 wt. % EC:EMC using cyclic voltammetry. The standard error is from measuring  $D_{eff}$  in three independent experiments.**

Redox Shuttle	Chemical Structure	Half-Wave Potential (V vs Li/Li <sup>+</sup> )	Diffusion Coefficient, $D_{eff}$ (cm <sup>2</sup> s <sup>-1</sup> )
1,1'-Dimethylferrocene (DMFc)		3.10	$(2.20 \pm 0.27) \times 10^{-6}$
Ethylferrocene (EFc)		3.17	$(3.34 \pm 0.82) \times 10^{-6}$
Ferrocene (Fc)		3.25	$(1.92 \pm 0.56) \times 10^{-6}$
Ferrocenium carboxaldehyde (FcCX <sup>+</sup> )		3.55	$(8.15 \pm 1.25) \times 10^{-7}$
1, 1'-Dibromoferrocenium (DBFc <sup>+</sup> )		3.57	$(9.81 \pm 6.03) \times 10^{-7}$
1, 1'-Diacetylferrocenium (DAFc <sup>+</sup> )		3.76	$(1.28 \pm 0.44) \times 10^{-8}$

One possible contributor to the measured currents during CV sweeps would be the solid electroactive materials themselves, as has been previously reported for Li-ion battery particle suspensions<sup>39</sup>, although those previous reports were under different shear conditions, suspension compositions, working electrode area and orientation, and/or particle loading. To evaluate the possible contributions of electrochemical current from the particles themselves, a control experiment was conducted with CV scans at 100 mV s<sup>-1</sup> between -0.7 - 0.1 V vs 10 mM Ag/AgNO<sub>3</sub>, where 500 mg LFP powder (e.g. 200 mM particle concentration) was added to the three-electrode batch reactor without redox shuttles present. There were no clear peaks in measured currents during CV sweeps to indicate significant contributions from oxidation/reduction of the solid electroactive particles from encountering the microelectrode probe. The background current was generally <0.1 mA cm<sup>-2</sup>, which amounts to approximately 1-2% of the current response from 100 mM redox shuttle solutions (see Appendix B, Figure B7). This result supported neglecting the contributions from solid particle collisions in using peak currents from CV scans to determine the change in concentration of the oxidized/reduced form of the redox shuttles, and neglecting changes in oxidation state or lithiation of the LFP/FP due to electrochemical reactions with the working electrode. It is also noted that at the conclusion of experiments visual inspection of the electrode did not suggest the attachment of LFP/FP particles.

Kinetic parameters for the oxidation of LFP and reduction of FP with redox shuttles were determined using the Johnson Mehl Avrami- Erofeyev- Kolmogorov (JMAEK) equation<sup>40</sup>. The JMAEK equation can be written as:

$$x = 1 - \exp(-k^*t)^n \quad (3)$$

Where  $x$  is conversion,  $k^*$  is a pseudo-first order rate constant,  $t$  is time and  $n$  is Avrami coefficient. Additional details for applying the JMAEK equation to the systems in this study can be found in

the Appendix B. Similar analysis has previously been used to characterize batch reactor redox reaction rates between redox shuttles and Li-ion battery electroactive materials<sup>12,28</sup>. It is noted here that the JMAEK model used herein assumed first order reaction with respect to solid electroactive material, which would be applicable only during conditions where the redox shuttles were not subject to transport or equilibrium limitations to driving the reaction rate. This condition would not be satisfied for particle-rich or equimolar conditions after extended extents of conversion of the electroactive material. To accommodate this limitation, rate constants were only calculated from analysis of the first 100 minutes of reaction for all reaction systems investigated. The conversion (e.g., delithiation/oxidation of LFP or lithiation/reduction of FP) at the end of the first 100 minutes ( $x$ ), rate constant normalized by surface area of LFP/FP ( $k^*$ ), and Avrami coefficient ( $n$ ) for the experiments varying solid electroactive material:redox shuttle molar ratios can be found in Table 2. The conversion referenced in this work was with respect to solid electroactive material. For delithiation/oxidation of LFP, equimolar conditions resulted in the highest conversion after 100 minutes of the reaction proceeding, followed by the particle-rich and then the particle-lean cases. In contrast, lithiation/reduction of FP followed the same trajectory for conversion irrespective of particle loading. It is noted that only 50% stoichiometric conversion of solid electroactive material is possible for particle-rich scenario.

**Table 2. Reaction parameters determined for different molar ratios of solid electroactive material:redox shuttles during chemical reduction of FP with Fc and oxidation of LFP with FcBr<sub>2</sub><sup>+</sup>. x is the extent of reduction/lithiation of FP or oxidation/delithiation of LFP after the first 100 minutes of the redox reaction, k\* is the pseudo first-order rate constant per surface area electroactive material, and n is the Avrami coefficient from Equation 3. x was calculated based on total moles of solid electroactive materials. Values are averages with errors representing the standard error of three independent experiments.**

Solid Particle :Redox Shuttle (mol:mol)	FePO <sub>4</sub> + Fc + Li <sup>+</sup> → LiFePO <sub>4</sub> + Fc <sup>+</sup>			LiFePO <sub>4</sub> + FcBr <sub>2</sub> <sup>+</sup> → LiFePO <sub>4</sub> + FcBr <sub>2</sub> + Li <sup>+</sup>		
	x	k* × 10 <sup>-3</sup> (m <sup>-2</sup> min <sup>-1</sup> )	n	x	k* × 10 <sup>-3</sup> (m <sup>-2</sup> min <sup>-1</sup> )	n
2 : 1	0.18 ± 0.03	2.18 ± 1.00	0.40 ± 0.09	0.36 ± 0.05	2.92 ± 0.58	0.52 ± 0.10
1 : 1	0.22 ± 0.01	2.95 ± 0.51	0.44 ± 0.04	0.43 ± 0.04	8.35 ± 0.14	0.52 ± 0.06
1 : 2	0.17 ± 0.03	1.64 ± 0.67	0.38 ± 0.13	0.28 ± 0.07	7.57 ± 2.52	0.54 ± 0.12

After the comparison of the progression of the chemical redox for the LFP/DBFc<sup>+</sup> and the FP/Fc systems using varying molar ratios of solid electroactive material:redox shuttle, the next outcome investigated was how different redox shuttles, all of them functionalized ferrocene derivatives, progressed in their chemical redox reactions with FP or LFP. For the comparison between redox shuttles, the particle-rich reaction condition was selected. The particle-rich ratio for

some conditions reached equivalent levels of conversion faster, and avoiding extended reaction durations was desirable to avoid any potential effects of side reactions of the redox shuttles<sup>41</sup>. It is noted that even for the particle-rich condition the reaction progressed slow enough that the time resolution of the analytical methods were appropriate and there was confidence in having enough concentration data points to extract kinetic parameters from fitting the data. For reduction/lithiation of FP, similar experimental conditions as the particle-rich case for reaction of FP with Fc were used, with only the redox shuttles DMFc and EFc being substituted for Fc. Likewise, FcCX<sup>+</sup> and DAFc<sup>+</sup> replaced DBFc<sup>+</sup> as the oxidizing redox shuttle under equivalent conditions as were used for oxidation of LFP. The resulting conversion of the solid electroactive material after 100 minutes reaction, normalized rate constants, and Avrami coefficients for all redox shuttles reactions with either FP or LFP are listed in Tables 3 and 4, for reduction of FP and oxidation of LFP, respectively.

The diffusion coefficient for each redox shuttle was also determined using linear sweep voltammetry<sup>38</sup>, with sweep rates of 20, 40, 50, 60, 80, and 100 mV s<sup>-1</sup>. The peak current plotted vs. square root of scan rate yielded linear curves for all redox shuttles indicating diffusion-limited reaction. The electrochemical analysis for determining the diffusion coefficient of the redox shuttles was conducted prior to the chemical redox reaction (e.g., electroactive solid particle addition). The effective diffusion coefficients for the redox shuttles determined using linear sweep voltammetry can be found in Table 1.

### 3.6 Discussion

In a previous work, the steps for chemical redox reactions between a redox shuttle and a solid electroactive material were described<sup>12</sup>. Using DBFc<sup>+</sup> chemical oxidation and delithiation of LFP as an example, the proposed steps would be:

- 1) DBFc<sup>+</sup> molecules diffuse from the bulk electrolyte towards the surface of LFP particles.
- 2) DBFc<sup>+</sup> molecules adsorb on the surface of LFP particles.
- 3a) DBFc<sup>+</sup> locally oxidizes Fe in LFP (net reaction  $\text{LiFe}^{2+}\text{PO}_4 \rightarrow x \text{Li}^+ + \text{Li}_{(1-x)}(\text{Fe}_{(1-x)}^{2+}\text{Fe}_x^{3+})\text{PO}_4$  for the LFP and  $x \text{DBFc}^+ \rightarrow x\text{DBFc}$  for the redox shuttle for each x moles of forward reaction).
- 3b) Li<sup>+</sup> locally moves from within solid LFP to the solvated electrolyte phase.
- 4) DBFc desorbs from the surface particle
- 5) Li<sup>+</sup> and an e<sup>-</sup> undergo co-diffusion from inside the particle towards the surface of the LFP (which will be some fraction FP after the reaction initiates).
- 6) Li<sup>+</sup> solvated in the electrolyte diffuses from the particle near surface region to the bulk electrolyte.

In quantifying the progression of the total reaction, which requires all the steps listed above to propagate forward, previous reports for reactions between soluble redox shuttles and solid electroactive Li-ion battery materials have quantified the reaction rate information in the context of the JMAEK kinetic model<sup>12,29</sup>.

#### 3.6.1 JMAEK kinetic model

The JMAEK model assumes single step nucleation, infinite system volume, and homogeneous distribution of nucleation sites in the system volume<sup>40</sup>. JMAEK has been applied for the analysis of LFP redox kinetics, both for chemical and electrochemical redox<sup>42-44</sup>. Previous use of JMAEK for LFP redox has assumed that the nucleation and propagation of FP phase to/from LFP phase was the rate limiting step. This assumption, while likely acceptable for many cases of electrochemical lithiation/delithiation of LFP within thin film composite electrodes, may not be applicable in all cases for chemical redox. For example, a previous study concluded that the JMAEK model did not appropriately fit expected analysis for chemical reduction of FP by LiI<sup>29</sup>. The oxidation of LFP and reduction of FP by redox shuttles have been analyzed using JMAEK herein such that the results in this work can be compared to prior studies. The ability of the parameters extracted from JMAEK analysis to reproduce the conversion profile for the reaction were also explored to provide insights into how well the JMAEK analysis captures the reaction progression.

### 3.6.2 Avrami coefficient and its interpretation

The Avrami coefficient,  $n$  can be written as

$$n = a + b.c \quad (4)$$

Where  $a$  is nucleation index,  $b$  is dimensionality of growth, and  $c$  is growth index of the transformation which can be either phase boundary-controlled or diffusion-controlled growth. Detailed analysis of Avrami coefficients under various conditions has been described elsewhere<sup>40,45,46</sup>. For the chemical redox of LFP,  $a$  can be interpreted as nucleation of the FP or LFP phase during reduction/lithiation or oxidation/delithiation reactions.  $b$  and  $c$  are intrinsic properties of LFP/FP and are therefore held constant for all the reaction conditions studied. The phase

transformation of LFP has been reported to be one-dimensional ( $b=1$ ) and diffusion-limited ( $c=0.5$ )<sup>44,47</sup>. The nucleation rate, a function of  $a$ , therefore varies across experiments.

**Table 3. Reaction parameters determined for different redox shuttles during chemical reduction/lithiation of FP at a molar ratio of solid electroactive material:redox shuttles of 2:1.  $x$  was the extent of reduction/lithiation of FP after the first 100 minutes of the redox reaction,  $k^*$  was the pseudo first-order rate constant per surface area electroactive material, and  $n$  was the Avrami coefficient from Equation 3.  $x$  was calculated based on total moles of solid electroactive material. Values are averages with errors representing the standard error of three independent experiments. The overpotential ( $\Delta E$ ) was calculated using the half-wave potential difference between FP and redox shuttles.**

Redox Shuttle	$\Delta E$ (V)	$x$	$k^* \times 10^{-3} \text{ m}^{-2} \text{ min}^{-1}$	$n$
1, 1'-Dimethylferrocene (DMFc)	0.35	$0.22 \pm 0.04$	$2.25 \pm 0.38$	$0.43 \pm 0.05$
1-Ethylferrocene (EFc)	0.28	$0.22 \pm 0.02$	$2.56 \pm 0.13$	$0.31 \pm 0.05$
Ferrocene (Fc)	0.2	$0.18 \pm 0.03$	$2.18 \pm 1.00$	$0.40 \pm 0.09$

From Tables 2, 3, and 4 it is evident that  $n$  was similar for all particle loading and redox shuttle variations for oxidation/delithiation of LFP (range for values calculated was 0.52 to 0.54). The same behavior was also observed for reduction/lithiation of FP with regards to very little variation seen between different particle loadings or redox shuttles used (0.38 to 0.44), although the range of values observed were somewhat lower than those for LFP oxidation. With  $b = 1$  and  $c = 0.5$ ,  $a$  was nearly zero for delithiation of LFP indicating instantaneous nucleation. For lithiation

of FP however, the value for  $a$  would have to be slightly negative (assuming the same assumptions for  $b$  and  $c$  still hold for converting FP to LFP). A negative nucleation index would imply a decrease of nucleation sites with time. To the best of the authors' knowledge, there are no studies supporting a decrease of nucleation sites over time for chemical reduction of FP. Hence, a slightly negative  $a$  was also interpreted as instantaneous nucleation for lithiation of FP as well, which was consistent with a previous report<sup>12,44</sup>. Combining the Avrami analysis for all redox shuttles and reaction conditions, it was concluded that the nucleation rate was independent of particle loading or redox shuttle added. The latter suggested that phase transformation of LFP/FP during chemical redox was not a function redox shuttle overpotential or interactions with the solid electroactive material, since all redox shuttles had different half-wave potentials and variety of molecular sizes and chemical functional moieties.

### 3.6.3 Oxidation/ Delithiation of LFP

To understand the reaction mechanism involved in delithiation of LFP, the reaction progression with time for different particle loadings and redox shuttles was conducted and analyzed. While the rate constants and conversion after 100 minutes of reaction were similar for all particle to redox shuttle molar ratios, the equimolar case had the highest rate constant and conversion of solid electroactive material (Table 2). One possible explanation for this observation, though speculative, is that the particle-rich and particle-lean cases had slightly lower conversion due to relatively greater transport limitations for those cases. For the particle-lean case, the  $\text{Li}^+$  would have to be extracted from greater distances from within the particles undergoing reaction, and for the particle-rich case the redox shuttle concentration in the external environment would be more excessively depleted of the oxidized and reactive form of the redox shuttle.

**Table 4. Reaction parameters determined for different redox shuttles during chemical oxidation/delithiation of LFP at a molar ratio of solid electroactive material:redox shuttles of 2:1.  $x$  was the extent of oxidation/delithiation of LFP after the first 100 minutes of the redox reaction,  $k^*$  was the pseudo first-order rate constant per surface area electroactive material, and  $n$  was the Avrami coefficient from Equation 3.  $x$  was calculated based on total moles of solid electroactive material. Values are averages with errors representing the standard error of three independent experiments. The overpotential ( $\Delta E$ ) was calculated using the half-wave potential difference between LFP and redox shuttles.**

<b>Redox Shuttle</b>	<b><math>\Delta E</math> (V)</b>	<b><math>x</math></b>	<b><math>k^* \times 10^{-3}</math> (<math>m^{-2} min^{-1}</math>)</b>	<b><math>n</math></b>
Ferrocenium Carboxaldehyde (FcCX <sup>+</sup> )	0.10	0.19 ± 0.01	1.31 ± 0.04	0.52 ± 0.14
1, 1'-Dibromoferrocenium (DBFc <sup>+</sup> )	0.12	0.36 ± 0.05	2.92 ± 0.58	0.52 ± 0.10
1, 1'-Diacetylferrrocenium (DAFc <sup>+</sup> )	0.31	0.25 ± 0.03	3.48 ± 0.44	0.51 ± 0.01

Additionally, despite having similar half-wave potential and  $D_{eff}$ , DBFc<sup>+</sup> had much higher conversion and rate constant than FcCX<sup>+</sup> (Table 4). This outcome suggests that the rate of chemical delithiation is not dependent simply upon overpotential or  $D_{eff}$  of the redox shuttles. The potential difference between these two redox shuttles was only 20 mV, which for an electrochemical cell that difference in driving force would not be expected to have such a dramatic difference in the oxidation rate of LFP (an example of the difference in conversion for a much greater difference in potential for the electrochemical analogue experiment can be found in Appendix B, Figure B9a).

Given that the redox shuttles also have very similar  $D_{eff}$  in the electrolyte and that the same electrolyte and electroactive particles were used for the experiments, this outcome suggests there must be redox shuttle-particle interactions that are significantly impacting the reaction rate. The other redox shuttle evaluated for oxidation of LFP was  $DAFc^+$ , which based on half wave potential had the greatest overpotential relative to LFP of  $\sim 300$  mV.  $DAFc^+$  had the highest rate constant and the most rapid initial oxidation of LFP over the first  $\sim 10$  minutes of the reaction, however, the redox reaction plateaued and the final conversion after 100 minutes was lower for  $DAFc^+$  compared to  $DBFc^+$ , even though  $DAFc^+$  has a much greater overpotential (Figure 2). An additional consideration for  $DAFc^+$  was that it was observed to form a highly viscous solution (see Appendix B, Figure B10), which resulted in the low diffusion coefficient (Table 1). Thus, these results suggest that  $DAFc^+$  has high initial conversion, but that a stability limitation may be limiting the conversion that can be achieved in the redox reaction. The results above, when combined, suggest that in cases where excess overpotential of the shuttle does not drive the reaction faster, it may be desirable to focus more on other metrics of the system where the redox shuttles and solid electroactive particles are being used, such as the stability and solubility of the redox shuttles in the electrolyte. The fundamentals behind the redox shuttle-particle interactions will be the subject of future investigations. The nature of such interactions will likely be challenging to probe experimentally. Computational approaches that provide insights into the electron transfer process for explicit molecular orientations of the redox shuttles at the solid electroactive material surface and for explicit chemical moiety modifications, combined with experimental assessment of reactions with the same redox shuttles, may provide supporting evidence for these effects.

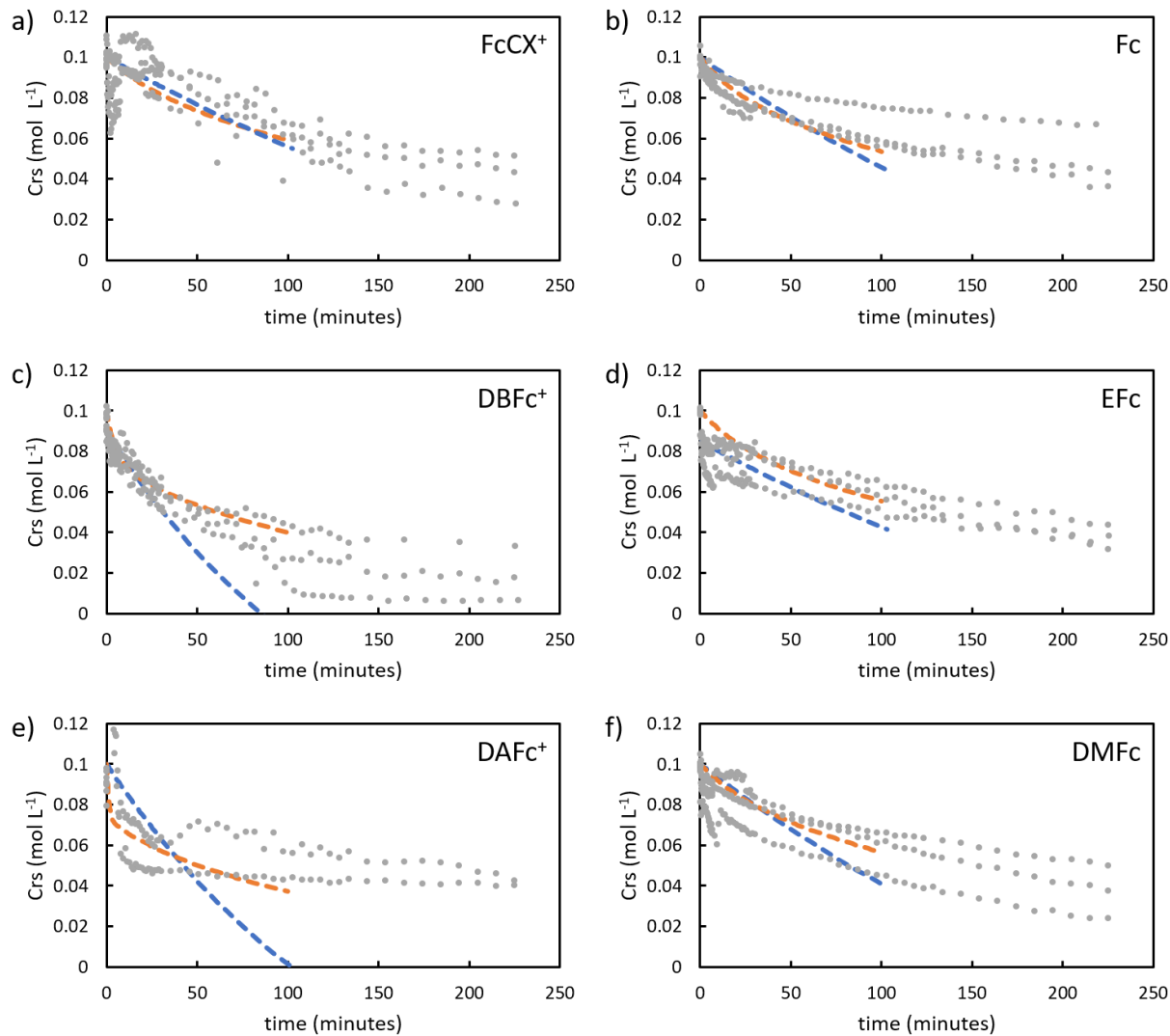


**Figure 2. Redox shuttle concentration,  $C_{rs}$ , as a function of time during chemical redox reaction with LFP or FP. Initial concentrations for the redox shuttles were 100 mM of a) ferrocenium carboxaldehyde ( $FcCX^+$ ), b) ferrocene ( $Fc$ ), c) dibromoferrocenium ( $DBFc^+$ ), d) ethylferrocene ( $EFc$ ), e) 1, 1'- diacetylferrocenium ( $DAFc^+$ ) and, f) 1, 1'- dimethylferrocene ( $DMFc$ ). Note that a), c), e) are for oxidation of 200 mM LFP and b), d) and, f) are for reduction of 200 mM FP. The grey dots represent experimental data from triplicates and the dashed lines represent the JMAEK kinetic model (blue) and 1-D kinetic model (orange) back fitted for first 100 minutes of the reaction.**

With regards to the stability of the redox shuttles, it has been previously reported that the stability of ferrocenes or ferrocenium ions is dependent upon the nature of substituents<sup>38,48</sup>. Electron-donating groups such as methyl/ethyl promote stability whereas electron-withdrawing groups such as acyl decrease stability. An unstable ferrocenium ion has been shown to decompose into Fe (II) and Fe (III) ions under acidic conditions<sup>49</sup>. While several reports have shown comparable diffusion coefficients of ferrocene and acyl substituted ferrocenes, these have been limited to concentrations of  $10^{-3} - 10^{-2}$  M, and it is possible that instability effects such as side reactions with the electrolyte or dimerization become more pronounced at higher concentrations. Side reactions of the redox shuttles may have been the cause of the observed turbidity in the 100 mM DAFc<sup>+</sup> solution during electrochemical oxidation (Appendix B, Figure B10).

#### *3.6.4 Reduction/Lithiation of FP*

Similar to chemical delithiation/oxidation of LFP, lithiation/reduction of FP under different solid particle ratios and using different redox shuttles was evaluated. For every reaction condition, the conversion of FP to LFP of ~ 20% was achieved. This indicates that conversion in the case of chemical lithiation and reduction of FP was relatively insensitive to relative molar ratios of redox shuttle to FP, the overpotential (driving force), and the diffusion coefficient of redox shuttles (Tables 1-3). Also, the reduction of FP with redox shuttles was generally slower than the oxidation of LFP. A few causes are speculated to have resulted in these observations. First, the FP was prepared from a prior chemical oxidation/delithiation step of LFP. While care was taken during this material preparation step (e.g., stirring was avoided), this process has been previously demonstrated to impact the surface composition and morphology of the LFP/FP material<sup>31</sup>. Though not as pronounced as the prior report which had significant stirring during chemical oxidation, the initial discharge with the FP prepared from chemical oxidation had greater polarization and less

gravimetric capacity than the initial discharge of the as-received LFP at the same rate (Appendix B, Figure B11). A surface more resistive to electron transfer, and chemically distinct from the initial LFP surface, may have been responsible for the reduced reaction rate and conversion for the FP reduction/lithiation relative to LFP oxidation/delithiation. This resistive surface layer may have also reduced the impact of different reaction conditions to substantially modify the chemical redox rate. It is noted that the first discharge polarization curve and reduced rate capability for the FP material would support the speculation (Appendix B, Figure B3). Another difference to consider between the reduction/lithiation of FP and oxidation/delithiation of LFP is the direction and accessibility of  $\text{Li}^+$  during the reaction. For oxidation of LFP, the net change of in oxidation state of the Fe in the LFP would be expected to provide a repulsive driving force for  $\text{Li}^+$  to leave the structure, and the immediate redox shuttle in the vicinity would be net neutral charge. However, for reduction/lithiation of FP  $\text{Li}^+$  must arrive from the surrounding electrolyte. There is significant excess of  $\text{Li}^+$  in the electrolyte phase, however, the molar concentration is much lower than in the solid phase of the LFP.

The redox reaction rate was similar across all redox shuttles, even though they had varying half-wave potentials (e.g., overpotential driving force, which relative to FP to LFP reaction ranged for 200 to 350 mV) and effective diffusion coefficients. The lack of a dependence on the effective potential of the redox shuttles contrasted with electrochemical lithiation of FP, where potentiostatic reduction of FP at 3.15 V vs  $\text{Li}/\text{Li}^+$  (~350 mV overpotential) was significantly slower than potentiostatic discharge at 3.25 V vs  $\text{Li}/\text{Li}^+$  (~200 mV overpotential). The electrochemical FP reduction results for FP can be found in Appendix B, Figure B9b. This outcome suggests the potential of the redox shuttles may not be as important to modifying the rate of chemical redox relative to how the applied electrochemical potential impacts the electrochemical redox rate for

LFP/FP. More redox shuttles need to be evaluated under different reaction conditions to confirm the generality of this observation, but given the importance of redox shuttle potential for many applications where redox shuttle-electroactive particle redox reactions would be taken advantage of, such as a for a redox shuttle mediated flow battery, relatively low sensitivity of the reaction rate to the redox shuttle potential would simplify the design of the overall system<sup>33</sup>.

### *3.6.5 Alternative One-Dimensional Kinetic Model*

When the results from obtaining the kinetic parameters from JMAEK analysis were applied for comparison to the experimental outcomes (Figure 2 and Appendix B, Figure B8), in many cases the first 100 minutes of reaction had a good match. For example, the  $R^2$  for reduction of FP cases was more than 0.9 suggesting a good representation of the model in capturing the early portion of the reaction progression. However, for some cases, especially oxidation of LFP with the two shuttles besides  $\text{DBFc}^+$ , the match between the JMAEK kinetic model and the experimental outcomes was not as good and the  $R^2$  was less than 0.9. This suggested that JMAEK may not have been an appropriate model for these cases, and other reports have suggested that JMAEK does not always provide an appropriate description for chemical redox of LFP/FP materials<sup>12</sup>.

Towards achieving a better match with the experimental data, an additional model of the system was explored. This model was based on a one-dimensional (1-D) diffusion model within the batch reactor system. The system of equations can be found in the Supplementary Information, and some key assumptions of model were a) uniform spatial distribution of redox shuttle and  $\text{Li}^+$ , b) LFP/FP particles were spheres with a uniform radius, and c) the rate of reaction has a first order rate dependence upon internal diffusion of  $\text{Li}^+$  into the LFP/FP particle. This model does not have a dependence on overpotential, and assumes stoichiometric changes in  $\text{Li}^+$  and redox shuttle changes in the liquid phase, and then matches the  $\text{Li}^+$  concentrations in the solid phase through

balancing the flux of  $\text{Li}^+$  at the solid particle interface which is dictated by the rate of the redox reaction. The  $\text{Li}^+$  also must also diffuse through the solid particle, which is assumed to proceed through diffusive processes defined using spherical 1-D transport governed by Fick's law<sup>50</sup>, and a solid phase  $\text{Li}^+$  diffusion coefficient for LFP from the literature was used<sup>51</sup>. The rate constants ( $k'$ ) derived using the 1-D model for different reaction conditions used in this study can be found in Table 5.

**Table 5: Rate constants from different reaction conditions extracted from fitting a 1-D diffusion model to experimental measurements of the reaction progression with time.  $k'$  was normalized by the surface area of solid electroactive particles added.**

	$\text{FePO}_4 + \text{RS}_{\text{red}} + \text{Li}^+ \rightarrow \text{LiFePO}_4 + \text{RS}_{\text{red}}^+$		$\text{LiFePO}_4 + \text{RS}_{\text{ox}}^+ \rightarrow \text{LiFePO}_4 + \text{RS}_{\text{ox}} + \text{Li}^+$	
<b>Solid Particle : Redox Shuttle (mol:mol)</b>	$\text{RS}_{\text{red}}$	$k' \times 10^{-13} (\text{m}^{-1} \text{s}^{-1})$	$\text{RS}_{\text{ox}}^+$	$k' \times 10^{-13} (\text{m}^{-1} \text{s}^{-1})$
1:2	Ferrocene (Fc)	0.43	1, 1'-Dibromoferrocenium (DBFc <sup>+</sup> )	2.43
1:1	Ferrocene (Fc)	1.21	1, 1'-Dibromoferrocenium (DBFc <sup>+</sup> )	15.34
2:1	Ferrocene (Fc)	0.96	1, 1'-Dibromoferrocenium (DBFc <sup>+</sup> )	4.50
2:1	1- Ethylferrocene (EFc)	0.85	Ferrocenium Carboxaldehyde (FcCX <sup>+</sup> )	0.66
2:1	1, 1'-Dimethylferrocene (DMFc)	0.80	1, 1'-Diacetylferrocenium (DAFc <sup>+</sup> )	16.67

The 1-D model had a significantly better fit ( $R^2 > 90\%$  for all conditions) of the experimental data compared to the JMAEK model (Figure 2 and Appendix B, Figure B8), particularly the cases where the initial rate of reaction was faster as was the case for some of the experiments of oxidation

of LFP. The fit of the experimental data was improved, although the general trends for rate constants ( $k^*$  for JMAEK and  $k'$  for the alternative 1-D model) were similar. In particular,  $k'$  was also greatest for the equimolar scenario in the experiments evaluating the influence of the solid particle:redox shuttle molar ratios and the  $k'$  values were generally greater for oxidation of LFP compared to reduction of FP, consistent with  $k^*$  values. However, the relative magnitudes of differences of the rate constants for different reaction conditions was different for the JMAEK and 1-D model. For example, the rate constant for delithiation using  $\text{DBFc}^+$  versus  $\text{FcCX}^+$  is 7 times higher using 1-D model, compared to twice as high using JMAEK. The 1-D model thus suggests even greater sensitivity to specific particle-redox shuttle interactions, as this was the case where the differences in redox potential and  $D_{\text{eff}}$  between the shuttles was relatively small. While this 1-D model is an initial effort to better describe the experimental outcomes from chemical redox between redox shuttles and solid electroactive materials, it highlights that results from JMAEK should be carefully assessed and compared with the measured conversion as a function of time to determine if such analysis is appropriate.

### ***3.7 Conclusions***

In this work, chemical redox of solid electroactive materials using redox shuttles was investigated. The Li-ion cathode material LFP/FP was used as the solid material, and the influence of different solid particle:redox shuttle molar ratios and the use of different redox shuttles was analyzed using an electrochemical cell and technique to track progression of conversion of the redox shuttle. It was found that for the batch reactor system employed that equimolar feeds of solid particles and redox shuttles resulted in the highest conversion, and the oxidation of LFP was generally faster than the reduction of FP. In comparative analysis of the different redox shuttles,

there were cases where even though the differences in electrochemical potential and diffusion coefficient of the redox shuttles were modest, the reaction rates were significantly different. This suggests there are specific redox shuttle-particle interactions that are influencing the reaction rate. The conversion data for the different reaction conditions was also evaluated using the JMAEK model and an alternative 1-D kinetic model. Both models provide access to rate constants for relative comparison between the redox shuttles, where JMAEK values can be compared to the existing literature for chemical redox of LFP/FP and the 1-D model had a better fit to the experimental data. This study provided an experimental system which took advantage of electrochemical analysis to evaluate the relative reaction rates of redox shuttles used to chemically oxidize/reduce Li-ion active materials, which is relevant to applications such as redox mediated flow batteries and overcharge protection in Li-ion cells. This method, and the analysis to extract rate constants for ease of comparison between redox shuttles, provides a robust approach to comparing candidate redox shuttle compounds.

### 3.8 References

1. Chen, Z., Qin, Y. & Amine, K. Redox shuttles for safer lithium-ion batteries. *Electrochim. Acta* **54**, 5605–5613 (2009).
2. Chen, J., Buhrmester, C. & Dahn, J. R. Chemical Overcharge and Overdischarge Protection for Lithium-Ion Batteries. *Electrochem. Solid-State Lett.* **8**, A59 (2005).
3. Leonet, O. *et al.* Improving the Safety of Lithium-Ion Battery via a Redox Shuttle Additive 2,5-Di- tert -butyl-1,4-bis(2-methoxyethoxy)benzene (DBBB). *ACS Appl. Mater. Interfaces* **10**, 9216–9219 (2018).
4. Khakani, S. El, Forgie, J. C., MacNeil, D. D. & Rochefort, D. Redox Shuttles for Lithium-Ion Batteries at Concentrations up to 1 M Using an Electroactive Ionic Liquid Based on 2,5-di- tert -butyl-1,4-dimethoxybenzene . *J. Electrochem. Soc.* **162**, A1432–A1438 (2015).
5. Yu, J., Wang, X., Zhou, M. & Wang, Q. A redox targeting-based material recycling strategy for spent lithium ion batteries. *Energy Environ. Sci.* **12**, 2672–2677 (2019).
6. Huang, Q., Li, H., Grätzel, M. & Wang, Q. Reversible chemical delithiation/lithiation of LiFePO<sub>4</sub>: towards a redox flow lithium-ion battery. *Phys. Chem. Chem. Phys.* **15**, 1793–7 (2013).
7. Zanzola, E. *et al.* Redox Solid Energy Boosters for Flow Batteries: Polyaniline as a Case Study. *Electrochim. Acta* **235**, 664–671 (2017).
8. Páez, T., Martínez-Cuezva, A., Palma, J. & Ventosa, E. Mediated alkaline flow batteries: From fundamentals to application. *ACS Appl. Energy Mater.* **2**, 8328–8336 (2019).
9. Vivo-Vilches, J. F. *et al.* LiFePO<sub>4</sub>-ferri/ferrocyanide redox targeting aqueous posolyte: Set-up, efficiency and kinetics. *J. Power Sources* **488**, 229387 (2021).
10. Li, Q., Li, N. & Zhou, H. Saving electric energy by integrating a photoelectrode into a Li-

- ion battery †. 20903–20907 (2015). doi:10.1039/c5ta06908d
11. Liao, S. *et al.* Integrating a dual-silicon photoelectrochemical cell into a redox flow battery for unassisted photocharging. *Nat. Commun.* **7**, (2016).
  12. Gupta, D. & Koenig, G. M. Analysis of Chemical and Electrochemical Lithiation/Delithiation of a Lithium-Ion Cathode Material. *J. Electrochem. Soc.* **167**, 020537 (2020).
  13. Yan, R. *et al.* Determining  $\text{Li}^+$ -Coupled Redox Targeting Reaction Kinetics of Battery Materials with Scanning Electrochemical Microscopy. *J. Phys. Chem. Lett.* 491–496 (2018). doi:10.1021/acs.jpcclett.7b03136
  14. Sharma, A. K., Birgersson, E., Pan, F. & Wang, Q. Mathematical modeling and experiments of a half-cell redox flow lithium ion battery system. *Electrochim. Acta* **204**, 1–8 (2016).
  15. Hailu, Y. M., Nguyen, M. T. & Jiang, J. C. Theoretical study on the interaction of iodide electrolyte/organic dye with the  $\text{TiO}_2$  surface in dye-sensitized solar cells. *Phys. Chem. Chem. Phys.* **22**, 26410–26418 (2020).
  16. Chung, S. Y., Bloking, J. T. & Chiang, Y. M. Electronically conductive phospho-olivines as lithium storage electrodes. *Nat. Mater.* **1**, 123–128 (2002).
  17. Liu, Q., Sleightholme, A. E. S., Shinkle, A. A., Li, Y. & Thompson, L. T. Non-aqueous vanadium acetylacetonate electrolyte for redox flow batteries. *Electrochem. Commun.* (2009). doi:10.1016/j.elecom.2009.10.006
  18. Padhi, A. K., Nanjundaswamy, K. S. & Goodenough, J. B. Phospho-olivines as positive-electrode materials for rechargeable lithium batteries. *J. Electrochem. Soc.* (1997). doi:10.1149/1.1837571
  19. Malik, R., Abdellahi, A. & Ceder, G. A Critical Review of the Li Insertion Mechanisms in

- LiFePO<sub>4</sub> Electrodes. *J. Electrochem. Soc.* **160**, A3179–A3197 (2013).
20. Kasnatscheew, J. *et al.* Determining oxidative stability of battery electrolytes: Validity of common electrochemical stability window (ESW) data and alternative strategies. *Phys. Chem. Chem. Phys.* **19**, 16078–16086 (2017).
  21. Golovin, M. N. Applications of Metallocenes in Rechargeable Lithium Batteries for Overcharge Protection. *J. Electrochem. Soc.* **139**, 5 (1992).
  22. Adachi, M., Tanaka, K. & Sekai, K. Aromatic Compounds as Redox Shuttle Additives for 4 V Class Secondary Lithium Batteries. *J. Electrochem. Soc.* **146**, 1256–1261 (1999).
  23. Buhrmester, C. *et al.* Studies of Aromatic Redox Shuttle Additives for LiFePO<sub>4</sub>-Based Li-Ion Cells. *J. Electrochem. Soc.* **152**, A2390 (2005).
  24. Behl, W. K. Anodic Oxidation of Lithium Bromide in Tetrahydrofuran Solutions. *J. Electrochem. Soc.* **136**, 2305–2310 (1989).
  25. Behl, W. K. Electrochemical Overcharge Protection of Rechargeable Lithium Batteries. *J. Electrochem. Soc.* **135**, 21 (1988).
  26. Zhou, M. *et al.* Nernstian-Potential-Driven Redox-Targeting Reactions of Battery Materials. *CHEMPR* **3**, 1036–1049
  27. Jennings, J. R., Huang, Q. & Wang, Q. Kinetics of Li<sub>x</sub>FePO<sub>4</sub> Lithiation/Delithiation by Ferrocene-Based Redox Mediators: An Electrochemical Approach. *J. Phys. Chem. C* **119**, 17522–17528 (2015).
  28. Lepage, D., Sobh, F., Kuss, C., Liang, G. & Schougaard, S. B. Delithiation kinetics study of carbon coated and carbon free LiFePO<sub>4</sub>. *J. Power Sources* **256**, 61–65 (2014).
  29. Kuss, C., Carmant-Dérival, M., Trinh, N. D., Liang, G. & Schougaard, S. B. Kinetics of

- heterosite iron phosphate lithiation by chemical reduction. *J. Phys. Chem. C* **118**, 19524–19528 (2014).
30. Kuss, C., Lepage, D., Liang, G. & Schougaard, S. B. Ultrafast charging of LiFePO<sub>4</sub> with gaseous oxidants under ambient conditions. *Chem. Sci.* **4**, 4223–4227 (2013).
  31. Geng, L., Foley, S. B., Dong, H. & Koenig, G. M. LiFePO<sub>4</sub> -Accelerated Change in Surface and Electrochemical Properties in Aqueous Systems Induced by Mechanical Agitation. *Energy Technol.* **7**, 1–10 (2019).
  32. Qi, Z., Dong, H. & Koenig, G. M. Electrochemical Characterization of Lithium-Ion Battery Cathode Materials with Aqueous Flowing Dispersions. *Electrochim. Acta* **253**, 163–170 (2017).
  33. Jia, C. *et al.* High – energy density nonaqueous all redox flow lithium battery enabled with a polymeric membrane. *Sci. Adv.* **1**, 1–7 (2015).
  34. McCormack, P. M., Luo, H., Geise, G. M. & Koenig, G. M. Conductivity, permeability, and stability properties of chemically tailored poly(phenylene oxide) membranes for Li<sup>+</sup> conductive non-aqueous redox flow battery separators. *J. Power Sources* **460**, 228107 (2020).
  35. Zhao, Y. *et al.* Sustainable electrical energy storage through the ferrocene/ferrocenium redox reaction in aprotic electrolyte. *Angew. Chemie - Int. Ed.* **53**, 11036–11040 (2014).
  36. Ding, Y., Zhao, Y., Li, Y., Goodenough, J. B. & Yu, G. A high-performance all-metallocene-based, non-aqueous redox flow battery. *Energy Environ. Sci.* **10**, 491–497 (2017).
  37. Branch, J. A., Cook, D. A. & Bartlett, P. N. Electrochemical studies of decamethylferrocene in supercritical carbon dioxide mixtures. 261–267 (2015). doi:10.1039/c4cp04545a

38. Ates, M. N., Allen, C. J., Mukerjee, S. & Abraham, K. M. Electronic Effects of Substituents on Redox Shuttles for Overcharge Protection of Li-ion Batteries. *J. Electrochem. Soc.* **159**, A1057–A1064 (2012).
39. Qi, Z. & Koenig, G. M. Electrochemical Evaluation of Suspensions of Lithium-Ion Battery Active Materials as an Indicator of Rate Capability. *J. Electrochem. Soc.* **164**, A151–A155 (2017).
40. Avrami, M. Granulation, phase change, and microstructure kinetics of phase change. III. *J. Chem. Phys.* (1941). doi:10.1063/1.1750872
41. Singh, A. *et al.* A kinetic study of ferrocenium cation decomposition utilizing an integrated electrochemical methodology composed of cyclic voltammetry and amperometry. *Analyst* **139**, 5747–5754 (2014).
42. Allen, J. L., Jow, T. R. & Wolfenstine, J. Analysis of the FePO<sub>4</sub> to LiFePO<sub>4</sub> phase transition. *J. Solid State Electrochem.* **12**, 1031–1033 (2008).
43. Allen, J. L., Richard Jow, T. & Wolfenstine, J. Kinetic study of the electrochemical FePO<sub>4</sub> to LiFePO<sub>4</sub> phase transition. *Chem. Mater.* **19**, 2108–2111 (2007).
44. Xiang, K., Yang, K., Carter, W. C., Tang, M. & Chiang, Y. M. Mesoscopic Phase Transition Kinetics in Secondary Particles of Electrode-Active Materials in Lithium-Ion Batteries. *Chem. Mater.* (2018). doi:10.1021/acs.chemmater.7b05407
45. Avrami, M. Kinetics of phase change. I: General theory. *J. Chem. Phys.* **7**, 1103–1112 (1939).
46. Avrami, M. Kinetics of phase change. II Transformation-time relations for random distribution of nuclei. *J. Chem. Phys.* (1940). doi:10.1063/1.1750631
47. Malik, R., Abdellahi, A. & Ceder, G. A Critical Review of the Li Insertion Mechanisms in

- LiFePO<sub>4</sub> Electrodes. *J. Electrochem. Soc.* **160**, A3179–A3197 (2013).
48. Golovin, M. N., Wilkinson, D. P., Dudley, J. T., Holonko, D. & Woo, S. Applications of Metallocenes in Rechargeable Lithium Batteries for Overcharge Protection. *J. Electrochem. Soc.* **139**, 5–10 (1992).
49. Huang, W. H. & Jwo, J. -J. Kinetics of the Decomposition of Ferrocenium Ion and Its Derivatives. *J. Chinese Chem. Soc.* **38**, 343–350 (1991).
50. Deen, W. M. *Analysis of Transport Phenomena. Journal of Chemical Information and Modeling* (1998).
51. Tang, K., Yu, X., Sun, J., Li, H. & Huang, X. Kinetic analysis on LiFePO<sub>4</sub> thin films by CV, GITT, and EIS. *Electrochim. Acta* **56**, 4869–4875 (2011).

## Chapter IV. Chemical Redox of Lithium-Ion Solid Electroactive Material in a Packed Bed Flow Reactor

### 4.1 Overview

In this chapter, we have used reaction-engineering principles to design the chemical reservoir of the redox-targeting flow battery- where a packed bed reactor (PBR) of  $\text{LiFePO}_4$  (LFP) is oxidized by solvated ferricyanide redox shuttle. Four variables: LFP bed-height, shuttle concentration, flow-rate, and operating temperature were varied to assess the molar conversion of LFP. The progress of the reaction were measured using cyclic voltammetry. X-ray computed tomography was used to investigate the pore and particle distribution of PBR. Preliminary evidence suggests that the reaction mechanism follows a topochemical model and the rate-limiting step varies under certain operating conditions. These insights form the basis of Chapter 4, where spatiotemporal progress of chemical redox in packed bed reactor is characterized.

A manuscript based on this chapter has been submitted to the journal Chemical Engineering Science as a full research paper-

- D. Gupta, Y. Zhang, Z. Nie, J. Wang, G.M. Koenig, Chemical Redox of Lithium Ion Solid Electroactive Material in a Packed Bed Flow Reactor. *Submitted. Chemical Engineering Science.*

Author contributions:

Y.Zhang: XCT collection and analysis, Z. Nie, Sintered pellet synthesis, J. Wang: PBR setup

## ***4.2 Abstract***

Chemical redox reactions between solid electroactive materials and dissolved electroactive compounds are a necessary component of emerging technologies relevant to renewable energy including high energy density flow batteries and battery material recycling. In this work, the initial investigation of heterogeneous chemical redox for a packed bed reactor configuration between solid electroactive material and dissolved redox shuttles will be described. Experimental conditions including the height of the packed bed, the redox shuttle solution concentration, solution flow rate, and operating temperature were varied and their impact on the molar conversion of the solid electroactive material in the packed bed was quantified using electroanalytical techniques on the reactor effluent. The progression of the reaction and its dependence on the different variables explored will be discussed in the context of the limiting processes for porous packed aggregates of the solid electroactive material undergoing chemical oxidation.

### ***4.3. Introduction***

With widespread deployment of renewable power sources such as solar and wind, large-scale energy storage will be needed to level these generation sources' intermittent loads [1]. Among the electrochemical energy storage options available, redox flow batteries provide the advantage of separation of energy and power design and components, modularity, long cycle life, and versatility for stationary applications[2]. Conventional redox flow batteries use soluble electroactive species to store electrochemical energy. Hence, their volumetric energy density is limited by the solubility of the electroactive species, for example  $<25 \text{ Wh L}^{-1}$  reported for systems such as all-vanadium [3]. Recently, redox-targeting flow batteries (RTFBs) have been reported as a method to dramatically increase the energy density of flow batteries [4–8] In a RTFB system, the soluble electroactive species, referred to as redox shuttles, provide power in an electrochemical flow cell, as is the case for a conventional redox flow battery. However, unlike a conventional flow battery where the redox shuttles would also serve the role of storing all energy in the system, in a RTFB the vast majority of the energy is stored in solid electroactive species. Energy stored in the solid electroactive species is reversibly extracted via the redox shuttles by chemical reduction/oxidation reactions. The chemical redox of solid electroactive material is facilitated by contact with the soluble redox shuttles, provided the soluble shuttle is in the appropriate oxidation state and has sufficient potential. The solid electroactive material is typically much more energy dense and is not limited by solubility in the electrolyte, and thus the incorporation of solid electroactive material can dramatically increase the volumetric energy density of the flow battery. Compared to redox flow batteries based on only soluble electroactive materials, it has been estimated that RTFBs could have ten times the volumetric energy density [9]. In contrast to alternative methods for high volumetric energy density flow batteries that take advantage of solid electroactive materials such as the use of suspensions or slurries [10,11], RTFBs have advantages of much lower viscosity in

flowing through the electrochemical cell, while retaining the advantages of large surface area electrodes available for electrochemical reactions to occur and enable high current densities.

A RTFB overall system consists of coupled electrochemical and chemical reactors, as illustrated in Figure 1a. There is a power stack where redox shuttles are electrochemically oxidized/reduced, and reservoirs where solid electroactive material is kept and undergoes chemical redox with the redox shuttles. At scaled operation, there will also be recirculation loops with pumps that transport redox shuttles between cell stacks and the chemical reservoirs, as well as additional components not shown such as power conditioning systems, controllers, etc. The design considerations of the electrochemical cell power stacks in RTFBs are similar to those of redox flow batteries and have been described previously [12]. However, to the best of the authors' knowledge, the design principles for the chemical reservoir of the RTFB have not been well defined. Previous reports pertaining to the chemical reservoir have included characterization of the redox targeting process where the solid electroactive material was in the form of dispersed particles [9,13–15], porous pellets [5], or electrode strips[16,17] have been reacted systems including batch reactors and continuous stirred tank reactors. These studies have provided fundamental insights to the chemical redox process and characterization of RTFB-type systems, however, it is not clear how well these model systems would translate at larger scales. While batch and stirred tank reactors with relatively low particle loadings are desirable for monitoring the chemical redox process, RTFB redox reactors will need to be flow-through to couple with the electrochemical cell, and low particle loadings reduce the volumetric energy density advantages of an RTFB system. Therefore, a packed bed reactor (PBR) comprised of a bed of the solid electroactive material particles could achieve both high volumetric chemical redox capacity and allow flow through of the electrolyte for coupling to the electrochemical flow cell [18].

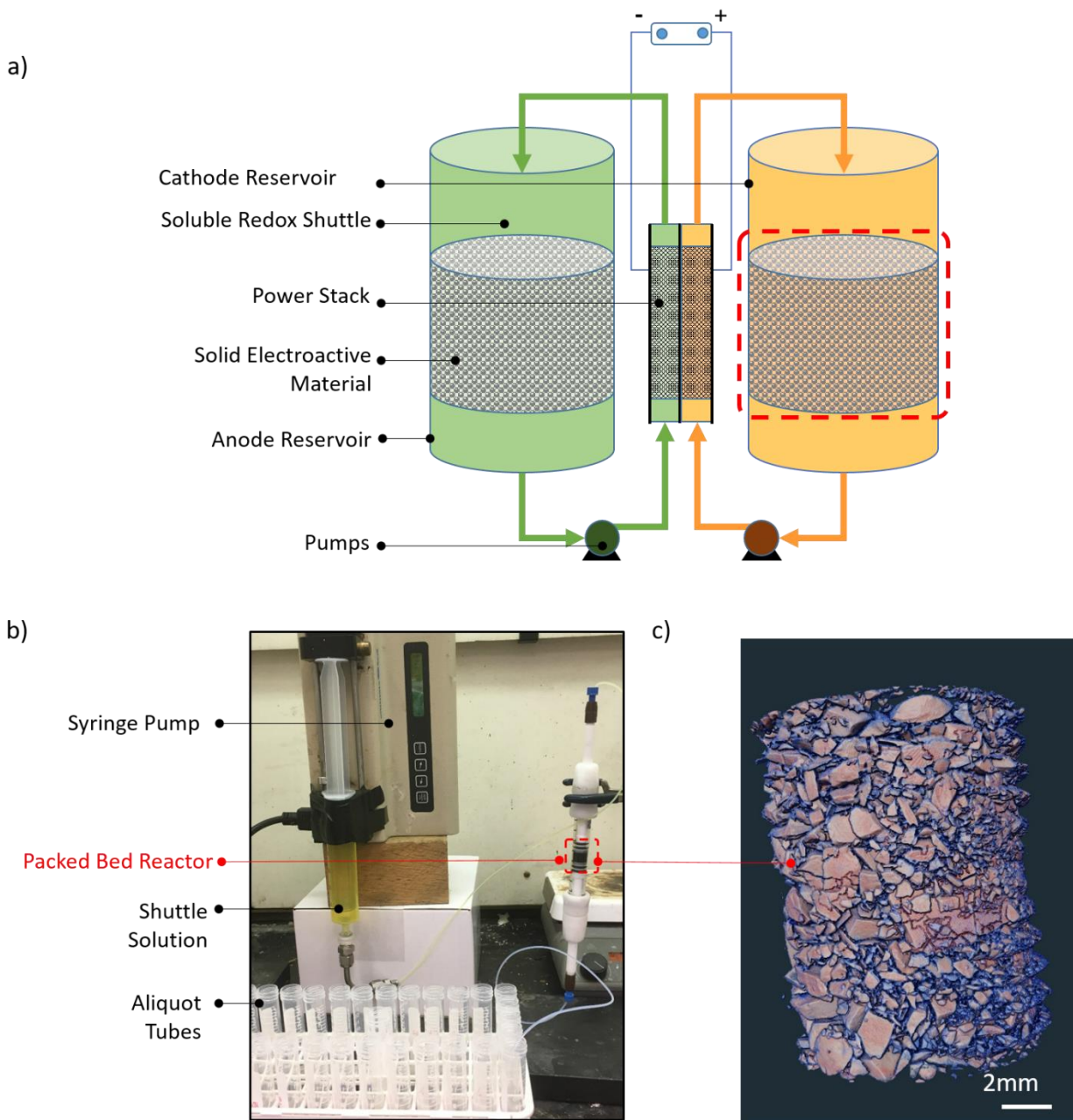
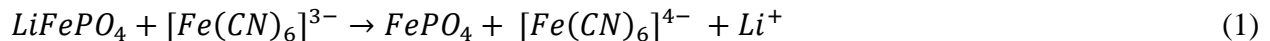


**Figure 1. a) Illustration of a full redox targeting flow battery system, with a red dashed box around the chemical redox reactor reservoir which this model study is directed towards. b) Photograph of the experimental setup for assessing the oxidation of  $\text{LiFePO}_4$  with  $[\text{Fe}(\text{CN})_6]^{3-}$ . c) Three-dimensional reconstruction of a packed bed of  $\text{LiFePO}_4$  as used in the experimental setup (the particle packed bed would be in the region with a red dashed box in b) from X-ray computed tomography.**

In this study, a PBR has been evaluated where the solid electroactive material  $\text{LiFePO}_4$  (LFP) was oxidized by the redox shuttle  $[\text{Fe}(\text{CN})_6]^{3-}$  (a photograph of the PBR can be found in Figure 1b). As an initial investigation of a PBR for chemical redox relevant to a RTFB, the evaluation was focused on a single reaction (oxidation of LFP by the redox shuttle) in the PBR. It is noted that in a full system two reactions (oxidation and reduction of the solid electroactive material by redox shuttle(s)) will be needed for each chemical redox tank, and the tanks will need to be coupled to an electrochemical flow cell. LFP has advantages for use in a chemical redox PBR. LFP has a flat charge/discharge voltage at 3.45 V (vs.  $\text{Li}/\text{Li}^+$ ), and it has been well studied and commercialized for Li-ion battery applications and thus the detailed physical properties have been previously reported [19]. During oxidation of LFP,  $\text{Li}^+$  is removed from the structure and the Fe is oxidized from  $\text{Fe}^{2+}$  to  $\text{Fe}^{3+}$ , resulting in  $\text{FePO}_4$  (FP). The flat charge/discharge voltage is desirable for a chemical redox PBR because the potential needed to oxidize or reduce the electroactive material does not shift as a function of the extent of lithiation of the solid electroactive material. The reaction between LFP and  $[\text{Fe}(\text{CN})_6]^{3-}$  is expected to proceed as shown below:



In this manuscript, the influence of four variables on the measured conversion of  $[\text{Fe}(\text{CN})_6]^{3-}$  to  $[\text{Fe}(\text{CN})_6]^{4-}$  in the effluent of a PBR loaded with LFP (which was correspondingly converted to FP) will be investigated. The LFP –  $[\text{Fe}(\text{CN})_6]^{3-}$  redox system was recently reported to have fast kinetics [20] and excellent first-cycle reversibility of 99% [5], making it a robust choice for assessing the design of the chemical reservoir of an RTFB. The four variables evaluated were: height of the LFP packed bed, concentration of  $[\text{Fe}(\text{CN})_6]^{3-}$  in the electrolyte, flow-rate of electrolyte containing  $[\text{Fe}(\text{CN})_6]^{3-}$ , and the temperature of the reactor and solution fed. Three to four variations were conducted for each variable evaluated. Single variable analysis of variance

(ANOVA) was used to assess whether there were measurable changes in the conversion of the LFP in the PBR. This study provides insights useful to designing chemical redox-based systems and a framework for evaluating redox shuttles and solid electroactive material pairings. While the chemical redox has been motivated by RTFBs, such experiments can provide insights relevant to other applications/systems relying on chemical redox as well, such as photochemical flow batteries [21,22], overcharge protection of Li-ion batteries [23,24], and battery recycling [20].

## **4.4. Materials and Methods**

### *4.4.1 Materials*

Commercial carbon coated LFP (Xiamen TOB New Energy Technology, China), potassium ferricyanide ( $K_3[Fe(CN)_6]$ , Sigma Aldrich), potassium ferrocyanide ( $K_4[Fe(CN)_6]$ , Sigma Aldrich), and lithium sulfate ( $Li_2SO_4$ , Fisher Scientific) were used as received without further purification.

### *4.4.2 Methods*

#### *4.4.2.1 Mildly sintered LFP pellet preparation*

Directly packing the column with the fine LFP powder resulted in low flow rates of the fluid through the column, thus the LFP was mildly sintered to prepare coarser aggregates. To prepare the sintered LFP pellet, 1.5 g LFP active material powder was loaded into a 16 mm diameter Carver pellet die and pressed with 12,000 lbf for 2 minutes in a Carver hydraulic press. Next, the pellets were heated in a Lindberg/Blue M tube furnace from room temperature to 400 °C at a ramp rate of 1 °C min<sup>-1</sup> under N<sub>2</sub> atmosphere, with an inert atmosphere chosen to minimize the possibility

of oxidation of the LFP. After holding at 400 °C for 1 h, the furnace was cooled to room temperature at a rate of 1 °C min<sup>-1</sup>. The diameter of the sintered pellets was ~16 mm and thicknesses were approximately 2.5 mm.

#### 4.4.2.2 Powder X-ray Diffraction

The structure of the active material that comprised the sintered pellets was confirmed to contain the same bulk material structure as the as-received LFP material using X-ray diffraction (XRD). XRD was collected using Panalytical X'pert diffractometer with Cu K $\alpha$  radiation between 2 $\theta$  values of 15 and 40 degrees.

#### 4.4.2.3 Packed bed reactor

Sintered LFP pellets were coarsely pulverized using a mortar and pestle by hand. After that, the sintered LFP powder was weighed and then loosely packed into a glass chromatography column (Cole Parmer, 10 mm diameter, adjustable height). Teflon frits (Cole Parmer, 5  $\mu$ m) were used on either end of the packed bed to constrain sintered LFP powder inside the column. The flow rate of [Fe(CN)<sub>6</sub>]<sup>3-</sup> solution prepared by dissolving K<sub>3</sub>[Fe(CN)<sub>6</sub>] in deionized (DI) water was regulated using a syringe pump (KDS 100 series). A picture of the PBR experimental setup can be found in Figure 1b.

The experimental conditions used in this study are listed in Table 1. The bed height was varied from 0.5-1.5 cm with corresponding loading of 0.5-1.5 g sintered LFP resulting in the total combined pore/void volume fraction being constant at approximately 0.63. To study the effects of varying [Fe(CN)<sub>6</sub>]<sup>3-</sup> concentration on LFP conversion, [Fe(CN)<sub>6</sub>]<sup>3-</sup> concentrations of 0.1, 0.2, and 0.3 mol L<sup>-1</sup> were evaluated. For estimating the LFP conversion dependence upon flow rate of [Fe(CN)<sub>6</sub>]<sup>3-</sup> solution, flow rates of 30, 42, 54 and, 66 mL h<sup>-1</sup> were used. Except for the experiments

where concentration was varied, a  $[\text{Fe}(\text{CN})_6]^{3-}$  concentration of  $0.2 \text{ mol L}^{-1}$  was used. Except for experiments where bed height was varied, a bed height of 1 cm was used. Except for experiments where temperature was varied, the reaction was conducted at room temperature, measured to be  $22.4 \text{ }^\circ\text{C}$ .

The effects of temperature on conversion in the PBR were conducted at 4.0, 13.0, 22.4, and 40.0  $^\circ\text{C}$ . The 22.4  $^\circ\text{C}$  case was room temperature. For the other 3 cases, a water bath (Lauda Brinkmann RC-20) was used to maintain both the packed bed and the  $[\text{Fe}(\text{CN})_6]^{3-}$  feed solution at 4.0, 13.0, or 40.0  $^\circ\text{C}$ . The feed solution and LFP packed bed setup were equilibrated at 4.0, 13.0, or 40.0  $^\circ\text{C}$  for 1 hour in the water bath before running the reaction. The water bath temperature was observed to always stay within  $\pm 0.2 \text{ }^\circ\text{C}$  of the set point. The measured temperature of the feed solution in the syringe was typically offset by  $-0.5 \text{ }^\circ\text{C}$  relative to the water bath set point.

Before starting to feed the  $[\text{Fe}(\text{CN})_6]^{3-}$  solution, the packed LFP bed was rinsed using DI water at the same flow rate as used during the reaction. Thus, there was an initial volume of water that exited the reactor which was accounted for in conversion determinations. After each experiment, the packed LFP bed was purged with 60 mL DI water at  $40 \text{ mL h}^{-1}$  to remove any remaining  $[\text{Fe}(\text{CN})_6]^{3-}$ . The remaining powder (usually a blend of unreacted LFP and LFP converted to FP) was then dried overnight in a fume hood, and subsequently dried an additional 8 hours in an ambient oven at  $80 \text{ }^\circ\text{C}$ , followed by an additional 4 hours of drying in a vacuum oven at  $80 \text{ }^\circ\text{C}$ . In some cases, the dried LFP/FP after reaction of the LFP with  $[\text{Fe}(\text{CN})_6]^{3-}$  was used for further electrochemical and materials characterization.

#### *4.4.2.4 Cyclic voltammetry*

Under every experimental condition described in the previous section, the effluent from the reactor was continuously collected in 2 mL increments. Each 2 mL aliquot was analyzed using cyclic voltammetry (CV) sweeps in a three-electrode system: Pt microelectrode (100- $\mu\text{m}$  diameter, BASi) as the working electrode, Pt wire (1 mm diameter, 4 cm length, Sigma Aldrich) as the counter electrode, and Ag/AgCl (immersed in KCl gel electrolyte, 74 mm length Ag wire, Pine research) as the reference electrode. The feed solution of  $[\text{Fe}(\text{CN})_6]^{3-}$  was analyzed at 20, 40, 60, 80, and 100  $\text{mV s}^{-1}$  from 0.0 to 0.5 V (vs. Ag/AgCl) before each experiment to assess that the effective diffusion coefficient of the redox shuttle and the measured currents were consistent. The diffusion coefficient of  $[\text{Fe}(\text{CN})_6]^{3-}$  estimated using Randles-Sevcik Equation<sup>3</sup> was found to be  $2.49 \pm 1.15 \times 10^{-6} \text{ cm}^2 \text{ s}^{-1}$ , in agreement with previous reports [25]. For each aliquot of the reactor effluent, CV sweeps were conducted at 20  $\text{mV s}^{-1}$  between 0.0 to 0.5 V (vs. Ag/AgCl) and using the diffusion coefficient estimated from the previous step and the Randles-Sevcik equation, the concentration of the  $[\text{Fe}(\text{CN})_6]^{3-}$  species was determined. In general, the  $[\text{Fe}(\text{CN})_6]^{3-}$  in the effluent was lower than the  $[\text{Fe}(\text{CN})_6]^{3-}$  in the feed due to conversion to  $[\text{Fe}(\text{CN})_6]^{4-}$ , and reduction of each mol of  $[\text{Fe}(\text{CN})_6]^{3-}$  was assumed to correspond to the oxidation of one mol of LFP to FP. The measured peak current from the CV scans was confirmed to have a linear dependence on the relative fraction of  $[\text{Fe}(\text{CN})_6]^{3-}$  in solution (see Appendix C for additional details and CV results in Figure C1).

CV scans were also conducted on the LFP solid electroactive material. For electrochemical evaluation, the LFP powder was processed into an electrode. LFP electrodes were made by mixing a slurry of LFP, carbon black, and polyvinylidene fluoride (PVDF, Sigma Aldrich) in 8:1:1 ratio by mass using N-methyl-2-pyrrolidone (NMP, Sigma Aldrich) as solvent. The slurry was then coated on rectangular strips of Ni foam (1 cm  $\times$  5 cm) and dried overnight at 80  $^\circ\text{C}$  in a

conventional oven. Electrodes were then evaluated in a three-electrode system: LFP coated within Ni foam as the working electrode, Pt wire as the counter electrode, and Ag/AgCl (in concentrated KCl gel) as the reference electrode. The electrolyte was 0.1 mol L<sup>-1</sup> Li<sub>2</sub>SO<sub>4</sub> dissolved in DI water. CV scans of the LFP electrode were collected at 0.02 mV s<sup>-1</sup> between -0.1 – 0.5 V vs. Ag/AgCl (example scans can be found in Appendix C, Figure C2a). The half-wave potential of LFP determined from the scans was 0.186 V (vs. Ag/AgCl), which translated to 3.425 V vs Li/Li<sup>+</sup> and was consistent with previous reports [26,27].

The CV scans for 0.1 mol L<sup>-1</sup> [Fe(CN)<sub>6</sub>]<sup>3-</sup> solution in the electrolyte used for the LFP CV experiments (0.1 mol L<sup>-1</sup> Li<sub>2</sub>SO<sub>4</sub> aqueous solution) can be found in Appendix C, Figure C2b. The estimated half-wave potential of [Fe(CN)<sub>6</sub>]<sup>3-</sup> was 0.247 V (vs. Ag/AgCl), consistent with previous literature [28].

#### 4.4.2.5 X-ray Computed Tomography

The column samples for X-Ray computed tomography (XCT) were made using Teflon cylinders, and mimicked the PFR column shown in Fig. 1 b (details in Appendix C, Figure C3). XCT was performed on a Zeiss Xradia Versa 520 at Oak Ridge National Laboratory. The X-ray source was tuned to 80 kV and operated at 6 W to achieve ~20% transmission. And 0.4x optics was chosen on the detector side to fill the detector field of view (FOV) with the full Teflon cylinder. Under this configuration, the effective pixel size is about 16 μm. For the XCT acquisition, 1601 evenly spaced projections, each with 4 s exposure, were collected over 360° rotation. These collected projections were then loaded into Zeiss reconstruction tool, which completes the filtered-back-projection (FBP) based reconstruction. Image processing and analysis were performed using Amira Avizo software. The XCT setup is detailed in the Appendix C and a 3-D reconstruction of LFP packed bed is shown in Figure 1c.

#### 4.4.2.6 Coin Cell Fabrication and Electrochemical Characterization

The electrochemical properties of as-received LFP, sintered LFP, and the oxidized LFP (FP) after reaction with  $[\text{Fe}(\text{CN})_6]^{3-}$  was evaluated using 2032-type coin cells on a MACCOR battery cycler. The FP after oxidation by  $[\text{Fe}(\text{CN})_6]^{3-}$  was harvested from the column after the following reaction conditions:  $0.3 \text{ mol L}^{-1} [\text{Fe}(\text{CN})_6]^{3-}$  was flowed at  $54 \text{ mL hr}^{-1}$  for 67 minutes through a 1.0 cm LFP packed bed height (containing 1.0 g LFP powder). Based on CV scans on the PBR effluent aliquots, the conversion of the LFP was estimated to be 100%. Using the electroactive materials, cathodes were fabricated consisting of a slurry of 80:10:10 (by wt%) active material : carbon black : PVDF, where the active material was LFP, sintered LFP, or FP after oxidation by  $[\text{Fe}(\text{CN})_6]^{3-}$  (which was the sintered LFP after the chemical oxidation process). The components were blended into a slurry with NMP as solvent. Prior to adding NMP, the active material and carbon black were blended together using a mortar and pestle. Hence, the materials with aggregation due to the mild sintering process (LFP after sintering, and the material after sintering and then oxidation to FP using  $\text{K}_3[\text{Fe}(\text{CN})_6]$ ) likely had some reduction in aggregate size due to pulverization with the mortar and pestle. The slurry was cast on an aluminum current collector using a doctor blade with a gap height of  $125 \text{ }\mu\text{m}$ . The electrodes were then dried overnight in an ambient oven at  $80 \text{ }^\circ\text{C}$ , and then in a vacuum oven for two hours at  $80 \text{ }^\circ\text{C}$ . The thickness of the electrodes, measured using a digital micrometer, was found to be  $100 \pm 5 \text{ }\mu\text{m}$  for LFP,  $70 \pm 3 \text{ }\mu\text{m}$  for sintered LFP and,  $70 \pm 3 \text{ }\mu\text{m}$  for FP from oxidation of sintered LFP with  $[\text{Fe}(\text{CN})_6]^{3-}$ . The active material loading was  $9.7 \pm 0.2 \text{ mg cm}^{-2}$  for LFP,  $9.4 \pm 0.2 \text{ mg cm}^{-2}$  for sintered LFP and,  $9.1 \pm 0.1 \text{ mg cm}^{-2}$  for FP from oxidation of sintered LFP with  $[\text{Fe}(\text{CN})_6]^{3-}$ . The errors were the standard deviation of three independent measurements of thickness and loading on separate electrode regions or punched samples, respectively. Punched Li foil discs ( $1.6 \text{ cm}^2$  area,  $100 \text{ }\mu\text{m}$  thickness) were used as the

anode, 1.2 mol L<sup>-1</sup> LiPF<sub>6</sub> in 3:7 vol% ethylene carbonate:ethyl methyl carbonate (Gotion Inc.) was used as the electrolyte, and electrodes were separated using glass fiber separators (Fischer Scientific, G6 0.32 mm thickness). Three cells were made for each cathode active material. The cells were charged at room temperature with the same charge and discharge rate at C/20, C/10, C/5, C/2, 1 C and, C/20, where 1C was assumed to correspond to 160 mAh g<sup>-1</sup> active material in the electrode, based on the voltage profiles obtained at C/20 rates for each material (Appendix C, Figure C4). Three cycles at each C rate were performed, totaling 18 cycles. Representative charge/discharge capacities for the cycling of the cells at different C rates can be found in the Appendix C, Figure C5. Note that the Li/LFP and Li/sintered LFP cells were started with a charge cycle and Li/FP (where FP was LFP after chemical oxidation by K<sub>3</sub>Fe(CN)<sub>6</sub>) cells were started with a discharge cycle. The voltage window for all electrochemical measurements was 2.5 to 4 V (vs. Li/Li<sup>+</sup>)

#### 4.4.2.7 Material characterization and analysis

The morphologies of original LFP, sintered LFP (after breaking into aggregates using mortar and pestle by hand), and FP (oxidized with [Fe(CN)<sub>6</sub>]<sup>3-</sup>) were observed using scanning electron microscopy (SEM, Quanta 650 SEM). X-ray diffraction patterns were taken of these three materials along with FP prepared via chemical oxidation with an alternative previous reported method as a reference [29]. The surface area of the original and sintered LFP, as determined using the Brunauer-Emmett-Teller (BET) method, was measured using a Micromeritics ASAP 2020 at 77 °K using nitrogen as the adsorbing gas. Pore sizes from the nitrogen adsorption isotherms were calculated using the Barrett-Joyner-Halenda (BJH) method.

## 4.5. Results and Discussion

LFP is a popular electroactive material used in the cathode of Li-ion batteries, containing earth-abundant Fe as the transition metal and demonstrated to have favorable cycle life and safety outcomes [26,30]. These features make LFP an attractive option for RTFBs designed for grid-scale storage, as resource abundance/low cost and long-term reliability/cycling are key qualities for the stationary energy storage applications likely best suited to RTFBs [4]. LFP also has a flat half-wave potential at 3.45 V (vs. Li/Li<sup>+</sup>) which offers advantages for RTFBs. First, a flat potential means that the overpotential needed from the redox shuttle to drive LFP oxidation or FP reduction would be expected to be relatively constant across a wide range of states of charge. Second, the half-wave potential of LFP is well within the stability window of both aqueous and non-aqueous electrolytes, hence allowing a significant range of oxidizing redox shuttles and electrolytes that would be compatible with LFP.

[Fe(CN)<sub>6</sub>]<sup>3-</sup> and its reduced form, [Fe(CN)<sub>6</sub>]<sup>4-</sup> are stable and reversible redox shuttles that have been demonstrated in aqueous flow batteries with excellent cyclability [28,31,32]. Recently, rapid kinetics were demonstrated for chemical oxidation of LFP with [Fe(CN)<sub>6</sub>]<sup>3-</sup> in a three-electrode cell, where 95% of [Fe(CN)<sub>6</sub>]<sup>3-</sup> was reduced by 3 times equivalent capacity of LFP [20]. Hence, this promising reported result motivated the selection of the LFP and [Fe(CN)<sub>6</sub>]<sup>3-</sup> chemical redox reaction for the initial demonstration of a chemical redox PBR [5,33]. CV scans on [Fe(CN)<sub>6</sub>]<sup>3-</sup>/[Fe(CN)<sub>6</sub>]<sup>4-</sup> solutions resulted in a measured half-wave potential of 0.247 V (vs. Ag/AgCl), which was 60 mV higher than LFP (relevant CV scans can be found in Appendix C, Figure C2) . As the relative fraction of [Fe(CN)<sub>6</sub>]<sup>3-</sup> in prepared solutions with different concentrations of [Fe(CN)<sub>6</sub>]<sup>3-</sup>/[Fe(CN)<sub>6</sub>]<sup>4-</sup> was varied, relatively small variations in half-wave potential were observed (from 0.248 V – 0.220 V vs. Ag/AgCl, as shown in Appendix C, Figure

C1). Therefore, a driving potential of 30-60 mV was assumed between LFP and  $[\text{Fe}(\text{CN})_6]^{3-}$  to favor reaction (1) proceeding throughout the PBR, until the LFP was nearly completely converted to FP.

Since chemical redox between solid electroactive materials and redox shuttles occurs on the surface of solid particles, the rate of the chemical redox can be increased by selecting smaller solid electroactive materials with higher surface area. However, with high surface area solid electroactive material, a PBR configuration results in high pressure drop and therefore high parasitic loss in pumping the electrolyte solution through [18]. Even in the experimental system herein, directly packing the as received LFP material in the column significantly reduced the achievable flow rates. In addition, it was desired to minimize the possibility of the particles leaving the reactor. In a full RTFB, free particles would start to aggregate at the porous electrodes in the electrochemical power stack, resulting in increased pressure drop and parasitic pumping losses. For the experimental analysis in this study, free particles could potentially continue chemical redox within the collected aliquots, which would have resulted in higher observed chemical redox reactions across the column than what was actually achieved. Thus, to mitigate these issues, the as-received LFP powder was mildly thermally treated in a flowing  $\text{N}_2$  atmosphere to provide coarser LFP aggregates – although it is noted the aggregates are still expected to contain internal porosity in the PBR.

These design considerations were navigated by sintering fine LFP powder (~60 nm average particle lengths) into pellets. Those pellets were then coarsely pulverized to secondary particle sizes ranging from 16  $\mu\text{m}$  to several mm, as can be seen in the XCT image in Figure 2.

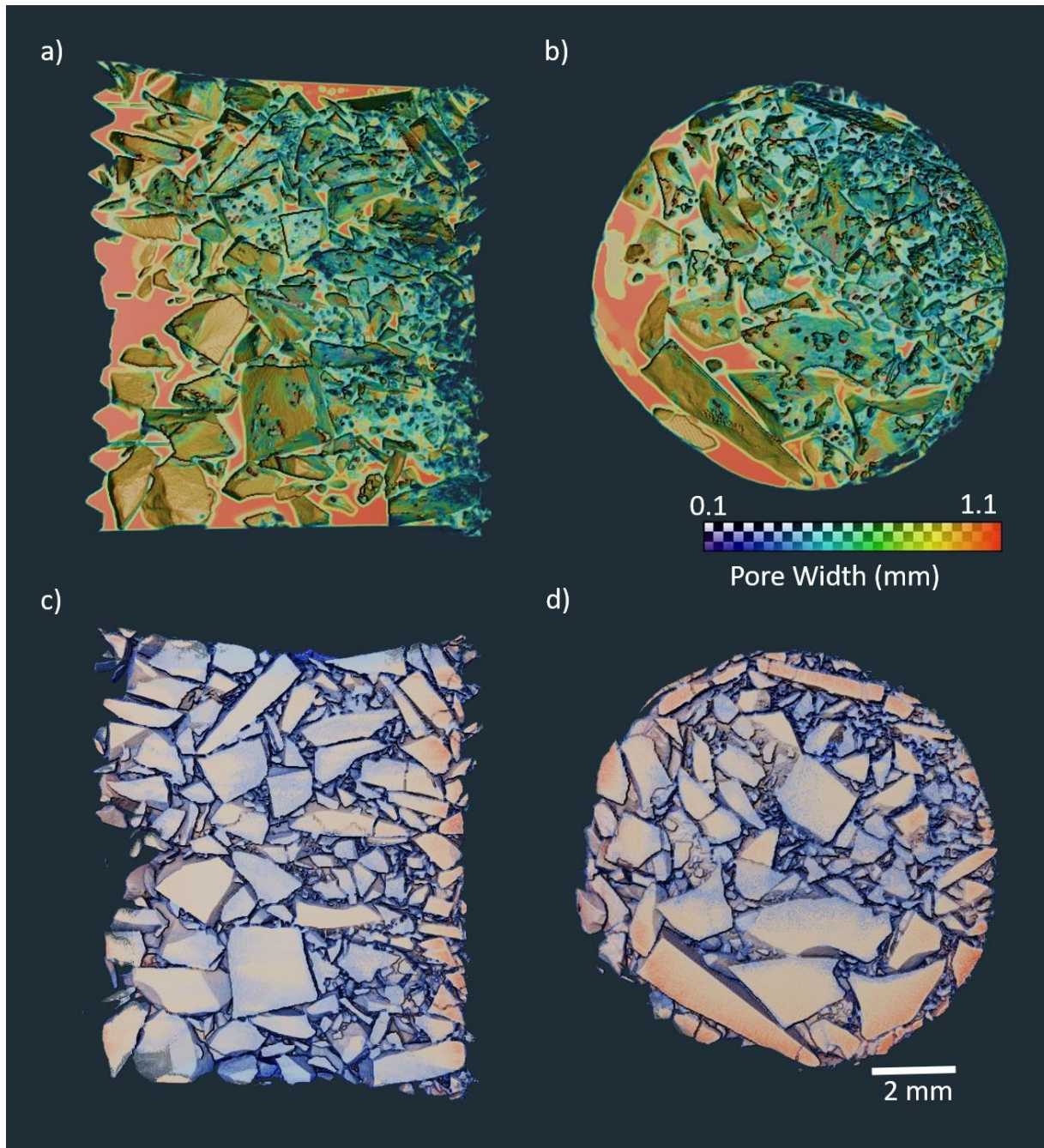


**Figure 2. XCT reconstructions of the packed bed reactor. Two-dimensional slices of the pore volumes are shown for a) the vertical length of the column and b) the horizontal radial axis at the center of the column. The color scale corresponds to the relative longest lengths of a given pore/void. Two-dimensional slices of the LFP aggregates are shown for c) the vertical length of the column and d) the horizontal radial axis at the center of the column. Note that XCT resolution was not sufficient to show internal porosity in the LFP aggregates.**

#### *4.5.1 LFP/FP characterization as-received, after sintering, and after chemical oxidation*

The sintering of LFP powder was performed to mitigate the extreme pressure drop originating from a packed bed composed of fine particles (LFP primary particle size was observed to be  $<1$   $\mu\text{m}$  in diameter, with many particles 50 nm or less). However, it was desired to retain the primary particle size of the LFP to maintain high total surface area available for chemical redox reactions and to mitigate transport of  $\text{Li}^+$  and  $\text{e}^-$  within the primary particles drastically reducing the achievable reaction rate [34]. Mild sintering at 400  $^\circ\text{C}$  has been shown to be sufficient to form particle connections but still retain electrochemical activity for LFP [35]. SEM images show that sintering of LFP particles at 400  $^\circ\text{C}$  confirmed the primary particle size did not dramatically increase (Figure 3). Secondary particle aggregates were difficult to assess; however, secondary aggregates tens of micrometers were observed in SEM (examples can be found in Appendix C, Figure C6). Furthermore, the XRD patterns revealed peaks consistent with LFP were observed both before and after the mild sintering step, and no impurity peaks were observed in either pattern (Figure 4a). Electrochemical analysis of coin cells with LFP active material both before and after the sintering process demonstrated that the capacity at cycling rates between C/20 and C/5 were nearly identical, suggesting that electrochemically active LFP was retained after the sintering and hand grinding process (see Appendix C, Figure C5). It is noted that the capacity at the two highest rates was significantly lower for the sintered LFP, although the capacity at low rates conducted after the high rate cycling was recovered, suggesting the decreased capacity was not due to irreversible capacity loss. The lower capacity at high rates may have been due to different transport properties in the electrode microstructure for the larger aggregates, though exploration of the root cause of the high rate capacity difference was not pursued.

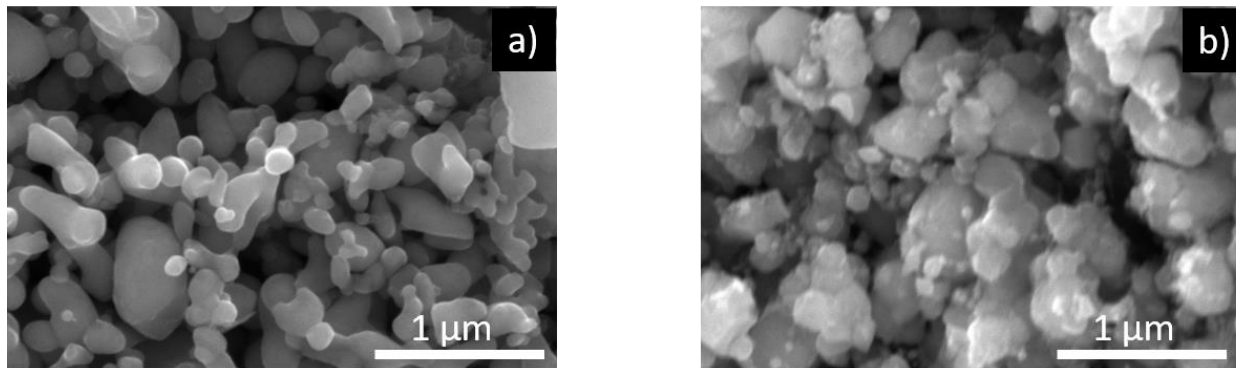


**Figure 3. SEM images of a) as-received LFP and b) sintered LFP after grinding by hand.**

The sintered LFP was used in the PBR experiments. To confirm the material was still an electroactive powder after chemical oxidation, the powder was harvested after being oxidized in the PBR and then characterized. The LFP was chemically oxidized using  $0.3 \text{ mol L}^{-1} [\text{Fe}(\text{CN})_6]^{3-}$ , and via analysis of the effluent the conversion of the LFP to FP was estimated as 100%. This powder of LFP oxidized to FP was evaluated using XRD, and the patterns were in agreement with a previously established method for chemically oxidizing LFP to FP with  $\text{H}_2\text{O}_2$  [29]. Coin cells made using LFP chemically oxidized to FP from the PBR had a reversible electrochemical capacity at  $C/20$  comparable to the as-received material (for charge and discharge capacity from rate capability testing, see Appendix C, Figure C5). SEM images of the material collected after oxidation and 100% conversion to FP in the PBR can be found in Appendix C, Figure C7. The SEM results suggested the primary particle morphology was retained after the reaction in the PBR.

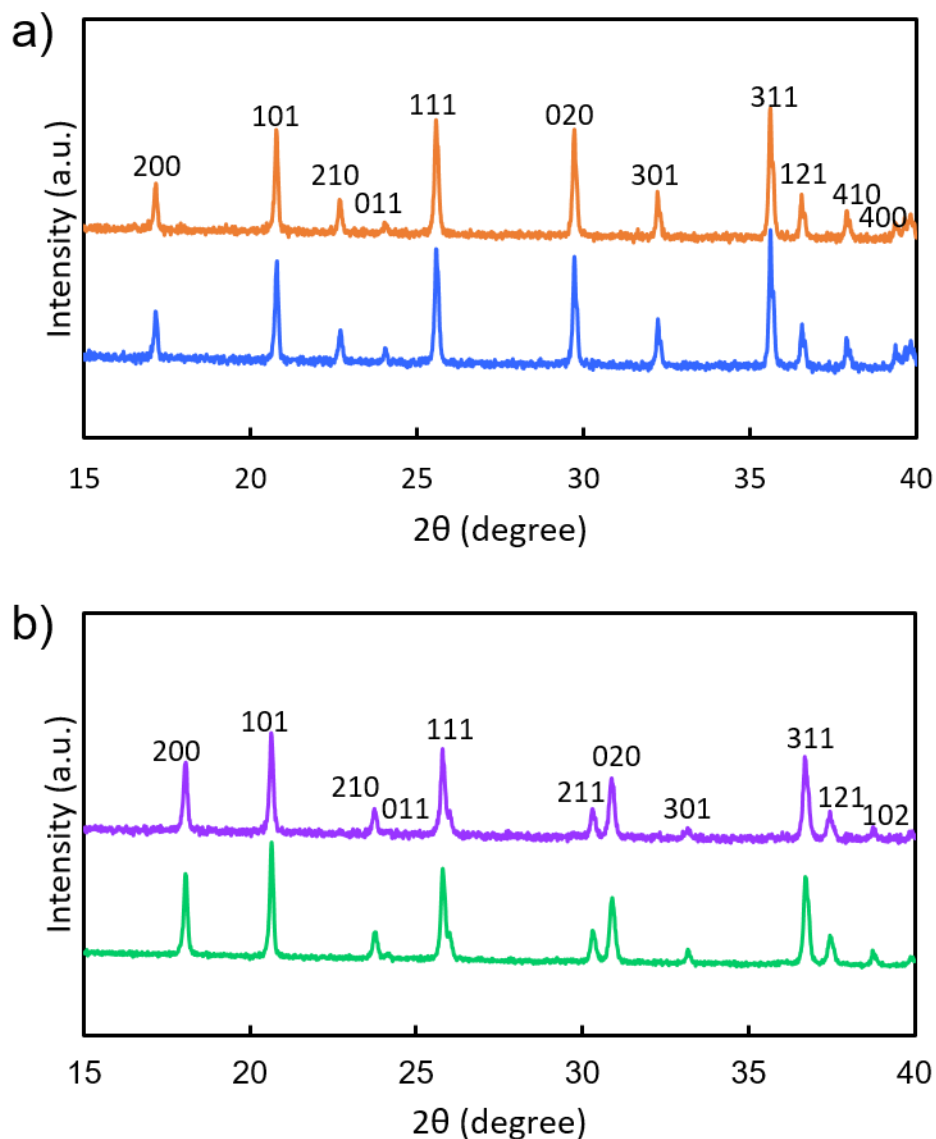


**Figure 4. a) XRD patterns of as-received LFP (blue) and sintered LFP (orange). b) XRD patterns of FP obtained after oxidation of the LFP to FP using hydrogen peroxide via a procedure previously reported (green) [48], and LFP after reaction with  $[\text{Fe}(\text{CN})_6]^{3-}$  (purple), where analysis of reactor effluent indicated full conversion of the LFP to FP. Patterns were consistent with PDF- 01-078-7908 for LFP in a) and PDF- 04-017-0610 for FP in b).**

#### 4.5.2 Pore structure and XCT analysis

The BET surface area of sintered particles was  $8.8 \text{ m}^2 \text{ g}^{-1}$  compared to  $11.3 \text{ m}^2 \text{ g}^{-1}$  for the original LFP powder. This reduction of surface area may have in part been due to increases in primary particle size, but even though the heat treatment was in inert atmosphere there was likely some oxidation of the carbon coating which may have significantly contributed to the surface area reduction. The pore width distribution was calculated using the BJH method, and can be found in Appendix C, Figure C8)

The particle and pore/void distribution in the PBR were also analyzed using the XCT images. Figures 2a,b are the distance maps of the pores along the length and radial direction, respectively in the LFP PBR. XCT pixel pitch was  $15.9 \text{ }\mu\text{m}$ , so only relatively large-scale pores and particles can be analyzed, and internal porosity of the LFP aggregates was not accessible. The pore area distribution is shown in Appendix C, Figure C9. On a number basis many of the pores were near the limit of what can be detected in XCT, and thus the extent to which some of the smallest pores from XCT were artifacts was less clear. In any case, the analysis suggested there were many pores with areas  $<0.1 \text{ mm}^2$  both on a number and total volume basis, and on a volume basis there was also a significant number of pores between  $0.2$  to  $0.4 \text{ mm}^2$  area. Figures 2c,d show the 3D reconstruction of LFP particles. The particle size distribution was extracted from this XCT image and the outcomes can be found in Appendix C, Figure C10. On a number basis, most particles detected in XCT were only a few pixels in size, where it would be difficult to resolve the detailed distribution. However, on a volume basis, over 99.7% of the particle volume was particles with lengths over  $0.5 \text{ mm}$ . As the total moles of LFP available is dependent on particle volume,  $>99.7\%$  of the LFP available to react was in particle aggregates  $>0.5 \text{ mm}$  as determined by XCT analysis.

Based upon the mass of LFP added in the column analyzed with XCT and the crystal density of LFP, volume fraction of pores/voids should have been 0.634. The total pore void fraction was 0.138 from the XCT analyzed region. This would suggest that ~41% of the particle aggregates were voids/pores to match the geometric porosity for the column based on the particle loading. Thus, the XCT analysis suggests the LFP moles available to react was primarily in large aggregates with approximately 41% porosity which would be filled with electrolyte, although here were likely smaller particles between the large aggregates that contributed a relatively small amount to the chemical redox reaction but may have interacted with the electrolyte fluid flowing past to for example provide additional drag.

#### *4.5.3 Reactor Parameters Investigated*

Four parameters were independently adjusted to evaluate their influence on the conversion in the PBR as a function of time during chemical oxidation of LFP with  $[\text{Fe}(\text{CN})_6]^{3-}$ : 1) height of the bed packed with solid electroactive material, 2) flow-rate of the feed containing redox shuttle, 3) redox shuttle ( $[\text{Fe}(\text{CN})_6]^{3-}$ ) concentration and, 4) temperature of the chemical reservoir and the feed solution (with both matched to the same temperature). Bed height and concentration of redox shuttle are design variables and can be built into the design of the PBR prior its operation. Flow rate of redox shuttle containing electrolyte was an operational variable and can be varied during the operation of the PBR, although for a given experimental run the flow rate was maintained at a single value. Temperature could in principal be actively adjusted within the PBR, though for the experiments herein it was maintained at a single value through immersion of the PBR and feed solution reservoir in a temperature-controlled bath. All experimental test conditions are listed in Table 1. Outcomes were assessed using single-factor ANOVA [36]. In this study, conversion of LFP in the packed bed was the dependent variable, and bed height, flow rate,  $[\text{Fe}(\text{CN})_6]^{3-}$

concentration, and reactor temperature were the independent variables. The null hypothesis was that observed variation in conversion for a sample set was due to the random variation in the measured conversions. Rejection of the null results in acceptance of the alternative hypothesis, which in this study was the conclusion that conversion of LFP was influenced by changes in the variable of interest. The p-value, that measures the plausibility of the null hypothesis, was used at the threshold of 5%. If p-value was less than 0.05, the null hypothesis was rejected, and the alternative hypothesis was accepted. However, if the p-value was greater than 0.05, then the null was not rejected. In that case, both null and alternative hypothesis were plausible.

**Table 1: Experimental conditions used in this study.**

Temperature (°C)	LFP bed-height (cm)	Flow rate (mL hr <sup>-1</sup> )	Shuttle concentration (mol L <sup>-1</sup> )	Shuttle Volume (mL)
22.4	0.5	30	0.2	30
22.4	1.0	30	0.2	60
22.4	1.5	30	0.2	90
22.4	1.0	42	0.2	60
22.4	1.0	54	0.2	60
22.4	1.0	66	0.2	60
22.4	1.0	54	0.1	60
22.4	1.0	54	0.3	60
4.0	1.0	54	0.2	60
13.0	1.0	54	0.2	60
40.0	1.0	54	0.2	60

#### 4.5.3.1 Bed-height

Keeping the mass of LFP powder per bed volume and flow-rate constant, the bed height of the PBR was varied at 0.5, 1.0, and 1.5 cm containing 0.5, 1.0, and 1.5 g LFP, respectively. The temperature for all experiments was room temperature, measured to be 22.4 °C. The feed solution for all experiments contained 0.2 mol L<sup>-1</sup> [Fe(CN)<sub>6</sub>]<sup>3-</sup>, and the feed solution flow rate was 30 mL hr<sup>-1</sup>. The duration of time that the feed solution was fed through the PBR was chosen such that the volume of electrolyte flown through each bed height contained a total of ~2 times moles of redox shuttle relative to the moles of LFP in the packed bed reactor. In other words, the total [Fe(CN)<sub>6</sub>]<sup>3-</sup> fed through the PBR for each experiment was chosen to result in ~2 times the stoichiometric moles required to fully oxidize the LFP powder in the PBR. The results of varying bed height are shown in Figure 5. The molar conversion of LFP to FP after completing flowing 2 mol [Fe(CN)<sub>6</sub>]<sup>3-</sup> per mol of LFP for the different bed heights varied between 81-88%, with the 1.5 cm bed height having a slightly higher conversion (Appendix C, Table C1). However, there was not a significant difference of conversion between the three bed heights after flowing through equivalent molar stoichiometries of [Fe(CN)<sub>6</sub>]<sup>3-</sup>, as determined by one-way ANOVA (p = 0.624). Hence, when proportional total moles of [Fe(CN)<sub>6</sub>]<sup>3-</sup> solution was flown through different packed bed heights, similar molar conversion of LFP was achieved. However, when LFP conversion was measured for the same amount of [Fe(CN)<sub>6</sub>]<sup>3-</sup> solution (30 mL, 6 moles) flown through, there was a significant difference between molar conversion of LFP in different bed heights (p = 0.000236). Thus, if same amount of [Fe(CN)<sub>6</sub>]<sup>3-</sup> was flown then the molar conversion of LFP had a linear correlation to bed height, as shown in Figure 5b. Therefore, molar conversion of LFP was dependent upon bed-height for the same moles of redox shuttle flown through, but for the same molar ratio of LFP to redox shuttle there was no difference in conversion.

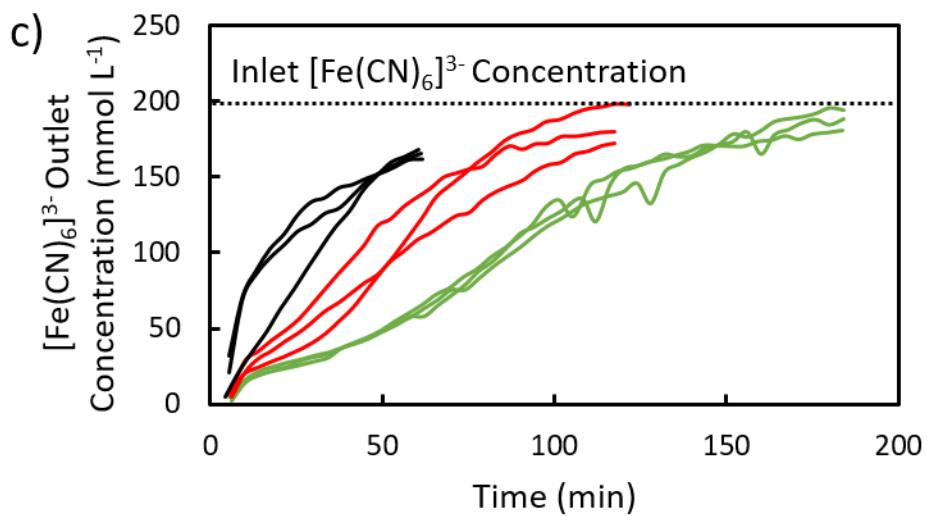
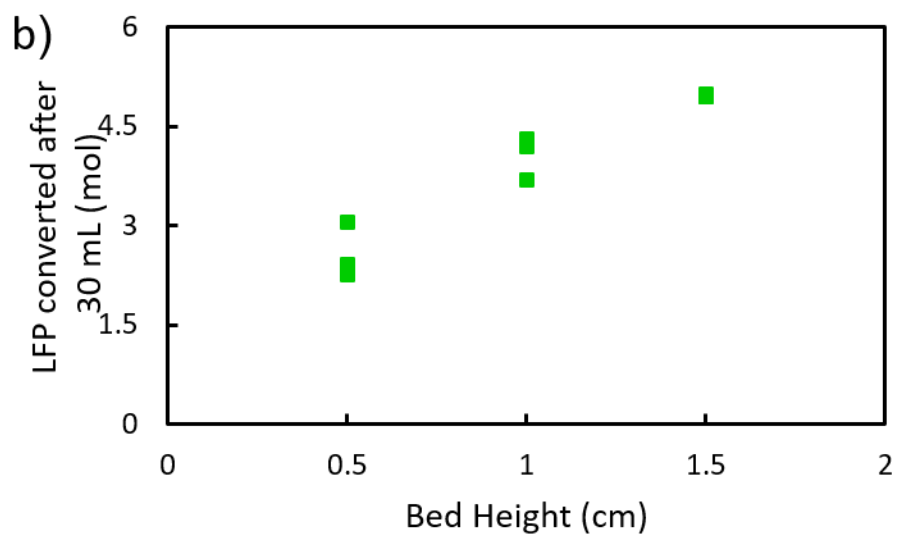
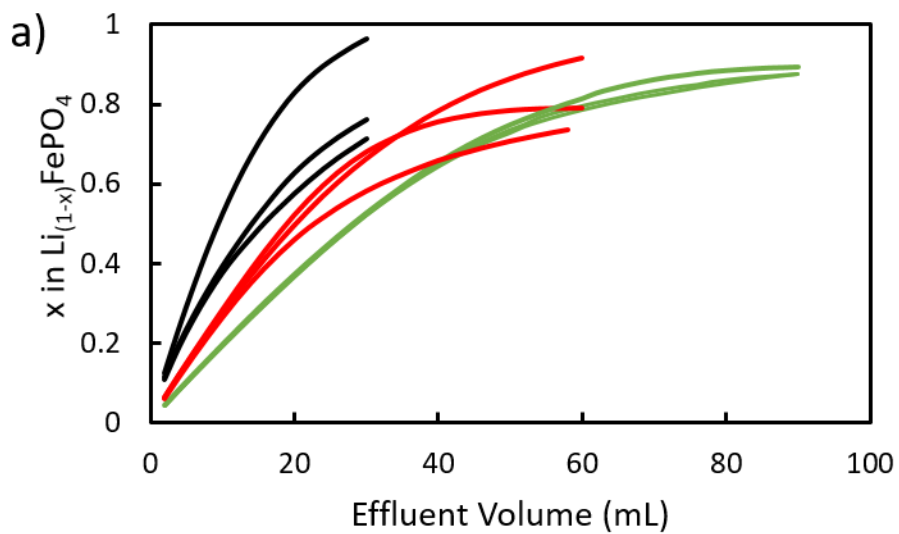


**Figure 5. a) Conversion of LFP solid material in the reactor at different bed heights of 0.5 cm (black), 1.0 cm (red), and 1.5 cm (green) as a function of volume of redox shuttle solution fed. b) Total moles of LFP converted (FP generated) as a function of bed height for the same 30 mL volume of 0.2 mol L<sup>-1</sup> [Fe(CN)<sub>6</sub>]<sup>3-</sup> flowed through the column. c) Outlet [Fe(CN)<sub>6</sub>]<sup>3-</sup> concentration as a function of time. Experimental conditions were run in triplicate, and each experiment is a different line in a) and c), and data point in b).**

#### 4.5.3.2 Flow rate variation

For constant bed height (1.0 cm) and concentration (0.2 M [Fe(CN)<sub>6</sub>]<sup>3-</sup>), four flow rates were evaluated at room temperature: 30, 42, 54, and 66 mL h<sup>-1</sup> corresponding to average residence times of 94, 67, 52, and 43 seconds, respectively. The molar ratio of total moles [Fe(CN)<sub>6</sub>]<sup>3-</sup> fed to the column to LFP in the packed bed was again two for the conditions tested. The Reynolds number for the range of flow rates was estimated as  $1.0 \times 10^{-2}$  to  $2.2 \times 10^{-2}$  [37], hence the flow through the column was expected to occur in the laminar regime. As shown in Figure 6, the molar conversion of LFP for 30 and 54 mL hr<sup>-1</sup> was ~ 82%, whereas it was 73% and 77% for 42 and 66 mL h<sup>-1</sup>, respectively, after flowing all the electrolyte through the PBR. Therefore, flow-rate of [Fe(CN)<sub>6</sub>]<sup>3-</sup> solution did not have a significant effect on the molar conversion of the LFP packed bed for the range of flow rates tested ( $p = 0.428$ ). As there was not any observed effect on molar conversion of LFP by varying flow rates between 30-66 mL hr<sup>-1</sup>, slower flow rates were not investigated. At the other extreme, flow rates of 72 mL hr<sup>-1</sup> sometimes resulted in leaks at fixtures/connections, and thus experiments did not exceed 66 mL hr<sup>-1</sup>. Varying flow-rates would affect the bulk transport of the [Fe(CN)<sub>6</sub>]<sup>3-</sup> reactant in the packed bed, and increased conversion with increasing flow rate would have indicated overcoming external mass transport resistances in

the PBR [37]. The lack of flow rate dependence indicated the PBR was operating in a regime without external mass transport resistances at the secondary LFP/FP particle surfaces.

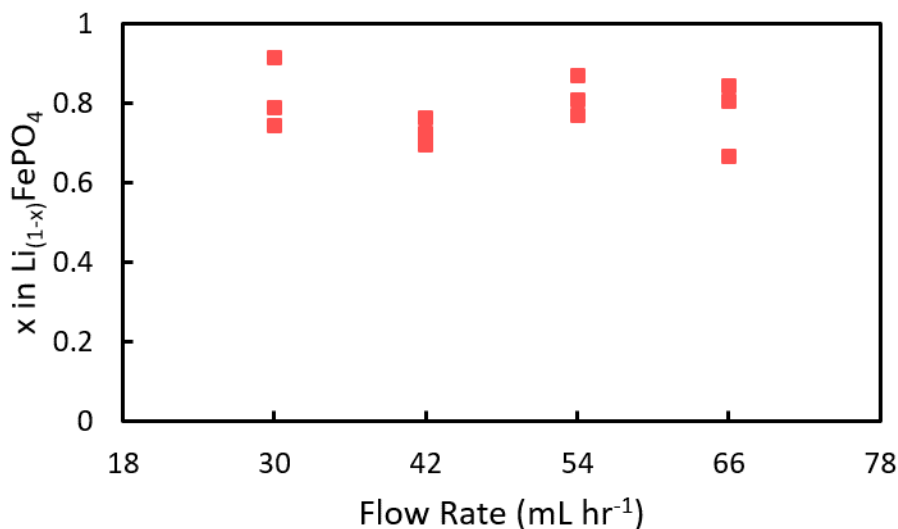


**Figure 6: Conversion of LFP to FP after flowing 60 mL of 0.2 mol L<sup>-1</sup> [Fe(CN)<sub>6</sub>]<sup>3-</sup> in a 1.0 cm packed bed of LFP at different flow rates. Experimental conditions were run in triplicate and each data point is a different experimental run.**

#### 4.5.3.3 Redox Shuttle Concentration Variation

At a bed height of 1.0 cm (with 1.0 g LFP) and a constant flow rate of 54 mL h<sup>-1</sup>, three concentrations of [Fe(CN)<sub>6</sub>]<sup>3-</sup> solution were evaluated at room temperature: 0.1, 0.2, and 0.3 mol L<sup>-1</sup>. For each concentration, 60 mL of redox shuttle solution traversed the PBR, meaning the total number of moles (×10<sup>-3</sup>) of [Fe(CN)<sub>6</sub>]<sup>3-</sup> through the reactor was 6, 12, and 18 for 0.1, 0.2, and 0.3 mol L<sup>-1</sup> concentration, respectively. Thus, the ratio between moles of LFP in packed bed reactor to total moles of [Fe(CN)<sub>6</sub>]<sup>3-</sup> fed was 1:1, 1:2, and 1:3 for 0.1, 0.2, and 0.3 mol L<sup>-1</sup> concentration, respectively. As shown in Figure 7a, concentration of redox shuttle impacted the molar conversion of LFP in the packed bed reactor, with faster conversion of the LFP to FP with increasing

concentration. The LFP in the PBR was completely delithiated after 60 mL of 0.3 mol L<sup>-1</sup> [Fe(CN)<sub>6</sub>]<sup>3-</sup> solution passed through, whereas for 0.1 mol L<sup>-1</sup> the same volume resulted in ~56% conversion of LFP to FP. Due to the different concentrations but same flow rate and total volume, the total stoichiometry of [Fe(CN)<sub>6</sub>]<sup>3-</sup>:LFP was different. For 0.3 mol L<sup>-1</sup> [Fe(CN)<sub>6</sub>]<sup>3-</sup> the total moles fed stoichiometric ratio was 3:1, while for 0.1 mol L<sup>-1</sup> it was 1:1.

Due to the differences in concentration and total moles fed, the conversion of LFP based on total moles of [Fe(CN)<sub>6</sub>]<sup>3-</sup> flown through the PBR was considered (Figure 7b). Due to normalizing based on total stoichiometry, the differences in the rate of conversion of LFP were less apparent on the moles of [Fe(CN)<sub>6</sub>]<sup>3-</sup> fed basis. At the end of the 0.1 mol L<sup>-1</sup> case (6 × 10<sup>-3</sup> moles of [Fe(CN)<sub>6</sub>]<sup>3-</sup> flown through the PBR), the conversion of LFP in for 0.1, 0.2, and 0.3 mol L<sup>-1</sup> [Fe(CN)<sub>6</sub>]<sup>3-</sup> was 56, 59, and 66 %, respectively. While the magnitude of the differences in LFP conversion on the total moles of reactant fed basis was less than on a volume of reactant solution fed, the difference for the three different concentrations was still significant on the moles reactant fed bases (p = 0.039).

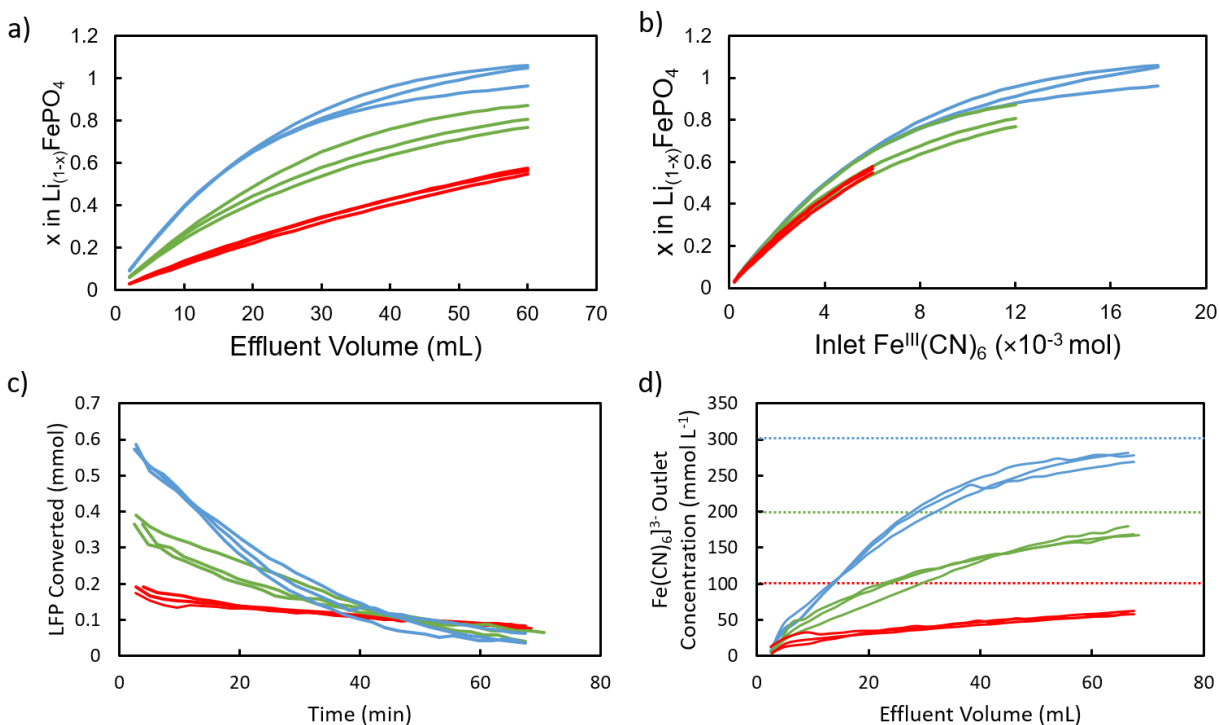


**Figure 7. Conversion of LFP to FP with the redox shuttle in the feed concentration of 0.1 mol L<sup>-1</sup> (red), 0.2 mol L<sup>-1</sup> (green), and 0.3 mol L<sup>-1</sup> (blue). The conversion is shown on the basis of a) volume of feed solution passed through the reactor and b) total moles of [Fe(CN)<sub>6</sub>]<sup>3-</sup> flowed through the reactor. c) Moles of LFP converted in the PBR as a function of time, and d) outlet [Fe(CN)<sub>6</sub>]<sup>3-</sup> concentration as a function of effluent volume. The horizontal bars in d) correspond to the initial concentration fed to the PBR. The bed height was 1.0 cm and the flow rate was 54 ml h<sup>-1</sup>. Experimental conditions were run in triplicate, and each experiment is a different line.**

#### 4.5.3.4 Temperature Variation

The effect of varying temperature on the conversion of the PBR with LFP was evaluated at 4.0, 13.0, 22.4, and 40.0 °C. For these experiments, the bed height was kept constant at 1.0 cm bed height, the flow rate was 54 mL h<sup>-1</sup>, and the [Fe(CN)<sub>6</sub>]<sup>3-</sup> feed concentration was 0.2 mol L<sup>-1</sup>. The

22.4 °C temperature was achieved by running the reactor at room temperature in the setup shown in Figure 1b. For 4, 13, and 40 °C, a water bath was used to keep the PBR at constant temperature. The  $[\text{Fe}(\text{CN})_6]^{3-}$  feed solution was also kept at the temperature of the PBR for each temperature.

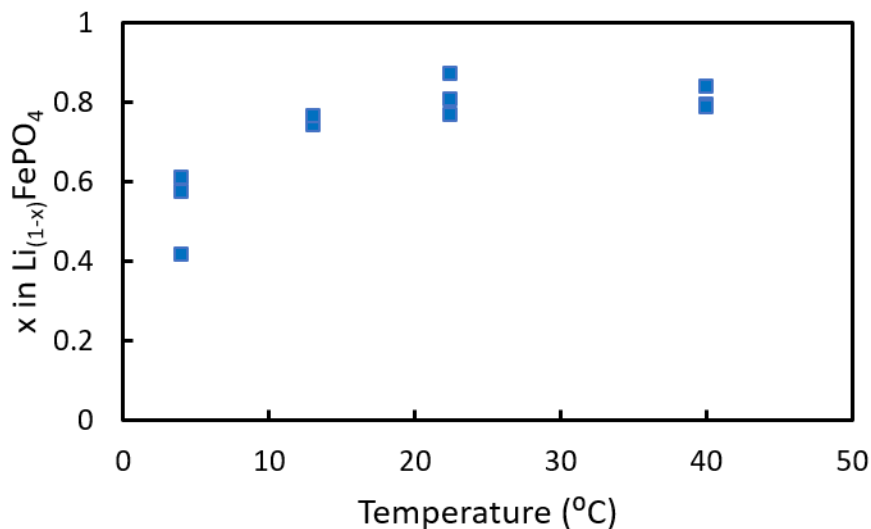


**Figure 8. Conversion of LFP to FP after flowing 60 mL of 0.2 M  $[\text{Fe}(\text{CN})_6]^{3-}$  through the reactor at different temperatures. as a function of temperature for 1 cm bed-height at 54 mL  $\text{h}^{-1}$  solution feed. Triplicates at each temperature are shown in this plot.**

As shown in Figure 8, the conversion of LFP in PBR after 60 mL of the feed solution had exited the reactor for 4.0 and 13.0 °C was 53.5% and 75%, respectively, and at 22.4 and 40.0 °C both were similar at ~80 %. There was a significant difference between the conversion obtained for the four temperature variations ( $p = 1.2 \times 10^{-3}$ ). However, the conversion at 4 °C (53.5%) was much lower than the conversion at higher temperatures. It has been shown previously that phase boundary movement during electrochemical redox in micron sized LFP is controlled by surface reaction (i.e.  $\text{Li}^+$  diffusion in different crystallographic planes) [44] and bulk diffusion limitations (solid-state  $\text{Li}^+$  diffusion along [101] direction) [39–41]. Although these observations were for electrochemical redox in LFP,  $\text{Li}^+$  transport through [101] channels in the crystal plane is a

behavior inherent to olivine LFP. Hence, the internal  $\text{Li}^+$  transport behavior is likely similar during chemical redox of LFP. The rate-limiting step in electrochemical investigations has been  $\text{Li}^+$  diffusion-controlled phase boundary movement in the direction perpendicular to the surface, i.e. core-shell mechanism on an individual primary particle level. In a previous temperature dependent electrochemical analysis, the first-order rate constant for delithiation in  $\text{LiMn}_{0.4}\text{Fe}_{0.6}\text{PO}_4$  was shown to decrease by an order of magnitude for a temperature decrease from 20 °C to 0 °C [42]. The particle size in that report was 50 nm, similar to this report. It is possible that processes at the primary particle level (electron transfer kinetics and/or solid-state  $\text{Li}^+$  diffusion) become limiting processes below a threshold temperature for the PBR in this study (at temperatures below 20 °C). Since  $[\text{Fe}(\text{CN})_6]^{3-}$  transport in the liquid phase would also be slowed at lower temperatures due to the diffusion coefficient dependence of  $[\text{Fe}(\text{CN})_6]^{3-}$ , however, if that was the limiting process across all the temperatures evaluated a difference in conversion would also be expected between the two highest temperatures, and this was not the case.

#### *4.5.4 Reaction mechanism and kinetics*

The reaction between the redox shuttle,  $[\text{Fe}(\text{CN})_6]^{3-}$  and LFP in the PBR is an example of a heterogeneous reaction that is proposed to occur in the following steps:

- 1) External transport of  $[\text{Fe}(\text{CN})_6]^{3-}$  from the flowing bulk solution in the PBR to the surface of the porous LFP aggregate particles.
- 2) Internal diffusion of  $[\text{Fe}(\text{CN})_6]^{3-}$  in the fluid-filled porous channels of the LFP aggregates.
- 3) Reaction between LFP and  $[\text{Fe}(\text{CN})_6]^{3-}$  as described in equation (1) would occur in multiple steps-

3a) Adsorption of  $[\text{Fe}(\text{CN})_6]^{3-}$  on the surface of LFP primary particle.

3b) Internal coupled solid-state  $\text{Li}^+/\text{e}^-$  diffusion to the surface of the primary particles or more locally crystal grains.

3c) Electron transfer between  $[\text{Fe}(\text{CN})_6]^{3-}$  and LFP (with the electron coming from the Fe in the LFP):



3d) Desorption of  $[\text{Fe}(\text{CN})_6]^{4-}$  from the surface of LFP.

3e) Transfer of  $\text{Li}^+$  from the solid particle phase to the solution phase.

4) Diffusion of the  $[\text{Fe}(\text{CN})_6]^{4-}$  and  $\text{Li}^+$  away from the LFP surface and through the LFP aggregate to the edge of the aggregate secondary particle.

5) Transport of the  $[\text{Fe}(\text{CN})_6]^{4-}$  (and  $\text{Li}^+$ ) to the bulk fluid passing through the PBR.

According to the proposed reaction steps and experimental observations, it was speculated that the heterogeneous reaction in the PBR follows a shrinking core process with regards to the LFP aggregate particles. Note that this shrinking core description for the LFP aggregates in the PBR is at a much larger length scale (tens of micrometers to millimeters), which is different from LFP phase transitions models which have included shrinking core that has been discussed for primary particles undergoing electrochemical reactions in LFP electrodes [38]. For the shrinking core in the PBR, the LFP primary particles on the outer region of the aggregate would convert to FP first, and the conversion of primary LFP particles to FP would then proceed towards the aggregate core.

Thus, the diffusion distance of  $[\text{Fe}(\text{CN})_6]^{3-}$  becomes greater through the pore microstructure and past reacted FP primary particles towards the core to find LFP for undergoing reaction as the reaction time and volume of feed solution progressed. The independence of conversion with flow rate suggested external mass transport resistance to the  $[\text{Fe}(\text{CN})_6]^{3-}$  entering the LFP particle aggregates was not influencing the LFP conversion. For the bed height variation experiments, as the bed was made taller the  $[\text{Fe}(\text{CN})_6]^{3-}$  concentration in the outlet remained lower for longer (and thus conversion of LFP in the packed bed was higher for longer). This outcome would be consistent with the  $[\text{Fe}(\text{CN})_6]^{3-}$  reacting with the more easily accessible outer regions of the LFP particles first, and then as  $[\text{Fe}(\text{CN})_6]^{3-}$  must diffuse further in the LFP aggregates to react the conversion of  $[\text{Fe}(\text{CN})_6]^{3-}$  tapers off. For the longer column that tapering off would be delayed due to more total LFP particle aggregates available and thus more total moles of LFP that were less limited by transport of the soluble redox shuttle through the microstructure. For the experiments where  $[\text{Fe}(\text{CN})_6]^{3-}$  concentration was varied, not only did the highest concentration have the highest conversion on a volume of feed solution basis (Figure 6a), but also on a total mole fed basis (Figure 7b). For the moles fed basis, this may have been because the higher concentration redox shuttle solution can achieve higher concentrations deeper into the pellet, which would increase the overall moles reacted. With regards to temperature, molar conversion of LFP was found to decrease significantly at 4.0 and 13.0 °C, but was unaffected at 22.4 and 40 °C. The temperature insensitivity at the highest temperatures would be consistent with the shrinking core concept, as the expected change in the diffusion coefficient of the  $[\text{Fe}(\text{CN})_6]^{3-}$  in the liquid would be relatively small (<10%). However, the transition to much lower conversion at the lowest temperatures suggests a new process may be playing a role. For LFP, previous electrochemical measurements have suggested the oxidation kinetics for LFP undergo a dramatic decrease at 20 °C [42]. suggesting

that after a certain temperature that the kinetics rather than the transport may become the rate limiting process. Understanding and confirming the rate-limiting process for the PBR under different conditions will continue to be the focus of future efforts and characterization development.

It is noted here that LFP has been well known as a fast charge/discharge (oxidation/reduction) material in electrochemical studies [43,44]. However, the electrodes usually studied are typically less than 200  $\mu\text{m}$  thick. For this study, most of the capacity came from particles in aggregates which were a couple of mm from the core to the surface. For such thick porous aggregate sizes, the analogy to limitation in an electrochemical system would be for much thicker electrodes where solution-phase transport limitations limit the rate of the electrochemical reactions. Such phenomena has been reported, for example porous thick sintered electrodes (from few hundred  $\mu\text{m}$  to couple mm thickness) have been reported where the interstitial  $\text{Li}^+$  transport in the electrolyte phase through tortuous paths has been responsible for limiting electrochemical reaction rates [45], and thus high rates of discharge were not accessible due to electrolyte depletion [46]. For the PBR reactor, the description of the limiting process postulated above is similar in that it is transport of a species through the electrolyte phase in the interstitial regions between particles, although the species in the PBR was the redox shuttle rather than  $\text{Li}^+$ .

The PBR reactor system was similar to that of chemical looping combustion, where gaseous fuel/air reacts with metal oxide particles [47]. Metal oxides are reduced and oxidized in a fuel reactor and air reactor, respectively, and are transferred to separate reactors for oxidation and reduction. Despite this operational/application difference (and contacting phases in many cases), it is like the PBR system in that the particles forming the packed bed are themselves reactants that have spatial and temporal functionalities sensitivity to the reaction progression. Therefore,

qualitative inferences could be derived from the chemical looping combustion. For instance, a comparison done on pilot-scale fuel reactors of 1 MW, 100 kW, and 50 kW capacity found that intermediate sizes (90-300  $\mu\text{m}$ ) of metal oxide particles (i.e. the solid reactant) were preferred [47]. If the particles were too big ( $> 8 \text{ mm}$ ), there was insufficient conversion. If the particles were too small, they were elutriated into the gas stream. Additionally, the ideal particle size distributions vary between pilot scale and full-scale plants (100-1000 MW), as the residence time for gases was higher in full-scale plants. The impact of aggregate size distributions on the PBR system will be explored in future work, as the processes used to make the aggregates in this study did not lend to control over aggregate size. Analogous to chemical looping combustion, in the chemical reservoir of a RTFB, it will be desirable to convert the fluid reactant stream 100% with every flow cycle. Hence, particle engineering of solid electroactive material is expected to impact the molar conversion of redox shuttles for RTFBs and other redox shuttle/electroactive material coupled chemical redox applications.

#### ***4.6 Conclusions***

In this work, a reactor system was reported which enabled evaluation of the extent of chemical oxidation of a solid Li-ion electroactive material, LFP, with a dissolved redox shuttle compound. The conversion in the reactor was tracked as a function of time for variations of different reactor conditions: bed-height, concentration of redox shuttle, flow rate of feed solution, and operating temperature. The dependence between molar conversion of LFP and the different variables was assessed using single variable ANOVA. It was found that flow rate did not influence the conversion, and bed-height did not impact the molar conversion of LFP when stoichiometric

amounts of shuttle were flown. It was also found that the molar conversion of LFP has a strong dependence on the concentration of the redox shuttle. Additionally, it was observed that at the highest temperatures that there was not a temperature dependence, but that below a certain operating temperature the molar LFP conversion became dependent upon temperature. A reaction mechanism based on these observations was suggested where a shrinking core of LFP conversion to FP propagated at the LFP aggregate level, where for most reaction conditions the conversion was limited by the process of the redox shuttle diffusion in the solution phase through the LFP aggregate microstructure. This study provides a framework for investigating packed beds of Li-ion electroactive materials undergoing chemical redox, which is relevant for redox targeting flow battery applications and potentially others such as the recycling and extraction of  $\text{Li}^+$  from spent Li-ion battery materials.

### **Acknowledgement**

This research used resources at the High Flux Isotope Reactor, a DOE Office of Science User Facility operated by the Oak Ridge National Laboratory under contract DE-AC05-00OR22725 with UT-Battelle, LLC.

## 4.7 References

- [1] T.M. Gür, Review of electrical energy storage technologies, materials and systems: Challenges and prospects for large-scale grid storage, *Energy Environ. Sci.* 11 (2018) 2696–2767. <https://doi.org/10.1039/c8ee01419a>.
- [2] B. Dunn, H. Kamath, J.M. Tarascon, Electrical energy storage for the grid: A battery of choices, *Science* (80-. ). 334 (2011) 928–935. <https://doi.org/10.1126/science.1212741>.
- [3] W. Wang, Q. Luo, B. Li, X. Wei, L. Li, Z. Yang, Recent Progress in Redox Flow Battery Research and Development, (2013) 970–986. <https://doi.org/10.1002/adfm.201200694>.
- [4] R. Yan, Q. Wang, Redox-Targeting-Based Flow Batteries for Large-Scale Energy Storage, *Adv. Mater.* 1802406 (2018) 1802406. <https://doi.org/10.1002/adma.201802406>.
- [5] J.F. Vivo-Vilches, A. Nadeina, N. Rahbani, V. Seznec, D. Larcher, E. Baudrin, LiFePO<sub>4</sub>-ferri/ferrocyanide redox targeting aqueous posolyte: Set-up, efficiency and kinetics, *J. Power Sources.* 488 (2021) 229387. <https://doi.org/10.1016/j.jpowsour.2020.229387>.
- [6] T. Páez, A. Martínez-Cuezva, J. Palma, E. Ventosa, Mediated alkaline flow batteries: From fundamentals to application, *ACS Appl. Energy Mater.* 2 (2019) 8328–8336. <https://doi.org/10.1021/acsaem.9b01826>.
- [7] C.M. Wong, C.S. Sevov, All-Organic Storage Solids and Redox Shuttles for Redox-Targeting Flow Batteries, *ACS Energy Lett.* (2021) 1271–1279. <https://doi.org/10.1021/acsenerylett.1c00143>.
- [8] E. Zanzola, C.R. Dennison, A. Battistel, P. Peljo, H. Vrubel, V. Amstutz, H.H. Girault, Redox Solid Energy Boosters for Flow Batteries: Polyaniline as a Case Study, *Electrochim. Acta.* 235 (2017) 664–671. <https://doi.org/10.1016/j.electacta.2017.03.084>.

- [9] C. Jia, F. Pan, Y.G. Zhu, Q. Huang, L. Lu, Q. Wang, High – energy density nonaqueous all redox flow lithium battery enabled with a polymeric membrane, *Sci. Adv.* 1 (2015) 1–7. <https://doi.org/10.1126/sciadv.1500886>.
- [10] M. Duduta, B. Ho, V.C. Wood, P. Limthongkul, V.E. Brunini, W.C. Carter, Y.M. Chiang, Semi-solid lithium rechargeable flow battery, *Adv. Energy Mater.* 1 (2011) 511–516. <https://doi.org/10.1002/aenm.201100152>.
- [11] Z. Qi, G.M. Koenig, Review Article: Flow battery systems with solid electroactive materials, *J. Vac. Sci. Technol. B, Nanotechnol. Microelectron. Mater. Process. Meas. Phenom.* 35 (2017) 040801. <https://doi.org/10.1116/1.4983210>.
- [12] B.R. Chalamala, T. Soundappan, G.R. Fisher, M.R. Anstey, V. V. Viswanathan, M.L. Perry, Redox flow batteries: An engineering perspective, *Proc. IEEE.* 102 (2014) 976–999. <https://doi.org/10.1109/JPROC.2014.2320317>.
- [13] Q. Huang, H. Li, M. Grätzel, Q. Wang, Reversible chemical delithiation/lithiation of LiFePO<sub>4</sub>: towards a redox flow lithium-ion battery., *Phys. Chem. Chem. Phys.* 15 (2013) 1793–7. <https://doi.org/10.1039/c2cp44466f>.
- [14] D. Gupta, G.M. Koenig, Analysis of Chemical and Electrochemical Lithiation/Delithiation of a Lithium-Ion Cathode Material, *J. Electrochem. Soc.* 167 (2020) 020537. <https://doi.org/10.1149/1945-7111/ab6bbf>.
- [15] D. Gupta, C. Cai, G.M. Koenig, Comparative Analysis of Chemical Redox between Redox Shuttles and a Lithium-Ion Cathode Material via Electrochemical Analysis of Redox Shuttle Conversion, *J. Electrochem. Soc.* 168 (2021) 050546. <https://doi.org/10.1149/1945-7111/ac0068>.

- [16] F. Pan, J. Yang, Q. Huang, X. Wang, H. Huang, Q. Wang, Redox Targeting of Anatase TiO<sub>2</sub> for Redox Flow Lithium-Ion Batteries, *Adv. Energy Mater.* (2014) n/a-n/a. <https://doi.org/10.1002/aenm.201400567>.
- [17] R. Yan, J. Ghilane, K.C. Phuah, T.N. Pham Truong, S. Adams, H. Randriamahazaka, Q. Wang, Determining Li<sup>+</sup>-Coupled Redox Targeting Reaction Kinetics of Battery Materials with Scanning Electrochemical Microscopy, *J. Phys. Chem. Lett.* (2018) 491–496. <https://doi.org/10.1021/acs.jpcclett.7b03136>.
- [18] E.L. Cussler, E.L. Cussler, *Diffusion: mass transfer in fluid systems*, Cambridge university press, 2009.
- [19] S.Y. Chung, J.T. Bloking, Y.M. Chiang, Electronically conductive phospho-olivines as lithium storage electrodes, *Nat. Mater.* 1 (2002) 123–128. <https://doi.org/10.1038/nmat732>.
- [20] J. Yu, X. Wang, M. Zhou, Q. Wang, A redox targeting-based material recycling strategy for spent lithium ion batteries, *Energy Environ. Sci.* 12 (2019) 2672–2677. <https://doi.org/10.1039/c9ee01478k>.
- [21] Q. Li, N. Li, H. Zhou, Saving electric energy by integrating a photoelectrode into a Li-ion battery †, (2015) 20903–20907. <https://doi.org/10.1039/c5ta06908d>.
- [22] S. Liao, X. Zong, B. Seger, T. Pedersen, T. Yao, C. Ding, J. Shi, J. Chen, C. Li, Integrating a dual-silicon photoelectrochemical cell into a redox flow battery for unassisted photocharging, *Nat. Commun.* 7 (2016). <https://doi.org/10.1038/ncomms11474>.
- [23] L. Zhang, Z. Zhang, K. Amine, Redox Shuttle Additives for Lithium-Ion Battery, in: *Lithium Ion Batter. - New Dev.*, 2012. <https://doi.org/10.5772/26572>.

- [24] L.M. Moshurchak, C. Buhrmester, J.R. Dahn, X. Wei, W. Xu, J. Huang, L. Zhang, E. Walter, C. Lawrence, M. Vijayakumar, W.A. Henderson, T. Liu, L. Cosimbescu, B. Li, V. Sprenkle, W. Wang, E.I. Rogers, D.S. Silvester, D.L. Poole, L. Aldous, C. Hardacre, R.G. Compton, Spectroelectrochemical Studies of Redox Shuttle Overcharge Additive for LiFePO<sub>4</sub>-Based Li-Ion Batteries, *J. Electrochem. Soc.* 112 (2005) 2729–2735. <https://doi.org/10.1149/1.1896327>.
- [25] J.E. Baur, R.M. Wightman, Diffusion coefficients determined with microelectrodes, *J. Electroanal. Chem.* 305 (1991) 73–81. [https://doi.org/10.1016/0022-0728\(91\)85203-2](https://doi.org/10.1016/0022-0728(91)85203-2).
- [26] A.K. Padhi, K.S. Nanjundaswamy, J.B. Goodenough, Phospho-olivines as positive-electrode materials for rechargeable lithium batteries, *J. Electrochem. Soc.* (1997). <https://doi.org/10.1149/1.1837571>.
- [27] L.-X. Yuan, Z.-H. Wang, W.-X. Zhang, X.-L. Hu, J.-T. Chen, Y.-H. Huang, J.B. Goodenough, Development and challenges of LiFePO<sub>4</sub> cathode material for lithium-ion batteries, *Energy Environ. Sci.* 4 (2011) 269–284. <https://doi.org/10.1039/C0EE00029A>.
- [28] J. Luo, A. Sam, B. Hu, C. DeBruler, X. Wei, W. Wang, T.L. Liu, Unraveling pH dependent cycling stability of ferricyanide/ferrocyanide in redox flow batteries, *Nano Energy*. 42 (2017) 215–221. <https://doi.org/10.1016/j.nanoen.2017.10.057>.
- [29] D. Lepage, F. Sobh, C. Kuss, G. Liang, S.B. Schougaard, Delithiation kinetics study of carbon coated and carbon free LiFePO<sub>4</sub>, *J. Power Sources*. 256 (2014) 61–65. <https://doi.org/10.1016/j.jpowsour.2013.12.054>.
- [30] G. Zubi, R. Dufo-López, M. Carvalho, G. Pasaoglu, The lithium-ion battery: State of the art and future perspectives, *Renew. Sustain. Energy Rev.* 89 (2018) 292–308.

<https://doi.org/10.1016/j.rser.2018.03.002>.

- [31] K. Gong, Q. Fang, S. Gu, S.F.Y. Li, Y. Yan, Nonaqueous redox-flow batteries: organic solvents, supporting electrolytes, and redox pairs, *Energy Environ. Sci.* 8 (2015) 3515–3530. <https://doi.org/10.1039/C5EE02341F>.
- [32] J. Luo, B. Hu, C. Debruler, Y. Bi, Y. Zhao, B. Yuan, M. Hu, W. Wu, T.L. Liu, Unprecedented Capacity and Stability of Ammonium Ferrocyanide Catholyte in pH Neutral Aqueous Redox Flow Batteries, *Joule.* 3 (2019) 149–163. <https://doi.org/10.1016/j.joule.2018.10.010>.
- [33] Y. Chen, M. Zhou, Y. Xia, X. Wang, Y. Liu, Y. Yao, H. Zhang, Y. Li, S. Lu, W. Qin, X. Wu, Q. Wang, A Stable and High-Capacity Redox Targeting-Based Electrolyte for Aqueous Flow Batteries, *Joule.* 3 (2019) 2255–2267. <https://doi.org/10.1016/j.joule.2019.06.007>.
- [34] M. Gaberscek, R. Dominko, J. Jamnik, Is small particle size more important than carbon coating? An example study on LiFePO<sub>4</sub> cathodes, *Electrochem. Commun.* 9 (2007) 2778–2783. <https://doi.org/10.1016/j.elecom.2007.09.020>.
- [35] N. Ravet, M. Gauthier, K. Zaghbi, J.B. Goodenough, A. Mauger, F. Gendron, C.M. Julien, Mechanism of the Fe<sup>3+</sup> reduction at low temperature for LiFePO<sub>4</sub> synthesis from a polymeric additive, *Chem. Mater.* 19 (2007) 2595–2602. <https://doi.org/10.1021/cm070485r>.
- [36] W.C. Navidi, *Statistics for engineers and scientists*, McGraw-Hill Higher Education New York, NY, USA, 2008.
- [37] J.B. Rawlings, J.G. Ekerdt, *Chemical reactor analysis and design fundamentals*, Nob Hill

Pub, Llc, 2002.

- [38] R. Malik, A. Abdellahi, G. Ceder, A Critical Review of the Li Insertion Mechanisms in LiFePO<sub>4</sub> Electrodes, *J. Electrochem. Soc.* 160 (2013) A3179–A3197. <https://doi.org/10.1149/2.029305jes>.
- [39] L. Hong, L. Li, Y.K. Chen-Wiegart, J. Wang, K. Xiang, L. Gan, W. Li, F. Meng, F. Wang, J. Wang, Y.M. Chiang, S. Jin, M. Tang, Two-dimensional lithium diffusion behavior and probable hybrid phase transformation kinetics in olivine lithium iron phosphate, *Nat. Commun.* 8 (2017). <https://doi.org/10.1038/s41467-017-01315-8>.
- [40] V. Srinivasan, J. Newman, Existence of Path-Dependence in the LiFePO<sub>4</sub> Electrode, *Electrochem. Solid-State Lett.* 9 (2006) A110. <https://doi.org/10.1149/1.2159299>.
- [41] G. Oyama, Y. Yamada, R.I. Natsui, S.I. Nishimura, A. Yamada, Kinetics of nucleation and growth in two-phase electrochemical reaction of Li<sub>x</sub>FePO<sub>4</sub>, *J. Phys. Chem. C.* 116 (2012) 7306–7311. <https://doi.org/10.1021/jp300085n>.
- [42] K. Xiang, K. Yang, W.C. Carter, M. Tang, Y.M. Chiang, Mesoscopic Phase Transition Kinetics in Secondary Particles of Electrode-Active Materials in Lithium-Ion Batteries, *Chem. Mater.* (2018). <https://doi.org/10.1021/acs.chemmater.7b05407>.
- [43] K. Tang, X. Yu, J. Sun, H. Li, X. Huang, Kinetic analysis on LiFePO<sub>4</sub> thin films by CV, GITT, and EIS, *Electrochim. Acta.* 56 (2011) 4869–4875. <https://doi.org/10.1016/j.electacta.2011.02.119>.
- [44] S.J. Huang, B.G. Huang, F.S. Pai, Fast charge strategy based on the characterization and evaluation of LiFePO<sub>4</sub> batteries, *IEEE Trans. Power Electron.* 28 (2013) 1555–1562.

<https://doi.org/10.1109/TPEL.2012.2209184>.

- [45] J.P. Robinson, J.J. Ruppert, H. Dong, G.M. Koenig, Sintered electrode full cells for high energy density lithium-ion batteries, *J. Appl. Electrochem.* 48 (2018) 1297–1304. <https://doi.org/10.1007/s10800-018-1242-y>.
- [46] Z. Nie, S. Ong, D.S. Hussey, J.M. Lamanna, D.L. Jacobson, G.M. Koenig, Probing transport limitations in thick sintered battery electrodes with neutron imaging, *Mol. Syst. Des. Eng.* 5 (2020) 245–256. <https://doi.org/10.1039/c9me00084d>.
- [47] A. Lyngfelt, Chemical Looping Combustion: Status and Development Challenges, *Energy and Fuels.* 34 (2020) 9077–9093. <https://doi.org/10.1021/acs.energyfuels.0c01454>.
- [48] C. Kuss, M. Carmant-Dérival, N.D. Trinh, G. Liang, S.B. Schougaard, Kinetics of heterosite iron phosphate lithiation by chemical reduction, *J. Phys. Chem. C.* 118 (2014) 19524–19528. <https://doi.org/10.1021/jp502346f>.

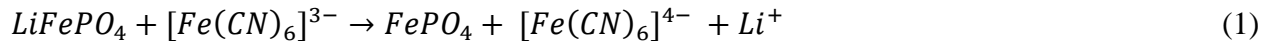
## **Chapter V. Neutron Tomography of Chemical Redox Progression of Lithium-Ion Solid Electroactive Material**

### ***5.1 Overview***

In this chapter, the progress of redox-targeting reaction between  $\text{LiFePO}_4$  and  $[\text{Fe}(\text{CN})_6]^{3-}$  in a packed bed reactor (PBR) is assessed using neutron tomography. Here, the PBR design and aliquot evaluation is similar to Chapter IV. The effects of particle size and pore distribution of the degree of delithiation are qualitatively assessed by aligning neutron and X-ray tomographs. In this chapter, preliminary data is discussed and a manuscript with the elements of this chapter is in preparation. This is the first time where chemical redox of lithium-ion solid electroactive material was characterized via neutron imaging.

## 5.2 Introduction

In the previous chapter, packed bed reactor (PBR) setup made up of  $\text{LiFePO}_4$  (LFP) particles as the chemical reservoir for the RTFB, which underwent chemical oxidation by  $[\text{Fe}(\text{CN})_6]^{3-}$  (FeCN) as the redox shuttle was examined. The reaction between LFP and FeCN occurs as shown below:



By changing several design variables, it was observed that for same amount of  $[\text{Fe}(\text{CN})_6]^{3-}$  flown through, the molar conversion of LFP is linearly dependent upon the bed-height. That is, for the same moles of FeCN shuttle flown through in a randomly packed bed made of sintered LFP particles, the moles of LFP converted increases if the bed-height (and thereby the amount of LFP) increases. This poses the question of the nature of delithiation occurring in the PBR. That is, are there radial and linear functionalities to the delithiation process and, how does the pore and particle distribution affect the delithiation process. Advanced tools and methods would be needed to determine that.

Neutron imaging is a non-destructive technique that has been successful in characterizing Li-ion batteries [1–3]. This is due to the interaction properties of the neutrons with light nuclei such as  $H$  or  $Li$  that greatly scatter neutrons. This property makes neutron radiography a powerful technique to qualitatively map the spatiotemporal variations in Li-ion in the LFP PBR at different stages of chemical oxidation. 3D tomographs reconstructed from neutron radiographs would give us the ability to locate regions of high versus low reactivity. However, since our PBR consists of pores and particles in the range  $10^0 - 10^3 \mu\text{m}$  (Appendix C, Figure C9 and C10), the neutron imaging resolution ( $43.4 \mu\text{m}$ ) is limited to larger particle aggregates and pores. Hence, neutron computed tomographs (NCTs) were complemented with x-ray computed tomography (XCT) which has a

higher resolution of 16  $\mu\text{m}$  to gain further insights to pore/particle size relationships to delithiation in LFP PBR[4,5].

In this work, by using an electrochemical technique to monitor the reactor effluent and conversion of FeCN to  $[\text{Fe}(\text{CN})_6]^{4-}$ , the overall conversion of LFP in the PBR could be tracked. Thus, it was possible to run nominally identical PBR experiments while stopping the reaction (by stopping the redox shuttle feed to the reactor) after overall conversions of the LFP material in the PBR to FP of ~25%, 50%, 75%, and 100%. At ambient temperatures, the lithiation/delithiation in LFP occurs via the two-phase formation of the form  $(\text{LiFe}^{2+}\text{PO}_4)_x - (\text{Fe}^{3+}\text{PO}_4)_{1-x}$ , instead of a solid solution of the form  $\text{Li}_x\text{Fe}^{2+x}\text{Fe}^{3+_{1-x}}\text{PO}_4$ , for  $0 \leq x \leq 1$ . Therefore, a 50% delithiated PBR column in theory would contain 50% LFP and 50% FP particles. For the sake of simplicity, a terminology of LFP-X would be used in this study, where X is the percentage of LFP in the PBR (assuming 100-X is constituted by FP). Therefore, reaction progression of 25% would indicate that 25% of LFP has been delithiated, and the sample PBR would be referred to as LFP-75.

### ***5.3 Experimental***

Packed bed columns (L= 12 mm, diameter= 10 mm) were filled with sintered then pulverized LFP particles supported by Teflon frits. Details of the reactor setup can be found in Section 4.4.2.3. A schematic for the reaction setup is shown in Figure 1 a). The reaction progress in the PBR were monitored using cyclic voltammetry (CV) of the aliquots (Figure 1 b), similar to Section 4.4.2.4. The concentration of FeCN was calculated from the CVs using Randles-Sevcik equation, which was then correlated to the LFP conversion in the PBR. Post-reaction capsules LFP-25, LFP-50, LFP-75 were dried and analyzed along with two baseline samples, LFP-100 and LFP-0 at the CG-1D neutron imaging beamline at the High Flux Isotope Reactor (HFIR) at Oak Ridge National

Laboratory (ORNL)[6]. The neutron beamline setup at CG-1D is shown in Figure 1c. The details of XCT setup are similar to Section 4.4.2.5. Image processing and analysis of NCTs and XCTs were performed using Amira Avizo software.

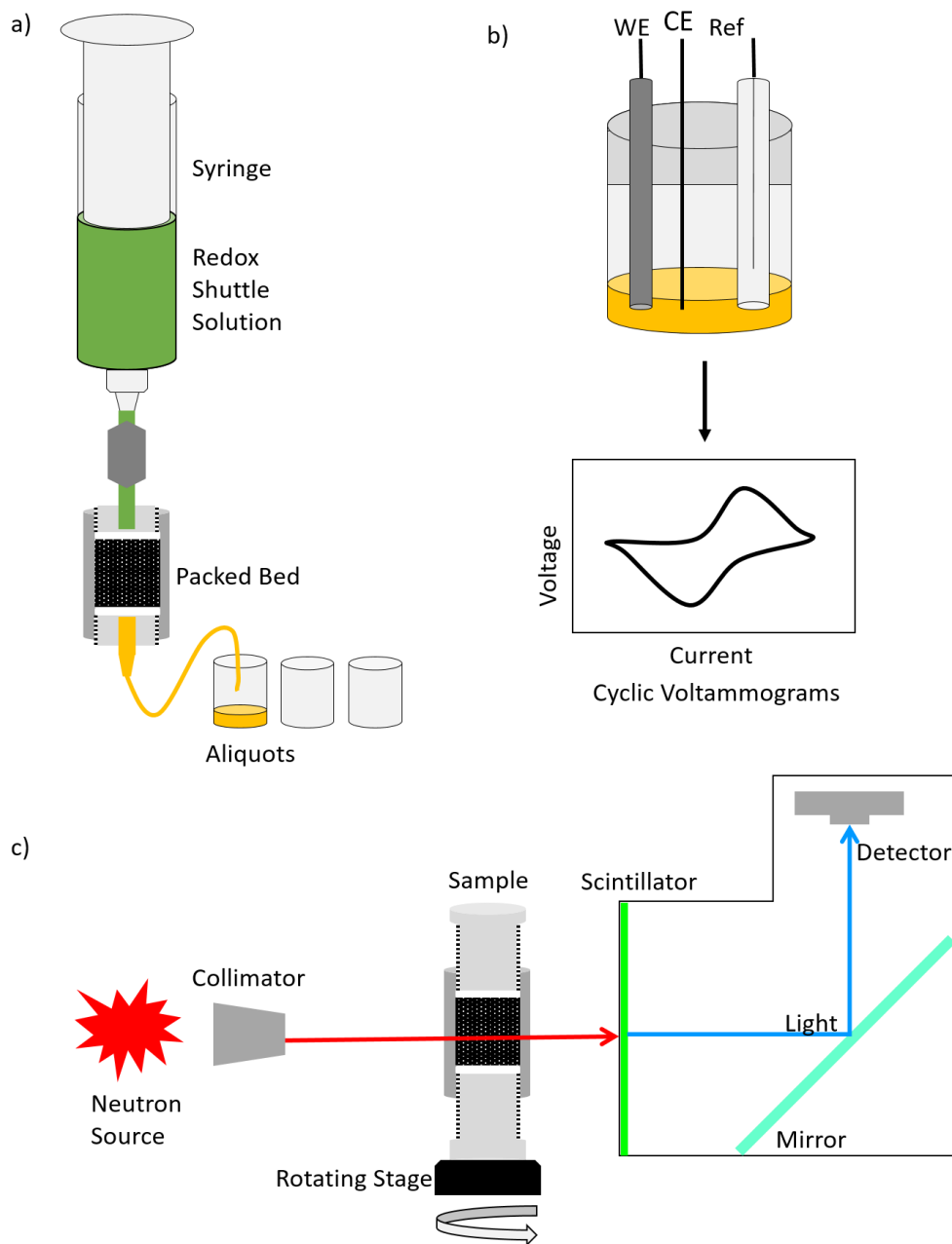


**Figure 1. Schematic of a) PBR setup, b) three-electrode cells used for CVs of aliquots, and c) CG-1D neutron imaging beamline at HFIR, ORNL. The objects are not drawn to scale and are for illustration only.**

#### ***5.4 Preliminary Results***

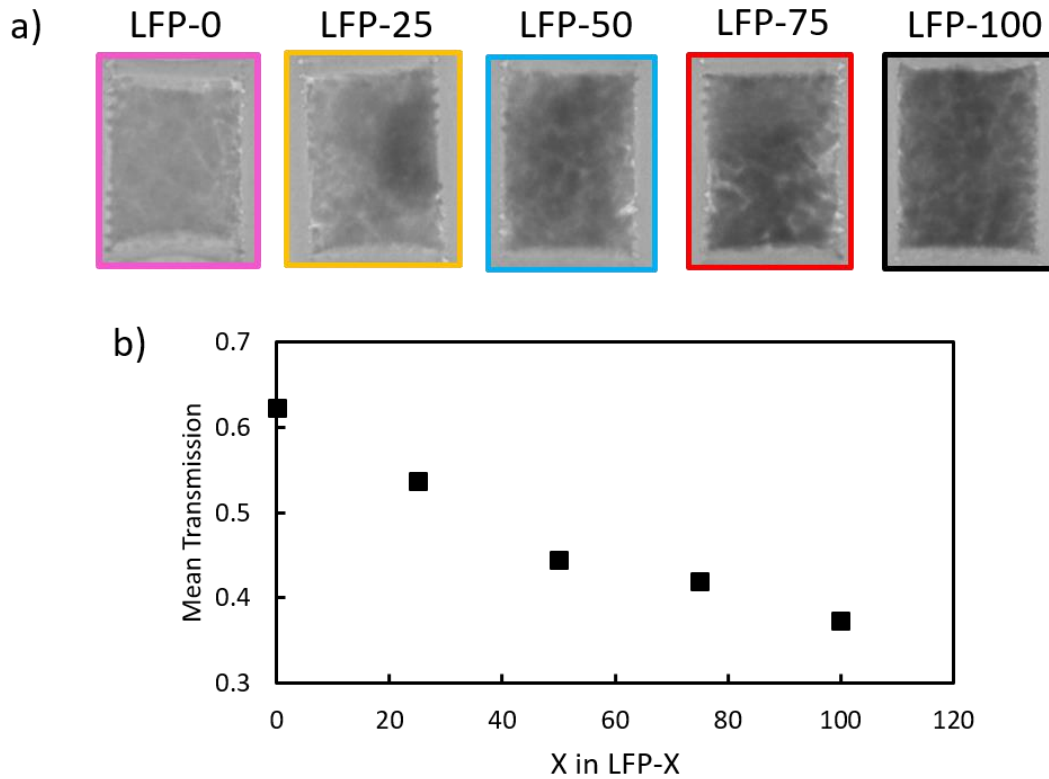
In this study, progress of reaction (1) in the PBR at different stages of chemical redox is visualized by the contrast obtained from the strong neutron radiography scattering by  $\text{Li}^+$ . Neutron radiography measures the attenuation of the neutron beam resulting from the adsorption and scattering by the atoms in a sample of uniform thickness, as governed by Beer-Lambert's law-

$$I(\lambda) = I_0(\lambda)e^{-\mu(\lambda)\Delta x} \quad (2)$$

Where,  $\lambda$  is the wavelength with incident,  $I_0$  and transmitted,  $I$  intensities.  $\Delta x$  is the thickness of the samples and  $\mu$  is the attenuation coefficient given by-

$$\mu(\lambda) = \frac{\sigma_t(\lambda)(\rho N_A)}{M} \quad (3)$$

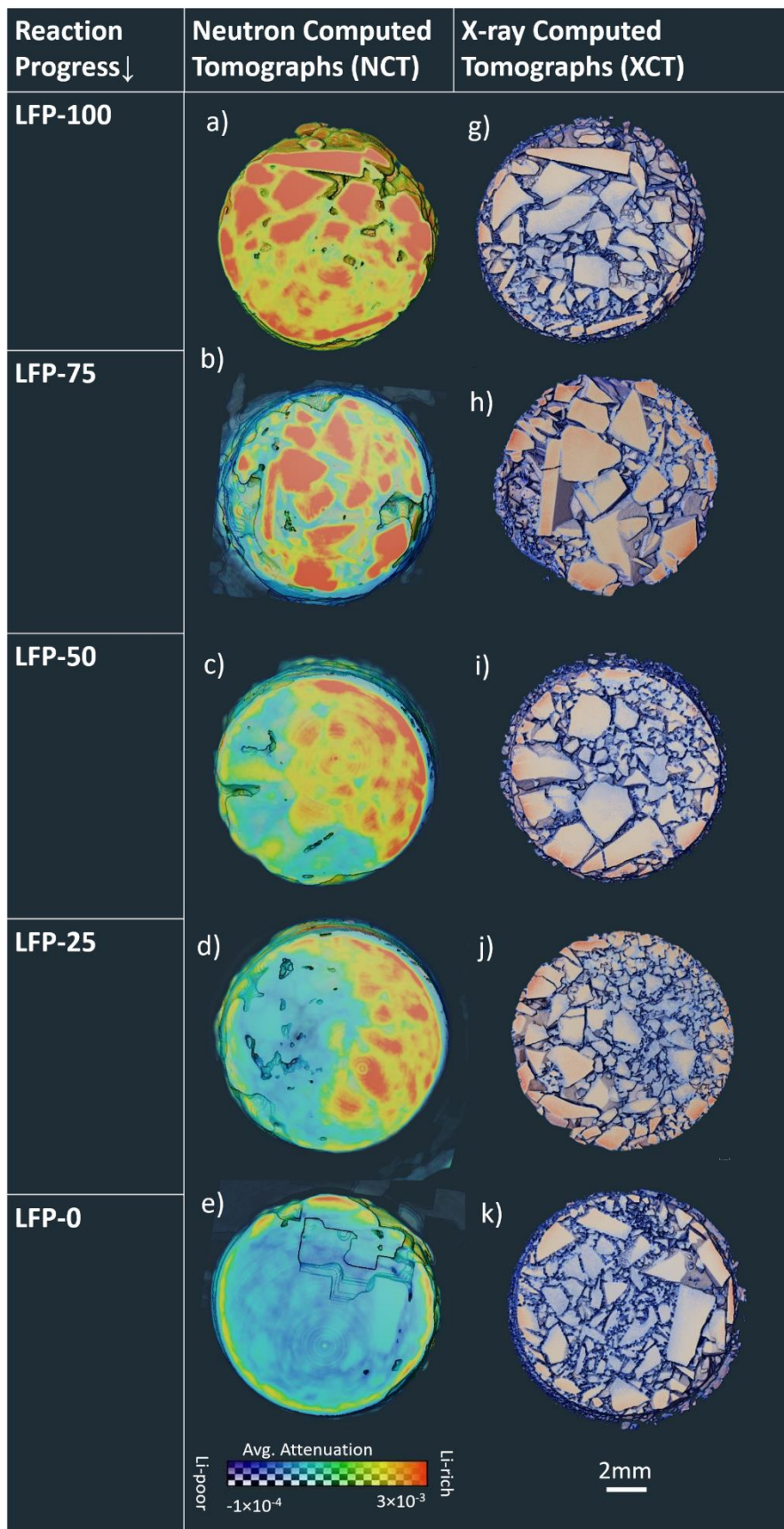
Where,  $\sigma_t(\lambda)$  is the cross-section for neutrons of the material with density  $\rho$ .  $N_A$  is Avogadro's number and  $M$  is molar mass. Equation (2) and (3) can be extended to heterogeneous and irregular thickness samples, such as ours for neutron radiography.



**Figure 2. a) Normalized radiographs at five stages of chemical oxidation of LFP PBR by FeCN. b) Mean transmission of neutron beam versus percentage of LFP in the PBR.**

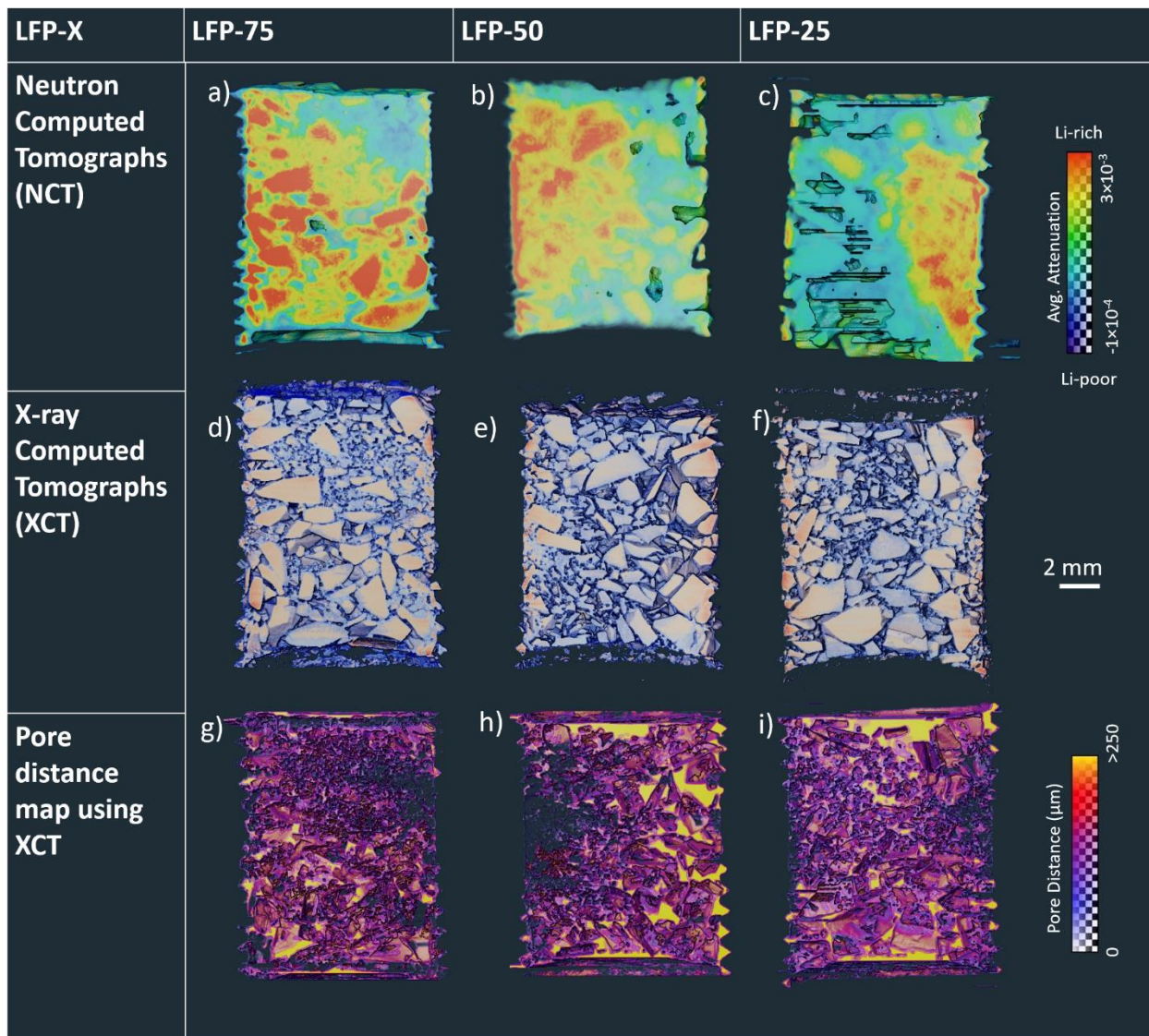
Due to the fundamental nature of neutron interaction with particles as described by equation (2) and (3), LFP shows great sensitivity to the Li-ion concentration when exposed to a neutron beam[7]. In Figure 2, neutron radiographs of five samples with incremental degrees of delithiation are shown. The mean transmission of neutrons is normalized to the cylindrical sample, and is found to be linearly dependent upon Li-ion concentration in the sample ( $R^2= 95.6\%$ ), with LFP-100 and LFP-0 (no lithium) as the highest and lowest scattering samples. However, in 2 a) LFP-25 shows heterogeneity in transmission which can be correlated to Li-ion concentration. Such features, along with local variations were studied using reconstructed NCTs as seen in Figure 3 a)-e) and Figure 4 a)-c).

Figure 3 shows radial cross-sections midway across the lengths of the PBR samples, aligned for NCTs and XCTs. The average attenuation of the neutron beam by the LFP particles is represented by prismatic color scheme in Figure 3 a)-e), with bright reds and oranges correlating to regions of Li-rich concentrations and blues and violets being Li-poor zones. Therefore, as expected there is an immense contrast in attenuation between LFP-100 and LFP-0, with near homogeneity of Li-ion concentration in the two samples. LFP-75, LFP-50, and LFP-25 on the other hand show substantial heterogeneity with Li-rich and Li-poor zones. However, the Li-ion concentration does not appear to have a radial dependence in LFP-75, LFP-50, and LFP-25. There is an observed dependence of Li-ion concentration on aggregate size for LFP-100 and LFP-75. This could be due to the fact that secondary particle agglomerates in mm range are more densely packed internally when compared to the dispersed micron sized aggregates. Hence, the attenuation in mm range particles is higher at the core of the particles. Interestingly, regions of larger particle aggregates in LFP-50 and LFP-25 do not exhibit higher attenuation. Instead, the dispersed smaller aggregates in LFP- 50 and LFP-25 appear to have high attenuation, and therefore Li-rich concentration. Hence, it is inferred that particle size alone does not determine the degree of delithiation in the samples.



**Figure 3. 3D reconstructed NCTs (left) and XCTs (right) radial cross-sections of LFP PBR. On the left, (a-e) average attenuation of neutron beam is represented by the contrast between the particles (refer to color scale on the left). On the right (g-k), aligned XCT images show LFP aggregates. Note that the color scheme on the right for XCTs is for illustration purposes only.**

Random distribution of LFP aggregates in the PBR can be understood in terms of the surrounding pores. Hence, the local packing of LFP particles in the could be extrapolated from the distance between the pores in the 3D volume. In Figure 4., linear cross-sections along the center of LFP PBR for LFP-75, LFP-50, and LFP-25 as NCTs (a-c), XCT (d-f), and pore distance maps (g-i) are shown.



**Figure 4.** 3D reconstructed cross sections along the length of the reacted LFP PBRs – the top row are NCTs (a-c), the middle row are XCTs (d-f), and the bottom row are distance maps of pores (g-i). The color scales for top and bottom row represent avg. attenuation of the neutron beam, and the distance between pores, respectively. The color scheme used for XCTs (d-f) is for illustration purposes only.

At 25% delithiation (LFP-75, Figure 4 a), smaller sized particles seem to be delithiated first as evidenced by aligned XCT images (Figure 4 d). However, the reaction seems to have occurred

more at the beginning ( $z = 0$ ) instead of towards the end ( $z = L$ ) of PBR. This is expected as particles near  $z = 0$  would come in contact with higher concentration of FeCN than toward  $z=L$ . As the electrolyte solution flows down along the bed height, reaction 1 would propagate and reactant shuttle would deplete. However, along with directionality, an interplay of particle size and pore arrangements appear to be playing a role in the degree of delithiation of LFP PBR. The top 2 mm in LFP 75 (Figure 4 a and d) are comprised of mm sized aggregates at the leftmost and rightmost corner of PBR, with the center being smaller sub-mm particles. However, the reaction has proceeded at a higher amount on the right, demonstrated by lower attenuation in that region. This could be due to the specific flow pattern of the redox shuttle containing electrolyte dictated by the particle arrangements. This effect is accentuated in LFP-50 (Figure 4 b, e, and h) and LFP-25 (Figure 4 c, f, and i) where interconnected networks of small pores ( $<10 \mu\text{m}$ ) render a condensed packing of particles in Li-rich regions. The convective transport limitations rendered by impenetrable regions or dead zones later resulted in reaction heterogeneity for LFP-50 and LFP-25.

## ***5.5 Conclusions***

Chemical oxidation progression in LFP PBR designed for redox-targeting batteries was mapped using neutron tomography, which showed sensitivity to local Li-ion concentration. NCTs were supported by XCTs to correlate particle and pore size distributions to degree of delithiation in LFP PBR. The random packing of LFP particles, along with aggregate size are observed to impact degree of delithiation, inferred from the attenuation contrast in separate regions. More analysis of the data is needed to shed light upon the reaction mechanism in this system.

## 5.6 References

- [1] Z. Nie, S. Ong, D.S. Hussey, J.M. Lamanna, D.L. Jacobson, G.M. Koenig, Probing transport limitations in thick sintered battery electrodes with neutron imaging, *Mol. Syst. Des. Eng.* 5 (2020) 245–256. <https://doi.org/10.1039/c9me00084d>.
- [2] Z. Nie, P. McCormack, H.Z. Bilheux, J.C. Bilheux, J.P. Robinson, J. Nanda, G.M. Koenig, Probing lithiation and delithiation of thick sintered lithium-ion battery electrodes with neutron imaging, *J. Power Sources.* 419 (2019) 127–136. <https://doi.org/10.1016/j.jpowsour.2019.02.075>.
- [3] J.B. Siegel, X. Lin, A.G. Stefanopoulou, D. Gorsich, Neutron imaging of lithium concentration in battery pouch cells, *Proc. Am. Control Conf.* (2011) 376–381. <https://doi.org/10.1109/acc.2011.5990883>.
- [4] R.F. Ziesche, T. Arlt, D.P. Finegan, T.M.M. Heenan, A. Tengattini, D. Baum, N. Kardjilov, H. Markötter, I. Manke, W. Kockelmann, D.J.L. Brett, P.R. Shearing, 4D imaging of lithium-batteries using correlative neutron and X-ray tomography with a virtual unrolling technique, *Nat. Commun.* 11 (2020) 1–11. <https://doi.org/10.1038/s41467-019-13943-3>.
- [5] J.M. LaManna, D.S. Hussey, E.M. Baltic, D.L. Jacobson, Improving material identification by combining x-ray and neutron tomography, 1039104 (2017) 3. <https://doi.org/10.1117/12.2274443>.
- [6] L. Santodonato, H. Bilheux, B. Bailey, J. Bilheux, P. Nguyen, A. Tremsin, D. Selby, L. Walker, The CG-1D Neutron Imaging Beamline at the Oak Ridge National Laboratory High Flux Isotope Reactor, *Phys. Procedia.* 69 (2015) 104–108. <https://doi.org/10.1016/j.phpro.2015.07.015>.

- [7] N. Sharma, D.H. Yu, Y. Zhu, Y. Wu, V.K. Peterson, In operando neutron diffraction study of the temperature and current rate-dependent phase evolution of LiFePO<sub>4</sub> in a commercial battery, *J. Power Sources.* 342 (2017) 562–569. <https://doi.org/10.1016/j.jpowsour.2016.12.048>.

## Chapter VI. Future Work

Several research prospects arise from the research presented in this dissertation. The future work and recommendations are outlined below-

### *1) Redox shuttles*

1 a) Based on the experimental evidence seen in Chapter IV, concentration of redox shuttles is the strongest factor dictating the rate of reaction. Hence, in theory, high solubility redox shuttles should be able to improve the power density of RTFBs by increasing the charge transfer kinetics. Our group has collaborated with Prof. Odom's lab at University of Kentucky to test phenothiazine derivatives as redox shuttles in RTFBs. Phenothiazine derivatives have shown stability at high concentrations (>1 M) in non-aqueous electrolytes, hence making them an interesting choice for redox shuttles in the RTFBs[1,2]. It is possible that at concentrations higher than 1 M redox shuttle, the viscosity of redox shuttles impedes the rate of redox-targeting reactions. Therefore, it is important to optimize the benefits of using high-concentration redox shuttles.

1 b) In Chapter III, it was observed that redox shuttles with a large overpotential difference such as 1,1'-diacetylferrocene (3.76 V vs Li/Li<sup>+</sup>) and 1,1'-dimethylferrocene (3.1 V vs Li/Li<sup>+</sup>) did not improve the kinetics of chemical redox of LiFePO<sub>4</sub>. On the contrary, redox shuttles with smaller overpotential, such as 1,1'-dibromoferrocene (3.55 V vs Li/Li<sup>+</sup>) and potassium ferricyanide (3.52 V vs Li/Li<sup>+</sup>) showed fast kinetics and improved voltaic efficiency during oxidation of LFP. Hence, redox shuttles with an overpotential of ±100 mV should be used to minimize the overpotential loss in RTFBs. Furthermore, redox shuttles with near-identical redox potential to solid electroactive material can perform reversible redox-targeting reactions based on Nernstian potential difference originated by activity changes of redox shuttles during chemical redox in RTFBs[3,4]. The

previous studies on Nernstian-potential difference have shown a solid electroactive material utilization of 95% [4] and therefore, this strategy should be investigated further for chemistries optimized for packed bed reactor configuration.

## **2) *Packed bed reactor***

LFP particles in a packed bed reactor were shown to follow a core-shell mechanism during redox-targeting oxidation (Chapter IV and V). Aligned pores in the direction of flow could, in theory improve the interfacial charge transfer kinetics between redox shuttles and solid electroactive material. Therefore, aggregate particle size/shape effects should be investigated based on the observations and speculation of internal solution phase transport in the aggregates limiting reaction rate

## **3) *in-operando neutron imaging***

In Chapter V, the spatiotemporal variation of Li-ion concentrations in a packed bed reactor at various stages of chemical oxidation were mapped using neutron tomography. This approach, paired with high resolution x-ray computed tomography provided fundamental insights towards particle size and pore distribution affecting the reaction propagation in RTFB systems. The knowledge towards designing packed bed reactors for large scale RTFBs can be further complemented by analyzing *in-operando* Li-ion variation in RTFBs undergoing chemical redox. Coupled with computational modeling including packed bed reactor equations and fluid dynamics, *in-operando* Li-ion variation would enable modeling of RTFB chemical redox.

## **4) *Full-cell RTFB***

A natural progression would be to design a full-cell RTFB based on packed-bed reactor design. However, it would require addressing the following challenges-

4a) In a full-cell RTFB, the charge storage capacity of solid electroactive material in the chemical reservoir would far exceed the charge storage capacity of redox shuttles. The volume of redox shuttles is thereby limited to less than the combined volume of voids in porous electrodes in electrochemical cell, circulation tubes, and voids in chemical reservoir.

4b) The overall battery performance is a function of charge-transfer kinetics in the chemical reservoir between solid electroactive material and redox shuttles, and across the membrane. An ideal membrane would have ideal ion-selectivity that can prevent crossover of redox shuttles, chemical stability, and mechanical robustness for long cycle life.

Therefore, it is imperative to design a full cell RTFB that addresses a) the optimum volumetric ratio of solid electroactive material and redox shuttles, and b) an ion-exchange membrane that can support RTFB cell performance at high rates of charge/discharge.

## References-

- [1] J.D. Milshtein, A.P. Kaur, M.D. Casselman, J.A. Kowalski, S. Modekrutti, P.L. Zhang, N. Harsha Attanayake, C.F. Elliott, S.R. Parkin, C. Risko, F.R. Brushett, S.A. Odom, High current density, long duration cycling of soluble organic active species for non-aqueous redox flow batteries, *Energy Environ. Sci.* 9 (2016) 3531–3543. <https://doi.org/10.1039/c6ee02027e>.
- [2] J.A. Kowalski, M.D. Casselman, A.P. Kaur, J.D. Milshtein, C.F. Elliott, S. Modekrutti, N.H. Attanayake, N. Zhang, S.R. Parkin, C. Risko, F.R. Brushett, S.A. Odom, A stable two-electron-donating phenothiazine for application in nonaqueous redox flow batteries, *J. Mater. Chem. A* 5 (2017) 24371–24379. <https://doi.org/10.1039/c7ta05883g>.
- [3] J.F. Vivo-Vilches, A. Nadeina, N. Rahbani, V. Seznec, D. Larcher, E. Baudrin, LiFePO<sub>4</sub>-ferri/ferrocyanide redox targeting aqueous posolyte: Set-up, efficiency and kinetics, *J. Power Sources* 488 (2021) 229387. <https://doi.org/10.1016/j.jpowsour.2020.229387>.
- [4] M. Zhou, Q. Huang, L. Fan, Q. Wang, M. Zhou, Q. Huang, T. Nguyen, P. Truong, J. Ghilane, Y.G. Zhu, Nernstian-Potential-Driven Redox-Targeting Reactions of Battery Materials Nernstian-Potential-Driven Redox-Targeting Reactions of Battery Materials, *CHEMPR* 3 (n.d.) 1036–1049. <https://doi.org/10.1016/j.chempr.2017.10.003>.

## Acknowledgements

It is bittersweet for me to have reached the end of my graduate school journey. I was fortunate to meet incredible mentors, collaborators, and friends during my time at the University of Virginia (UVA). My graduate school experience was extremely positive and I am very grateful to these people for everything they have provided for me.

First, I would like to extend my deepest gratitude to my thesis advisor Prof. Gary Koenig for his mentorship and guidance. Through him, I learned critical thinking, scientific integrity, resilience, and humility. He gave me the freedom to explore multiple ways to solve problems while still providing guidance and structure to my research. Along with helping me become an independent researcher, Prof. Koenig has helped me develop my communication skills by enabling me to present my work to audiences of varying expertise. Through these experiences, I have learned the importance of scientific communication to peers as well as public and my confidence in public speaking has vastly improved. I have appreciated the opportunity to work with the talented and supportive members of Koenig lab: Dr. Zhaoxiang (Colin) Qi, Dr. Pierce Robinson, Ethan Paharik, Dr. Hongxu (Spring) Dong, Dr. Linxiao Geng, Ziyang Nie, Patrick MacCormack, Chen Cai, and Jing Wang. Every member of the group has helped me in some way in developing as a scientist ranging from stimulating scientific discussions, talks at various conferences, help with setting experiments, and guidance through struggles in graduate school, making the lab environment positive and productive. I also had great pleasure working with my collaborators: Dr. Yuxuan Zhang, Dr. Hassina Bilheaux, Dr. Jean-Christoph Bilheaux, Dr. Aman Preet Kaur, and Prof. Susan Odom. I would also like to thank my thesis committee members: Prof. Roseanne Ford, Prof. Robert Davis, Prof. Charles Machan, and Prof. Geoffrey Geise. All of them have provided

invaluable feedback towards experimental design and data interpretation that has helped me develop my scientific approach.

Next, I would like to thank the National Science Foundation (NSF) for providing a steady source of funding throughout my time at UVA that allowed me to pursue my research. I would like to acknowledge the assistance of the School of Engineering and Applied Sciences (SEAS) and the Office of Graduate and Postdoctoral affairs at UVA for offering professional development courses that have helped me improve my communication, programming, and networking skills.

I would like to extend my sincere thanks to my amazing classmates that later turned into some of my best friends. My time at UVA would have been very different if it were not for these people. My gratitude goes out to Erica Hui, Katelyn Dagnall, Naomi Miyake, and Dr. Lucy Yoon for their love and friendship in the past five years. They were the first to show up to celebrate my smallest victories and stand by me during the biggest hardships. I would like to thank Dr. Hongxi Luo for his resilience and scientific ingenuity, and Dr. Luke Huelsenbeck, for his kindness and optimism, that have inspired me to become a better scientist and a person. I am thankful to Dr. Kevin Gu, Dr. Kevin Chang, Dr. Lucas Kimerer, Joey Roberts, Xueying Zhao, and Dr. Saring Agata for being the talented, hardworking, and fun individuals that they are, and being my friends during the ebbs and flows of the past five years. I also wish to thank my many friends outside of my class, especially Dr. Alex Chen and Preetha Saha for their support in navigating the course of my PhD and helping me adjust to a new country.

I would like to dedicate this entire endeavor to my parents, Dharmendra and Asha Gupta. It is fair to say that while growing up, I could not have even dreamed of being accepted to the upper echelons of education, let alone graduating with a PhD. I am eternally indebted to the sacrifices and the courage of my parents who did not allow societal and financial pressures obstruct

my pursuit of knowledge in any way. I am also grateful to my undergraduate advisors: Prof. Praveen Meduri, Prof. Chandra Sekhar Sharma, and Prof. Dayadeep Monder for introducing me to the field of energy storage and encouraging me to pursue higher education.

Finally, I am grateful to my partner, Brian Dregne who has been my source for strength and love. His unrelenting support and profound belief in my abilities has helped me overcome many professional challenges during my PhD. In addition, he introduced me to our three guinea pigs- Fermin, Chikoo, and Cappie – who are adorable and were a source of comfort after long hours at lab.

## Appendix A

**Table A1.** ICP-OES data for purchased LFP and FP prepared by oxidation with hydrogen peroxide. Fe and Li concentrations are those from the solution of the dissolved solid that was analyzed in the instrument.

Compound	Fe (mg/ml)	Li (mg/ml)	Molar Ratio (Li:Fe)
LiFePO <sub>4</sub> (LFP)	3.308	0.425	1.034
FePO <sub>4</sub> (FP)	3.27	0.015	0.039

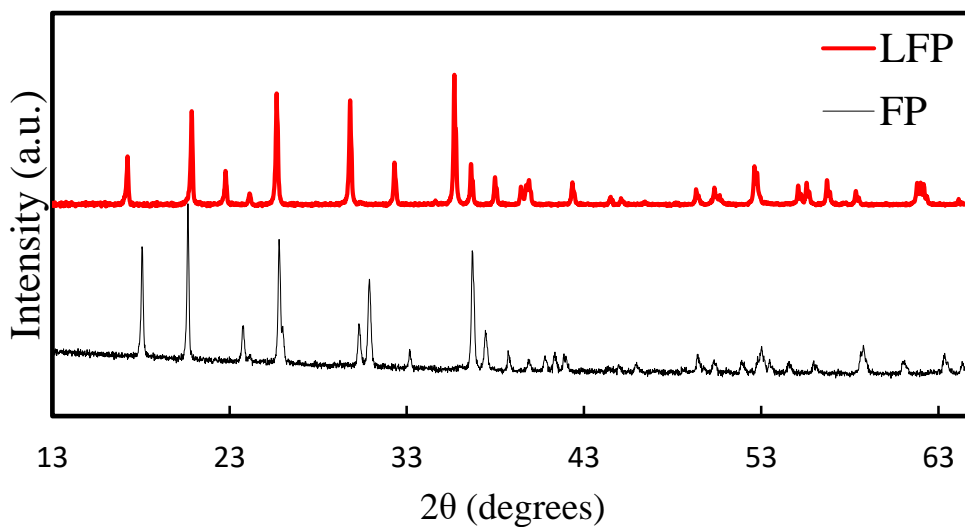
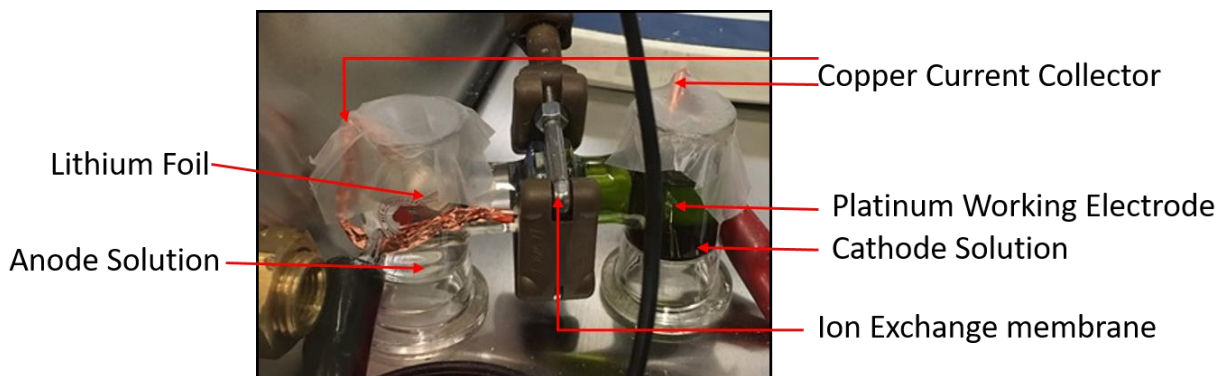


**Figure A1.** X-ray diffraction curves of LFP received from supplier (red) and delithiated product (black) of the reaction between 2.4% hydrogen peroxide, 0.1% acetic acid and, LFP.

a)



b)

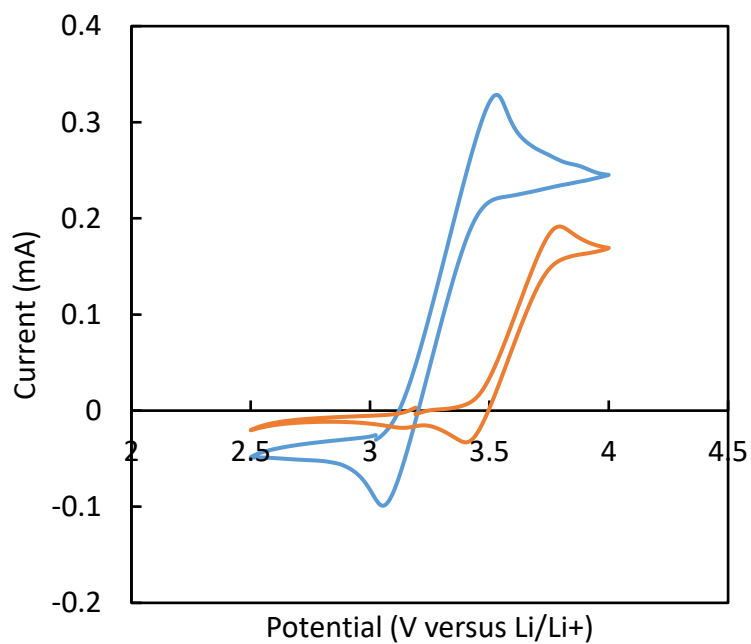


**Figure A2.** a) Photograph of custom glass cell for electrochemical oxidation of FcBr<sub>2</sub> and cyclic voltammetry of redox shuttles. Cell had a platinum wire working electrode and Li foil as both reference and counter electrode. b) Cyclic voltammetry curves for 8 mM Fc (blue) and 2 mM FcBr<sub>2</sub> (orange) using the cell in a).

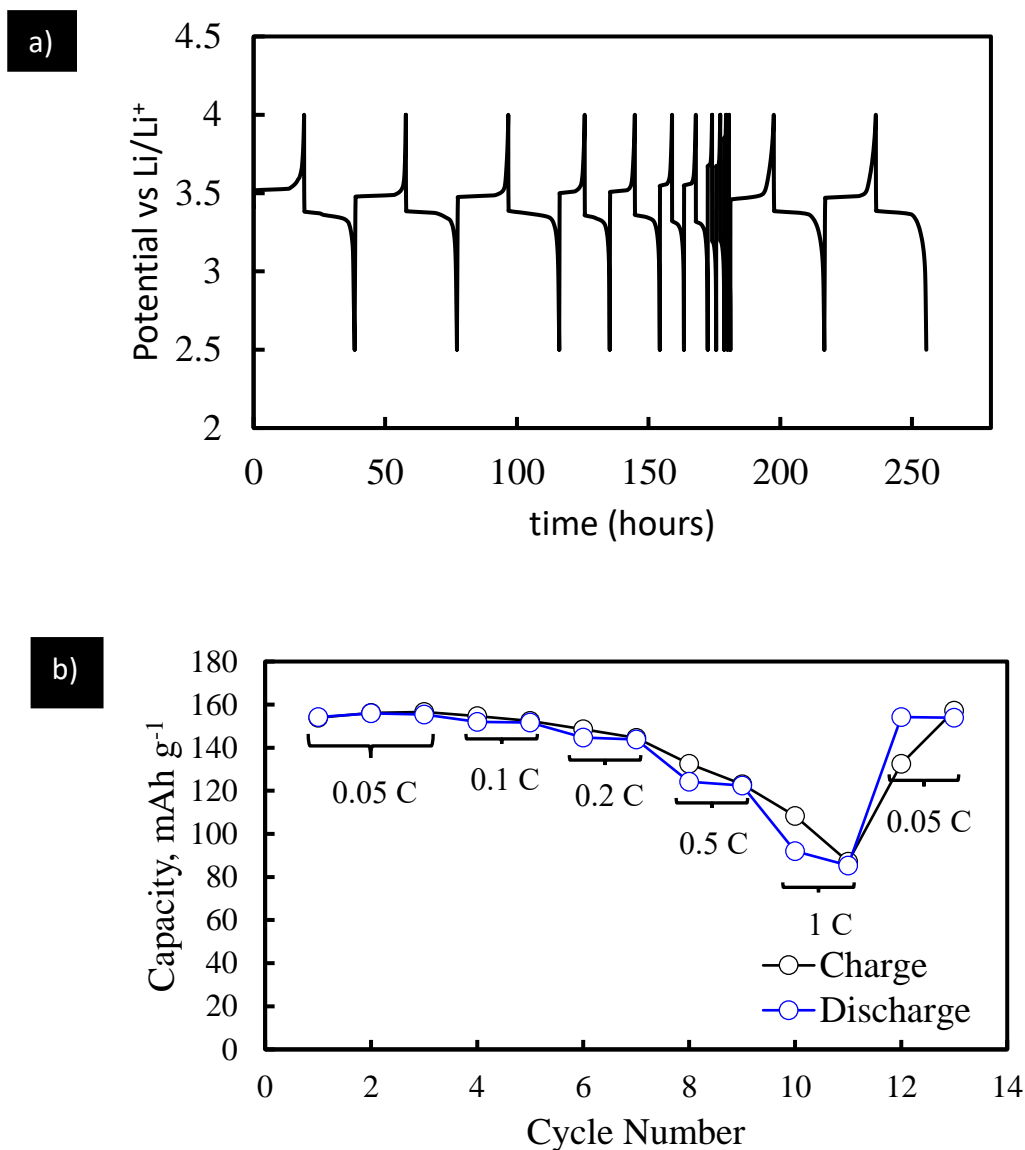


**Figure A3.** Rate capability testing of coin cells with LFP cathodes at room temperature: a) Voltage versus time and, b) capacity at different rates of charge/discharge. The cathode contained a ratio by weight of 80:10:10 LFP: carbon black: PVDF binder and was 70  $\mu\text{m}$  thick. The anode was lithium metal foil. All charge and discharge cycles were conducted at the same rate and as indicated in b). 1C was assumed to correspond to 160  $\text{mA g}^{-1}$  LFP.

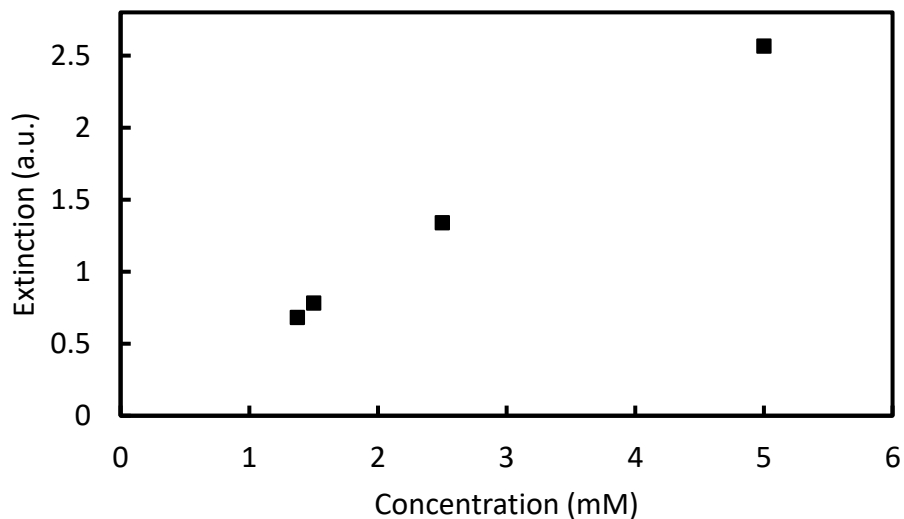


**Figure A4.** UV-Vis extinction at 705 nm for different concentration of  $\text{FcBr}_2^+$  in the carbonate solvent electrolyte used in this study. The extinction values at these  $\text{FcBr}_2^+$  concentrations were exclusive of solid LFP particles.

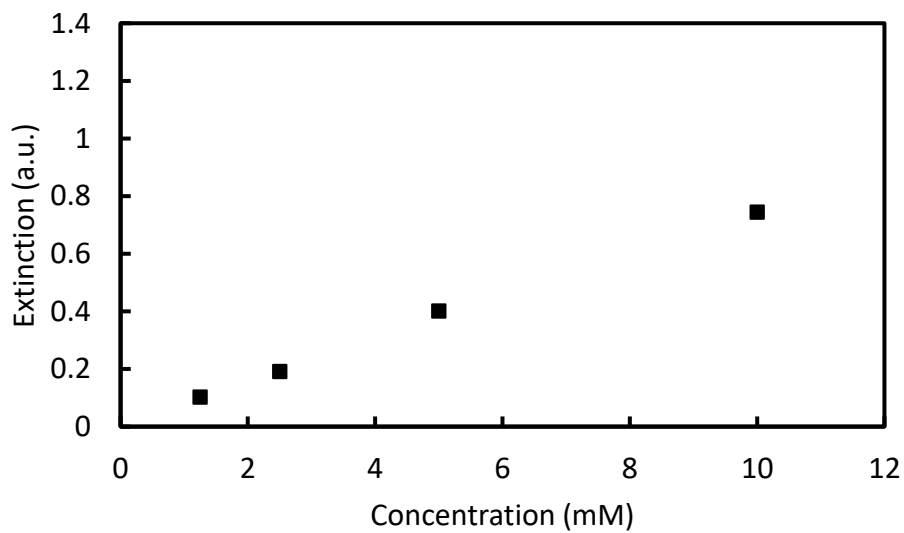


**Figure A5.** UV-Vis extinction at 615 nm for different concentration of  $\text{Fc}^+$  in the carbonate solvent electrolyte used in this study. The extinction values at these  $\text{Fc}^+$  concentrations were exclusive of solid FP particles.

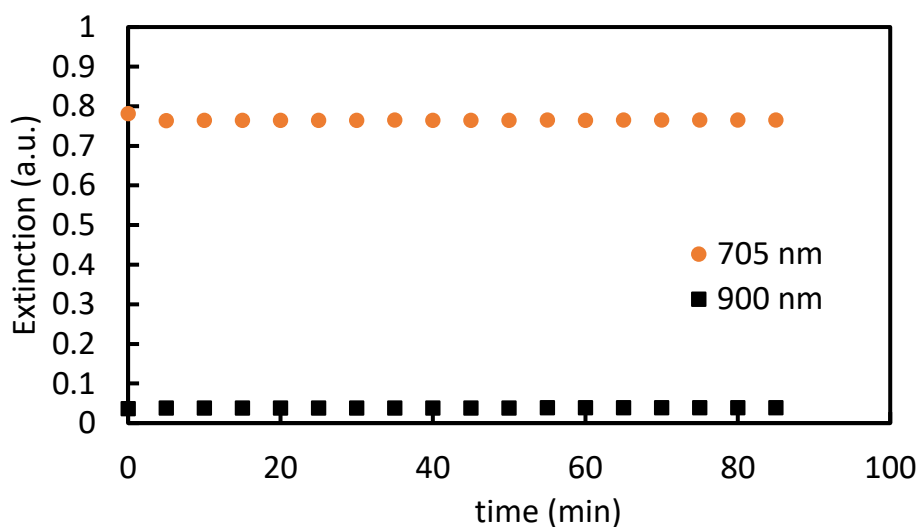


**Figure A6.** Stability of 2 mM  $\text{FcBr}_2^+$  solution in electrolyte at  $45^\circ\text{C}$ . The UV-Visible extinction at the peak wavelength of 705 nm (orange circles) associated with  $\text{FcBr}_2^+$  was monitored over a period of 90 minutes. The decrease in absorbance at 705 nm when adjusted for the extinction at a reference wavelength of 900 nm (black squares) was determined to be 2% reduction of  $\text{FcBr}_2^+$  in the electrolyte.

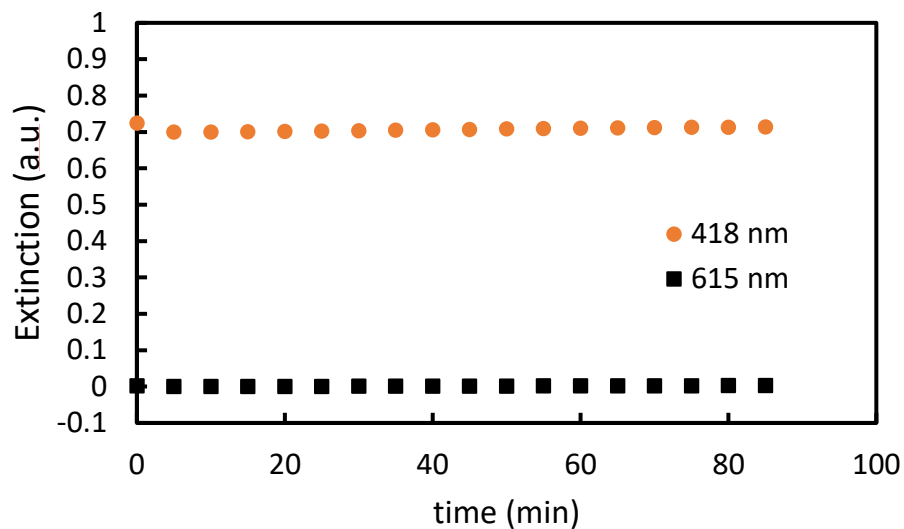
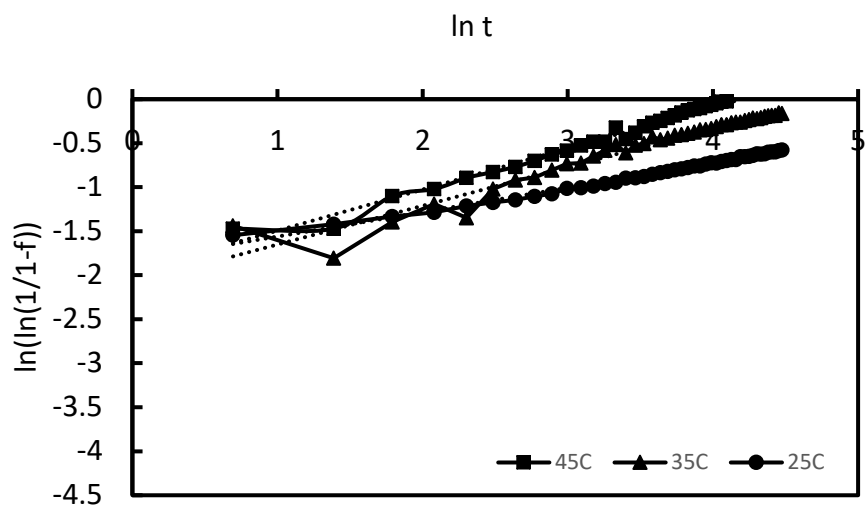


**Figure A7:** Stability of 8 mM Fc solution in electrolyte at 45<sup>0</sup>C. The UV-Visible extinction at the peak wavelength of 615 nm (black squares) associated with Fc<sup>+</sup> was monitored over a period of 90 minutes. The change in absorbance at 615 nm when adjusted for the extinction at a reference wavelength of 418 nm (orange circles) was determined to be 0.3% oxidation of Fc in the electrolyte.

a)



b)

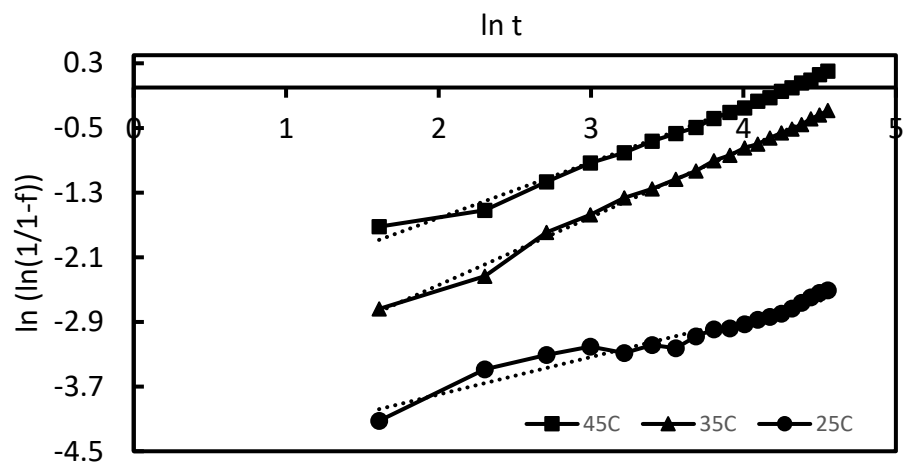


**Figure A8:**  $\log(\log(-(1-f)))$  vs  $\log t$  curves where  $f$  is conversion and  $t$  is time for a) chemical oxidation of LFP and b) chemical reduction of FP, at 25 °C (black circles), 35 °C (black triangles), and 45 °C (black squares). Dashed lines represent linear fits of the data.

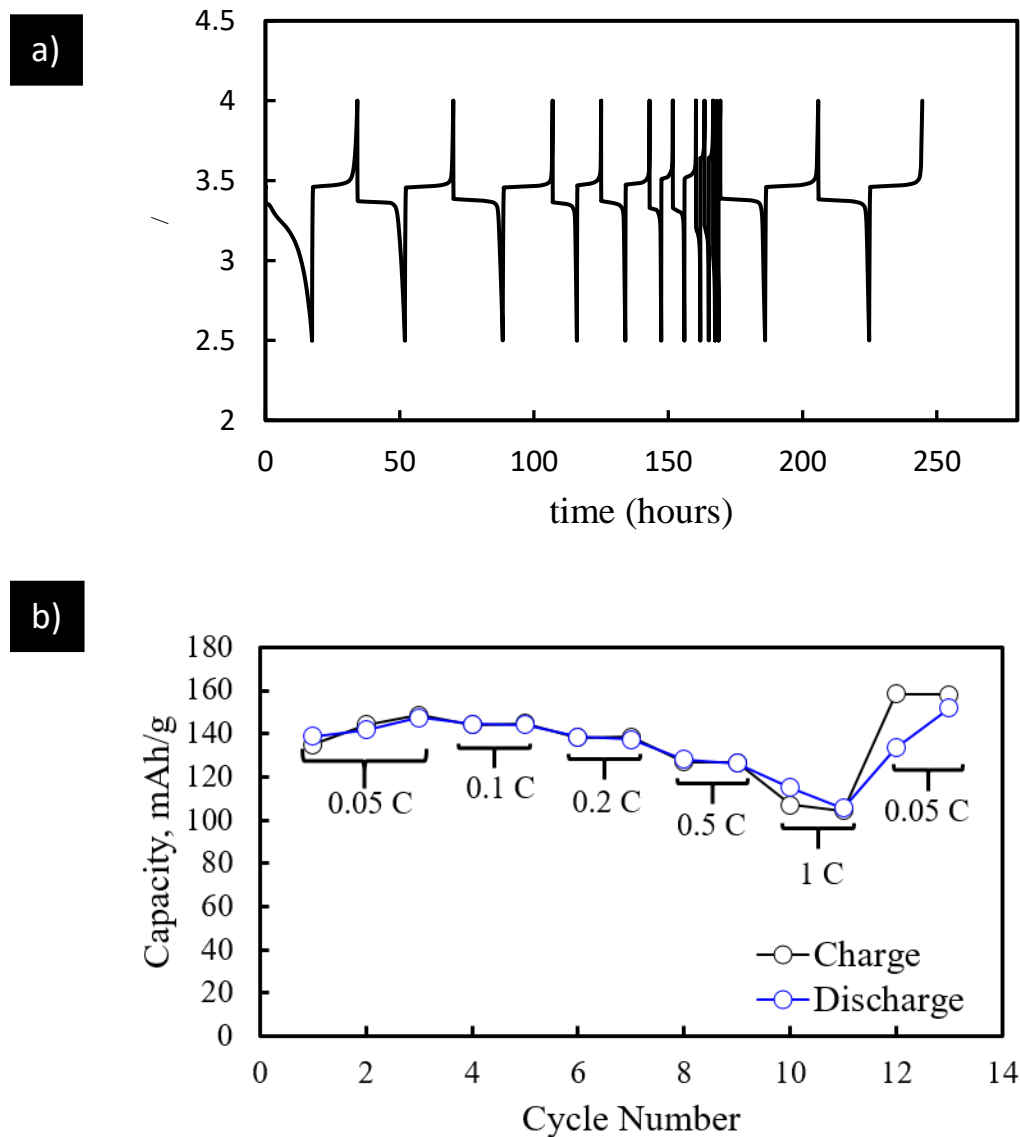
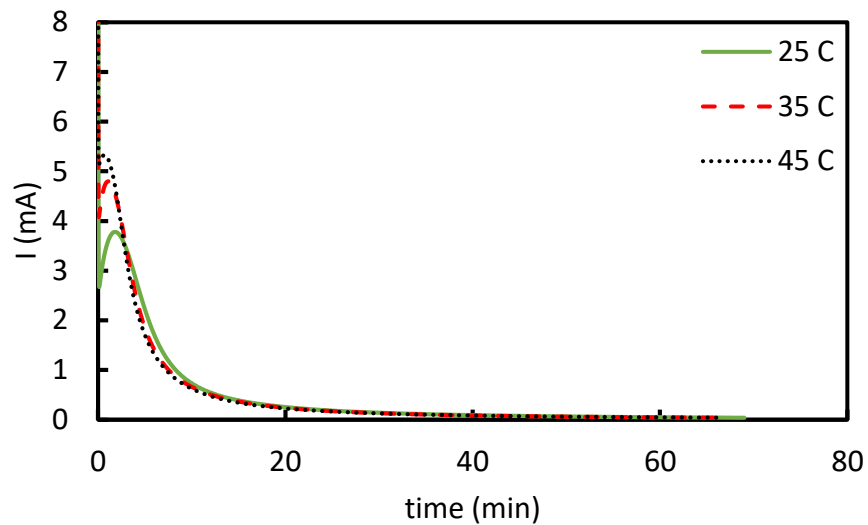


**Figure A9.** Rate capability testing of coin cells at room temperature with cathodes containing active material which was FP produced by oxidation of LFP with  $H_2O_2$ : a) Voltage versus time and, b) Capacity at different rates of charge/discharge. The cathode contained a ratio by weight of 80:10:10 FP: carbon black: PVDF binder and was  $70 \mu m$  thick. The anode was lithium metal foil. All charge and discharge cycles were conducted at the same rate and as indicated in b). 1C was assumed to correspond to  $160 \text{ mA g}^{-1}$  LFP.

a)



b)

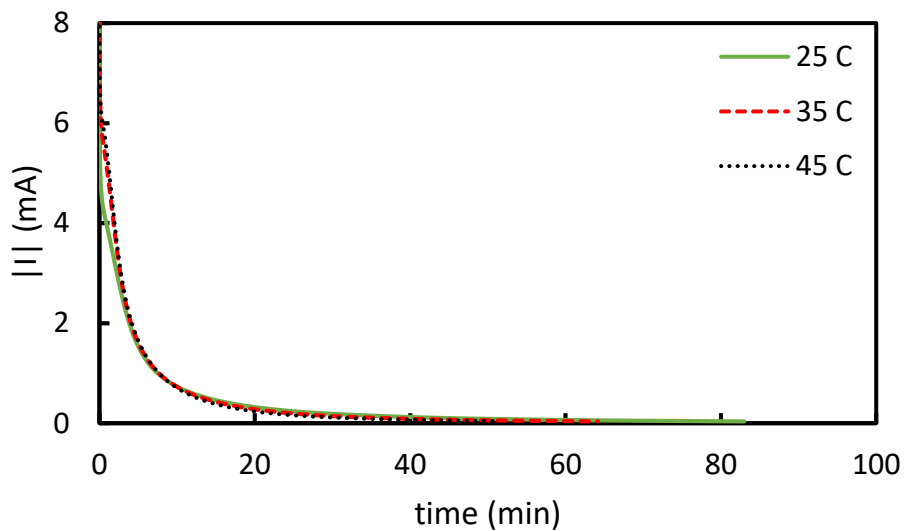
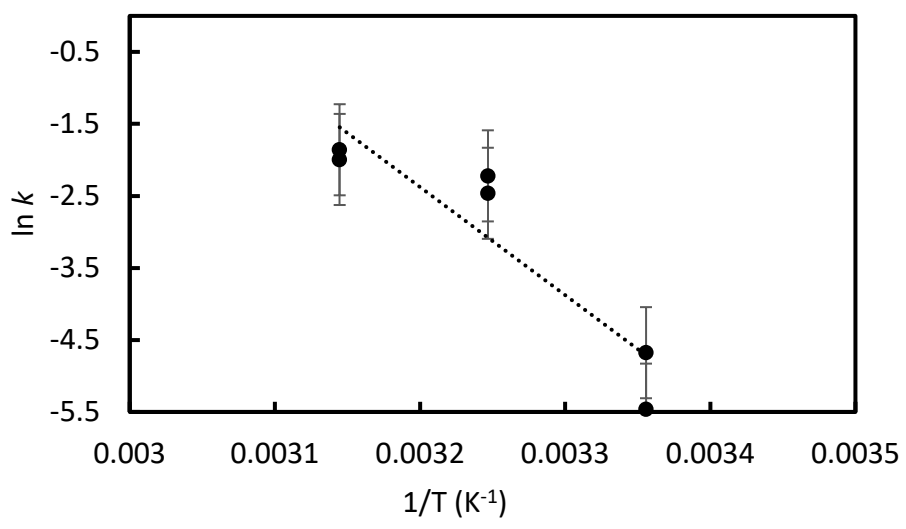
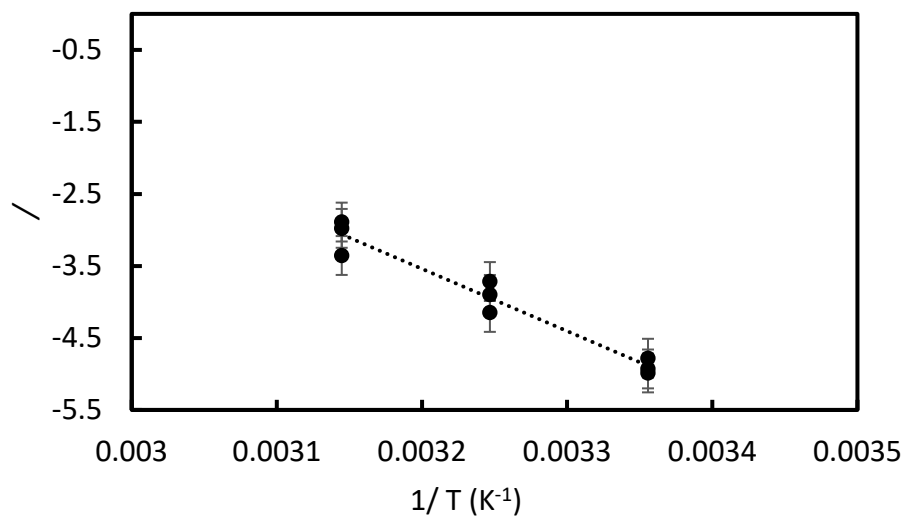


**Figure A10.** Chronoamperometry of Li/LFP coin cells under conditions of a) oxidation of LFP at 3.6 V (vs. Li/Li<sup>+</sup>) and b) reduction of FP at 3.3 V (vs. Li/Li<sup>+</sup>). Experiments were conducted at 25 °C (green solid line), 35 °C (red dashed line), and 45 °C (black dashed line).

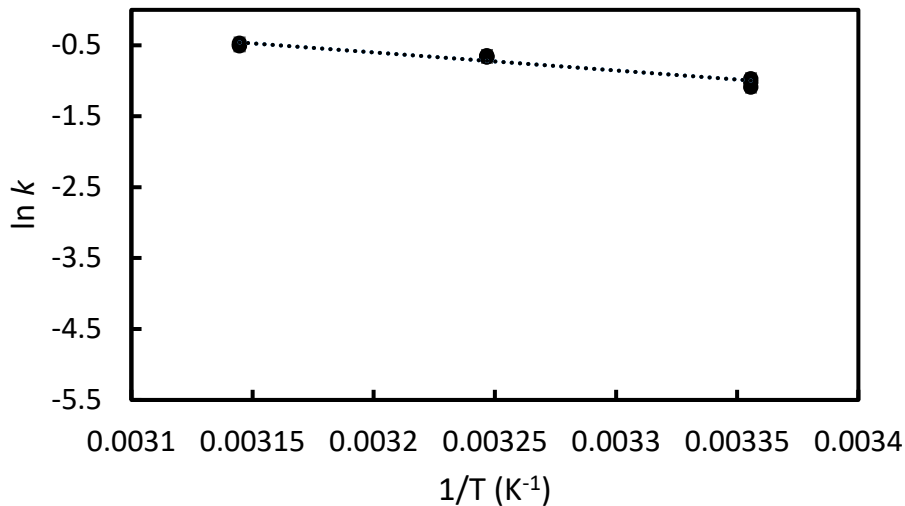
a)



b)



c)



d)

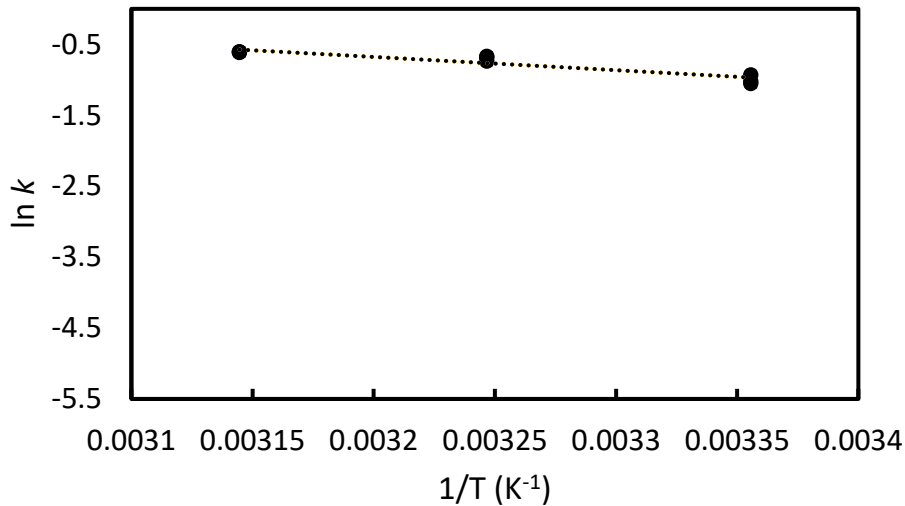


**Figure A11.** Plots of the ln of the first order rate constant as a function of the inverse temperature (in °K) for a) chemical oxidation of LFP, b) chemical reduction of FP, c) electrochemical oxidation of LFP and, d) electrochemical reduction of FP. Error bars represent the sample standard deviation of 3 measurements. In cases where error bars are not evident, the error bars are smaller than the size of the data points. Dashed lines represent linear regression lines of best fit.

## Appendix B

This section provides additional information for Chapter III.

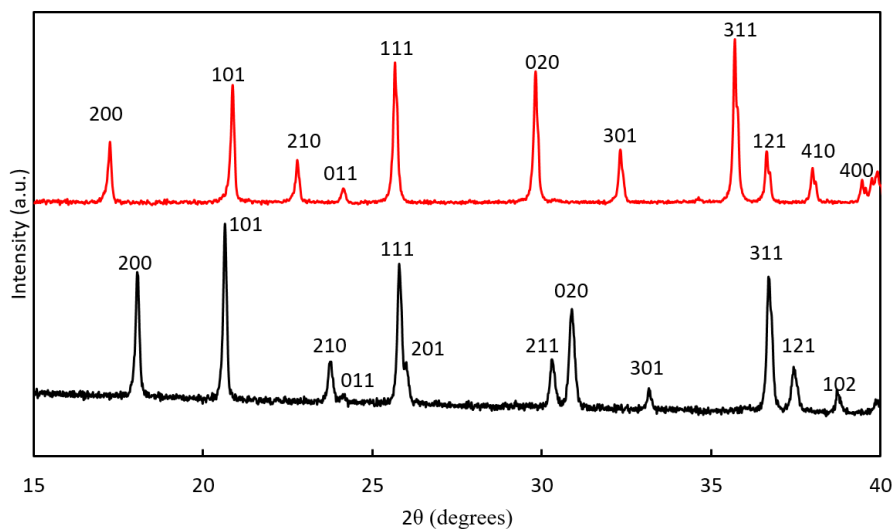


**Figure B1.** X-ray diffraction patterns of LiFePO<sub>4</sub> (LFP) received from supplier (red) and the delithiated FePO<sub>4</sub> (FP) product (black) after reaction of the LFP with 2.4% (vol) hydrogen peroxide and 0.1% (vol) acetic acid. Patterns were consistent with PDF- 01-078-7908 for LFP and PDF- 04-017-0610 for FP.

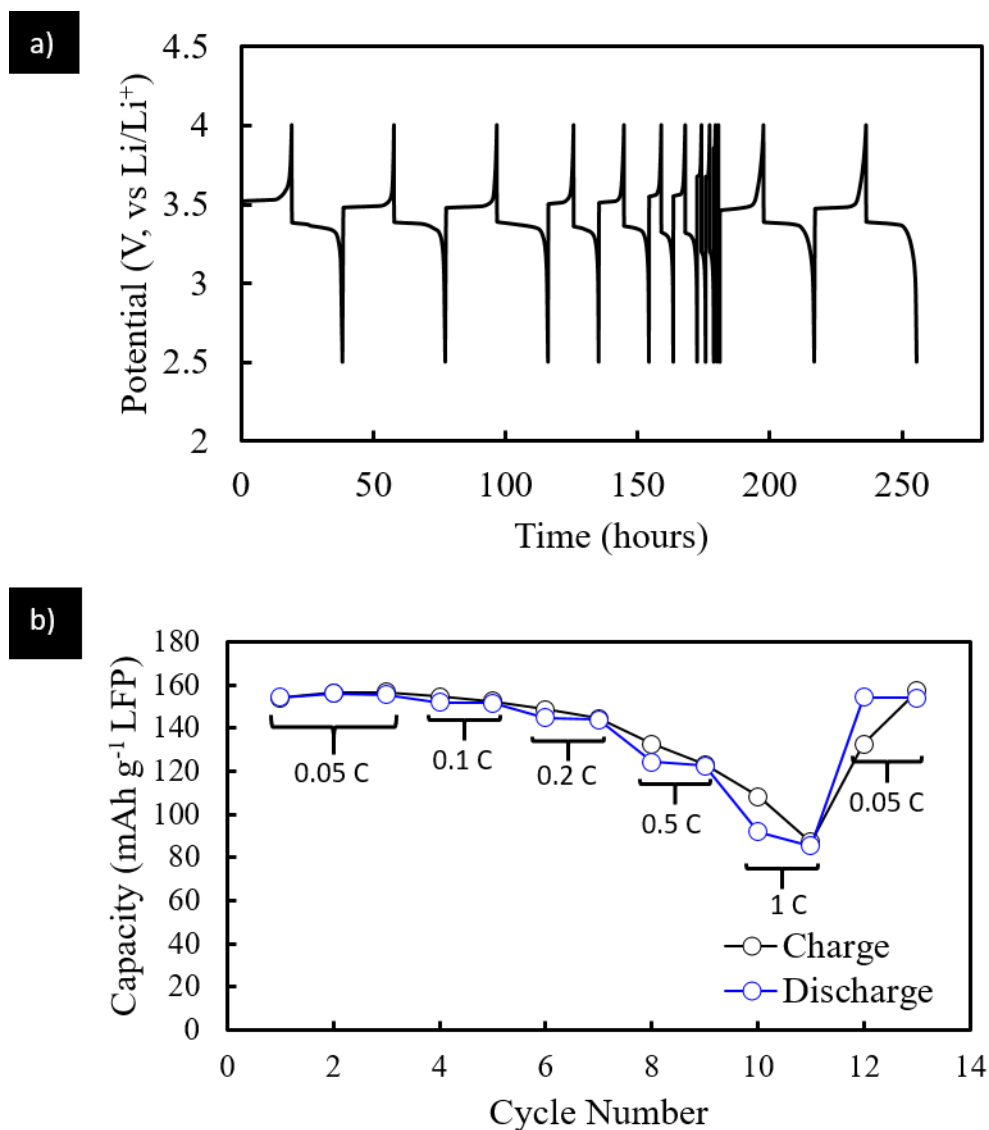


**Figure B2.** Rate capability testing of coin cells with LFP cathodes (LFP used as received) at room temperature: a) Voltage versus time and b) capacity at different rates of charge/discharge. The cathode contained a ratio by weight of 80:10:10 LFP:carbon black:binder and was  $\sim 70 \mu\text{m}$  thick. The anode was Li metal foil. All charge and discharge cycles were conducted at the same rate and as indicated in b). 1C was assumed to correspond to  $160 \text{ mA g}^{-1} \text{ LFP}$  ( $0.1 \text{ mA cm}^{-2}$ ).

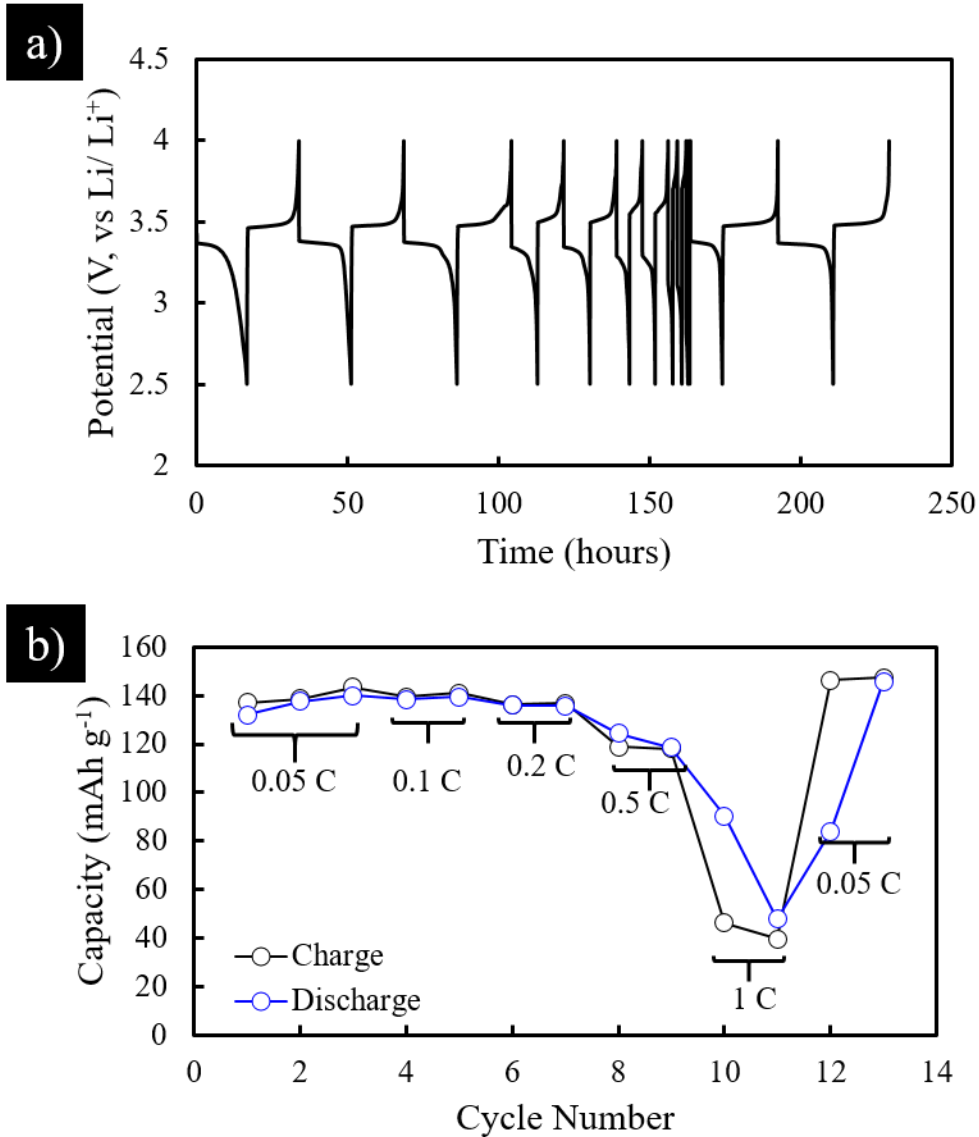


**Figure B3.** Rate capability testing of coin cells at room temperature with cathodes containing active material which was FP produced by oxidation of LFP with H<sub>2</sub>O<sub>2</sub> and acetic acid solution: a) Voltage versus time and b) Capacity at different rates of charge/discharge. The cathode contained a ratio by weight of 80:10:10 FP:carbon black:binder and was ~70 μm thick. The anode was lithium metal foil. All charge and discharge cycles were conducted at the same rate and as indicated in b). 1C was assumed to correspond to 160 mA g<sup>-1</sup> LFP (0.1 mA cm<sup>-2</sup>).

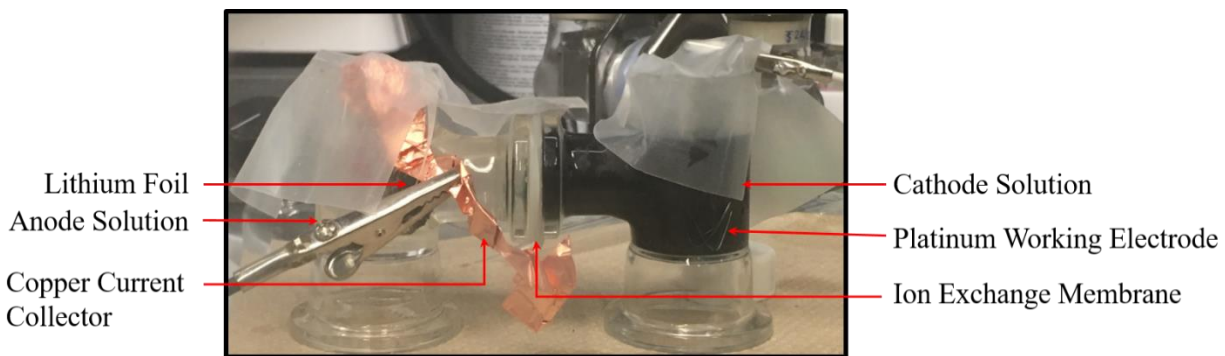


**Figure B4.** Photograph of custom glass cell for electrochemical oxidation and cyclic voltammetry of redox shuttles. The cell had a platinum wire working electrode, Li foil as both reference and counter electrode, and Nafion/PVDF composite ion exchange membrane.

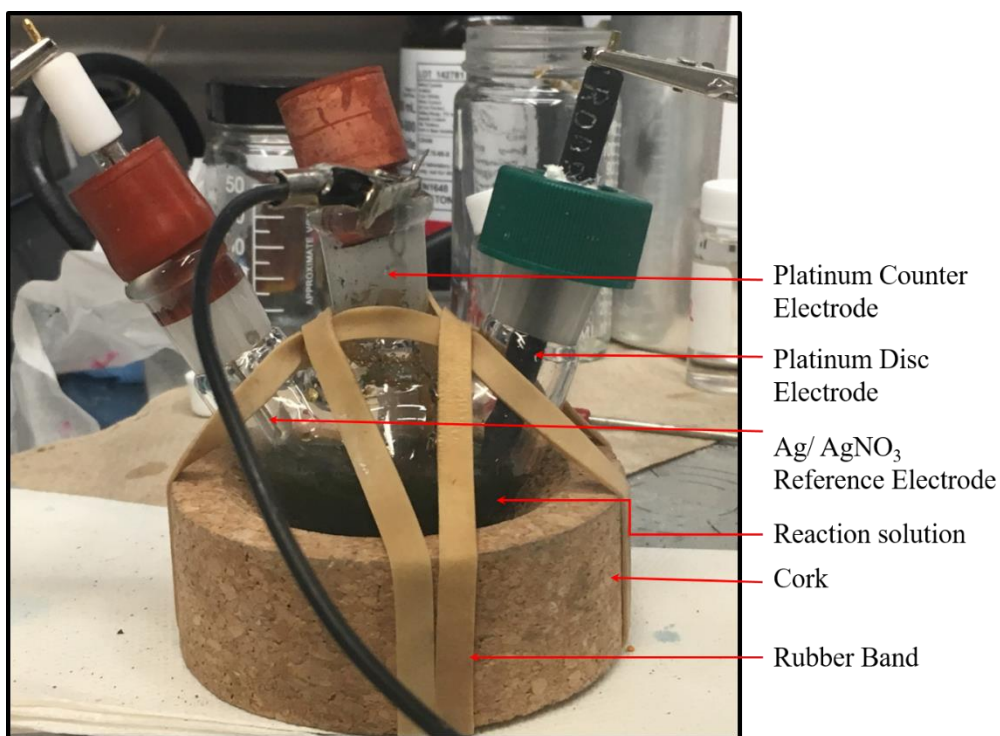


**Figure B5.** Photograph of three electrode reaction cell setup.

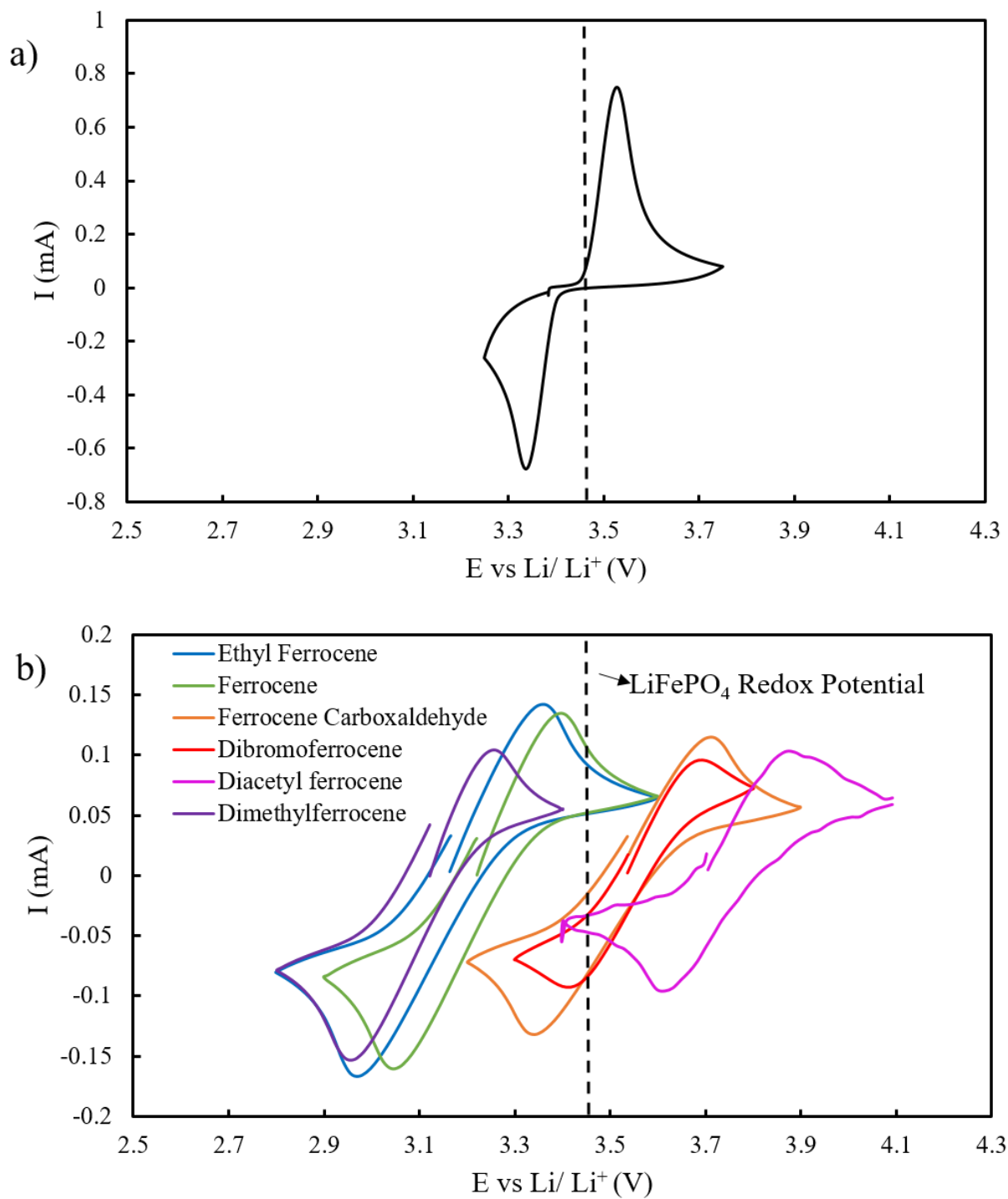


**Figure B6.** Cyclic voltammetry (CV) of a) LFP coin cell, and b) 100 mM redox shuttles dissolved in electrolyte solutions. The CV plots in b) were collected using 50/50 blends with regards to

molarity of the oxidized and reduced form of the redox shuttles. The CV sweep rates were 0.1 mV s<sup>-1</sup> for a) and 100 mV s<sup>-1</sup> for b).

### **Randles-Sevcik equation**

The Randles-Sevcik equation was used to measure the concentration of redox shuttle species as a function of time in the batch reactor<sup>1</sup>. CV sweeps were continuously run at constant sweep rate, and peak currents were extracted as a function of time. The Randles-Sevcik equation is:

$$i_p = 0.4463nFAC \left( \frac{nFD}{RT} \nu \right)^{0.5} \quad (1)$$

where  $i_p$  is the peak current in amperes,  $n$  is the number of participating electrons,  $A$  is the area of electrode in cm<sup>2</sup>,  $R$  is the universal gas constant,  $T$  is the temperature in Kelvin,  $\nu$  is scan rate in volts s<sup>-1</sup>,  $D$  is the diffusion coefficient in cm<sup>2</sup> s<sup>-1</sup> and,  $C$  is the concentration of the species in mol cm<sup>-3</sup>. During the experiment, the peak current ( $i_p$ ) will have a linear response to the changes in concentration of the reduced or oxidized form of the redox shuttle, although the total redox shuttle concentration should remain constant. The only variable expected to change in Equation 1 as the redox reaction progresses is the concentration, and thus the peak currents were used to track the progression of the chemical redox reaction as a function of time.

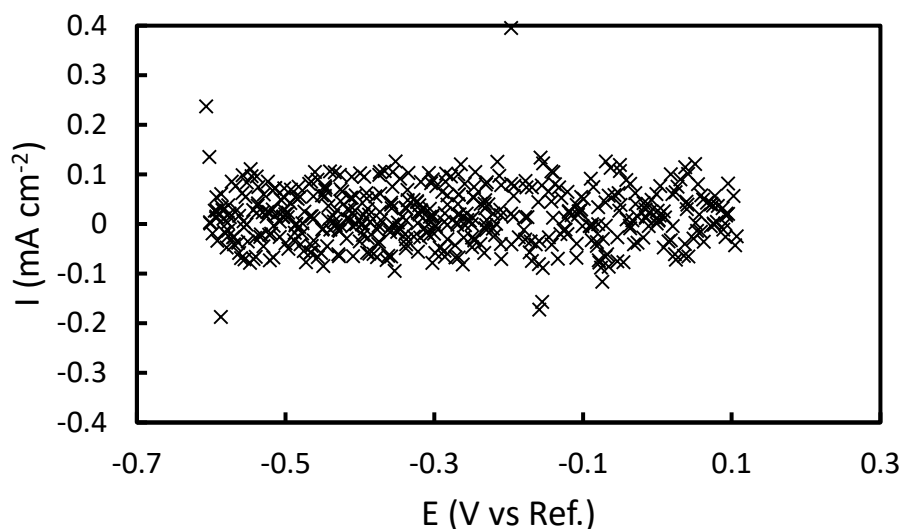


**Figure B7.** Background current of 500 mg LFP in three-electrode setup. The CV measurement was conducted at  $100 \text{ mV s}^{-1}$  with stirring at 130 rpm. A 1.6 mm Pt disc was the working electrode, a 4 cm long 0.5 mm diameter Pt wire was the counter electrode, and a Ag wire in an electrolyte containing 10 mM  $\text{AgNO}_3$  in 1.2 M  $\text{LiPF}_6$  in 3:7 ethylene carbonate:ethyl methyl carbonate (wt%:wt %) was used as the reference electrode. 500 data points are shown for clarity.

#### **Conversion and Kinetics using Johnson-Mehl- Avrami Erofeyev-Kolmogorov Analysis**

The Johnson-Mehl- Avrami Erofeyev-Kolmogorov (JMAEK) equation was used to derive the rate constant and phase transformation parameters for oxidation or reduction of solid electroactive material using redox shuttles. Use of the JMAEK model assumed single step nucleation, infinite system volume, and homogeneous distribution of nucleation sites within the system volume. Previously, this model has been used for electrochemical<sup>2-4</sup> and chemical<sup>5,6</sup> redox of LFP/FP under the assumption that nucleation and propagation of the phase transformation of LFP/FP was the rate limiting step. To apply JMAEK model,

conversion of solid electroactive material must be measured as a function of time and then applied in the following equation:

$$f = 1 - \exp(-kt)^n \quad (2)$$

where  $f$  is the volume fraction of the material that has been oxidized or reduced during the reaction,  $k$  is a first order rate constant,  $t$  is time, and  $n$  indicates Avrami exponent, which is related to the dimensionality of growth.  $n$  can be written as:

$$n = a + bc \quad (3)$$

where  $a$  is the nucleation index defined as  $N \approx t^a$ .  $N$  is the number of nuclei per unit volume and  $t$  is time.  $b$  is the dimensionality of the growth and  $b = 1, 2, 3$  for 1-D, 2-D, and 3-D growth, respectively.  $c$  is the growth index of the transformation and can take the value 1 for phase boundary control or 0.5 for diffusion-controlled growth.

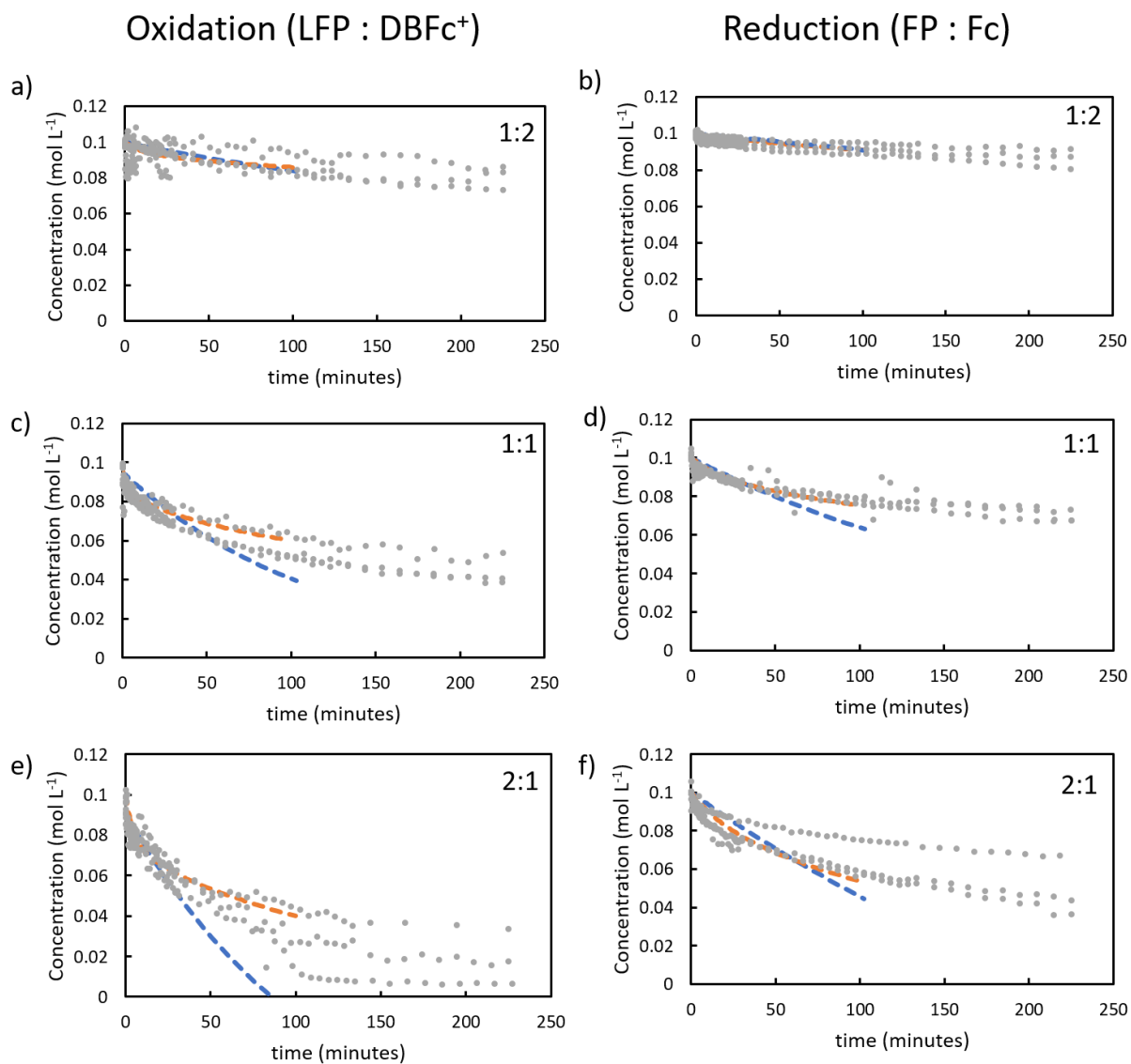


**Figure B8.** Redox shuttle concentrations as a function of time after initiating the batch reactor redox process. The solids used and their solution concentrations were a) 50 mM LFP, c) 100 mM LFP, e) 200 mM LFP, b) 50 mM FP, d) 100 mM FP and, f) 200 mM FP. For a), c), and e), the concentration displayed is for dibromoferrocenium (DBFc<sup>+</sup>) which was initially 100 mmol L<sup>-1</sup>, and for b), d) and, f) the concentration displayed is for ferrocene (Fc) which was initially 100 mmol L<sup>-1</sup>. The grey dots represent experimental data (there are triplicate runs in each plot) and the dashed

lines represent fits of the JMAEK kinetic model (blue) and 1-D kinetic model (orange) over the initial 100 minutes of the redox reaction.

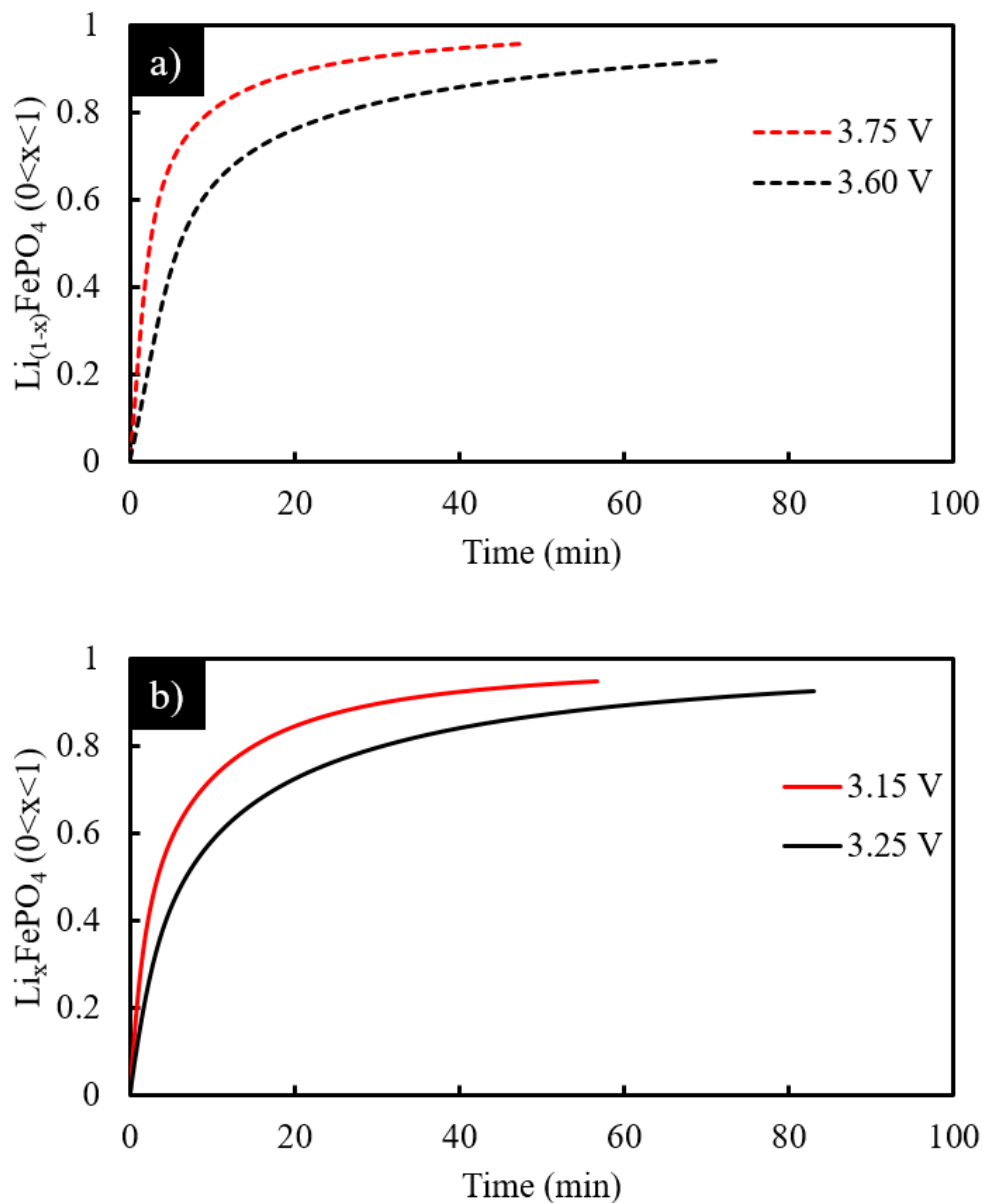


**Figure B9.** Conversion vs time curves for a) charge, and b) discharge of 2032-type coin cells containing of LFP cathodes and Li foil anodes. The cells were potentiostatically charged at 3.75

V (red, dashed) and 3.60 V (black, dashed) and potentiostatically discharged at 3.15 V (red, solid) and 3.25 V (black, solid), where all potentials were relative to Li/Li<sup>+</sup>.



**Figure B10.** Pt mesh coated from viscous DAFc<sup>+</sup> solution after performing bulk electrolysis on 100 mM DAFc (sample on left). A clean Pt mesh on the right is displayed for comparison.

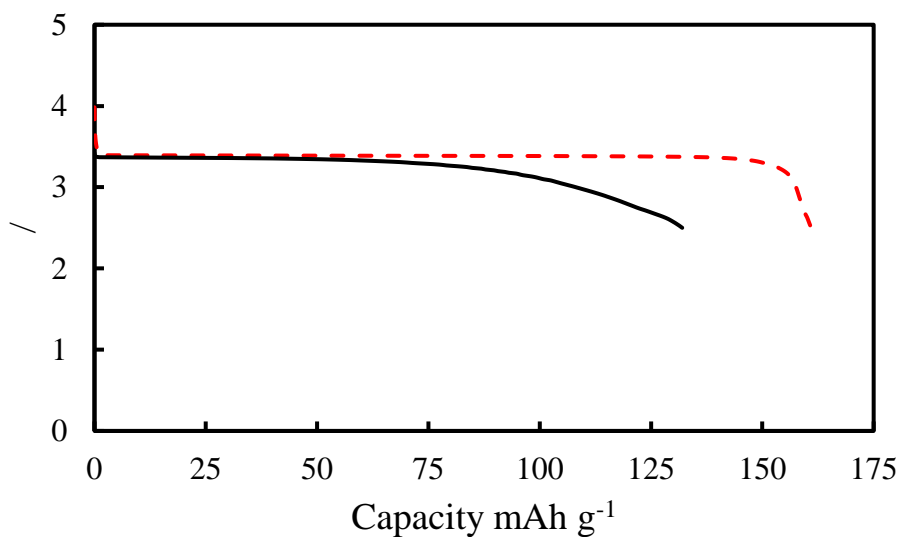


**Figure B11.** The first discharge cycle of a cathode containing as-prepared LFP (red, dashed) and FP prepared from chemical oxidation by H<sub>2</sub>O<sub>2</sub> (black, solid) paired with a lithium metal anode in

a coin cell. Discharge rate was C/20 for both cells, and the LFP electrode was charged at C/20 before discharge.

### 1- D Kinetic Model Description

Continuously stirring the batch reactor led to the assumption of spatially uniform redox shuttle and  $\text{Li}^+$  concentrations in the electrolyte phase (e.g., perfect mixing). The LFP/FP particles were assumed as spheres of uniform radius  $R$ , such that  $\text{Li}^+$  concentration in the solid phase was governed by the 1-D spherical transport equations listed below. These equations were solved by an implicit numerical method. The interfacial area per volume according (as used in electrochemical models such as Newman's work <sup>7</sup>) were calculated using the Brunauer-Emmett-Teller method on adsorption isotherms for the particles. Implicit numerical method solutions of the time-dependent differential equations below resulted in the concentration of redox shuttles as a function of time. The rate constant,  $k$ , was adjusted to minimize the difference between experimental and calculated concentration as a function of time during the first 100 minutes of the reaction.

### Equations

Reaction kinetics at the Solid/Liquid interface:

$$j = k \times c_{surface}^{Li}{}^p \times (c_{surface}^{Li,max} - c_{surface}^{Li})^q \quad (4)$$

$p = 1$  and  $q = 0$  during LFP oxidation/delithiation,  $p = 0$  and  $q = 1$  during FP reduction/lithiation

Lithium ion concentration in the liquid phase:

$$\varepsilon \frac{\partial c_t^{Li}}{\partial t} = Aj \quad (5)$$

Redox shuttle concentration in Liquid phase:

$$\varepsilon \frac{\partial c_t^{Rs}}{\partial t} = Aj \quad (6)$$

Lithium ion flux across the Solid/Liquid interphase:

$$j = -D_s \frac{\partial c_s^{Li}}{\partial r}, \text{ at } r = R \quad (7)$$

Lithium ion concentration in the solid phase:

$$\frac{\partial c_s^{Li}}{\partial t} = D_s \left( \frac{1}{r^2} \frac{\partial}{\partial r} \left( r^2 \frac{\partial c_s^{Li}}{\partial r} \right) \right) \quad (8)$$

## Model Inputs and Nomenclature

Properties	Symbol	Value	Source
Electrolyte Volume Fraction	$\varepsilon$	0.9977	Calculated based on experimental conditions
Solid State Diffusivity	$D_s$	$1.0 \times 10^{-17} \text{ cm}^2 \text{ s}^{-1}$	<sup>8</sup>
Interfacial Area	A	$2.61 \times 10^6 \text{ m}^{-1}$	Calculated from BET
Solid particle radius	R	30 nm	<sup>9</sup>
Redox shuttle Concentration	$c^{Rs}$	initially at $0.1 \text{ mol L}^{-1}$	
Li Concentration in Electrolyte	$c_l^{Li}$	initially $1.2 \text{ mol L}^{-1}$	
Li Concentration in Solid	$c_s^{Li}$	initially 22.059 or $0 \text{ mol L}^{-1}$	
$\text{Li}^+$ Flux Across Interface	J	varies with reaction progression	
Reaction rate Constant	k	determined for each case	
Reaction order	p, q	See Equation 4	

## References

1. M. N. Ates, C. J. Allen, S. Mukerjee, and K. M. Abraham, *J. Electrochem. Soc.*, **159**, A1057–A1064 (2012).
2. J. L. Allen, T. Richard Jow, and J. Wolfenstine, *Chem. Mater.*, **19**, 2108–2111 (2007).
3. J. L. Allen, T. R. Jow, and J. Wolfenstine, *J. Solid State Electrochem.*, **12**, 1031–1033 (2008).
4. K. Xiang, K. Yang, W. C. Carter, M. Tang, and Y. M. Chiang, *Chem. Mater.* (2018).

5. C. Kuss, M. Carmant-Dérival, N. D. Trinh, G. Liang, and S. B. Schougaard, *J. Phys. Chem. C*, **118**, 19524–19528 (2014).
6. D. Gupta and G. M. Koenig, *J. Electrochem. Soc.*, **167**, 020537 (2020).
7. T. F. Fuller, M. Doyle, and J. Newman, *J. Electrochem. Soc.*, **141**, 1–10 (1994).
8. K. Tang, X. Yu, J. Sun, H. Li, and X. Huang, *Electrochim. Acta*, **56**, 4869–4875 (2011).
9. Z. Qi, H. Dong, and G. M. Koenig, *Electrochim. Acta*, **253**, 163–170 (2017).

## *Appendix C*

This section provides additional information for Chapter IV and V.

Cyclic voltammetry on  $[\text{Fe}(\text{CN})_6]^{3-}/[\text{Fe}(\text{CN})_6]^{4-}$  solutions.

Ten solutions of predetermined blends of  $[\text{Fe}(\text{CN})_6]^{3-}$  and  $[\text{Fe}(\text{CN})_6]^{4-}$  were prepared in water ranging from 0 – 100%  $[\text{Fe}(\text{CN})_6]^{3-}$ . The total molarity of the solution was  $0.1 \text{ mol L}^{-1}$  (e.g. the 50% solution had  $0.05 \text{ mol L}^{-1}$   $[\text{Fe}(\text{CN})_6]^{3-}$  and  $0.05 \text{ mol L}^{-1}$   $[\text{Fe}(\text{CN})_6]^{4-}$ ). CV sweeps of each solution were collected using a Pt microelectrode working electrode ( $100 \mu\text{m}$  diameter) and Pt wire counter electrode, with a sweep rate of  $100 \text{ mV s}^{-1}$  between  $-0.05$  to  $0.5 \text{ V}$  (vs Ag/AgCl). Representative sweeps can be seen in Figure S1a, and the absolute value of the peak current for the different relative fractions of  $[\text{Fe}(\text{CN})_6]^{3-}$  can be found in Figure S1b.

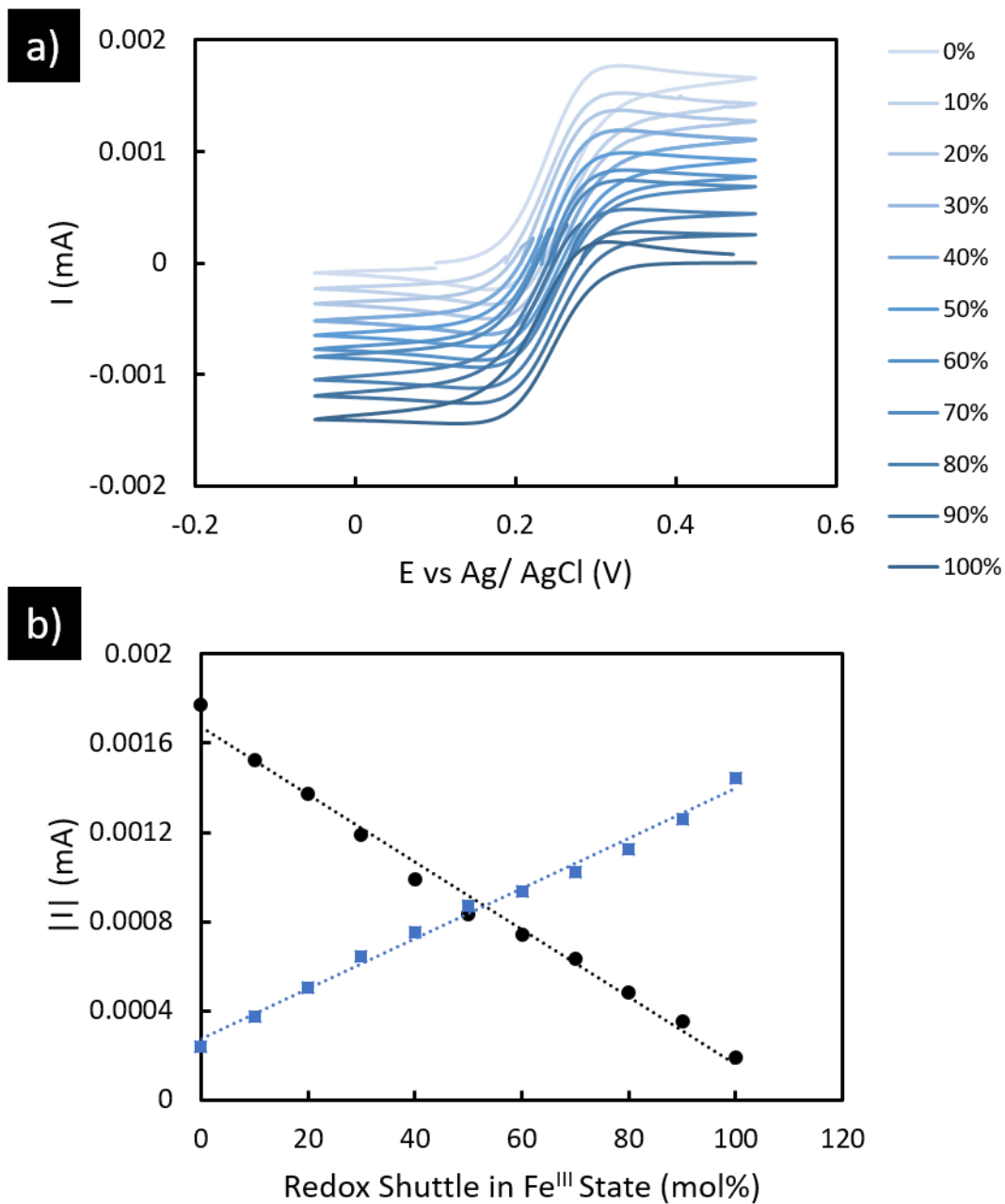


**Figure C1.** a) Cyclic voltammograms of different relative fractions of  $[\text{Fe}(\text{CN})_6]^{3-}$  and  $[\text{Fe}(\text{CN})_6]^{4-}$  in water, with the total concentration  $0.10 \text{ mol L}^{-1}$  and the fraction of that concentration which was  $[\text{Fe}(\text{CN})_6]^{3-}$  indicated on the legend to the right. b) Absolute value of peak currents from the CV

sweeps from oxidation of  $[\text{Fe}(\text{CN})_6]^{4-}$  to  $[\text{Fe}(\text{CN})_6]^{3-}$  (black circles) and reduction of  $[\text{Fe}(\text{CN})_6]^{3-}$  to  $[\text{Fe}(\text{CN})_6]^{4-}$  (blue squares). Trend lines added to guide the eye.

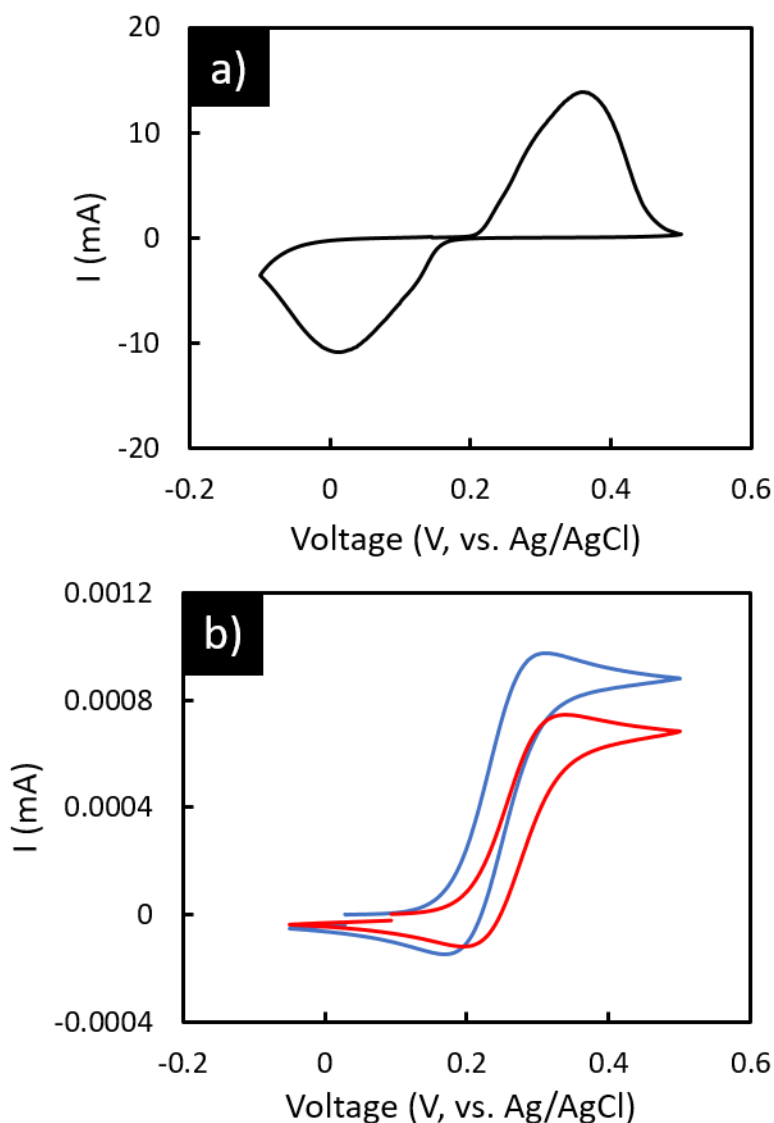


**Figure C2.** Cyclic voltammograms of a) LFP in 0.1 M Li<sub>2</sub>SO<sub>4</sub> solution, and b)  $[\text{Fe}(\text{CN})_6]^{3-}$  in water (blue) and 0.1 M Li<sub>2</sub>SO<sub>4</sub> solution (red). The working electrode for a) was LFP composite with carbon black and PVDF impregnated into Ni foam and, b) was 100  $\mu\text{m}$  Pt microelectrode. The reference electrode and counter electrode in both the experiments was Ag/AgCl (immersed in KCl gel electrolyte) and Pt wire, respectively. Sweeps were between -0.1 V and 0.5 V at 0.02  $\text{mV s}^{-1}$  for a) and 20  $\text{mV s}^{-1}$  for b).

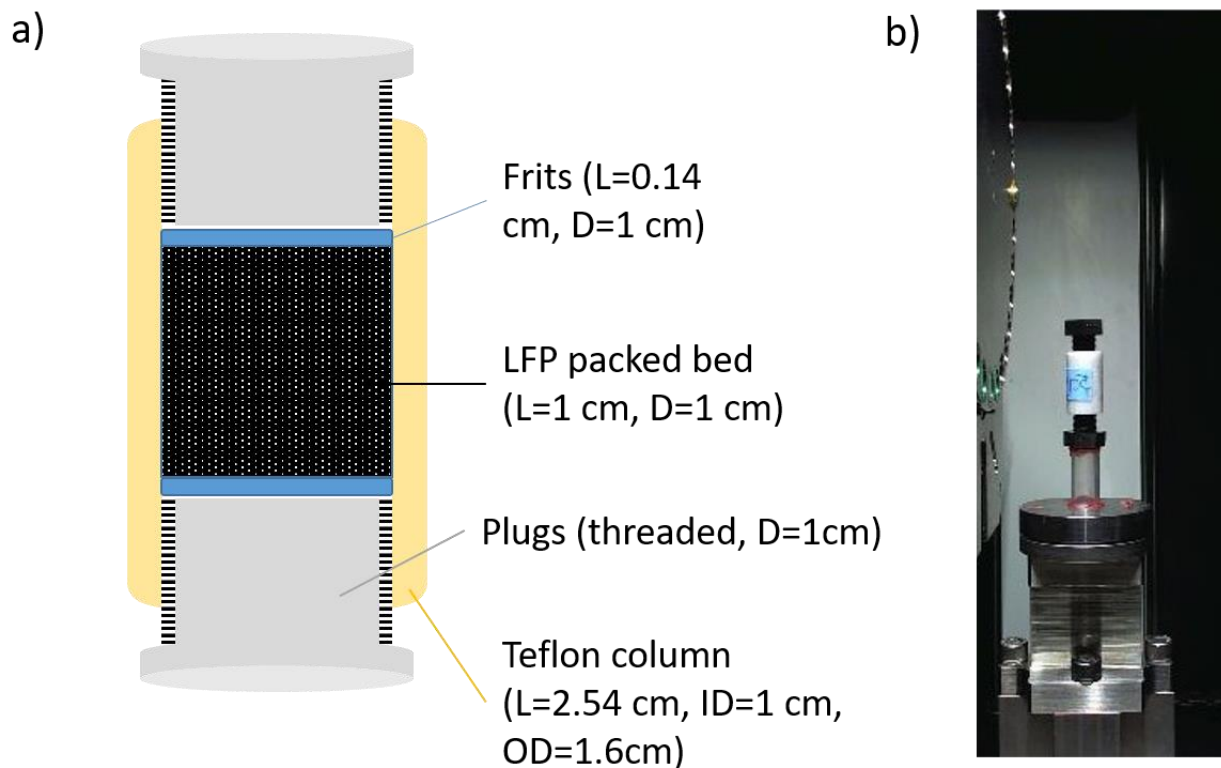


**Figure C3.** a) Illustration of sample used for X-ray computed tomography (XCT) and b) a photograph of the sample in the XCT instrument. LFP was packed in a custom capsule made by boring out a polytetrafluoroethylene (PTFE) column and was supported by PTFE frits on top and bottom and closed with polypropylene plugs. The bed area and powder loading were matched to experimental conditions used for the glass column shown in Figure 1a.

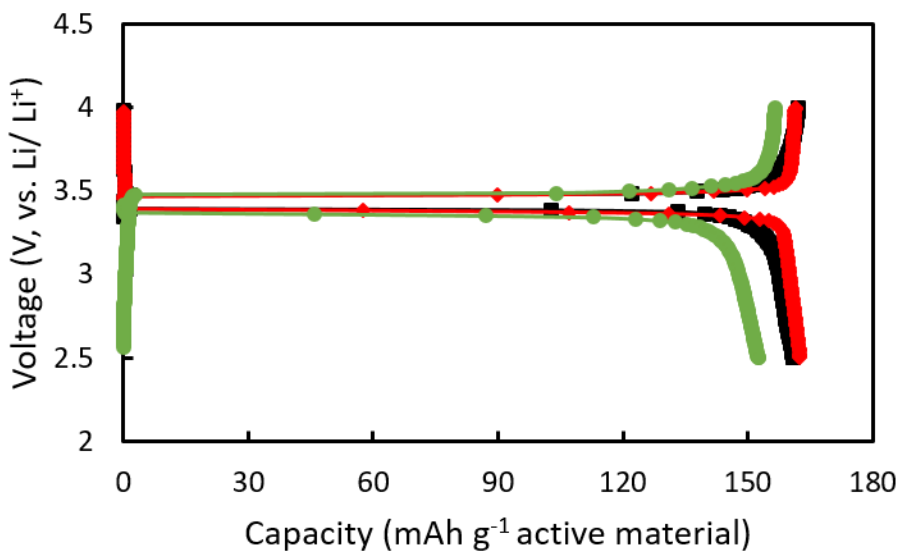


**Figure C4.** Charge and discharge voltage profiles for LFP as-received (black, squares), LFP sintered (red, diamonds), and LFP after chemical oxidation to FP after reaction with  $[\text{Fe}(\text{CN})_6]^{3-}$  in the packed bed (green, circles). The profiles shown are the initial charge/discharge cycles at a rate of C/20. The electroactive materials were in composite electrodes, had been paired with Li metal anodes, and were cycled between 4 and 2.5 V (vs. Li/Li<sup>+</sup>).

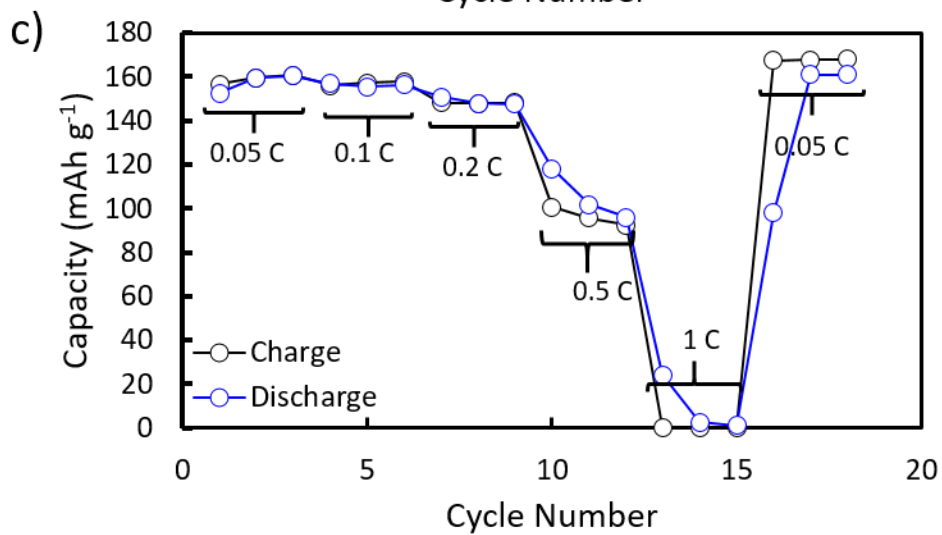
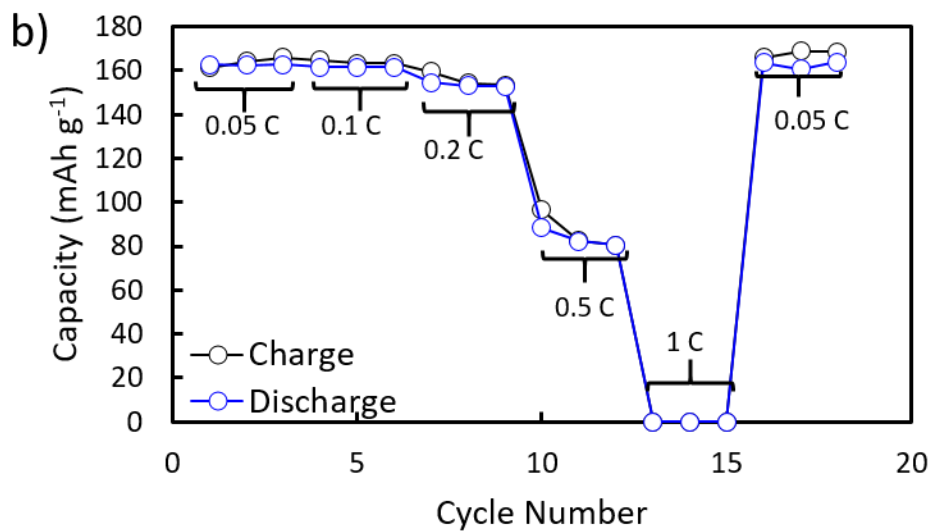
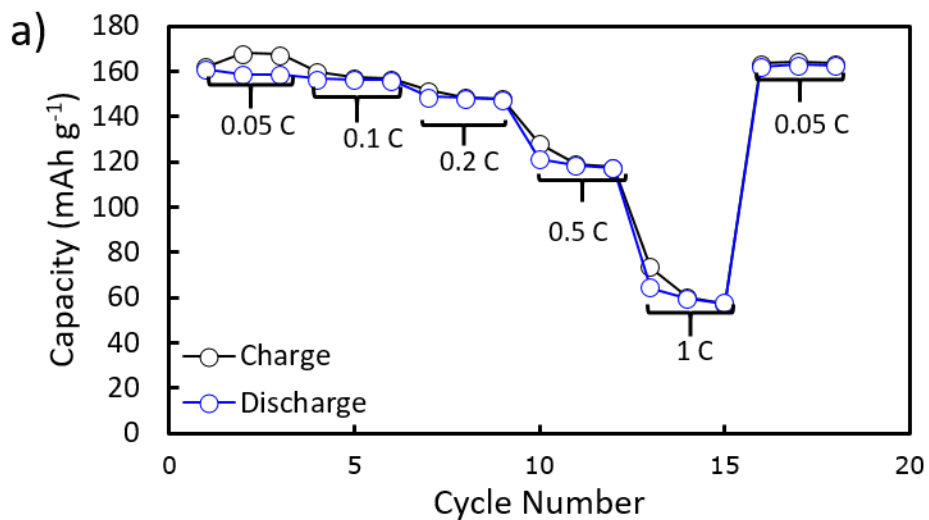


**Figure C5.** Charge (black circles) and discharge (blue circles) capacities during cycling at increasing C rates. The anodes were Li metal and the cathodes were composites containing a) as-received LFP, b) LFP-sintered cathodes, and c) LFP after chemical oxidation to FP after reaction with  $[\text{Fe}(\text{CN})_6]^{3-}$  in the packed bed. The cathode contained a ratio by weight of 80:10:10 LFP:carbon black:binder and the thickness was  $\sim 100 \mu\text{m}$  for a), and  $\sim 70 \mu\text{m}$  for b) and c). All charge and discharge cycles were conducted at the same rate with the rates indicated in the figures. 1C was assumed to correspond to  $160 \text{ mA g}^{-1}$  LFP, which resulted in 1C current densities of  $1 \pm 0.1 \text{ mA cm}^{-2}$  (with the variation reflecting variations in areal loading of active material).

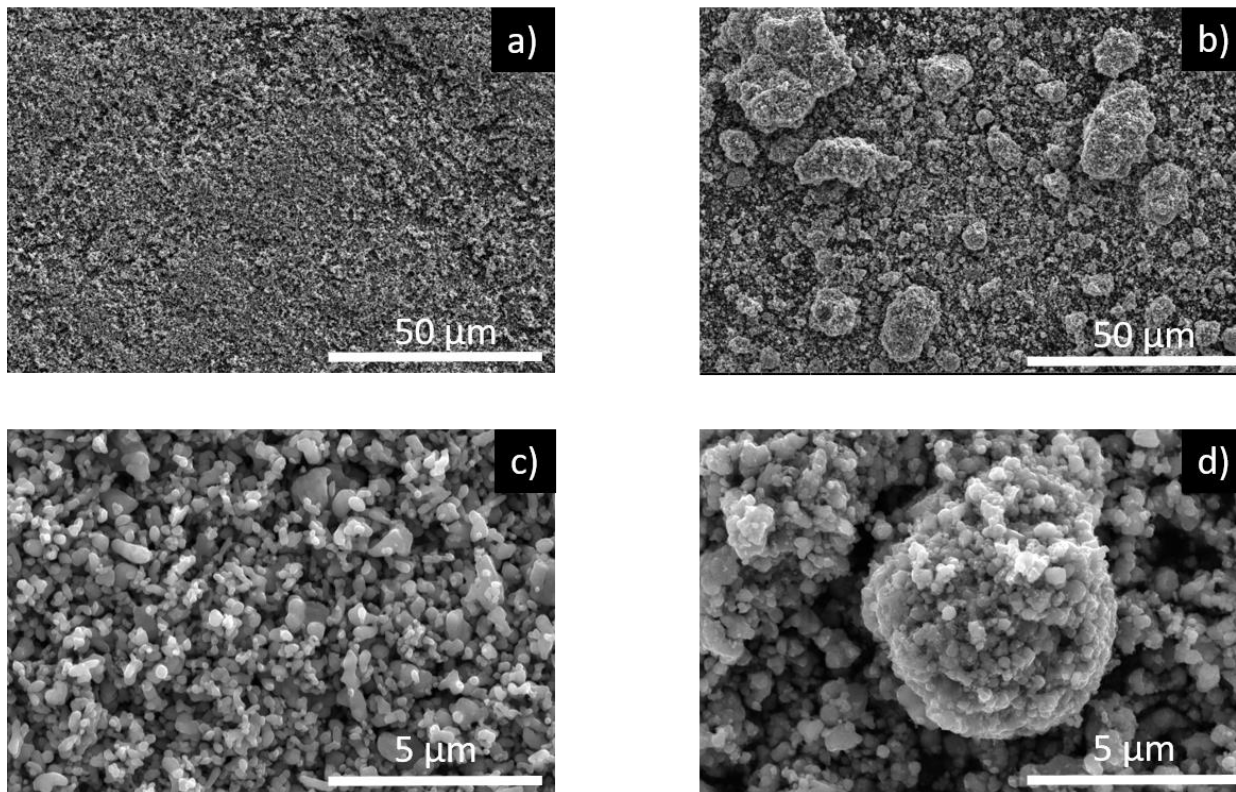


**Figure C6.** SEM images at relatively (a,b) lower and (c,d) higher magnification of (a,c) the as-received LFP and (b,d) LFP powder after sintering and grinding by hand.

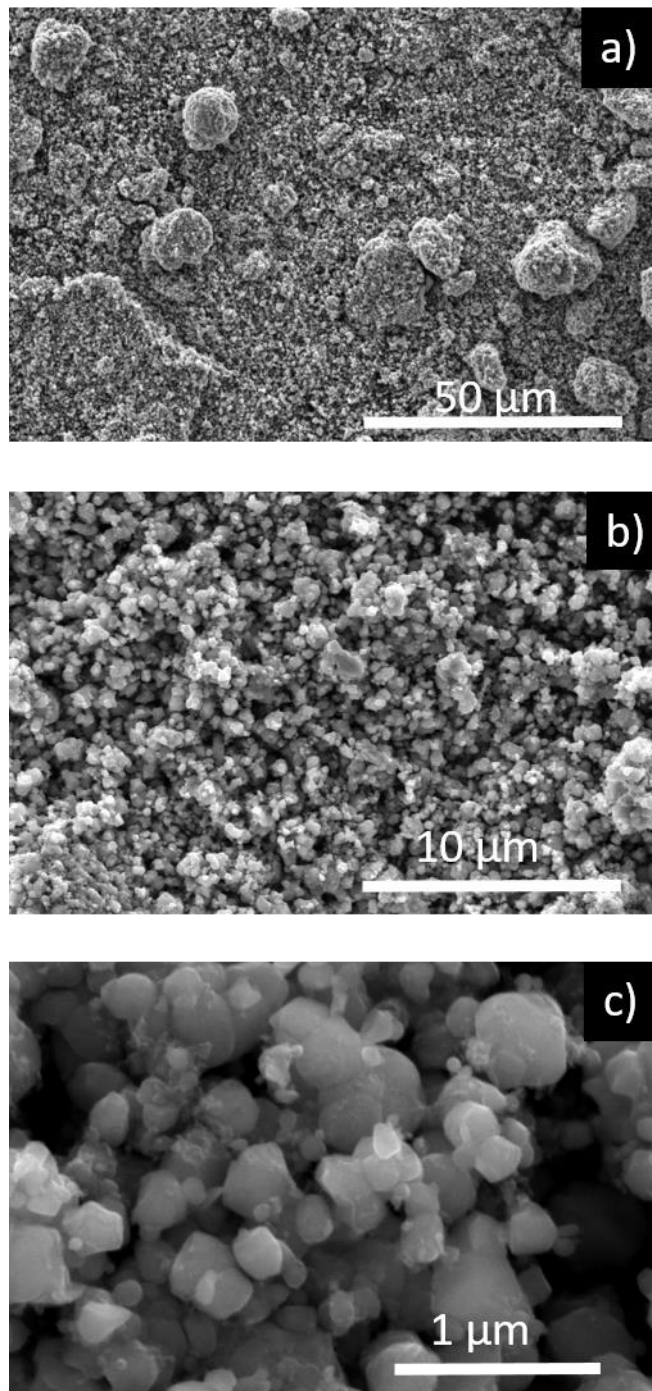


**Figure C7.** SEM images of LFP after oxidation of 100% to FP with  $[\text{Fe}(\text{CN})_6]^{3-}$  in the packed bed reactor at relatively a) low, b) higher, and c) highest resolution.

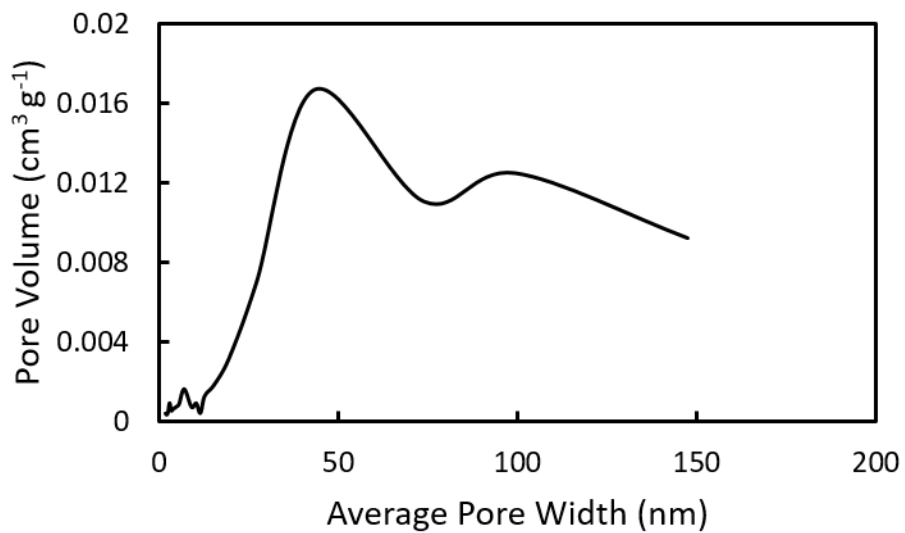


**Fig C8.** BJH incremental pore distribution of sintered (then pulverized by hand) LFP. The total pore volume was  $0.071\text{cm}^3\text{g}^{-1}$  LFP.

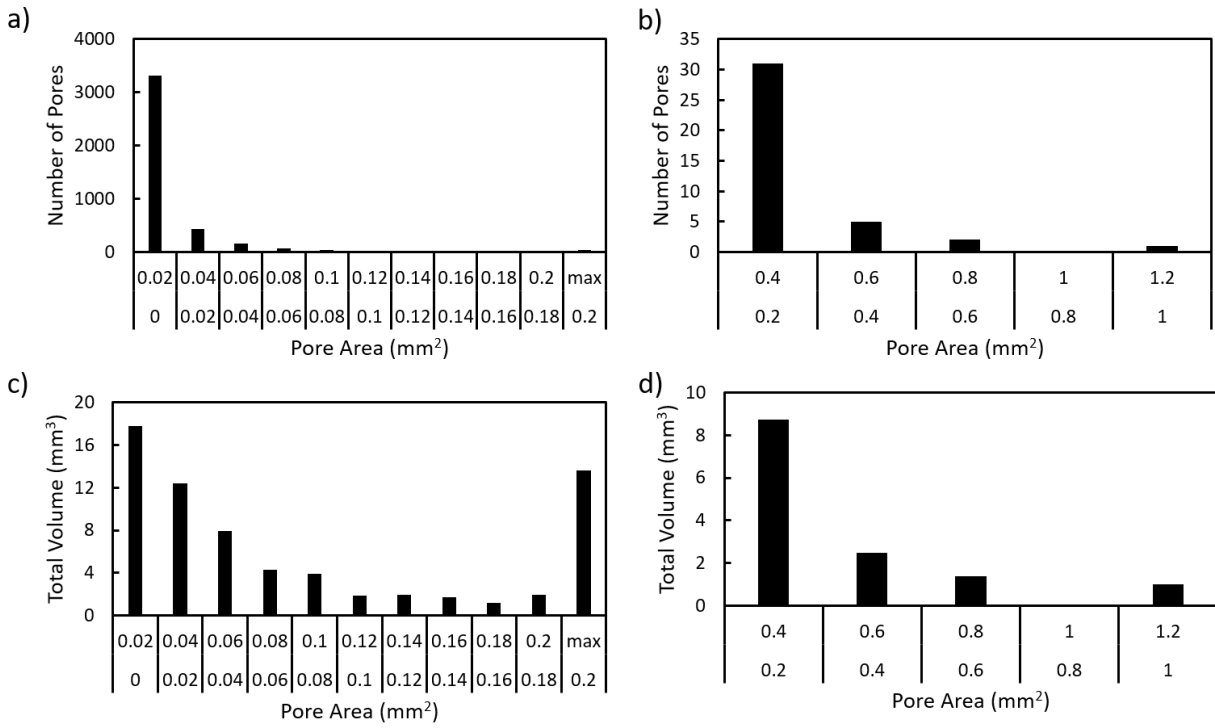


**Figure C9.** Quantitative analysis of pore sizes in LFP PBR determined using XCT: a) Pore size distribution of all pores, b) pore size distribution of 39 largest pores (those over 0.2 mm<sup>2</sup>), c) total volume of pores in each area segment, and d) total volume of pores with area greater than or equal to 0.2 mm<sup>2</sup>.

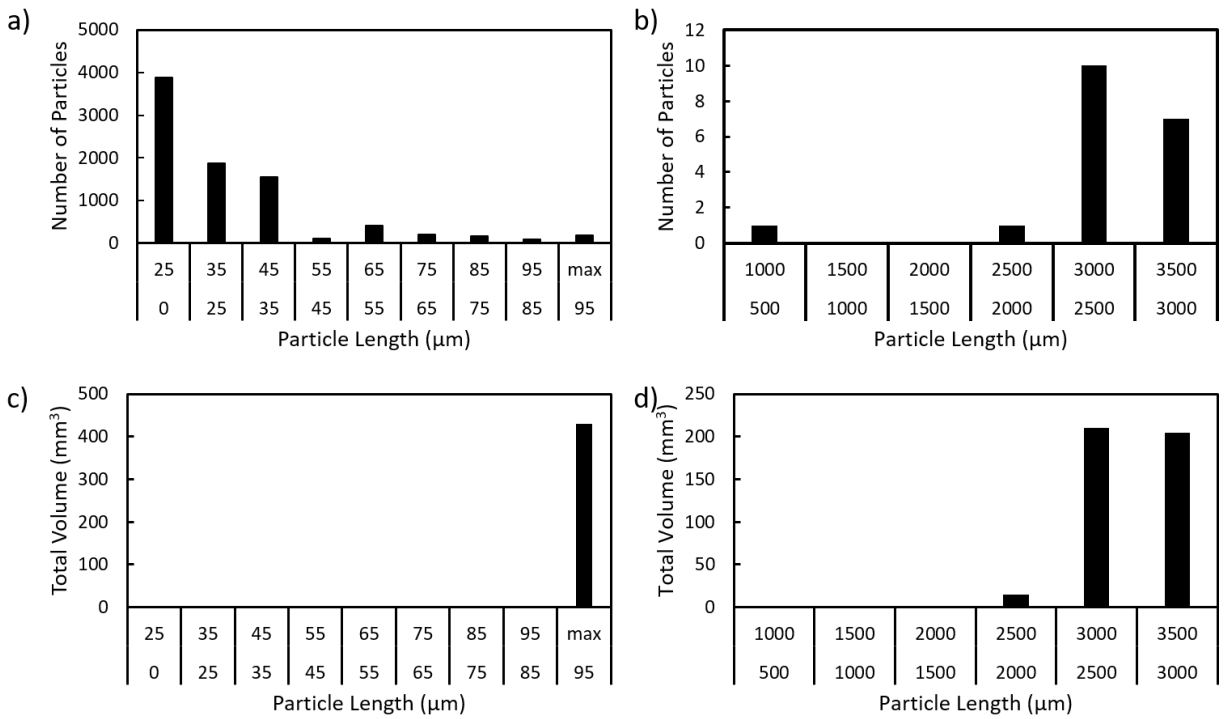


**Fig. C10.** Quantitative analysis of particle sizes in LFP PBR determined using XCT: a) Particle size distribution, b) particle size distribution of 20 largest particles (over 500 μm), c) total volume of particles in each length segment, and d) total volume of particles sized greater than or equal to 500 μm.

Equation to calculate Reynold's number (Re) through a packed bed [1]

$$Re = \frac{xU\rho_f}{\mu(1-\varepsilon)} \quad (1)$$

Definitions:

Abbreviation		Value
$\mu$	Viscosity of fluid flowing through the packed bed (Pa.s)	$9.532 \times 10^{-4}$ Pa. s
U	Superficial fluid velocity (m s <sup>-1</sup> )	Flow rate/Bed area
$\varepsilon$	Bed Voidage	0.634
x	Spherical equivalent particle diameter (m)	$33 \times 10^{-6}$ m
$\rho_f$	Density of fluid flowing through packed bed (kg m <sup>-3</sup> )	998 kg m <sup>-3</sup>

**Table C1.** Experimental conditions and LFP conversion at the end of each experiment. The final total molar ratio of  $[\text{Fe}(\text{CN})_6]^{3-}$  flown through the PBR relative to the moles of LFP was two in every condition listed below except for the 0.1 and 0.3 mol L<sup>-1</sup> shuttle concentrations, where it was 1 and 3, respectively. The conversion is after all the shuttle electrolyte had passed.

Temperature (°C)	LFP bed-height (cm)	Flow rate (mL hr <sup>-1</sup> )	Shuttle concentration (mol Lt <sup>-1</sup> )	Shuttle Volume (mL)	x in Li <sub>(1-x)</sub> FePO <sub>4</sub>
22.4	0.5	30	0.2	30	0.81±0.13
22.4	1.0	30	0.2	60	0.82±0.09
22.4	1.5	30	0.2	90	0.88±0.01
22.4	1.0	42	0.2	60	0.73±0.04
22.4	1.0	54	0.2	60	0.82±0.05
22.4	1.0	66	0.2	60	0.77±0.09
22.4	1.0	54	0.1	60	0.56±0.02
22.4	1.0	54	0.3	60	1.02±0.05
4.0	1.0	54	0.2	60	0.54±0.10
13.0	1.0	54	0.2	60	0.75±0.01
40.0	1.0	54	0.2	60	0.81±0.03

#### References-

- [1] J.B. Rawlings, J.G. Ekerdt, Chemical reactor analysis and design fundamentals, Nob Hill Pub, Llc, 2002.